Magneto-Inertial Dead-Reckoning in inhomogeneous field and indoor applications

Charles-Ivan Chesneau

To cite this version:

Charles-Ivan Chesneau. Magneto-Inertial Dead-Reckoning in inhomogeneous field and indoor applications. Optics / Photonic. Université Grenoble Alpes, 2018. English. NNT : 2018GREAT083 . tel-01966619v2

HAL Id: tel-01966619

https://theses.hal.science/tel-01966619v2

Submitted on 9 Apr 2019

Communauté
UNIVERSITÉ Grenoble Alpes

THÈSE
pour obtenir le grade de

DOCTEUR DE LA
COMMUNAUTÉ UNIVERSITÉ GRENOBLE ALPES
Spécialité : **AUTOMATIQUE-PRODUCTIQUE**
Arrêté ministériel : 25 mai 2016

Présentée par

Charles-Ivan CHESNEAU

Thèse dirigée par **Christophe PRIEUR**, Directeur de Recherche

préparée au sein du **Laboratoire**
Grenoble Images Parole Signal Automatique (GIPSA-lab)

dans **l'École Doctorale Eletronique Electrotechnique Automatique et Traitement du Signal (EEATS)**

Navigation à l'estime magnéto-inertielle en champ inhomogène et applications en intérieur

Magneto-Inertial Dead-Reckoning in inhomogeneous field and indoor applications

Thèse soutenue publiquement le **15 novembre 2018**,
devant le jury composé de:

Monsieur Vincent ANDRIEU
Chargé de Recherche, CNRS, LAGEP, Rapporteur
Monsieur Carlos SYLVESTRE
Professeur, Université de Macao, Chine, Rapporteur
Monsieur Silvère BONNABEL
Professeur, Mines ParisTech, Examinateur
Monsieur Nicolas LE BIHAN
Directeur de Recherche, CNRS, GIPSA-lab, Président
Monsieur Philippe MOUYON
Directeur de Recherche ONERA, Examinateur
Monsieur Christophe PRIEUR
Directeur de Recherche, CNRS, GIPSA-lab, Directeur de thèse
Monsieur Mathieu HILLION
Ingénieur de Recherche, SYSNAV, Encadrant

Magneto-Inertial Dead Reckoning in inhomogeneous field and indoor applications

---

Navigation à l'estime magnéto-inertielle en champ inhomogène et applications en intérieur

Charles-Ivan CHESNEAU

Résumé

Cette thèse concerne l'exploitation des inhomogénéités locales du champ magnétique en complément de techniques de navigation inertielles à composants liés “strapdown”, et son application à la navigation à l'estime en intérieur avec des capteurs magnéto-inertiels miniatures à bas-coût. Cette méthode permet une mesure indirecte de la vitesse du système indépendemment des mouvements de son porteur et fonctionne sans cartographie préalable du champ magnétique, ni infrastructure dédiée. Ce travail étudie la modélisation du problème de navigation, celle des capteurs utilisés, ainsi que l'effet des incertitudes de mesure sur la précision de reconstruction du mouvement et les limites de cette technique. Des algorithmes de navigation mettant en œuvre le filtrage de Kalman étendu sont implémentés, et évalués expérimentalement. Enfin, deux techniques de calibration de gradiomètres magnétiques sont proposées et testées, dans le double objectif d'en faciliter la réalisation à la fois en production et au cours de la vie d'un système.

Abstract

This thesis is about complementing strapdown inertial navigation techniques with the use of local magnetic inhomogeneity, and the application thereof to indoor dead-reckoning with low-cost micro-electromechanical magneto-inertial sensors. This method provides an indirect velocity measurement of the system independently of its wearer's movements and works without neither mapping of the magnetic field beforehand, nor dedicated infrastructure. Modelization of the navigation problem and our sensors are studied, together with the effect of measurement uncertainty on movement estimation accuracy and the limits of this technique. Navigation algorithms based on extended Kalman filtering are implemented and evaluated in experiments. Lastly, two magnetic gradiometers calibration techniques are introduced and tested, to ease its realization both in production and during the system's lifetime.

Remerciements

Je souhaite d'abord exprimer ma gratitude à mon directeur de thèse, Christophe Prieur, de m'avoir accompagné dans cette aventure, et pour la simplicité, la patience, et la responsabilité dont il a fait preuve tout au long de ma thèse.

I want to thank Professor Carlos Silvestre and Dr Vincent Andrieu for accepting to take the time to review my manuscript. Merci à Philippe Mouyon, Silvère Bonnabel et Nicolas Le Bihan d'avoir accepté de participer à mon jury.

J'aimerais également remercier Mathieu Hillion. Encadrant de mon premier stage en entreprise, à Sysnav, en 2011, son management m'a motivé à y revenir en thèse quelques années plus tard pour accélérer le développement de sa technologie magnéto-inertielle. Je garderai comme référence la méthode qu'il a su mettre en œuvre lors de mon stage et au début de ma thèse, pour en faire profiter à leur tour ceux sous ma responsabilité, comme l'a été Rémi Robin, dont il m'a confié l'encadrement, et à qui je suis reconnaissant pour cette collaboration qui a permis d'aboutir aux résultats présentés au chapitre 6 de ce manuscrit.

Mon expérience à Sysnav m'a démontré par l'exemple comment la recherche et l'innovation pouvaient bénéficier d'une dynamique d'équipe. C'est pourquoi j'aimerais remercier spécialement David Caruso, Quentin Desile, Georges Guy, Jean-Philippe Dugard, Hendrik Meier, et Adrien Rigaud pour le rôle direct qu'ils ont joué dans l'obtention des résultats des travaux que j'ai pu présenter. En particulier, Georges et Quentin pour leur disponibilité, leur pédagogie et leur savoir-faire précieux, chacun à leur manière, concernant le fonctionnement des capteurs et de l'électronique embarquée. Georges et Jean-Philippe pour les discussions instructives et animées que j'ai pu avoir avec eux sur la navigation inertielle, la modélisation physique, et les systèmes informatiques. Encore Georges, Mathieu, Quentin et Adrien pour le rôle que chacun a pu jouer et l'expertise de chacun d'eux dans les travaux sur la caractérisation et la calibration des capteurs. Merci vivement à David Caruso, dont la thèse s'est déroulée parallèlement à la mienne, dont la clairvoyance a contribué à guider mes recherches, et avec qui j'ai été et je serais heureux de travailler encore. Et enfin, Hendrik Meier, pour les nombreuses discussions techniques que nous avons pu avoir, sa curiosité et sa culture scientifique, et avec qui je partage la paternité de l'idée du chapitre 5 de mon manuscrit. Ces remerciements ne seraient pas complets sans mentionner Ludivine Mathé, Eric-Olivier Perrin, Jonathan Szabo, Pierre-Jean Bristeau, Augustin Jouy, mais aussi ceux qui ont quitté Sysnav avant que je soutienne, Samuel Cotard, Dominique Baëcile, Antoine Beaussire, Louis le Tarnec, Eric Dorveaux et Xavier Dorveaux, qui ont tous contribué à rendre mon travail possible ou à le faciliter.

Je remercie particulièrement Sonia Nogueira qui, efficace et chaleureuse, m'a donné le sourire à chacune de mes visites au laboratoire. Merci à Matthieu Muschinowski et Jonathan Dumon pour leur soutien dans la mise en oeuvre de la salle VICON au Gipsa-lab.

Je suis aussi profondément redevable à Patrick Rémy (Rémy), de m'avoir donné l'opportunité d'accomplir une mission d'ingénieur de recherche. Cette expérience m'a permis de prendre conscience des compétences développées au long de mon doctorat, et de celles sur lesquelles je dois encore travailler dans mon avenir profesionnel.

Merci à mes parents et à ma sœur de m'avoir conseillé et soutenu tout au long de mes travaux.

Pour conclure, je remercie David Vissière de m'avoir fait confiance après mon diplôme pour reprendre le flambeau, après Eric Dorveaux et Mathieu Hillion, des travaux sur la technique de navigation qui fait la signature de Sysnav, d'avoir pensé à moi lorsqu'il fallut réaliser des travaux en lien avec l'aéronautique, et de m'avoir accordé un peu de temps pour rédiger mon manuscrit et soutenir dans les délais.

Contents

List of Figures

List of Tables

Nomenclature

${}_j\mathbf{a}^{\mathrm{b}}$	Coordinates in body frame of the co-vector representing the j-th magnetometer scale factor and sensitive axis. Its components are denoted ${}_j a_i^{\mathrm{b}}$, $1 \leqslant i \leqslant 3$, except in Ch. 5 where they are denoted $\mathfrak{a}^j{}_i$.
${}_j\mathbf{p}^{\mathrm{b}}$	Coordinates in body frame of the vector representing the j-th magnetometer effective position. Its components are denoted ${}_j p_i^{\mathrm{b}}$, $1 \leqslant i \leqslant 3$, except in Ch. 5 where they are denoted ${}_j\mathfrak{p}^i$.
${}_j b$	Bias of the j-th magnetometer
${}_j y$	Theoretical output of the (uncalibrated) j-th magnetometer
μ_0	Magnetic constant
$[\boldsymbol{\omega}\times]$	Antisymmetric matrix that represents the cross product on by $\boldsymbol{\omega}$ on the left
$\mathbf{u} \cdot \mathbf{v}$	Dot product of vectors $\mathbf{u}$ and $\mathbf{v}$
$\mathrm{O}(3)$	Orthogonal group of dimension 3
$\mathrm{SE}(3)$	Special Euclidean group, representing rigid body motion in 3D
$\mathrm{SO}(3)$	Special orthogonal group of order 3 (or group of rotations in 3D)
Tr	Trace (sum of the diagonal elements of a square matrix)
$R_{\mathrm{f}_2 \leftarrow \mathrm{f}_1}$	Rotation matrix between two reference frames $\mathfrak{R}_{\mathrm{f}_1}, \mathfrak{R}_{\mathrm{f}_2}$ such that the change of coordinates verifies $R_{\mathrm{f}_2 \leftarrow \mathrm{f}_1} = \frac{\partial \mathbf{P}^{\mathrm{f}_2}}{\partial \mathbf{P}^{\mathrm{f}_1}}$
$\mathfrak{R}_{\mathrm{a}}$	Reference frame in which accelerometers are calibrated
$\mathfrak{R}_{\mathrm{b}}$	Reference frame moving with the rigid body and the sensors
$\mathfrak{R}_{\mathrm{g}}$	Reference frame in which gyrometers are calibrated
$\mathfrak{R}_{\mathrm{i}}$	Inertial frame of reference
$\mathfrak{R}_{\mathrm{m}}$	Reference frame in which magnetometers are calibrated
$\mathfrak{R}_{\mathrm{n}}$	Navigation frame (fixed with respect to the earth), in which the trajectory is estimated
$\mathcal{B}_{\mathrm{b}}$	Orthonormal basis associated with $\mathfrak{R}_{\mathrm{b}}$

$\mathcal{B}_\mathrm{i}$	Orthonormal basis associated with $\mathfrak{R}_\mathrm{i}$
$\mathcal{B}_\mathrm{n}$	Orthonormal basis associated with $\mathfrak{R}_\mathrm{n}$
$\chi_u(t, x_{t_0})$	Solution of the state equation Eq. (2.9) under the application of input u on $[t_0, t]$ and satisfying $\chi_u(t_0, x_{t_0}) = x_{t_0}$
$\mathcal{U}$	Open subset of $\mathbb{R}^m$ to which values of the input vector $u(t)$ belong
$\mathcal{X}$	Manifold in which lie values of $x(t)$
$\mathcal{Y}$	Open subset of $\mathbb{R}^p$ to which values of the output vector $y(t)$ belong
$u(t)$	Input vector in continuous-time state-space models
$x(t)$	State vector in continous-time state-space models
$y(t)$	Output vector in continuous-time state-space models
$\boldsymbol{\gamma}_\mathrm{meas}$	Biased accelerometer measurement ($\boldsymbol{\gamma}^\mathrm{b} + \mathbf{b}_\gamma$)
$\boldsymbol{\omega} = \boldsymbol{\omega}^{\mathrm{b/n}}$	Angular velocity of $\mathfrak{R}_\mathrm{b}$ with respect to $\mathfrak{R}_\mathrm{n}$
$\boldsymbol{\omega}^{\mathrm{b/i}}$	Angular velocity vector of $\mathfrak{R}_\mathrm{b}$ with respect to $\mathfrak{R}_\mathrm{i}$, and (unbiased) gyrometer measurement
$\boldsymbol{\omega}^{\mathrm{n/i}}$	Angular velocity vector of $\mathfrak{R}_\mathrm{n}$ with respect to $\mathfrak{R}_\mathrm{i}$
$\boldsymbol{\omega}_\mathrm{meas}$	Biased gyrometer measurement ($\boldsymbol{\omega}^{\mathrm{b/n}} + \mathbf{b}_\omega$)
$\boldsymbol{\gamma}^\mathrm{b}$	Proper acceleration vector (specific forces) in body frame, and (unbiased) accelerometer measurement
$\boldsymbol{\gamma}^\mathrm{n}$	Proper acceleration vector (specific forces) in the navigation frame
$\mathbf{a}^\mathrm{b}$	Acceleration vector of $\mathbf{M}$ in the navigation frame, expressed in body coordinates
$\mathbf{a}^\mathrm{n}$	Acceleration vector of $\mathbf{M}$ in the navigation frame
$\mathbf{B}^\mathrm{n}(\mathbf{P}^\mathrm{n}, t)$	Magnetic field in the navigation frame at position $\mathbf{P}^\mathrm{n}$ and time t
$\mathbf{g}^\mathrm{n}$	Gravity vector in the navigation frame
$\mathbf{v}^\mathrm{b}$	Velocity vector of $\mathbf{M}^\mathrm{n}$ in body frame coordinates
$\mathbf{v}^\mathrm{n}$	Velocity vector of $\mathbf{M}^\mathrm{n}$ in the navigation frame
$\nabla\mathbf{B}^\mathrm{n}(\mathbf{P}^\mathrm{n}, t)$	Gradient of the magnetic field at position $\mathbf{P}^\mathrm{n}$ and time t
$\mathbf{b}_\gamma$	Accelerometer biases
$\mathbf{b}_\omega$	Gyrometer biases
R	Attitude matrix, representing the orientation of the rigid body in $\mathfrak{R}_\mathrm{n}$

1. General Introduction

Contents

1.1. The subject

Location In France, in 2017, 73% of the population owned a smartphone.[1] These devices, along with many other consumer products, come with GPS chips, sensors, navigation software, developing the general perception that knowing one's position, or one's directions to anywhere is a given. This perception is consolidated by the tens of millions of commercial airplanes that take off every year in the world without getting lost (for most of them),[2] or missions such as Rosetta, a space probe which was accurately guided towards the comet 67P/Churyumov–Gerasimenko after a more than ten years flight. This observation originates from the spectacular technology advances in navigation and related fields, but should not overshadow that they still have limits associated with their accuracy, availability, and cost.

Inertial navigation One particular area of navigation techniques is called inertial navigation. It consists of exploiting inertia, the resistance of any massive object to changes in speed, direction... in order to deduce one's position, movement. The advantage of these techniques is that they are self-contained, in that they do not necessarily need to continually rely on dedicated infrastructure in order to keep their functionality. These techniques are widely used in aerospace applications and are being made accessible at lower cost with the advent of Microelectromechanical Systems (MEMS) sensors that are now ubiquitous in consumer electronics.

---

[1] Source: "Baromètre du numérique 2017", `https://www.arcep.fr/uploads/tx_gspublication/barometre_du_numerique-2017-271117.pdf`, July 2018

[2] Source: ICAO, `https://www.icao.int/sustainability/Pages/FR/FactsFigures_FR.aspx`, July 2018

Indoor navigation In indoor environments, buildings, in urban canyons and other situations, GPS is unreliable. Hence the active research on indoor positioning and navigation, with or without dedicated infrastructures. In the latter case, inertial navigation has naturally become of interest to researchers.

Low cost inertial indoor navigation, the need for auxiliary velocity information Contrary to their high-end counterparts, low-cost MEMS inertial sensors do not allow an accurate tracking over more than a few seconds up to a minute (see Ref. Woodman [2007]). Thus, so-called strapdown inertial navigation techniques have been combined with auxiliary velocity information in order to be made usable, e.g., Pedestrian Dead Reckoning (PDR) (see Ref. Foxlin [2005]). Let us illustrate the situation in the particular case of PDR. These algorithms apply when inertial sensors are worn on the foot of the user, and rely on the specific movement of the foot on the ground in order to provide an external velocity measurement whenever such a situation is detected. Pure inertial navigation is then only required for a second when the foot is off the ground. However, this kind of technique suffers from a lack of genericity.

Magnetic navigation Many researchers have noticed that the magnetic field in indoor environments suffers from severe distortions from ferromagnetic materials. While this is a problem for magnetic compassing, the idea of using it for positioning instead has emerged, following several leads. With, for example, mapping (see Ref. Storms [2009]), fingerprinting (see Refs. Haverinen [2014], Haverinen and Kemppainen [2009]), Simultaneous Localization and Mapping (SLAM) (see Ref. Kok and Solin [2018]), most of the current research has focused on map-based approaches allowing magnetic-field based absolute positioning in the map, with a strong temptation to rely on other techniques apparently more promising, such as Bluetooth beacons, or Visual Inertial Navigation (VIN) techniques such as in ARKit. In the meantime, a few papers have been published since the seminal paper Ref. Vissière et al. [2007a] towards an alternative way of using the magnetic field in a dead-reckoning framework instead of absolute positioning.

Magneto-Inertial Dead-Reckoning (MIDR) Ref. Vissière et al. [2007a] showed a way to use the magnetic field as an external velocity information input in a sensor fusion framework as early as 2007. The idea they proposed comes from the observation that, on Earth, the magnetic field is mostly stationary on time-scales of a few seconds to hours. In indoor environments, not only is the magnetic field stationary, but it varies with respect to the position in space, as this is evident by efforts at making magnetic maps for fingerprinting purposes, see, e.g., Ref. de Vries et al. [2009]. Then in such an environment, one can relate the speed of variation of the measured magnetic field with the traveling speed of the magnetic sensor, as long as information about spatial variations of the magnetic field is available. It is then possible to combine distributed magnetometry with an Inertial Measurement Unit (IMU) and obtain velocity estimates, without building any map.

Why so little attention? Despite this concept's apparent viability and simplicity of implementation, this field of research has been mostly ignored by the magnetic navigation community, as is apparent from the small number of publications on this subject. Refs. Vissière et al. [2007b, 2008], Dorveaux et al. [2011], Dorveaux [2011], Dorveaux and Petit [2011b], Praly et al. [2013], Batista et al. [2013] are an *almost* exhaustive list of publications on this navigation technique before the start of this work, mostly by the same authors. In particular, Ref. Dorveaux [2011] presents encouraging theoretical and successful experimental results. While it is true that magnetometer arrays are not widespread, this reason does not suffice to explain the factual situation.

State of the art in 2015 At the start of this work, the only comprehensive work on MIDR was Ref. Dorveaux [2011], work during which Refs. Dorveaux and Petit [2011a], Dorveaux et al. [2009a,b, 2010, 2011] were published. Theoretical results were provided, and navigation algorithms and calibration techniques were designed and tested on real-world experiments. These showed a performance with a drift of a few percents of the traveled distance. Attitude and velocity estimation were achieved using two separate observers. Afterward, in Ref. Praly et al. [2013], the use of this navigation technique for space applications was studied, and Ref. Batista et al. [2013] investigated a possible extension of the theoretical observability results of Ref. Dorveaux [2011].

Related publications during this work After 2015 and in parallel of this work, Refs. Caruso et al. [2016, 2017a,b,c] were published, providing a framework in which VIN and MIDR can be combined seamlessly, resulting in a robust navigation solution, where each technique may fail in the dark or in homogeneous field conditions. Finally, Ref. Skog et al. [2018] rediscovered the technique from a Bayesian filtering viewpoint, proposing an extension enabling pure Magnetic Dead-Reckoning, by proving that in the presence of magnetic field gradient, magnetometer measurements suffice to obtain the rate of turn.

Why naming the technique MIDR? The navigation technique which is the main topic of this work was called in Ref. Dorveaux [2011] the Magneto-Inertial NAVigation (MINAV) technique. For the sake of precision in this manuscript, the MINAV technique described above will be referred to as MIDR. The reason for this choice is that it only uses magnetic and inertial measurements, hence the term "magneto-inertial". Moreover, as formulated since the seminal paper, it is *not* a positioning technique, but a velocity estimation technique. Thus, it only produces trajectories by path integration, hence the term "dead-reckoning".

Goals This work has been set up in order to understand the key factors that make an accurate and robust MIDR system and improve on them. Initially, the formulated goal used to be hybridization with PDR in real-time embedded systems with an Extended Kalman Filter (EKF). The direction taken during this work was to avoid restricting oneself into the PDR framework, because PDR is arguably distinct from MIDR, at least in its approach, usefulness, and sources of error, and to restart from strapdown inertial navigation principles instead.

1.2. Scope

The general problem studied in this work is the trajectory reconstruction of a sensor board equipped with low-cost MEMS inertial sensors and an array of at least three non-aligned 3-axis magnetometers. This theoretical and practical problem can be divided into two main parts, concerning navigation algorithms and estimation errors, and sensor model identification.

The targeted application is indoor navigation: the Earth's curvature and its angular velocity are neglected. No assumption is made about the nature of the movement or the carrier. However, assumptions are made on properties of the ambient magnetic field.

Navigation algorithms are restricted to dead-reckoning. They are considered as *nonlinear observers* for dynamical systems, and all experiments are carried out using EKFs.

The hardware configuration itself has been inherited from previous works (see, e.g., Ref. Dorveaux [2011]). The prototype described in Ch. 3, designed and provided by SYSNAV at the beginning of this work, which is a realization of this configuration, is therefore not a contribution of this work. However, it is mentioned that the MIDR navigation technique can be extended to higher spatial derivatives (see Sec. 2.2.2) with an adequate arrangement of magnetometers (see Sec. 3.2.6).

Navigation algorithms studied in Ch. 2 and 4 rely on the availability of direct measurements of the magnetic field gradient; an array of single-axis magnetometer is *one* possible way of obtaining them. Chapters 3, 5 and 6 are more specific to this hardware configuration.

1.3. Main contributions

The main contributions of this work are the following.

1. Modeling of the navigation problem, in a way that is suitable for MIDR with low-cost MEMS sensors and in indoor environments, with an initial study of observability issues. The approach is built on strapdown inertial navigation and compared with the state of the art. In an inertial frame, if the spatial gradient of the magnetic field is non-singular, attitude is proven observable, heading unobservable, and velocity observability depends on the trajectory if inertial sensor biases are considered.

2. Study of a hardware prototype and the effect of measurement errors on trajectory estimation. A model of a magnetometer array provided by SYSNAV is verified, and the effects of calibration errors are studied, providing insights for the prediction and interpretation of estimation errors in the context of MIDR.

3. Implementation and evaluation of discrete-time EKFs on experimental data, and study of a magnetic heading estimation method.

4. High precision calibration techniques suitable for the considered hardware. Two techniques are introduced. The first one is a flexible technique suitable for factory calibration of a magnetometer array, and enables the complete and accurate calibration of a magnetometer array with an arrangement of coils, together with the calibration of the coils. This process provides an accurate tracking of the array inside of the coils; such information greatly reduces the requirements on sensor placement inside of coils systems. It is illustrated with Helmholtz coils but is generalizable to other configurations (Braunbeck coils, Maxwell coils...). The second one is suitable for setups for which positioning information is available during the process, and enables the self-calibration of magnetometer arrays in such setups. It can be seen as a problem inverse of MIDR. Identifiability is mathematically proven, tested in simulation, and results of an identification experiment using motion capture equipment are provided.

1.4. Outline

This document is divided into two parts. Part I is about navigation algorithms. In this part, Ch. 2 models the navigation problem and studies observability issues, Ch. 3 studies measurement errors, and Ch. 4 describes the implementation and evaluation of EKF-based navigation algorithms. Part II is about parameter identification algorithms for the calibration of magnetometer arrays. A Helmholtz-coils based calibration (and localization) technique, generalizable to other arrangements of coils, is described in Ch. 5. Finally, the calibration of magnetometer arrays using motion information is studied in Ch. 6.

The list of used abbreviations is on p. 183.

1.5. Publications

Conference papers

- C.-I. Chesneau, M. Hillion, and C. Prieur. Motion estimation of a rigid body with an EKF using magneto-inertial measurements. In *2016 International Conference on Indoor Positioning and Indoor Navigation (IPIN)*, Alcalá de Henares, Spain, Oct 2016. doi: 10.1109/ipin.2016.7743702

- C.-I. Chesneau, M. Hillion, J.-F. Hullo, G. Thibault, and C. Prieur. Improving magneto-inertial attitude and position estimation by means of a magnetic heading observer. In *2017 International Conference on Indoor Positioning and Indoor Navigation (IPIN)*, Sapporo, Japan, Sep 2017. doi: 10.1109/ipin.2017.8115862

Journal paper

- C.-I. Chesneau, R. Robin, H. Meier, M. Hillion, and C. Prieur. Calibration of a magnetometer array using motion capture equipment (to appear). *Asian Journal of Control*, 2019

Patents

- Détermination de cap à partir du champ mesuré par des capteurs magnétiques. *Patent Application B250181FR*, 2017d
- Procédé et dispositif de caractérisation d'un cap déterminé à partir de la mesure du champ magnétique. *Patent Application B250150FR*, 2017b
- Procédé de calibration d'un magnétomètre. *Patent Application B250148FR*, 2017a
- Procédé de calibration d'un magnétomètre. *Patent Application B250151FR*, 2017c

Part I.

Magneto-Inertial Dead-Reckoning

2. Observability in the Magneto-Inertial Dead-Reckoning framework

Contents

2.1. Magnetic navigation using observers for non-linear dynamical systems

Objective Let us consider a rigid body strapped with inertial and magnetic sensors. Information on its trajectory is desired, and it is assumed that dead-reckoning solutions are an option. What technique is available to achieve this?

Strapdown inertial navigation Strapdown inertial navigation is defined by the use of gyrometers and accelerometers strapped onto the rigid-body whose localization is sought. It consists in integrating kinematics differential equations (see Refs. Savage [2000], Woodman [2007]) from their measurements. This formulation is well suited for being used in conjunction with so-called observers for nonlinear systems; therefore, this work is limited to this scope.

Magnetic navigation Usually, in this context, the magnetic field is only used as a heading reference in order to correct integration results. However, on earth, the magnetic field is generally not homogeneous (see. Fig. 2.1). This is so whatever the scale at which it is considered, as is evident from Ref. [Dorveaux, 2011, Table 2.1]. In particular, indoor environments are rich in ferromagnetic materials distorting the magnetic field, at a level measurable with low-cost magnetic sensors, see, e.g., Ref. de Vries et al. [2009], and compromising the use of the magnetic field as a heading reference. Nevertheless, this property makes it a variable of interest with regards to positioning instead, see, e.g., Refs. Gozick et al. [2011], Haverinen [2014], Haverinen and Kemppainen [2009], Shen et al. [2016], Storms et al. [2010], and more recently Ref. Kok and Solin [2018].

Usual, map-based approaches There is no single way of accounting for the magnetic field in the framework of observers for non-linear dynamical systems. In the usual fingerprinting/mapping approaches, the magnetic field inhomogeneity as a function of space is used to reconstruct the *absolute* trajectory by comparing it to a pre-existing map (see for example Ref. Storms [2009]). The various techniques revolve around mapping, for example, the intensity of the magnetic field in one dimension (in corridors for example), two, or three dimensions, then taking one or a sequence of measurements and matching them to the map.

Dead-Reckoning approaches By contrast with map-based approaches, in Magneto-Inertial Dead-Reckoning (MIDR) (see, e.g., Ref. Dorveaux [2011]), which is the topic of this work, the magnetic field is considered in that in the body frame, it is a function of *time*. Its temporal evolution is linked to velocity through the spatial gradient of the magnetic field, which enables trajectory reconstruction in a *dead-reckoning framework* when the latter is known.

Importance of the choice of model This model difference results in two entirely different approaches: magnetic fingerprinting involves a magnetic map, whereas MIDR

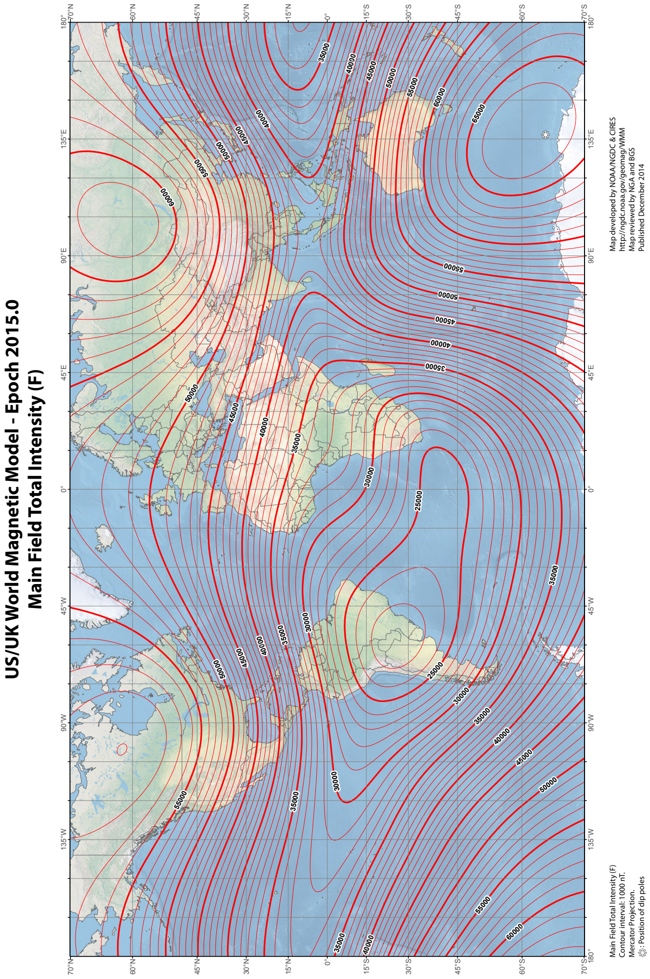

Figure 2.1: Total magnetic field intensity map, according to the WMM 2015 (World Magnetic Model)
https://www.ngdc.noaa.gov/geomag/WMM/data/WMM2015/WMM2015_F_MERC.pdf

does not. Magnetic fingerprinting provides absolute positioning in the map, whereas MIDR does not since no map is kept during the estimation process, but it provides velocity instead. Therefore it is clear that the choice of model for the same physical system is a crucial step that needs to be carefully considered.

Questions Given the importance of modeling choices, it is worth spending time considering the underlying model that one will later try to observe. That is to say, the following questions must be answered:

- What information do magnetic field measurements provide about the trajectory?
- What is the adequate state-space model that must be observed?

These questions will be answered more specifically in the scope of low-cost strapdown Microelectromechanical Systems (MEMS) inertial navigation in indoor environments.

Method Our approach is based on known MIDR models in the literature which we review critically with respect to observability. Possible model candidates are deduced from these references, and the distinguishability of trajectories from each other given available measurements is studied. To that end, the following references are considered: Ref. Dorveaux [2011], the Ph.D. Thesis of E. Dorveaux on the subject, Refs. Vissière et al. [2007a,b], seminal papers on the subject, and Ref. Batista et al. [2013], which is about observability in a previously identified corner case. This chapter then serves as a justification of the work regarding observer design and experimental evaluation that was undertaken mainly in Ch. 4 and Refs. Chesneau et al. [2016, 2017], but also of the rest of this thesis to a lesser extent.

Outline In Sec. 2.2, notations are defined, and a problem statement is formulated. In Sec. 2.3, results from Ref. Dorveaux [2011] are recalled, and reasons for considering alternative modeling architecture are provided. In Sec. 2.4, Refs. Vissière et al. [2007a,b] are briefly reviewed, and a minimal dynamical model is proposed and studied. Sec. 2.5 discusses the implications of using low cost inertial sensors in this context, and Sec. 2.6 concludes this chapter.

2.2. Problem statement

Let us come back to the considered rigid body that is moving in some navigation frame. It is equipped with strapdown MEMS inertial sensors, and with a magnetic measurement unit, such that both the vector components and the local spatial gradient of the magnetic field are measured at some fixed point of the rigid body. Moreover, let us assume that the magnetic field is stationary, that is to say, it is time-invariant in the navigation frame. The problem under consideration in this chapter is to provide a model that connects measurements and trajectory information together and determine what trajectories are distinguishable by only said measurements: those provided by the Inertial Measurement Unit (IMU) and those of the magnetic field. The underlying notion is that of observability.

2.2.1. Notations and definitions

Frames of reference

Let us consider three reference frames. Let $\mathfrak{R}_{\mathrm{b}}$ be a reference frame moving with the rigid body and $\mathcal{B}_{\mathrm{b}}$ an associated orthonormal basis. Sensors are fixed in this reference frame. Let $\mathfrak{R}_{\mathrm{n}}$ be the navigation frame, with $\mathcal{B}_{\mathrm{n}}$ an associated orthonormal basis. This is the frame in which the trajectory is estimated. Let us denote $\mathfrak{R}_{\mathrm{i}}$ an inertial frame of reference, and $\mathcal{B}_{\mathrm{i}}$ an associated orthonormal basis.

(Cartesian) coordinates in $\mathfrak{R}_{\mathrm{b}}$ (resp. $\mathfrak{R}_{\mathrm{n}}$ and $\mathfrak{R}_{\mathrm{i}}$) are denoted with the exponent $^{\mathrm{b}}$ (resp. $^{\mathrm{n}}$ and $^{\mathrm{i}}$). For example,

$$\mathbf{v}^{\mathrm{n}} = \begin{pmatrix} v_1^{\mathrm{n}} \\ v_2^{\mathrm{n}} \\ v_3^{\mathrm{n}} \end{pmatrix} ,$$

denotes the coordinates of a vector $\mathbf{v}^{\mathrm{n}}$ in $\mathfrak{R}_{\mathrm{n}}$.

In the following, $\mathfrak{R}_{\mathrm{n}}$ is assumed fixed with respect to the earth.

Trajectory

Let $\mathbf{M}$ be a fixed point of the rigid body. By convention, let us define its Cartesian coordinates in body frame as $\mathbf{M}^{\mathrm{b}}$. An attitude matrix $R \in \mathrm{SO}(3)$ representing the orientation of the rigid body in $\mathfrak{R}_{\mathrm{n}}$ is defined such that in terms of matrix relations, for any point $\mathbf{P}$ whose coordinates in $\mathfrak{R}_{\mathrm{b}}$ are $\mathbf{P}^{\mathrm{b}}$, the change of coordinates between $\mathfrak{R}_{\mathrm{n}}$ and $\mathfrak{R}_{\mathrm{b}}$ reads

$$\mathbf{P}^{\mathrm{n}} = R(\mathbf{P}^{\mathrm{b}} - \mathbf{M}^{\mathrm{b}}) + \mathbf{M}^{\mathrm{n}} . \tag{2.1}$$

The trajectory of the rigid body is defined as the evolution of $(R, \mathbf{M}^{\mathrm{n}}) \in \mathrm{SE}(3)$ with time, where SE(3) denotes the special Euclidean group that represents rigid body motion. Let us remark that since $R \in \mathrm{SO}(3)$, then $R^{-1} = R^{\top}$. The time variable is denoted t.

Eq. (2.1) implies

$$\frac{\partial \mathbf{P}^{\mathrm{n}}}{\partial \mathbf{P}^{\mathrm{b}}} = R .$$

Therefore, for any pair of reference frames $\mathfrak{R}_{\mathrm{f}_1}, \mathfrak{R}_{\mathrm{f}_2}$

$$R_{\mathrm{f}_2 \leftarrow \mathrm{f}_1} \doteq \frac{\partial \mathbf{P}^{\mathrm{f}_2}}{\partial \mathbf{P}^{\mathrm{f}_1}} . \tag{2.2}$$

The notation R is then an alias of $R_{\mathrm{n} \leftarrow \mathrm{b}}$.

Velocity

The velocity vector $\mathbf{v}^{\mathrm{n}}$ of $\mathbf{M}^{\mathrm{n}}$ in the navigation frame is defined as

$$\mathbf{v}^{\mathrm{n}} \doteq \frac{d\mathbf{M}^{\mathrm{n}}}{dt} . \tag{2.3}$$

This same 3-D vector can also be expressed in body frame while still representing the velocity vector of $\mathbf{M}$ in the navigation frame,

$$\mathbf{v}^{\mathrm{b}} \doteq R^{\top}\mathbf{v}^{\mathrm{n}} \ . \tag{2.4}$$

One must be careful that this definition of $\mathbf{v}^{\mathrm{b}}$ is *not objective* in that it is bound to the navigation frame $\mathfrak{R}_{\mathrm{n}}$. See also Ref. Matolcsi and Ván [2006]. This is deliberate, since the trajectory reconstruction problem is bound to $\mathfrak{R}_{\mathrm{n}}$: it would not make sense to define the change of frame in such a way that $\mathbf{v}^{\mathrm{b}}$ would become independent of $\mathfrak{R}_{\mathrm{n}}$. However, doing so might lead to some degree of confusion when computing time-derivatives not carefully. For instance, in general,

$$\mathbf{v}^{\mathrm{b}} \neq \frac{d\mathbf{M}^{\mathrm{b}}}{dt} \ .$$

Angular velocity

Let us denote $\boldsymbol{\omega} = \boldsymbol{\omega}^{\mathrm{b/n}} = (\omega_1, \omega_2, \omega_3)^{\top}$ the angular velocity of $\mathfrak{R}_{\mathrm{b}}$ with respect to $\mathfrak{R}_{\mathrm{n}}$. It is defined such that

$$\frac{dR}{dt} \doteq R[\boldsymbol{\omega}\times] \ , \tag{2.5}$$

where $[\boldsymbol{\omega}\times]$ denotes the antisymmetric matrix

$$[\boldsymbol{\omega}\times] \doteq \begin{pmatrix} 0 & -\omega_3 & \omega_2 \\ \omega_3 & 0 & -\omega_1 \\ -\omega_2 & \omega_1 & 0 \end{pmatrix} = -[\boldsymbol{\omega}\times]^{\top}.$$

The navigation frame $\mathfrak{R}_{\mathrm{n}}$ is fixed with respect to the Earth, which is not strictly speaking an inertial frame, because it is spinning. Thus, $\boldsymbol{\omega}^{\mathrm{b/n}}$ is not measurable directly with strapdown gyrometers. Instead, they are sensitive to the angular velocity vector of $\mathfrak{R}_{\mathrm{b}}$ with respect to $\mathfrak{R}_{\mathrm{i}}$ that is denoted $\boldsymbol{\omega}^{\mathrm{b/i}}$. Similarly, the angular velocity vector of $\mathfrak{R}_{\mathrm{n}}$ with respect to $\mathfrak{R}_{\mathrm{i}}$ is denoted $\boldsymbol{\omega}^{\mathrm{n/i}}$. The relationship between R, $\boldsymbol{\omega}^{\mathrm{b/i}}$ and $\boldsymbol{\omega}^{\mathrm{n/i}}$ is then

$$\frac{dR}{dt} = R[\boldsymbol{\omega}^{\mathrm{b/i}}\times] - [\boldsymbol{\omega}^{\mathrm{n/i}}\times]R \ . \tag{2.6}$$

Often, MEMS gyrometers are not considered sensitive enough to measure angular velocities whose magnitude is comparable with the earth's angular velocity.[1] This is why Eq. (2.5) is often used as if $\boldsymbol{\omega}^{\mathrm{b/n}}$ were measured directly, or as if the earth were not spinning.

Acceleration

Let us denote $\mathbf{a}^{\mathrm{n}}$ the acceleration vector of $\mathbf{M}$ in the navigation frame,

$$\mathbf{a}^{\mathrm{n}} \doteq \frac{d\mathbf{v}^{\mathrm{n}}}{dt} \ .$$

---

[1] The earth's angular velocity is ~ 15 deg /h

This same 3-D vector can also be expressed in body frame while still representing the same quantity[2],

$$\mathbf{a}^{\mathrm{b}} \doteq R^{\top}\mathbf{a}^{\mathrm{n}} \ .$$

Let us denote $\mathbf{g}^{\mathrm{n}}$ the local effective gravity vector in the navigation frame. Models of $\mathbf{g}^{\mathrm{n}}$ such as the World Gravity Model (WGM) include the effect of the Earth's rotation and the resulting centrifugal force.

Proper acceleration $\boldsymbol{\gamma}^{\mathrm{n}}$ is defined as the acceleration of $\mathbf{M}^{\mathrm{n}}$ with respect to a non-rotating reference frame that would be only subjected to gravity, that is to say (see Ref. Savage [2000]),

$$\mathbf{a}^{\mathrm{n}} = \boldsymbol{\gamma}^{\mathrm{n}} + \mathbf{g}^{\mathrm{n}} - 2\boldsymbol{\omega}^{\mathrm{n/i}} \times \mathbf{v}^{\mathrm{n}} \ , \tag{2.7}$$

where $-2\boldsymbol{\omega}^{\mathrm{n/i}} \times \mathbf{v}^{\mathrm{n}}$ represents the Coriolis acceleration. Equation (2.7) is only valid because of the choice of a Cartesian coordinatization, by neglecting the angular acceleration of $\mathfrak{R}_{\mathrm{n}}$, and by including the centrifugal force into $\mathbf{g}^{\mathrm{n}}$. Proper acceleration can also be expressed in body frame while still representing the same quantity,

$$\boldsymbol{\gamma}^{\mathrm{b}} \doteq R^{\top}\boldsymbol{\gamma}^{\mathrm{n}}$$

Strapdown accelerometers are sensitive to $\boldsymbol{\gamma}^{\mathrm{b}}$.

Magnetic field

Let us denote $\mathbf{B}$ the magnetic field. It is a vector field, which in general, depends on time and space. At any point $\mathbf{P}$ in space, the change of frame between $\mathfrak{R}_{\mathrm{b}}$ and $\mathfrak{R}_{\mathrm{n}}$ is assumed to be expressed as[3]

$$\mathbf{B}^{\mathrm{n}}(\mathbf{P}^{\mathrm{n}}, t) = R\mathbf{B}^{\mathrm{b}}(\mathbf{P}^{\mathrm{b}}, t) \ . \tag{2.8}$$

Admitting that the magnetic field is always regular enough, the Jacobian matrix at $\mathbf{M}$ of the magnetic field is defined as

$$\nabla\mathbf{B}^{\mathrm{n}}(\mathbf{M}^{\mathrm{n}}, t) \doteq \left.\frac{\partial(\mathbf{B}^{\mathrm{n}}(\mathbf{P}^{\mathrm{n}}, t))}{\partial(\mathbf{P}^{\mathrm{n}})}\right|_{\mathbf{P}^{\mathrm{n}}=\mathbf{M}^{\mathrm{n}}} ,$$

and

$$\nabla\mathbf{B}^{\mathrm{b}}(\mathbf{M}^{\mathrm{b}}, t) \doteq \left.\frac{\partial(\mathbf{B}^{\mathrm{b}}(\mathbf{P}^{\mathrm{b}}, t))}{\partial(\mathbf{P}^{\mathrm{b}})}\right|_{\mathbf{P}^{\mathrm{b}}=\mathbf{M}^{\mathrm{b}}} ,$$

with the change of frame

$$\nabla\mathbf{B}^{\mathrm{n}}(\mathbf{M}^{\mathrm{n}}, t) = R\nabla\mathbf{B}^{\mathrm{b}}(\mathbf{M}^{\mathrm{b}}, t)R^{\top}.$$

Magnetic sensors are assumed to provide direct and accurate measurements of $\nabla\mathbf{B}^{\mathrm{b}}(\mathbf{M}^{\mathrm{b}}, t)$ and $\mathbf{B}^{\mathrm{b}}(\mathbf{M}^{\mathrm{b}}, t)$. In this chapter, these notations are respectively shortened to $\nabla\mathbf{B}^{\mathrm{b}}$ and $\mathbf{B}^{\mathrm{b}}$ whenever these notations are non-ambiguous.

---

[2] This change of frame is not objective either

[3] Relativity and electrodynamics allow writing (2.8) as an approximation in $\frac{\|\mathbf{v}\|^2}{c^2}$ in absence of electric field and in $\frac{\|\mathbf{v}\|}{c}$ otherwise, where c is the speed of light. Even for $\|\mathbf{v}\|$ as high as 100m/s, neglecting this term is quite enough for use in pedestrian applications. By contrast, the same change of variable would not be valid with the electric field.

State-space model

Let us recall that the ideal outcome would be the ability to compute the trajectory $\mathbf{M}^{\mathrm{n}}(t)$ and $R(t)$ by using an observer for non-linear dynamical systems. Thus, the first step is to write the state-space model that needs to be observed in the form

$$\left\{\begin{array}{lcl} \dot{x}(t) & = & f(x(t), u(t)) \\ y(t) & = & h(x(t)) \end{array}\right. \tag{2.9}$$

where x is the state vector, y is the known output vector of the system, and u is the known input vector. In the following, $\mathcal{X}$ denotes the manifold to which values of x belong, $\mathcal{U}$ denotes the open subset of $\mathbb{R}^m$ to which values of the input vector u belong, and $\mathcal{Y}$ denotes the open subset of $\mathbb{R}^p$ to which values of the measured outputs belong.

If it is assumed that measurements can directly access $u(t)$ and $y(t)$, then one must be able to deduce $x(t)$, then the trajectory.

Observer and observability

Let us recall the definition of an *observer* from Ref. Besançon [2007].

Definition 1 (Observer [Besançon, 2007, Sec. 1.1.2, Def. 1])**.** *Considering a system* (2.9)*, an observer is given by an auxiliary system:*

$$\begin{aligned} \dot{X}(t) &= F(X(t), u(t), y(t), t) \\ \hat{x}(t) &= H(X(t), u(t), y(t), t) \end{aligned} \tag{2.10}$$

such that:

(i) $\hat{x}(0) = x(0) \Rightarrow \hat{x}(t) = x(t),\ \forall t \geqslant 0$

(ii) $\|\hat{x}(t) - x(t)\| \to 0$ *as* $t \to \infty$

Let us also recall the definition of *observability* from Ref. Besançon [2007]. Reproducing its notations, $\chi_u(t, x_{t_0})$ denotes the solution of the state equation Eq. (2.9) under the application of input u on $[t_0, t]$ and satisfying $\chi_u(t_0, x_{t_0}) = x_{t_0}$.

Definition 2 (Indistinguishability Ref. [Besançon, 2007, Sec. 1.2.1, Def. 2])**.** *A pair* $x_0, x_0' \in \mathbb{R}^n \times \mathbb{R}^n$ *is indistinguishable for a system* (2.9) *if:*

$$\forall u \in \mathcal{U},\ \forall t \geqslant 0,\ h(\chi_u(t, x_0)) = h(\chi_u(t, x_0'))$$

A state x *is indistinguishable from* x_0 *if the pair* (x, x_0) *is indistinguishable.*

Definition 3 (Observability Ref. [Besançon, 2007, Sec. 1.2.1, Def. 3])**.** *A system* (2.9) *is observable [resp. at* x_0*] if it does not admit any indistinguishable pair [resp. any state indistinguishable from* x_0*].*

2.2.2. The modeling problem

The whole point of this chapter is that the choice of dynamical model is neither completely straightforward nor neutral. *There is more than one possible model, some of whom leading to algorithms quite different from dead-reckoning.* Therefore, this work solely focuses on MIDR, as defined below.

MIDR solutions

MIDR is defined by

- The choice of the magnetic field vector $\mathbf{B}^{\mathrm{b}}$ (or $\mathbf{B}^{\mathrm{n}}$, or the same quantity in any other frame of reference or any reparameterization) as a state variable and as an output variable (in x and y). This is a model of measurements, therefore, no persistent map of the magnetic field is compiled;

- The ability to use direct measurements of the spatial derivative of the magnetic field $\nabla\mathbf{B}^{\mathrm{b}}$;

- The use of $\mathbf{v}^{\mathrm{b}}$ (or $\mathbf{v}^{\mathrm{n}}$, or the same quantity in any other frame of reference or any reparameterization) in the components of $f(x(t), u(t))$ corresponding to the time-derivative of $\mathbf{B}^{\mathrm{b}}$ (expressed in any frame of reference, or any reparameterization). More precisely, f includes an instance of the following equation,

$$\frac{d}{dt}\mathbf{B}^{\mathrm{n}}(\mathbf{M}^{\mathrm{n}}(t), t) = \nabla\mathbf{B}^{\mathrm{n}}(\mathbf{M}^{\mathrm{n}}(t), t)\mathbf{v}^{\mathrm{n}}(t) + \frac{\partial}{\partial t}\mathbf{B}^{\mathrm{n}}(\mathbf{M}^{\mathrm{n}}(t), t) \ . \tag{2.11}$$

If $\mathbf{B}$ is stationary in $\mathfrak{R}_{\mathrm{n}}$, that is to say, $\mathbf{B}^{\mathrm{n}}$ depends only on the space variable, then (2.11) reduces to

$$\frac{d\mathbf{B}^{\mathrm{n}}}{dt} = \nabla\mathbf{B}^{\mathrm{n}}\mathbf{v}^{\mathrm{n}} \ . \tag{2.12}$$

Equations (2.11) and (2.12) are central in Chapters 2 and 4 as the starting point of all dynamical models that are used.

Why this restriction? According to Sec. 2.2.1, measured quantities are $\mathbf{B}^{\mathrm{b}}$, $\nabla\mathbf{B}^{\mathrm{b}}$, $\boldsymbol{\omega}^{\mathrm{b/i}}$ and $\boldsymbol{\gamma}^{\mathrm{b}}$. Since the trajectory is defined as the orientation and position of the rigid body as a function of time, that is to say $t \mapsto (R(t), \mathbf{M}^{\mathrm{n}}(t))$, a natural way of forming the state-space model (2.9) is to combine the strapdown inertial navigation equations (2.3), (2.6), (2.7), with the magnetic field equation (2.8). For instance, as discussed in Sec. 2.1, one could choose to put $\mathbf{M}^{\mathrm{n}}$, R and $\mathbf{v}^{\mathrm{n}}$ into the state vector, use $\boldsymbol{\omega}^{\mathrm{b/i}}$ and $\boldsymbol{\gamma}^{\mathrm{b}}$ to form the input-vector, and use $\mathbf{B}^{\mathrm{b}}$ and $\nabla\mathbf{B}^{\mathrm{b}}$ as outputs. Assuming that the magnetic field is mapped beforehand, the function h could then be formed using this map, thus forming our state-space model. Such an approach would be a hybridization between magnetic fingerprinting and inertial navigation, augmented with measurements of the magnetic gradient, and not dead-reckoning.

Higher order spatial derivatives Let us remark that the definition of MIDR can stated by replacing $\mathbf{B}^{\mathrm{b}}$ and $\nabla\mathbf{B}^{\mathrm{b}}$ with their respective spatial derivatives, with an equation of the form

$$\frac{d}{dt}\nabla\mathbf{B}^{\mathrm{n}}(\mathbf{M}^{\mathrm{n}}(t),t) = f\left(\frac{\partial\nabla\mathbf{B}^{\mathrm{n}}(\mathbf{M}^{\mathrm{n}}(t),t)}{\partial\mathbf{M}^{\mathrm{n}}(t)}, \mathbf{v}^{\mathrm{n}}\right) , \tag{2.13}$$

If higher order spatial derivatives are measurable directly, both approaches could even be combined, with clear advantages of doing so (see Ref. Skog et al. [2018]).

2.2.3. Problem formulation

Now that notations, MIDR and *observability* are defined, the problem is answering the following two questions:

1. What dynamical system must be chosen?
2. How observable is each possible choice of dynamical system?

These two questions are essential because answering them is making sure that the right tool is used for the job. They highlight that observability is bound to a choice of dynamical system. They also emphasize that the modeling step is an essential part of solving an observation problem for our physical system. For example, questions such as "what order is the system", or "is it observable" only make sense once a model is chosen, and the choice of model can be questioned.

Modeling choices are based on the following criteria: one must be able to evaluate the model, it must accurately represent reality, and its observability properties must allow dead-reckoning. Let us start with equation (2.12), and study models in order of increasing complexity.

2.3. Minimal dynamical system for velocity computation

This section recalls some relevant results of Ref. Dorveaux [2011] in the context of modeling and observability studies, and discusses its choice of model. Said model is provided in Sec. 2.3.1. An observability result is provided in Sec. 2.3.2. Then, the choice is discussed in Sec. 2.3.3.

2.3.1. Model

Let us assume that the magnetic field is stationary in the navigation frame, that the navigation frame and inertial frame are identical, and that an unbiased strapdown 3-axis gyrometer is available. The state-space model (2.9) is chosen as

$$x(t) = \begin{pmatrix}\mathbf{B}^{\mathrm{b}}(\mathbf{M}^{\mathrm{b}},t)\\ \mathbf{v}^{\mathrm{b}}(t)\end{pmatrix},\ u(t) = \begin{pmatrix}\boldsymbol{\omega}^{\mathrm{b/n}}(t)\\ \nabla\mathbf{B}^{\mathrm{b}}(\mathbf{M}^{\mathrm{b}},t)\end{pmatrix},\ y(t) = \mathbf{B}^{\mathrm{b}}(\mathbf{M}^{\mathrm{b}},t)\ . \tag{2.14}$$

Using our notations, the following system reproduces the one presented and studied in Ref. [Dorveaux, 2011, Sec. 2.1.2, Eq. (2.8)], which is the simplest MIDR model of the state of the art,

$$f(x(t),u(t)) = \begin{pmatrix} -[\boldsymbol{\omega}^{\mathrm{b/n}}(t)\times] & \nabla\mathbf{B}^{\mathrm{b}}(\mathbf{M}^{\mathrm{b}},t) \\ 0 & -[\boldsymbol{\omega}^{\mathrm{b/n}}(t)\times] \end{pmatrix} x(t) \ . \tag{2.15}$$

If Eq. (2.15), is injected into Eq. (2.9), the following equation is obtained,

$$\frac{d}{dt}\mathbf{v}^{\mathrm{b}} = -\boldsymbol{\omega}^{\mathrm{b/n}} \times \mathbf{v}^{\mathrm{b}} \ , \tag{2.16}$$

which is equivalent to $\mathbf{a}^{\mathrm{n}} = 0$. In other words, this model is only accurate for *straight line trajectories at constant velocity in the navigation frame* $\mathfrak{R}_{\mathrm{n}}$. The unavailability of reliable accelerometers can nevertheless justify this strong assumption.

2.3.2. Observability

The model Eqs. (2.14)-(2.15) is proven observable in Ref. [Dorveaux, 2011, Appx. C], since as long as $\nabla\mathbf{B}^{\mathrm{b}}$ is non-singular, there exists a converging non-linear observer that reconstructs both the magnetic field and the velocity,

$$\begin{cases} \dfrac{d}{dt}\widehat{\mathbf{B}}^{\mathrm{b}} = -\boldsymbol{\omega}^{\mathrm{b/n}} \times \widehat{\mathbf{B}}^{\mathrm{b}} + \nabla\mathbf{B}^{\mathrm{b}} \left[\hat{\mathbf{v}}^{\mathrm{b}} - \ell_1 \left(\nabla\mathbf{B}^{\mathrm{b}}\right)^{\top} (\widehat{\mathbf{B}}^{\mathrm{b}} - y)\right] & (2.17) \\ \dfrac{d}{dt}\hat{\mathbf{v}}^{\mathrm{b}} = -\boldsymbol{\omega}^{\mathrm{b/n}} \times \hat{\mathbf{v}}^{\mathrm{b}} - \ell_2 \left(\nabla\mathbf{B}^{\mathrm{b}}\right)^{\top} (\widehat{\mathbf{B}}^{\mathrm{b}} - y) \ , & (2.18) \end{cases}$$

where $\ell_1 > 0$ and $\ell_2 > 0$ are constant gains.

Remark The convergence speed of $\widehat{\mathbf{B}}^{\mathrm{b}}$ towards $\mathbf{B}^{\mathrm{b}}$ in the above observer seems to decrease unnecessarily when the gradient is small. This motivates replicating the proof of convergence provided in Ref. [Dorveaux, 2011, Sec. 2.2] with a simpler observer,

$$\begin{cases} \dfrac{d}{dt}\widehat{\mathbf{B}}^{\mathrm{b}} = -\boldsymbol{\omega}^{\mathrm{b/n}} \times \widehat{\mathbf{B}}^{\mathrm{b}} + \nabla\mathbf{B}^{\mathrm{b}}\hat{\mathbf{v}}^{\mathrm{b}} - \ell_1(\widehat{\mathbf{B}}^{\mathrm{b}} - y) & (2.19) \\ \dfrac{d}{dt}\hat{\mathbf{v}}^{\mathrm{b}} = -\boldsymbol{\omega}^{\mathrm{b/n}} \times \hat{\mathbf{v}}^{\mathrm{b}} - \ell_2 \left(\nabla\mathbf{B}^{\mathrm{b}}\right)^{\top} (\widehat{\mathbf{B}}^{\mathrm{b}} - y) \ . & (2.20) \end{cases}$$

Proof. Consider the Lyapunov function W

$$W = \frac{1}{2}\left\|\widehat{\mathbf{B}}^{\mathrm{b}} - \mathbf{B}^{\mathrm{b}}\right\|^2 + \frac{1}{2\ell_2}\left\|\hat{\mathbf{v}}^{\mathrm{b}} - \mathbf{v}^{\mathrm{b}}\right\|^2 \tag{2.21}$$

Its time derivative can be written under the form

$$\begin{aligned}\frac{dW}{dt} &= \left(\widehat{\mathbf{B}}^{\mathrm{b}} - \mathbf{B}^{\mathrm{b}}\right)^\top \left[-\boldsymbol{\omega}^{\mathrm{b/n}} \times \left(\widehat{\mathbf{B}}^{\mathrm{b}} - \mathbf{B}^{\mathrm{b}}\right) + \nabla\mathbf{B}^{\mathrm{b}}\left(\widehat{\mathbf{v}}^{\mathrm{b}} - \mathbf{v}^{\mathrm{b}}\right) - \ell_1(\widehat{\mathbf{B}}^{\mathrm{b}} - \mathbf{B}^{\mathrm{b}})\right] \\ &\quad + \frac{1}{\ell_2}\left(\widehat{\mathbf{v}}^{\mathrm{b}} - \mathbf{v}^{\mathrm{b}}\right)^\top \left[-\boldsymbol{\omega}^{\mathrm{b/n}} \times \left(\widehat{\mathbf{v}}^{\mathrm{b}} - \mathbf{v}^{\mathrm{b}}\right) - \ell_2\left(\nabla\mathbf{B}^{\mathrm{b}}\right)^\top (\widehat{\mathbf{B}}^{\mathrm{b}} - \mathbf{B}^{\mathrm{b}})\right] \\ &= \left(\widehat{\mathbf{B}}^{\mathrm{b}} - \mathbf{B}^{\mathrm{b}}\right)^\top \left[\nabla\mathbf{B}^{\mathrm{b}}\left(\widehat{\mathbf{v}}^{\mathrm{b}} - \mathbf{v}^{\mathrm{b}}\right) - \ell_1(\widehat{\mathbf{B}}^{\mathrm{b}} - \mathbf{B}^{\mathrm{b}})\right] \\ &\quad + \frac{1}{\ell_2}\left(\widehat{\mathbf{v}}^{\mathrm{b}} - \mathbf{v}^{\mathrm{b}}\right)^\top \left[-\ell_2\left(\nabla\mathbf{B}^{\mathrm{b}}\right)^\top (\widehat{\mathbf{B}}^{\mathrm{b}} - \mathbf{B}^{\mathrm{b}})\right] ,\end{aligned} \tag{2.22}$$

because $\mathbf{u} \times \mathbf{v}$ and $\mathbf{v}$ are orthogonal.

$$\begin{aligned}\frac{dW}{dt} &= -\ell_1\left(\widehat{\mathbf{B}}^{\mathrm{b}} - \mathbf{B}^{\mathrm{b}}\right)^\top (\widehat{\mathbf{B}}^{\mathrm{b}} - \mathbf{B}^{\mathrm{b}}) \\ &\quad + \left(\widehat{\mathbf{B}}^{\mathrm{b}} - \mathbf{B}^{\mathrm{b}}\right)^\top \nabla\mathbf{B}^{\mathrm{b}}\left(\widehat{\mathbf{v}}^{\mathrm{b}} - \mathbf{v}^{\mathrm{b}}\right) \\ &\quad - \left(\widehat{\mathbf{v}}^{\mathrm{b}} - \mathbf{v}^{\mathrm{b}}\right)^\top \left(\nabla\mathbf{B}^{\mathrm{b}}\right)^\top (\widehat{\mathbf{B}}^{\mathrm{b}} - \mathbf{B}^{\mathrm{b}}) \\ &= -\ell_1\left\|\widehat{\mathbf{B}}^{\mathrm{b}} - \mathbf{B}^{\mathrm{b}}\right\|^2 .\end{aligned} \tag{2.23}$$

Since $\ell_1 > 0$, then $\dot{W} \leqslant 0$.

In order to complete the proof, let us show, following Ref. [Dorveaux, 2011, Sec. 2.2], that the invariant set defined by $\dot{W} = 0$ is reduced to

$$\left(\widehat{\mathbf{B}}^{\mathrm{b}} - \mathbf{B}^{\mathrm{b}}, \widehat{\mathbf{v}}^{\mathrm{b}} - \mathbf{v}^{\mathrm{b}}\right) = (0, 0) , \tag{2.24}$$

which, by LaSalle's invariance principle, implies that this set is globally asymptotically stable.

From Eq. (2.23), it is obvious that in this set,

$$\widehat{\mathbf{B}}^{\mathrm{b}} - \mathbf{B}^{\mathrm{b}} \equiv 0 . \tag{2.25}$$

Using Eqs. (2.15) and (2.17) to take the time derivative of the previous equation yields immediately,

$$\nabla\mathbf{B}^{\mathrm{b}}\left(\widehat{\mathbf{v}}^{\mathrm{b}} - \mathbf{v}^{\mathrm{b}}\right) \equiv 0 . \tag{2.26}$$

Because by assumption $\nabla\mathbf{B}^{\mathrm{b}}$ is non-singular, it follows that in this set,

$$\widehat{\mathbf{v}}^{\mathrm{b}} - \mathbf{v}^{\mathrm{b}} \equiv 0 , \tag{2.27}$$

which concludes the proof. □

The advantage of this observer over the one proposed in Ref. [Dorveaux, 2011, Sec. 2.2] is that $\widehat{\mathbf{B}}^{\mathrm{b}}$ converges towards $\mathbf{B}^{\mathrm{b}}$ independently of $\nabla\mathbf{B}^{\mathrm{b}}$.

2.3.3. Discussion: What about attitude estimation?

Not only is the model Eqs. (2.14)-(2.15) only accurate for straight line trajectories at constant velocity, which makes sense with unreliable accelerometers but is very restrictive, but it is also incomplete.

Attitude estimation is missing This observable state is not sufficient in order to compute a trajectory. Although $\mathbf{v}^{\mathrm{b}}$ is observable, the minimum requirement for computing the trajectory would be the ability to integrate the velocity in the navigation frame, Eq. (2.3). To achieve that, at least an estimate of the attitude matrix R is missing, and necessary to obtain $\mathbf{v}^{\mathrm{n}}$ in the navigation frame, Eq. (2.4). This issue is indeed discussed at the end of Ref. [Dorveaux, 2011, Sec. 2.2]. In this reference, the proposed design solution is to estimate the attitude matrix R in a separate state-observer as illustrated Fig. 2.2, since there is plenty of literature on the subject, see Refs. Michel et al. [2015], Makni [2016] and references therein.

The model is restrictive Attitude estimation algorithms using MEMS inertial sensors usually assume that the mean value of the acceleration vector $\mathbf{a}^{\mathrm{n}}$ is zero. Resorting to them makes sense considering that this assumption was implicitly taken. With this assumption, the gravity vector can be recovered from the measured proper acceleration vector. This is akin to using accelerometers as tilt sensors. This assumption is generally not true; there is no reason why all trajectories should follow straight lines at constant velocity. When gyrometers are available, they can be used to mitigate effects of non-zero $\mathbf{a}^{\mathrm{n}}$ with filtering (see Refs. Mahony et al. [2005, 2008]).[4] However, after browsing through the literature, it becomes clear that research on attitude estimation algorithms using MEMS inertial sensors mainly aims at mitigating the effects of accelerations, which are considered as disturbances. The trajectory itself being seen as a disturbance is an undesirable property highlighting a representativeness problem.

2.4. Velocity and attitude estimation in an inertial frame

Let us consider attitude estimation jointly with velocity estimation, with the assumption that the navigation frame is inertial, implying $\boldsymbol{\omega}^{\mathrm{n/i}} \approx 0$. In fact, the seminal papers on MIDR, Refs. Vissière et al. [2007a,b], do combine velocity and attitude estimation. Using our notations, the reduced state vector of the dynamic system in Ref. [Vissière et al., 2007a, Sec.II] whose observability is studied is equivalent to

$$x(t) = \begin{pmatrix} \mathbf{v}^{\mathrm{b}}(t) & R(t) & \boldsymbol{\omega}^{\mathrm{b/n}}(t) & \mathbf{a}^{\mathrm{b}}(t) & \mathbf{B}^{\mathrm{b}}(\mathbf{M}^{\mathrm{b}},t) & \nabla\mathbf{B}^{\mathrm{n}}(\mathbf{M}^{\mathrm{b}},t) \end{pmatrix}^{\top},$$

---

[4] Let us also remark that in this context, the magnetic field is usually used as a heading reference in outdoor environments. More sophisticated algorithms are used indoors to account for ubiquitous magnetic disturbances, see Refs. Afzal et al. [2011b], Renaudin and Combettes [2014].

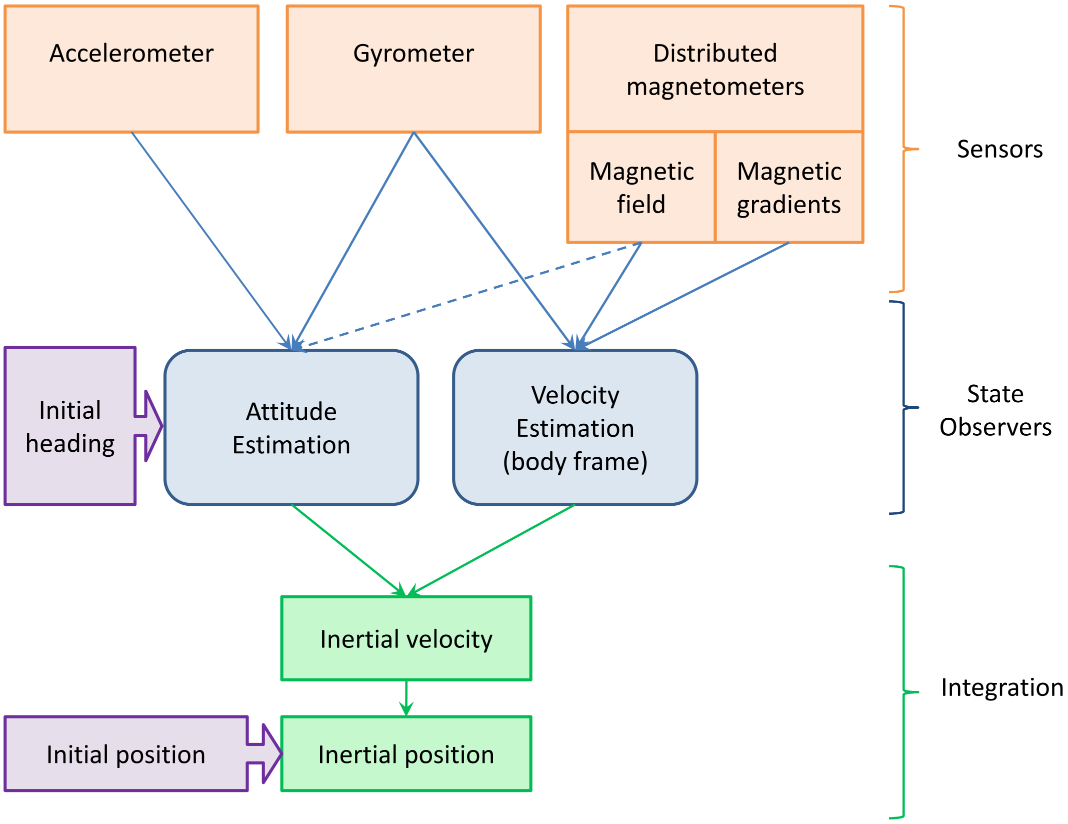

Figure 2.2: From Ref. [Dorveaux, 2011, Fig. 2.3], "Trajectory reconstruction with a Magneto-Inertial NAVigation (MINAV) system"
In Ref. Dorveaux [2011], velocity and attitude estimation are considered separately. A state-of-the-art attitude observer using accelerometers and gyrometers is implemented. The magnetic field can be used as a heading source. Velocity estimation is achieved in a separate observer, using gyrometers and magnetic field measurements. Outputs from both observers are combined in order to obtain velocity in the navigation frame, and integrated in order to compute a trajectory in a dead-reckoning framework.

with an output vector that reads

$$y(t) = \begin{pmatrix} \boldsymbol{\gamma}^{\mathrm{b}}(t) + \mathbf{b}_{\gamma} \\ \boldsymbol{\omega}^{\mathrm{b/n}}(t) + \mathbf{b}_{\omega} \\ \mathbf{B}^{\mathrm{b}}(\mathbf{M}^{\mathrm{b}}, t) \\ \mathbf{B}^{\mathrm{b}}(\mathbf{M}^{\mathrm{b}}, t) + \nabla\mathbf{B}^{\mathrm{b}}(\mathbf{M}^{\mathrm{b}}, t)({\mathbf{p}^{\mathrm{b}}}_1 - \mathbf{M}^{\mathrm{b}}) \\ \mathbf{B}^{\mathrm{b}}(\mathbf{M}^{\mathrm{b}}, t) + \nabla\mathbf{B}^{\mathrm{b}}(\mathbf{M}^{\mathrm{b}}, t)({\mathbf{p}^{\mathrm{b}}}_2 - \mathbf{M}^{\mathrm{b}}) \\ \mathbf{B}^{\mathrm{b}}(\mathbf{M}^{\mathrm{b}}, t) + \nabla\mathbf{B}^{\mathrm{b}}(\mathbf{M}^{\mathrm{b}}, t)({\mathbf{p}^{\mathrm{b}}}_3 - \mathbf{M}^{\mathrm{b}}) \end{pmatrix},$$

where $\mathbf{b}_{\omega}$ stands for gyrometer biases, $\mathbf{b}_{\gamma}$ stands for accelerometer biases, $\boldsymbol{\gamma}^{\mathrm{b}}$ and $\boldsymbol{\omega}^{\mathrm{b/n}}$ are defined according to Eqs. (2.7) and (2.5) with $\boldsymbol{\omega}^{\mathrm{n/i}} = 0$, and vectors ${\mathbf{p}^{\mathrm{b}}}_1$ to ${\mathbf{p}^{\mathrm{b}}}_3$ represent coordinates in body frame of additional 3-axis magnetometers. It is worth noting that Ref. Vissière et al. [2007a] does study the observability of this model but,

- Contrary to Ref. Dorveaux [2011], this work does not completely fit into the definition of MIDR in Sec. 2.2.2. While it does use an instance of Eq. (2.11), *direct* measurements of the magnetic field gradient are not considered available. Instead, the gradient is computed by the observer. Two configurations are mentioned at the end of Ref. [Vissière et al., 2007a, Sec.III.C] about experimental results: one with a single 3-axis magnetometer, and one with four 3-axis magnetometers. Using a single 3-axis magnetometer is not sufficient to provide *direct* measurements of $\nabla\mathbf{B}^{\mathrm{b}}$, and is outside the scope of this work; MIDR was probably not yet outlined at the time of writing.
- No clear justification is provided about the representativeness of the associated dynamic model $\frac{d}{dt}\nabla\mathbf{B}^{\mathrm{n}} \approx 0$; The single-3-axis-magnetometer configuration is probably the only reason why $\nabla\mathbf{B}^{\mathrm{n}}$ is considered as a part of the state vector, also when observability is assessed.
- The model description is completely invariant with respect to a change of heading, which casts some doubts over conclusions of Ref. [Vissière et al., 2007a, Sec.II] concerning heading observability.

2.4.1. Proposed model

Let us take an intermediate approach between Refs. Vissière et al. [2007a] and Dorveaux [2011] under the following guidelines,

- Quantities for which direct measurements are available and no representative dynamic model can be evaluated are removed from the state vector;
- Attitude is included into the state vector.

Since direct measurements of $\nabla\mathbf{B}^{\mathrm{b}}$ are available and no representative model for $\frac{d}{dt}\nabla\mathbf{B}^{\mathrm{b}}$ is available, the choice is made to use it as an input like in Ref. Dorveaux [2011] instead of as a state like in Ref. Vissière et al. [2007a]. Then, strapdown inertial navigation equations are included in the model like in Ref. Vissière et al. [2007a]

instead of using a constant-velocity assumption like in Ref. Dorveaux [2011]. Since direct measurements of $\boldsymbol{\omega}^{\mathrm{b/n}}$ and $\boldsymbol{\gamma}^{\mathrm{b}}$ are assumed available, they are not included in the state vector contrary to Ref. Vissière et al. [2007a]. The resulting system reads

$$x(t) = \begin{pmatrix} \mathbf{B}^{\mathrm{b}}(\mathbf{M}^{\mathrm{b}}, t) \\ \mathbf{v}^{\mathrm{b}}(t) \\ R(t) \end{pmatrix}, \; y(t) = \left(\mathbf{B}^{\mathrm{b}}(\mathbf{M}^{\mathrm{b}}, t)\right), \; u(t) = \begin{pmatrix} \nabla\mathbf{B}^{\mathrm{b}}(\mathbf{M}^{\mathrm{b}}, t) \\ \boldsymbol{\omega}^{\mathrm{b/n}}(t) \\ \boldsymbol{\gamma}^{\mathrm{b}}(t) \end{pmatrix}. \tag{2.28}$$

The state dynamics function f combines Eqs. (2.12), (2.7) and (2.5) into

$$\frac{d\mathbf{B}^{\mathrm{b}}}{dt} = -\boldsymbol{\omega}^{\mathrm{b/n}} \times \mathbf{B}^{\mathrm{b}} + \nabla\mathbf{B}^{\mathrm{b}}\mathbf{v}^{\mathrm{b}} \;, \tag{2.29}$$

$$\frac{d\mathbf{v}^{\mathrm{b}}}{dt} = -\boldsymbol{\omega}^{\mathrm{b/n}} \times \mathbf{v}^{\mathrm{b}} + \boldsymbol{\gamma}^{\mathrm{b}} + R^{\top}\mathbf{g}^{\mathrm{n}} \;, \tag{2.30}$$

$$\frac{dR}{dt} = R[\boldsymbol{\omega}^{\mathrm{b/n}} \times] \;. \tag{2.31}$$

2.4.2. Observability

Is the system formed by Eqs. (2.28)-(2.31) observable? Two cases can now be examined: the case of constant inputs, and the time-varying case.

Case of constant inputs: local weak observability

Let us examine whether the system formed by Eqs. (2.28) to (2.31) is *locally weakly observable*. Let us recall the definition that we use.

Definition 4 (Local weak observability Ref. [Besançon, 2007, Sec. 1.2.1, Def. 5])**.** *A system* (2.9) *is locally weakly observable [resp. at x_0] if there exists a neighborhood U of any x [resp. of x_0] such that for any neighborhood V of x [resp. x_0] contained in U, there is no indistinguishable state from x [resp. x_0] in V when considering time intervals for which trajectories remain in V.*

There is a systematic way of checking whether our system is locally weakly observable. First, the following definitions are recalled.

Definition 5 (Observation space Ref. [Besançon, 2007, Sec. 1.2.1, Def. 6])**.** *The observation space for a system* (2.9) *is defined as the smallest real vector space (denoted by $\mathcal{O}(h)$) of $\mathcal{C}^{\infty}$ functions containing the components of h and closed under Lie derivation along $f_u \doteq f(., u)$ for any constant $u \in \mathbb{R}^m$ (namely such that for any $\varphi \in \mathcal{O}(h)$, $L_{f_u}\varphi(x) \in \mathcal{O}(h)$, where $L_{f_u}\varphi(x) = \frac{\partial\varphi}{\partial x} f(x, u)$).*

Definition 6 (Observability rank condition [resp. at x_0] Ref. [Besançon, 2007, Sec. 1.2.1, Def. 7])**.** *A system* (2.9) *is said to satisfy the observability rank condition [resp. at x_0] if:*

$$\forall x, \; \dim d\mathcal{O}(h)|_x = n \; [\textit{resp.} \dim d\mathcal{O}(h)|_{x_0} = n]$$

where $d\mathcal{O}(h)|_x$ is the set of $d\varphi(x)$ with $\phi \in \mathcal{O}(h)$.

Then, the following theorem is recalled.

Theorem 2.4.1 (Ref. [Besançon, 2007, Sec.1.2.1, Thm.1])**.** *A system* (2.9) *satisfying the observability rank condition at* x_0 *is locally weakly observable at* x_0*.*
More generally, a system (2.9) *satisfying the observability rank condition is locally weakly observable.*
Conversely, a system (2.9) *locally weakly observable satisfies the observability rank condition in an open dense subset of* X*.*

In order to compute the system's observation space, the way to take Lie derivatives on the group of rotations SO(3) needs to be defined, because $R \in \mathrm{SO}(3)$. To that end, let us choose any element

$$x_0 = \begin{pmatrix} \mathbf{B}^{\mathrm{b}}{}_0 \\ \mathbf{v}^{\mathrm{b}}{}_0 \\ R_0 \end{pmatrix} \in \mathcal{X} \ .$$

The exponential mapping from the Lie algebra $\mathfrak{so}(3)$ to the Lie group SO(3) defined by

$$\begin{array}{rcl} \mathfrak{so}(3) & \rightarrow & \mathrm{SO}(3) \\ [\boldsymbol{\rho}\times] & \mapsto & R = \exp\left([\boldsymbol{\rho}\times]\right) R_0 \end{array}$$

can be used as a local parameterization of SO(3) around R_0 for the Rodrigues rotation vector $\boldsymbol{\rho}$ in a neighborhood of 0. Let us redefine $x(t)$ as

$$x(t) = \begin{pmatrix} \mathbf{B}^{\mathrm{b}}(\mathbf{M}^{\mathrm{b}}, t) & \mathbf{v}^{\mathrm{b}}(t) & \boldsymbol{\rho}(t) \end{pmatrix}^\top \ .$$

Eq. (2.31) becomes

$$\begin{aligned} \frac{d}{dt}\left[\exp([\boldsymbol{\rho}\times])R_0\right] &= \exp([\boldsymbol{\rho}\times])R_0[\boldsymbol{\omega}^{\mathrm{b/n}}\times] \\ \frac{d}{dt}\exp([\boldsymbol{\rho}\times]) &= \exp([\boldsymbol{\rho}\times])R_0[\boldsymbol{\omega}^{\mathrm{b/n}}\times]R_0^\top \\ &= \exp([\boldsymbol{\rho}\times])[(R_0\boldsymbol{\omega}^{\mathrm{b/n}})\times] \ , \end{aligned}$$

by invariance of the vector product by a direct isometry. This equation can be transformed into (see Ref. Jiang and Lin [1991] for full derivation)

$$\dot{\boldsymbol{\rho}} = \left[\mathbf{1} - \frac{\cos\|\boldsymbol{\rho}\|}{1-\cos\|\boldsymbol{\rho}\|}[\boldsymbol{\rho}\times] + \frac{1}{\|\boldsymbol{\rho}\|^2}\left(\mathbf{1} - \frac{\|\boldsymbol{\rho}\|\sin\|\boldsymbol{\rho}\|}{1-\cos\|\boldsymbol{\rho}\|}\right)[\boldsymbol{\rho}\times]^2\right] R_0\boldsymbol{\omega}^{\mathrm{b/n}} \ , \tag{2.32}$$

which, at $\boldsymbol{\rho} = 0$ simplifies further into

$$\dot{\boldsymbol{\rho}}\big|_{\boldsymbol{\rho}=0} = R_0\boldsymbol{\omega}^{\mathrm{b/n}} \ . \tag{2.33}$$

The system's observation space is spanned by

$$\begin{aligned}
h(x) &= \mathbf{B}^{\mathrm{b}} \ , \\
L_{f_u} h(x) &= -[\boldsymbol{\omega}^{\mathrm{b/n}}\times]\mathbf{B}^{\mathrm{b}} + \nabla\mathbf{B}^{\mathrm{b}}\mathbf{v}^{\mathrm{b}} \ , \\
L^2_{f_u} h(x) &= \begin{pmatrix} -[\boldsymbol{\omega}^{\mathrm{b/n}}\times] & \nabla\mathbf{B}^{\mathrm{b}} \end{pmatrix} \begin{pmatrix} -[\boldsymbol{\omega}^{\mathrm{b/n}}\times]\mathbf{B}^{\mathrm{b}} + \nabla\mathbf{B}^{\mathrm{b}}\mathbf{v}^{\mathrm{b}} \\ -[\boldsymbol{\omega}^{\mathrm{b/n}}\times]\mathbf{v}^{\mathrm{b}} + \boldsymbol{\gamma}^{\mathrm{b}} + R_0^\top \exp([-\boldsymbol{\rho}\times])\mathbf{g}^{\mathrm{n}} \end{pmatrix} \\
&= [\boldsymbol{\omega}^{\mathrm{b/n}}\times]^2\mathbf{B}^{\mathrm{b}} + (-[\boldsymbol{\omega}^{\mathrm{b/n}}\times]\nabla\mathbf{B}^{\mathrm{b}} - \nabla\mathbf{B}^{\mathrm{b}}[\boldsymbol{\omega}^{\mathrm{b/n}}\times])\mathbf{v}^{\mathrm{b}} \\
&\qquad\qquad\qquad + \nabla\mathbf{B}^{\mathrm{b}} R_0^\top \exp([-\boldsymbol{\rho}\times])\mathbf{g}^{\mathrm{n}} \ .
\end{aligned}$$

Thus,

$$d\mathcal{O}(h)|_{x_0} = \operatorname{span}\left\{ d\mathbf{B}^{\mathrm{b}}, \nabla\mathbf{B}^{\mathrm{b}} d\mathbf{v}^{\mathrm{b}}, \nabla\mathbf{B}^{\mathrm{b}} R_0^\top [\mathbf{g}^{\mathrm{n}}\times] d\boldsymbol{\rho} \right\} \ .$$

It is clear that dim $d\mathcal{O}(h)\big|_x \leqslant 8$ because $[\mathbf{g}^{\mathrm{n}}\times]$ is rank 2. More precisely, $\boldsymbol{\rho}$ is unobservable in the direction of $\mathbf{g}^{\mathrm{n}}$, which means that *heading is not locally weakly observable*. Moreover, velocity is locally weakly observable if and only if $\nabla\mathbf{B}^{\mathrm{b}}$ *is non-singular*. If $\nabla\mathbf{B}^{\mathrm{b}}$ is singular, tilt might not even be observable; in the worst case, $\nabla\mathbf{B}^{\mathrm{b}} = 0$, dim $d\mathcal{O}(h)\big|_x = 3$ and only the magnetic field is observable.

Time-varying case

Let us consider once more the system formed by Eqs. (2.28) to (2.31). Let us prove that if the spatial gradient of the magnetic field is non-singular, then the system is observable up to a heading difference.

Let us denote

$$x_0 = \begin{pmatrix} {\mathbf{B}^{\mathrm{b}}}_0 \\ {\mathbf{v}^{\mathrm{b}}}_0 \\ R_0 \end{pmatrix} , \ x'_0 = \begin{pmatrix} {\mathbf{B}^{\mathrm{b}'}}_0 \\ {\mathbf{v}^{\mathrm{b}'}}_0 \\ R'_0 \end{pmatrix} \ . \tag{2.34}$$

Let us denote $x(t)$ and $x'(t)$ two solutions of Eqs. (2.28) to (2.31) with their respective initial conditions $x(t_0) = x_0$ and $x'(t_0) = x'_0$ for a given input $u \in \mathcal{U}$ such that

$$u(t) = \begin{pmatrix} \nabla\mathbf{B}^{\mathrm{b}}(\mathbf{M}^{\mathrm{b}}, t) \\ \boldsymbol{\omega}^{\mathrm{b/n}}(t) \\ \boldsymbol{\gamma}^{\mathrm{b}}(t) \end{pmatrix} \ . \tag{2.35}$$

It is assumed that $\nabla\mathbf{B}^{\mathrm{b}}(\mathbf{M}^{\mathrm{b}}, t)$ is non singular and that $h(x(t)) = h(x'(t))$, for $t \in [t_0, T]$. Let us prove that

$$\begin{aligned}
{\mathbf{B}^{\mathrm{b}}}_0 &= {\mathbf{B}^{\mathrm{b}'}}_0 \ , \\
{\mathbf{v}^{\mathrm{b}}}_0 &= {\mathbf{v}^{\mathrm{b}'}}_0 \ , \\
\mathbf{g}^{\mathrm{n}} &= R'_0 R_0^\top \mathbf{g}^{\mathrm{n}} \ .
\end{aligned}$$

The equality ${\mathbf{B}^{\mathrm{b}}}_0 = {\mathbf{B}^{\mathrm{b}\prime}}_0$ is obviously true, because ${\mathbf{B}^{\mathrm{b}}}_0 = h(x(t_0)) = h(x'(t_0)) = {\mathbf{B}^{\mathrm{b}\prime}}_0$. The equality ${\mathbf{v}^{\mathrm{b}}}_0 = {\mathbf{v}^{\mathrm{b}\prime}}_0$ also holds, under the assumption that $\mathbf{v}^{\mathrm{b}}$ is of class at least $\mathcal{C}^1$ and that $\nabla\mathbf{B}^{\mathrm{b}}$ is non-singular, because

$$\mathbf{v}^{\mathrm{b}}(t) = \nabla\mathbf{B}^{\mathrm{b}}(\mathbf{M}^{\mathrm{b}},t)^{-1}\left(\frac{d}{dt}\mathbf{B}^{\mathrm{b}}(\mathbf{M}^{\mathrm{b}},t) + \boldsymbol{\omega}^{\mathrm{b/n}}(t)\times\mathbf{B}^{\mathrm{b}}(\mathbf{M}^{\mathrm{b}},t)\right) = \mathbf{v}^{\mathrm{b}\prime}(t) \tag{2.36}$$

for all $t \in [t_0, T]$. Taking the time-derivative of Eq. (2.36) and using Eq. (2.30) simplifies into

$$R^\top\mathbf{g}^{\mathrm{n}} = R'^\top\mathbf{g}^{\mathrm{n}} \ .$$

Because of Eq. (2.31),

$$\begin{aligned}
\frac{d}{dt}\left(R'R^\top\right) &= R'\left(\frac{dR}{dt}\right)^\top + \left(\frac{dR'}{dt}\right)R^\top \\
&= R'\left(R[\boldsymbol{\omega}^{\mathrm{b/n}}\times]\right)^\top + \left(R'[\boldsymbol{\omega}^{\mathrm{b/n}}\times]\right)R^\top \\
&= R'\left([\boldsymbol{\omega}^{\mathrm{b/n}}\times] - [\boldsymbol{\omega}^{\mathrm{b/n}}\times]\right)R \\
&= 0 \ .
\end{aligned}$$

It follows that the above equation holds if and only if $R_0^\top\mathbf{g}^{\mathrm{n}} = R_0'^\top\mathbf{g}^{\mathrm{n}}$, which concludes the proof.

2.4.3. Conclusion

Tilt and velocity are observable if $\nabla\mathbf{B}^{\mathrm{b}}$ is non-singular In the simple model proposed above, if $\nabla\mathbf{B}^{\mathrm{b}}$ is non-singular, then *everything but heading* is observable, *even for accelerated trajectories*. While this result holds in the case of constant inputs, varying inputs do not make heading any more observable, because this issue stems from the symmetry of the dynamic model with respect to a change of heading. This symmetry comes from the assumption that $\mathfrak{R}_{\mathrm{n}}$ is inertial (see Appx. A). Regarding the rest of the state, however, looking deeper at the time-varying case might be useful in cases where $\nabla\mathbf{B}^{\mathrm{b}}$ is singular.

The above condition might be restrictive According to Ref. Batista et al. [2013], the condition that $\nabla\mathbf{B}^{\mathrm{b}}$ be non-singular is unnecessarily restrictive. To support this statement, this reference provides several models that differ from the one discussed in Sec. 2.3 only by the definition of $\frac{d}{dt}\mathbf{v}^{\mathrm{b}}$: constant $\mathbf{v}^{\mathrm{b}}$ or constant $\mathbf{v}^{\mathrm{n}}$. The idea is that if the magnetic field is constant in one direction in $\mathfrak{R}_{\mathrm{n}}$, and if R is known at all times, without hypothesis about the evolution of $\mathbf{v}^{\mathrm{n}}$, movements along this direction are indistinguishable. However, if it is known that $\mathbf{v}^{\mathrm{n}}$ “rotates”, unobserved components of the velocity vector at a given date (along the direction of constant field) can be recovered by using measurements at a later date, once they have turned to another direction. This behavior is not captured using the local weak observability criterion, for neither does it consider variations of input nor does it consider observability over a time interval.

2.5. Low-cost inertial sensors: sensor biases, observability implications

One of the main drawbacks of low-cost MEMS inertial sensors is that their output is not accurate. In particular, the mean value of measurement noise, or bias, cannot be neglected in inertial navigation applications where performance is required (see, e.g., Ref. Woodman [2007]). Bias can be seen as an unknown constant parameter; but since it can change with time, it is arguably appropriate to consider it as part of the state vector.

2.5.1. Proposed model

Let us consider joint attitude, velocity and inertial sensors biases estimation, with the assumption that $\boldsymbol{\omega}^{\mathrm{n/i}} \approx 0$ (the Earth is not rotating). The resulting system reads

$$x(t) = \begin{pmatrix} \mathbf{B}^{\mathrm{b}}(\mathbf{M}^{\mathrm{b}}, t) \\ \mathbf{v}^{\mathrm{b}}(t) \\ R(t) \\ \mathbf{b}_{\gamma}(t) \\ \mathbf{b}_{\omega}(t) \end{pmatrix}, \; y(t) = (\mathbf{B}^{\mathrm{b}}(\mathbf{M}^{\mathrm{b}}, t)), \; u(t) = \begin{pmatrix} \nabla\mathbf{B}^{\mathrm{b}}(\mathbf{M}^{\mathrm{b}}, t) \\ \boldsymbol{\omega}_{\mathrm{meas}}(t) \\ \boldsymbol{\gamma}_{\mathrm{meas}}(t) \end{pmatrix}, \tag{2.37}$$

with inertial sensors measurements modeled by

$$\boldsymbol{\omega}_{\mathrm{meas}} \doteq \boldsymbol{\omega}^{\mathrm{b/n}} + \mathbf{b}_{\omega}, \tag{2.38}$$

$$\boldsymbol{\gamma}_{\mathrm{meas}} \doteq \boldsymbol{\gamma}^{\mathrm{b}} + \mathbf{b}_{\gamma}. \tag{2.39}$$

The state dynamic function f reads

$$\frac{d\mathbf{B}^{\mathrm{b}}}{dt} = -(\boldsymbol{\omega}_{\mathrm{meas}} - \mathbf{b}_{\omega}) \times \mathbf{B}^{\mathrm{b}} + \nabla\mathbf{B}^{\mathrm{b}}\mathbf{v}^{\mathrm{b}} \tag{2.40}$$

$$\frac{d\mathbf{v}^{\mathrm{b}}}{dt} = -(\boldsymbol{\omega}_{\mathrm{meas}} - \mathbf{b}_{\omega}) \times \mathbf{v}^{\mathrm{b}} + \boldsymbol{\gamma}_{\mathrm{meas}} - \mathbf{b}_{\gamma} + R^{\top}\mathbf{g}^{\mathrm{n}} \tag{2.41}$$

$$\frac{dR}{dt} = R[(\boldsymbol{\omega}_{\mathrm{meas}} - \mathbf{b}_{\omega})\times] \tag{2.42}$$

$$\frac{d\mathbf{b}_{\gamma}}{dt} = 0 \tag{2.43}$$

$$\frac{d\mathbf{b}_{\omega}}{dt} = 0 \; . \tag{2.44}$$

Remark This system is bilinear in the state because of gyrometer biases.

2.5.2. Observability

This section studies the system formed by Eqs. (2.37)-(2.44). The aim is to prove that it is *not* observable in the sense of Def. 3, such that even if heading is ignored and the gradient of the magnetic field is non-singular, there exists indistinguishable trajectories. To do that, Def. 3 is used directly, as in Sec. 2.4.2. It is equivalent to check whether or not given $u(t)$ and $y(t)$, there exists a unique $x(t)$ solving the system.

Let $x(t)$ and $x'(t)$ be two solutions of Eqs. (2.37)-(2.44) for $t \in [t_0, T]$ for a given input $u \in \mathcal{U}$ such that

$$u(t) = \begin{pmatrix} \nabla \mathbf{B}^{\mathrm{b}}(\mathbf{M}^{\mathrm{b}}, t) \\ \boldsymbol{\omega}_{\mathrm{meas}}(t) \\ \gamma_{\mathrm{meas}}(t) \end{pmatrix}. \tag{2.45}$$

Let us assume that $\nabla \mathbf{B}^{\mathrm{b}}(\mathbf{M}^{\mathrm{b}}, t)$ is non singular for $t \in [t_0, T]$ and that $y(t) = h(x(t)) = h(x'(t))$, for $t \in [t_0, T]$. Let us denote

$$x'(t) = \begin{pmatrix} \mathbf{B}^{\mathrm{b}'}(\mathbf{M}^{\mathrm{b}}, t) \\ \mathbf{v}^{\mathrm{b}'}(t) \\ R'(t) \\ \mathbf{b}'_\gamma(t) \\ \mathbf{b}'_\omega(t) \end{pmatrix}, \ \delta x(t) = \begin{pmatrix} \delta\mathbf{B}^{\mathrm{b}}(t) \\ \delta\mathbf{v}^{\mathrm{b}}(t) \\ \delta R(t) \\ \delta\mathbf{b}_\gamma(t) \\ \delta\mathbf{b}_\omega(t) \end{pmatrix} \doteq \begin{pmatrix} \mathbf{B}^{\mathrm{b}}(\mathbf{M}^{\mathrm{b}}, t) - \mathbf{B}^{\mathrm{b}'}(\mathbf{M}^{\mathrm{b}}, t) \\ \mathbf{v}^{\mathrm{b}}(t) - \mathbf{v}^{\mathrm{b}'}(t) \\ R'(t)R(t)^\top \\ \mathbf{b}_\gamma(t) - \mathbf{b}'_\gamma(t) \\ \mathbf{b}_\omega(t) - \mathbf{b}'_\omega(t) \end{pmatrix}. \tag{2.46}$$

If there exists a solution for $\delta x(t)$ different from $\begin{pmatrix}0, 0, \mathbf{1}, 0, 0\end{pmatrix}^\top$ identically, then the system is not observable.

The equation $y(t) = h(x(t)) = h(x'(t))$ forces $\delta\mathbf{B}^{\mathrm{b}} \equiv 0$. Then, Equation (2.40) yields

$$\frac{d}{dt}\delta\mathbf{B}^{\mathrm{b}} = \delta\mathbf{b}_\omega \times y + \nabla\mathbf{B}^{\mathrm{b}}\delta\mathbf{v}^{\mathrm{b}} = 0. \tag{2.47}$$

It appears that this time, contrary to the system studied in Sec. 2.4.2, simply taking the time derivative of the output does not provide an unambiguous value of the velocity. Let us find out whether this ambiguity remains in the rest of the model, by looking for constant solutions for $\delta\mathbf{b}_\omega$ and $\delta\mathbf{v}^{\mathrm{b}}$.

To that end, $u(t)$, $y(t)$, and $x(t)$ are assumed to describe a static trajectory. In particular, they are all constant, and

$$\boldsymbol{\omega}^{\mathrm{b/n}} = \boldsymbol{\omega}_{\mathrm{meas}} - \mathbf{b}_\omega = 0 \ .$$

Equation (2.41) now yields

$$\begin{aligned} \frac{d}{dt}\delta\mathbf{v}^{\mathrm{b}} &= -(\boldsymbol{\omega}_{\mathrm{meas}} - \mathbf{b}'_\omega) \times \delta\mathbf{v}^{\mathrm{b}} \\ &\quad + \delta\mathbf{b}_\omega \times \mathbf{v}^{\mathrm{b}} - \delta\mathbf{b}_\gamma + R^\top(\mathbf{1} - \delta R^\top)\mathbf{g}^{\mathrm{n}} \qquad (2.48) \\ &= -\delta\mathbf{b}_\omega \times \delta\mathbf{v}^{\mathrm{b}} - \delta\mathbf{b}_\gamma + R^\top(\mathbf{1} - \delta R^\top)\mathbf{g}^{\mathrm{n}}. \qquad (2.49) \end{aligned}$$

In order for $R^\top(\mathbf{1} - \delta R^\top)\mathbf{g}^{\mathrm{n}}$ to be identically zero, it is enough that $\left(\mathbf{1} - \delta R^\top\right)\mathbf{g}^{\mathrm{n}}$ be identically zero, or equivalently, that $\delta R^\top$ always leave $\mathbf{g}^{\mathrm{n}}$ invariant. Because of Eq. (2.42),

$$\left(\frac{d}{dt}\delta R\right)^\top = -R[\delta\mathbf{b}_\omega \times]R'^\top.$$

In order for $\delta R^\top$ to leave $\mathbf{g}^\mathrm{n}$ invariant, it is enough to choose any $R'(t_0) \in \mathrm{SO}(3)$, and $\delta\mathbf{b}_\omega$ such that

$$[\delta\mathbf{b}_\omega \times] R'(t_0)^\top \mathbf{g}^\mathrm{n} = 0. \tag{2.50}$$

In conclusion, one can choose $\delta\mathbf{v}^\mathrm{b}(t_0)$ such that Equation (2.47) is always true, because then, the right hand side of Eq. (2.49) can be arbitrarily set to 0 identically by the appropriate choice of $\delta\mathbf{b}_\gamma$. A family of trajectories described by the same inputs and outputs as a static one in $\mathfrak{R}_\mathrm{n}$ has successfully been found. The reader can check that they are shaped as vertical helices. Thus, the model formed by Eqs. (2.37)-(2.44) is not observable in the sense of Def. 3.

2.5.3. Conclusion and remarks

Unobservability of static trajectories If one takes into account inertial sensor biases, there exist some indistinguishable trajectories. The unobservable space is large and spans the attitude matrix, gyrometer and accelerometer biases, and velocity. Static trajectories (constant attitude, zero velocity) belong to this set of trajectories. This is problematic because this means that for a trajectory to be observable, it is necessary, but not sufficient, that the tracked object be continually moving. Imposing this constraint is impractical in a realistic use case.

Implications on the choice of inertial sensors This issue stems entirely from inertial sensor biases uncertainty because otherwise, no such issue occurs (see. Sec. 2.4). In practice, prior knowledge of biases should be exploited to help limit trajectory reconstruction uncertainty. This means that inertial sensors must be chosen for their bias stability.

Implications on attitude estimation Attitude and heading observers, *also in the static case*, display the same observability issue as this model: accelerometer biases and tilt errors are indistinguishable, and gyrometer biases interpreted as vertical (causing a heading drift) are unobservable. Knowing the magnetic field has not improved the situation. For gyrometer biases, this issue can be solved whenever the term $\nabla\mathbf{B}^\mathrm{b}\mathbf{v}^\mathrm{b}$ can be neglected, in approaches such as Ref. Afzal et al. [2011b] that rely on the fact that the direction of the magnetic field is constant (but unknown) in the inertial frame in such cases.

Unobservability of heading Despite the fact that static trajectories (having constant input and output) belong to an indistinguishable set, trajectories outside of this set (e.g., with non-constant inputs) might belong to indistinguishable sets of lower dimension. However, for symmetry reasons, one still cannot expect heading to be observable: in particular, for a given input, one can change the initial heading with no effect on the output. To solve this problem, the model has to be changed.

Higher order magnetic models Information about velocity and gyrometer biases may be recovered using more magnetic sensors. For example, if the second spatial derivative of the magnetic field is known and used as an input, then $\nabla \mathbf{B}^{\mathrm{b}}$ can be added to the state vector and moved from the input vector to the output vector because an equation similar to (2.40) can be written. In the special case where this second spatial derivative is zero, then it is expected that $\nabla \mathbf{B}^{\mathrm{b}}$ only rotates at the rate $\boldsymbol{\omega}^{\mathrm{b/n}}$. Measuring $\nabla \mathbf{B}^{\mathrm{b}}$ then gives access to the full angular velocity vector $\boldsymbol{\omega}^{\mathrm{b/n}}$, solving the unobservability problem in the above-mentioned static case for velocity and gyrometer biases. If the second spatial derivate is not zero, one may expect the observability issue to remain solved; more work on this subject is needed to draw a definite conclusion in the general case. Ref. Skog et al. [2018], published during the redaction of this document, does prove this result in a discrete-time Bayesian filtering framework.

Remark Ref. [Dorveaux, 2011, Appx. D] proves the observability of accelerometer biases under the assumption that the attitude matrix R is known. This assumption is not taken in this section, hence the different conclusion.

2.6. Conclusion

Chosen models In this chapter, a few existing models of the state of the art have been reviewed, and several models suitable for MIDR have been proposed. The two candidates considered as the best are proposed in Sec. 2.4 and 2.5 respectively. They are considered as the best models in that they are the most representative, compared with existing models proposed in the state of the art, and for their straightforwardness.

Observability issues Neither of these models is observable in the sense of Def .3. More precisely, the heading is unobservable in both cases. Moreover, it has been proven that with low-cost MEMS sensors, static trajectories belong to an unobservable set of helical trajectories of dimension at least 4, with attitude and the component of gyrometer biases corresponding to a heading drift both unobservable, with their associated values of velocity and accelerometer biases. These issues may be solved with hardware for which second-order spatial derivatives of the magnetic field can be measured directly. Since such hardware was never going to be available during this work, this case was not studied in this chapter.

Heading estimation issues Previous works on MIDR have mainly ignored the issue of (true or magnetic) heading estimation, in spite of the fact that it is one of the primary sources of error in dead-reckoning applications, even in Pedestrian Dead Reckoning (PDR). Solving this problem requires a model that is not symmetrical with respect to a change of initial heading. With accurate inertial sensors, this can be done by using a rotating Earth model. With low-cost MEMS sensors, this is for now unreachable, and the problem stays open.

Priorities Previous works have mostly focused on the ability to recover velocity and on cases in which the magnetic field gradient is singular. This study, in particular, Sec. 2.5, shows that this issue is secondary before the observability of inertial sensor biases, attitude and heading. These difficulties arise even before taking into account other measurement errors, such as the effect of uncertainties on the spatial gradient of the magnetic field on estimation, which remain to be addressed in later chapters. Despite all these difficulties, there remains some hope that generic trajectories be observable, and that an observer may be able to compute them.

Remark Let us remark that position has not been considered, because, in all of these models, the magnetic field output does not depend on it, but on time. Therefore, a change in initial position has *no influence* on the output. This characterizes dead-reckoning. A method must then be chosen in order to integrate the velocity, in a way that is robust to unknown initial conditions or to time-intervals during which observability is lost.

3. Measurement errors of magnetometer arrays combined with inertial sensors

Contents

3.1. Introduction

3.1.1. Hardware

Between 2007 and the beginning of this work, SYSNAV has been developing hardware capable of being used for Magneto-Inertial Dead-Reckoning (MIDR). It consists in two modules illustrated Fig. 3.1: a sensor board (Fig. 3.1a), and an operation unit (Fig. 3.1b). The sensor board of the Magneto-Inertial Measurement Unit (MIMU) device can be carried by hand (Fig. 3.1c) or can be strapped onto one's body. It carries Microelectromechanical Systems (MEMS) inertial sensors and several magnetometers arranged in a way that makes it possible to compute the spatial gradient of the magnetic field (Fig. 3.2). Thus, using the acquired measurements, one can integrate the differential equations that govern the dynamics of the chosen state-space model (Ch. 2) modeling movements of the sensor board. Said computation is done on an embedded microcontroller with a Floating-Point Unit (FPU)[1]designed for small systems, in the operation unit, to whom sampled data is sent from the sensor board.

3.1.2. Calibration

Sensors do not directly produce the desired measurements of angular velocity, acceleration, and (spatial gradient of the) magnetic field needed in navigation algorithms (Table 3.1). Instead, they produce voltages that depend on given physical quantities including those being measured. Said voltages can be sampled into numbers using Analog Digital Converters (ADCs), before being used into a digital computer. Therefore, a calibration step is needed (Fig. 3.3). Calibration of a measurement system is the identification of a function that yields the desired physical quantity from the measurement system output with minimal error. This function usually takes the form of a parametric model, whose parameters must be identified during a calibration procedure. Furthermore, voltage measurements are affected by random, unpredictable noise such as thermal noise, flicker noise... making any hope of having perfect measurements unrealistic.

3.1.3. Outline

This chapter aims at understanding the key points bridging raw sensor measurements to inputs of an MIDR algorithm (Table 3.1). The main points will be regarding magnetic field measurements and calibration issues of the array of sensors. Sec. 3.2 discusses magnetometer measurement models, and how to retrieve the magnetic field vector and the magnetic field gradient from sensor measurements. Sec. 3.3 discusses how and why inertial and magnetic sensors must be calibrated in the same frame of reference $\mathfrak{R}_\mathrm{b}$. Sec. 3.4 discusses the effect of calibration errors on the problem of trajectory reconstruction. Characteristics of inertial sensors are not discussed in-depth in this work. The reader is referred to Refs. Radix and de Cremiers [1991],

---

[1] e.g. Renesas SH7216

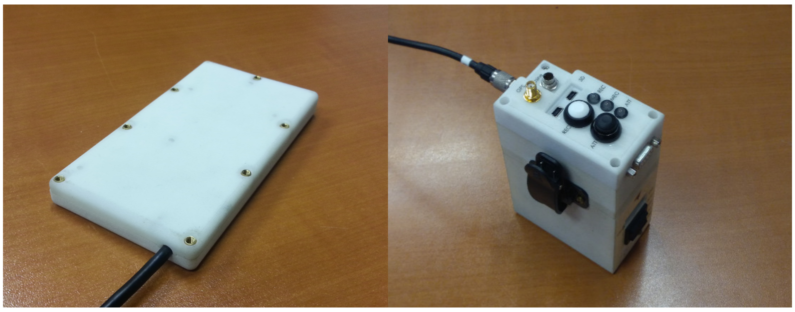

(a) Prototype sensor package (b) Prototype operation unit

(c) User carrying the hardware, a MIMU device

Figure 3.1: Hardware provided by SYSNAV during this work

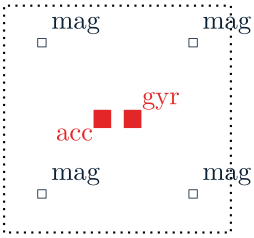

Figure 3.2: Simplified diagram of the sensor board

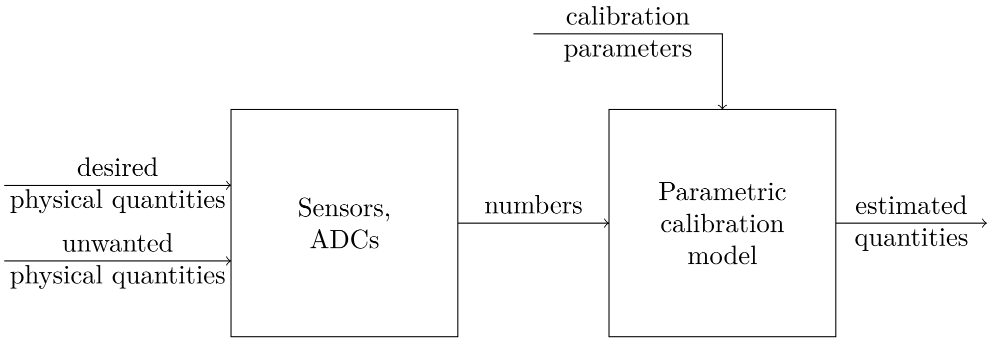

Figure 3.3: Sensors and ADCs yield numbers which are dependent both desired and unwanted physical quantities. Calibration refers both to the application of the parametric model, and to the estimation of calibration parameters minimizing the error between desired physical quantities and their estimated value.

Savage [2000], Woodman [2007] regarding the use of strapdown inertial sensors and their characterization with Allan variance (see Ref. [IEEE, 2003, Appx. C]).

3.2. Magnetic sensors

Context The MIMU device prototyped by SYSNAV is designed for indoor MIDR applications. Design constraints led the company to its choice of Anisotropic Magneto-Resistance (AMR) magnetometers (see Refs. Mohamadabadi [2013], Mohamadabadi and Hillion [2014], Mohamadabadi et al. [2013b]), and its research on their calibration (see Refs. Dorveaux et al. [2009a, 2010], Mohamadabadi and Hillion [2014], Mohamadabadi et al. [2013b]). This type of magnetometer is designed to measure the projection of the magnetic field along its sensitive axis. AMR magnetometers (see Refs. Groenland et al. [1992], Kuijk et al. [1975]) are known for their cross-axis effect and their overall non-linear response (see Refs. Ripka et al. [2009], Ripka and Butta [2009] and Fig. 3.4). The primary sources of errors for this type of sensors are relatively well known, along with their corresponding accuracy improvement strategies (see Ref. Ripka [2008]). Since here they are being used for navigation, this Section aims at verifying their measurement model with respect to predictable sources of errors, in their calibration, and in the way the magnetic field gradient can be computed from their output.

Hard- and Soft-iron The ambient magnetic field is distorted by materials whose relative permeability μ_r is different from 1. It is often the case that electronics carry paramagnetic materials (with $\mu_r > 1$, often called soft-irons), and ferromagnetic materials (that also display a hysteretic behavior). For example, sensitive elements of AMR magnetometers are ferromagnetic. The “Soft-iron” effect refers to the effect on

Table 3.1.: Quantities needed in MIDR algorithms and notations

Symbol	**Physical quantity**	**Associated position in body frame $\mathfrak{R}_\mathrm{b}$**	**Measurement method**
$\boldsymbol{\omega}^\mathrm{b}$	angular velocity	none	MEMS gyrometer
γ^b	proper acceleration	percussion point $\mathbf{M}^\mathrm{b}$	MEMS accelerometer
$\mathbf{B}^\mathrm{b}$	magnetic field vector	equivalent measurement point $\mathbf{N}^\mathrm{b}$	finite differences from MEMS magnetometers
$\nabla\mathbf{B}^\mathrm{b}$	magnetic field gradient		

magnetic measurements of materials whose relative permeability μ_r is different from 1. The "Hard-iron" effect is the effect on magnetic measurements of materials that retain a permanent magnetization (e.g., ferromagnets), resulting in biased readings. When the offending materials are part of the electronics, these effects must be calibrated out.

Outline In Sec. 3.2.1, the measurement model of linear single-axis point magnetometers is provided with its assumptions. In Sec. 3.2.2, the measurement and calibration model of linear tri-axis magnetometers in homogeneous field are provided. Sec. 3.2.3, presents the results of parameter identification of the above-mentioned linear calibration model. An alternative, non-linear model is deduced from measurement physics in Sec. 3.2.4, and tested in Sec. 3.2.5, concluding the accuracy of the derived calibration model and reproducing the outline of Ref. Ripka and Butta [2009] for the setup being used. Finally, the method by which spatial derivatives of the magnetic field can be computed from an array of such magnetometers is discussed in Sec. 3.2.6.

3.2.1. Ideal linear single-axis point magnetometers

Let $\mathbf{B}^\mathrm{b}(\mathbf{P}^\mathrm{b}, t)$ denote the magnetic field vector in body frame $\mathfrak{R}_\mathrm{b}$ at time t. Let us consider a number of n_mag ideal single-axis point-magnetometers on a sensor board, that is, by definition, fixed in $\mathfrak{R}_\mathrm{b}$. The following assumptions are made.

Assumption 3.2.1. *Each single-axis magnetometer output depends linearly on the value of the ambient magnetic field along a fixed direction in* $\mathfrak{R}_\mathrm{b}$.

Assumption 3.2.2. *Each single-axis magnetometer output depends* only *on the value of the ambient magnetic field at its effective position.*

The so-called *effective position* is defined by the above assumption, and corresponds to an equivalent position of the magnetometer's sensitive element.

Corollary 3.2.1 (Corollary of Assumption 3.2.2). *Either one of the following is true,*

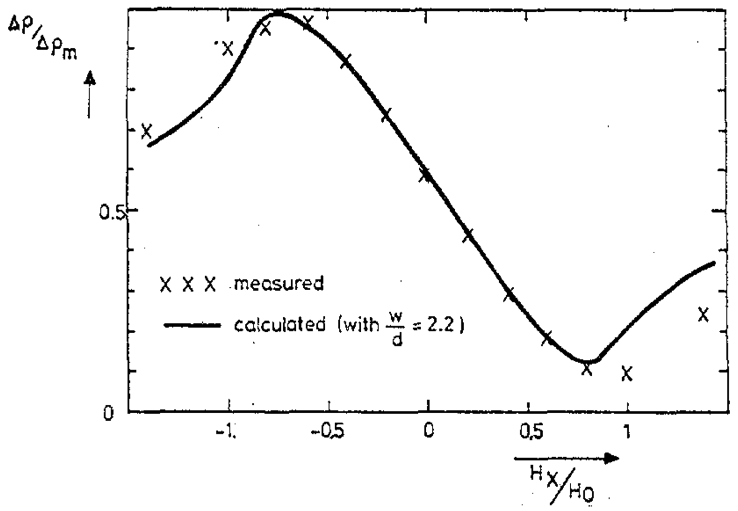

Figure 3.4: From Ref. Ripka et al. [2009] “Static curve of the barber pole”, showing the resistivity of a barber-pole AMR with respect to the magnetic field in its sensitive axis. Its response is clearly nonlinear.

(i) *Each single-axis magnetometer is only affected by soft-iron effects to a negligible extent;*

(ii) *All soft-irons affecting it are located at its effective position;*

(iii) *The ambient magnetic field is homogeneous.*

The (linear) measurement model assumption for the j-th sensor is then

$$\forall j \in \{1, ..., n_{\text{mag}}\},\ \forall t,\ {}_j y(t) = {}_j\mathbf{a}^{\text{b}}\mathbf{B}^{\text{b}}({}_j\mathbf{p}^{\text{b}}, t) + {}_j b\ , \tag{3.1}$$

where ${}_j\mathbf{a}^{\text{b}} = \begin{pmatrix} {}_j a_1^{\text{b}} & {}_j a_2^{\text{b}} & {}_j a_3^{\text{b}} \end{pmatrix}$ are coordinates in body frame of a co-vector representing the j-th magnetometer's scale factor and sensitive axis, ${}_j b$ its bias, ${}_j\mathbf{p}^{\text{b}}$ and its effective position in body frame.

3.2.2. Tri-axis magnetometers

Homogeneous field measurement and calibration models

Magnetometers are often arranged in groups of three *nearly* orthogonal sensors to form a tri-axis magnetometer. Four such tri-axis magnetometers are represented in Fig. 3.2. Let us assume that the first three single-axis magnetometers form such a tri-axis sensor. Assuming that the ambient magnetic field is homogeneous, that is to say, there exists some $\mathbf{B}^{\text{b}}{}_0(t)$ such that

$$\forall \mathbf{P}^{\text{b}} \in \mathbb{R}^3,\ \forall t,\ \mathbf{B}^{\text{b}}(\mathbf{P}^{\text{b}}, t) = \mathbf{B}^{\text{b}}{}_0(t)\ , \tag{3.2}$$

then the (linear) direct measurement model for a single tri-axis sensor in an homogeneous magnetic field is

$$\begin{pmatrix} {}_1y(t) \\ {}_2y(t) \\ {}_3y(t) \end{pmatrix} = \begin{pmatrix} {}_1a_1^{\mathrm{b}} & {}_1a_2^{\mathrm{b}} & {}_1a_3^{\mathrm{b}} \\ {}_2a_1^{\mathrm{b}} & {}_2a_2^{\mathrm{b}} & {}_2a_3^{\mathrm{b}} \\ {}_3a_1^{\mathrm{b}} & {}_3a_2^{\mathrm{b}} & {}_3a_3^{\mathrm{b}} \end{pmatrix} \mathbf{B}^{\mathrm{b}}{}_0(t) + \begin{pmatrix} {}_1b \\ {}_2b \\ {}_3b \end{pmatrix} . \tag{3.3}$$

The (linear) calibration model for a single tri-axis sensor in an homogeneous magnetic field is then

$$\mathbf{B}^{\mathrm{b}}{}_0(t) = A \begin{pmatrix} {}_1y(t) \\ {}_2y(t) \\ {}_3y(t) \end{pmatrix} + B , \tag{3.4}$$

where

$$A = \begin{pmatrix} {}_1a_1^{\mathrm{b}} & {}_1a_2^{\mathrm{b}} & {}_1a_3^{\mathrm{b}} \\ {}_2a_1^{\mathrm{b}} & {}_2a_2^{\mathrm{b}} & {}_2a_3^{\mathrm{b}} \\ {}_3a_1^{\mathrm{b}} & {}_3a_2^{\mathrm{b}} & {}_3a_3^{\mathrm{b}} \end{pmatrix}^{-1} , \ B = -A \begin{pmatrix} {}_1b \\ {}_2b \\ {}_3b \end{pmatrix} . \tag{3.5}$$

When tri-axis magnetometers are said to be “compensated for hard- and soft-iron effects”, it means that the A and B matrices have been identified respectively and also take these effects into account in homogeneous field conditions. This also means that, as explicitly stated in Ref. Foster and Elkaim [2008], it is assumed that “responses of soft iron materials are linear and without hysteresis”.

To summarize, the following assumptions have been made in order to derive this calibration model.

Assumption 3.2.3. *The ambient magnetic field is homogeneous, responses of potential soft iron materials that may influence measurements are linear and without hysteresis, and Assumption 3.2.1 is made.*

Calibration model identification

Ellipsoid fitting principle The problem of identifying A and B for a single tri-axis magnetometer is often solved using ellipsoid fitting methods (see e.g. Refs. Dorveaux et al. [2009a], Foster and Elkaim [2008], Renaudin et al. [2010], Vasconcelos et al. [2008, 2011]), for their low cost and their seemingly not needing additional hardware. Ellipsoid fitting calibration techniques rely on the fact that, when measurement data is collected in a place where the magnetic field is both stationary and homogeneous, the norm of the calibrated magnetic field must be invariant. That is to say; there exists some constant vector $\mathbf{B}^{\mathrm{n}}{}_0$ such that

$$\forall \mathbf{P}^{\mathrm{b}} \in \mathbb{R}^3, \ \forall t, \ \mathbf{B}^{\mathrm{b}}(\mathbf{P}^{\mathrm{b}}, t) = \mathbf{B}^{\mathrm{b}}{}_0(t) = R(t)^{\top}\mathbf{B}^{\mathrm{n}}{}_0$$

where $R(t) \in \mathrm{SO}(3)$ represents the attitude matrix of the sensor board (the attitude matrix R is defined in Sec. 2.2.1). The norm of the calibrated magnetic field must be invariant, since

$$\begin{aligned}\|\mathbf{B}^{\mathrm{b}}{}_0(t)\|^2 &= \mathbf{B}^{\mathrm{b}}{}_0(t)^\top \mathbf{B}^{\mathrm{b}}{}_0(t)\\ &= \mathbf{B}^{\mathrm{n}}{}_0^\top R(t) R(t)^\top \mathbf{B}^{\mathrm{n}}{}_0\\ &= \mathbf{B}^{\mathrm{n}}{}_0^\top \mathbf{B}^{\mathrm{n}}{}_0 \ .\end{aligned}$$

The following equality must then hold for all time t

$$\begin{aligned}&\left(A\begin{pmatrix}{}_1y(t)\\ {}_2y(t)\\ {}_3y(t)\end{pmatrix}+B\right)^\top \left(A\begin{pmatrix}{}_1y(t)\\ {}_2y(t)\\ {}_3y(t)\end{pmatrix}+B\right)\\ &= \mathbf{B}^{\mathrm{n}}{}_0^\top \mathbf{B}^{\mathrm{n}}{}_0\end{aligned} \tag{3.6}$$

The known advantages of ellipsoid fitting techniques is that they have no precision requirement on sensor orientation during calibration trials. However, two issues can immediately be noticed

1. Denoting O(3) the orthogonal group of dimension 3, for all $T \in \mathrm{O}(3)$, replacing A by TA and B by TB preserves the invariant that is the norm of the calibrated magnetic field.
2. The norm of the magnetic field must be known beforehand.

If the norm of the magnetic field is known, then Refs. Alonso and Shuster [2002a], Dorveaux et al. [2009a], Foster and Elkaim [2008], Renaudin et al. [2010], Vasconcelos et al. [2008, 2011] provide different schemes for computing instances of TA and TB, with $T \in \mathrm{O}(3)$. However, the frame of reference in which magnetometers are calibrated is unknown, because T itself is unknown.[2]

Identification schemes The different identification schemes of the state of the art differ by their choice of cost function. If the model were representative, this choice would be of little importance. Noise and sensor non-linearity justify using different cost functions to some extent.

The algorithm proposed in Ref. Foster and Elkaim [2008] stems from the fact that, by QR factorization, there exists $T' \in \mathrm{O}(3)$ such that

$$A' \doteq \begin{pmatrix} a'_{11} & a'_{12} & a'_{13}\\ 0 & a'_{22} & a'_{23}\\ 0 & 0 & a'_{33}\end{pmatrix} = T'A \tag{3.7}$$

$$B' \doteq \begin{pmatrix} b'_1\\ b'_2\\ b'_3\end{pmatrix} = T'B \ . \tag{3.8}$$

---

[2] The implication is that if magnetometers are used for heading estimation, with ellipsoid fitting techniques, two calibrations on the same data may result in completely different heading estimates if no subsequent alignment is performed.

Denoting the square positive symmetric matrix $Q \doteq A'^{\top}A$, the square matrix $L \doteq B'^{\top}A'$, and the scalar $\mu \doteq B'^{\top}B'$, one can define the function

$$g(Q, L, \mu, t) = \begin{pmatrix} {}_1y(t) \\ {}_2y(t) \\ {}_3y(t) \end{pmatrix}^{\top} Q \begin{pmatrix} {}_1y(t) \\ {}_2y(t) \\ {}_3y(t) \end{pmatrix} + 2L \begin{pmatrix} {}_1y(t) \\ {}_2y(t) \\ {}_3y(t) \end{pmatrix} + \mu - \mathbf{B^n}_0^{\top}\mathbf{B^n}_0 \ ,$$

and Eq. (3.6) implies

$$g(Q, L, \mu, t) = 0.$$

The term $g(Q, L, \mu, t)$ is a linear in Q, L and μ. With sampled measurements on times t_i, where i is an integer index, one can recover Q, L and μ minimizing $\sum_i g(Q, L, \mu, t_i)^2$, which is *quartic*, and not quadratic, in measurement errors. Parameters A' and B' can be solved algebraically. Since these parameters minimize an error that is *quartic*, not quadratic, in measurement errors, measurement error standard deviation is not minimized in the general case. In presence of significant Gaussian measurement noise, other techniques should be preferred.

The issue has been known at least since the proposal of the so-called *TWOSTEP* calibration methodology from Ref. Alonso and Shuster [2002b], extended in Ref. Alonso and Shuster [2002a] to take scale factors and non-orthogonality into account. Following a similar first step, a second step consists in using a Gauss-Newton method to correct the estimate of calibration parameters.

Similarly, in Ref. Renaudin et al. [2010], the proposed solution is instead to use the *adjusted least squares* estimator proposed in Ref. Markovsky et al. [2004] to find the parameters of the ellipsoid in a statistically consistent way.

The algorithm proposed in Ref. Dorveaux et al. [2009a] solves this problem with an iterative algorithm whose implementation only requires a least-squares solver. It consists in computing at each iteration k the values of A'_k and B'_k minimizing

$$J_k(A'_k, B'_k) = \sum_i \left\| A'_k \begin{pmatrix} {}_1y(t_i) \\ {}_2y(t_i) \\ {}_3y(t_i) \end{pmatrix} + B'_k - p\left(A'_{k-1} \begin{pmatrix} {}_1y(t_i) \\ {}_2y(t_i) \\ {}_3y(t_i) \end{pmatrix} + B'_{k-1} \right) \right\|^2 , \qquad (3.9)$$

where p is the projection on the sphere of radius $\|\mathbf{B^n}_0\|^2$. Thus, the minimized cost function is quadratic in measurement errors.

In Ref. Vasconcelos et al. [2008, 2011], the algorithm proposed in Ref. Foster and Elkaim [2008] is used to find an initial guess of calibration parameters. Then, calibration is modeled as a Maximum Likelihood Estimation problem including the magnetic field in body frame at each sample and solved directly using non-linear least-square algorithms.

3.2.3. Linear calibration experiments

Ellipsoid fitting calibration experiments have been carried out on the hardware used in this work (illustrated in Fig. 3.1), showing that *the linear model is not representative of measurements*, see Fig. 3.5a. Calibration residuals do not resemble a white noise.

They have a very definite structure, as is evident when the norm of the calibrated magnetic field is plotted against the latter in 3D, see Fig. 3.5b. This observation motivates investigating which measurement model is representative of these sensors.

3.2.4. Nonlinear measurement model

Each single-axis magnetometer used in experiments is a Wheatstone bridge formed by four arrays of magneto-resistive barber-poles (see Ref. Wan [1999], Fig. 3.6 and Fig. 3.7).

It is known that AMR sensors have a non-linear response (see Ref. Ripka et al. [2009]). This is why some magnetometer manufacturers have designed strategies to mitigate sensor non-linearity (see e.g. Wan [1999]), or why in Ref. Mohamadabadi et al. [2013a] a compensation method is proposed that relies on measurement physics (see also Ripka and Butta [2009]).

A representative model for magnetometer nonlinearities can be deduced from measurement physics. The method proposed below consists in

1. Expressing the resistance of each barber pole sensing element as a function of the magnetic field

2. Deducing the relationship between the input voltage of the Wheatstone bridge (VBRIDGE on Fig. 3.7) and its output voltage (difference between OUT+ and OUT- on Fig. 3.7), thus the output voltage from the input current of the Wheatstone bridge, thus the three output voltages of a tri-axis magnetometer from the homogeneous ambient magnetic field components

3. Deducing the calibration model needed to recover the magnetic field

Model of a barber pole AMR

Let us consider the magneto-resistive element in Fig. 3.8. An orthonormal basis (e_x, e_y, e_z) is chosen with e_x in the direction of anisotropy (to the right) and e_y in the plane of the film (to the top).

According to Ref. Kuijk et al. [1975], the resistivity ρ of an AMR is a function of the angle θ between the current vector $\mathbf{i}$ and the magnetization vector $\mathbf{m}$ of the sensitive element,

$$\rho = \rho_0 + \Delta\rho_m(1 - \sin^2\theta) \ . \tag{3.10}$$

Denoting $\kappa \doteq \frac{\Delta\rho_m}{\rho_0}$, the resistance R of an AMR can be written as

$$R = (1 + \kappa\cos^2\theta)R_0 \ , \tag{3.11}$$

where R_0 is the resistance of the AMR in the direction orthogonal to the magnetization vector. Let us now find an expression for θ.

According to Ref. Groenland et al. [1992], it is a very good approximation to assume that the magnetization vector $\mathbf{m}$ lies in the plane of the film. According to the same

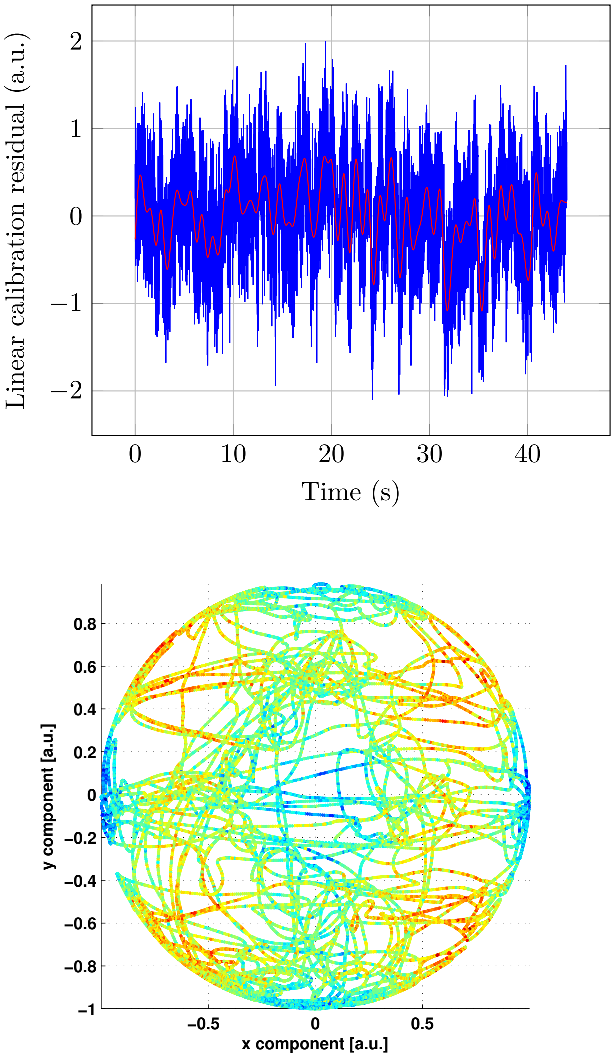

Figure 3.5: (top) Linear calibration residuals (in arbitrary units) with respect to time during a calibration trial. They are defined as the calibrated norm of the magnetic field after linear parameter identification, minus the reference norm. Residuals are visibly different from a white Gaussian noise. The solid red line represents the solid blue line filtered by a low pass filter with 2Hz cutoff frequency.
(bottom) Experimental linear calibration residuals (colors) with respect to the linearly calibrated magnetic field. The magnetic field norm is underestimated along sensitive axes, overestimated far from them. This suggests that residuals plotted Fig. 3.5a come from sensor non-linearities.

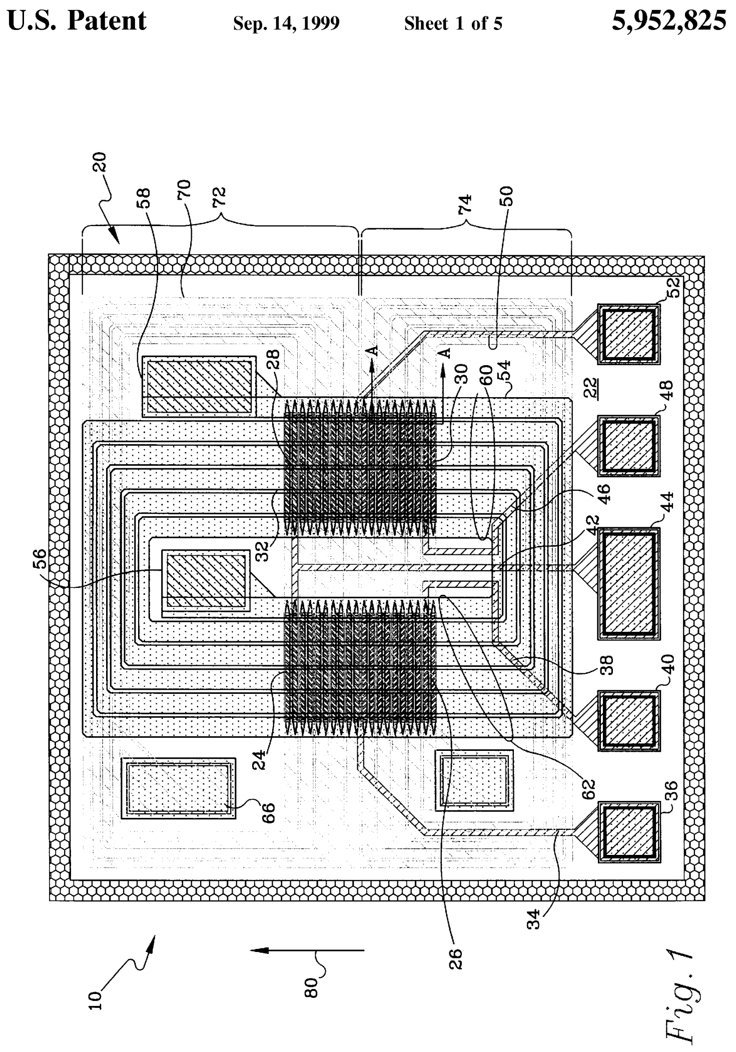

Figure 3.6: From Ref. Wan [1999], Architecture of a single axis magnetometer sensing element

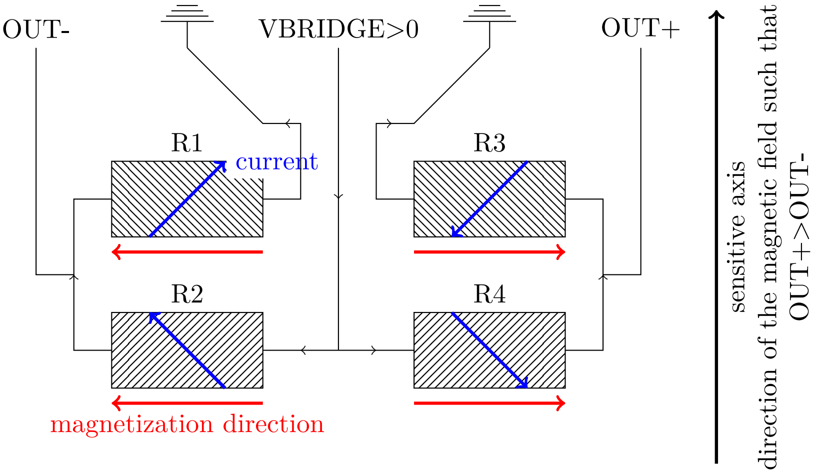

Figure 3.7: Diagram of a sensitive element described in Ref. Wan [1999] and represented Fig. 3.6. The diagram is deduced from Ref. Wan [1999] and from stripes orientation on barber poles.

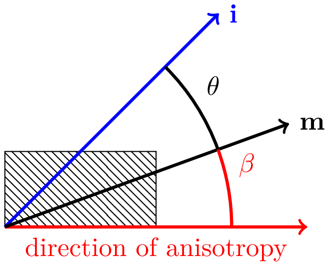

Figure 3.8: Angles notations in Sec. 3.2.4

reference, denoting β (cf. Fig. 3.8) the angle between $\mathbf{m}$ (assumed of fixed norm) and the anisotropy direction, the free energy density ϵ is

$$\epsilon \doteq K \sin^2 \beta - \mu_0 \mathbf{H} \cdot \mathbf{m} \ . \tag{3.12}$$

One can notice that if $\mathbf{m}$ lies in the plane of the film, the free energy density only depends on components of the field $\mathbf{H}$ in this plane.[3] The angle β minimizes ϵ in (3.12), that reads

$$\epsilon \doteq K \sin^2 \beta - \mu_0 \|\mathbf{m}\| \begin{pmatrix} H_x \\ H_y \\ H_z \end{pmatrix} \cdot \begin{pmatrix} \cos\beta \\ \sin\beta \\ 0 \end{pmatrix}$$

In a barber-pole, the direction of the current vector $\mathbf{i}$ is forced, by using conductive elements above the AMR at an angle of around $\pi/4$ radians compared to the direction of anisotropy, also called “easy-axis”, orthogonal to the so-called “sensitive axis” and contained in the plane of the film. Because the angle between the current vector $\mathbf{i}$ and the anisotropy direction is fixed, it is sufficient to know β (that minimizes ϵ) in order to deduce θ.

Denoting in this basis the dimensionless vector

$$\begin{pmatrix} h_x \\ h_y \\ h_z \end{pmatrix} \doteq \frac{1}{H_k} \mathbf{H} = \frac{1}{H_k} \begin{pmatrix} H_x \\ H_y \\ H_z \end{pmatrix} , \tag{3.13}$$

with $H_k = {}^{2K}/_{\mu_0 \|\mathbf{m}\|}$ denoting the anisotropy field where μ_0 is the magnetic constant, using formal calculation software, one can deduce from Eq. (3.12) an expression for β in the form of the following series expansion around $\begin{pmatrix} h_x \\ h_y \\ h_z \end{pmatrix} = 0$ up to order 5

$$\beta \approx h_y - h_x h_y + h_x^2 h_y + \frac{h_y^3}{6} - h_x^3 h_y - h_x h_y^3 + h_x^4 h_y + 3 h_x^2 h_y^3 + \frac{3 h_y^5}{40} . \tag{3.14}$$

To obtain $\frac{R}{R_0}$, it is sufficient to inject this series expansion into Eq. (3.11). For instance in Fig. 3.8, knowing that by construction of the barber-pole, $\theta + \beta = \pi/4$

$$\frac{R}{R_0} = 1 + \frac{\kappa}{2} + \kappa \left(h_y - h_x h_y + h_x^2 h_y - \frac{h_y^3}{2} - h_x^3 h_y + h_x h_y^3 + h_x^4 h_y - h_x^2 h_y^3 - \frac{h_y^5}{8} \right) \tag{3.15}$$

Model of the Wheatstone bridge

Referring to Fig. 3.7, let us choose e_x pointing to the right (easy axis), and e_y to the top (sensitive axis). Let us denote V_y = (OUT+) − (OUT−) the output voltage

---

[3] see also Ref. Lowes [1974]

of the Wheatstone bridge. Assuming that the four barber poles are perfectly aligned and identical, we obtain

$$\frac{R_1}{R_0}=1+\frac{\kappa}{2}+\kappa\left(-h_y-h_xh_y-h_x^2h_y+\frac{h_y^3}{2}-h_x^3h_y+h_xh_y^3-h_x^4h_y+h_x^2h_y^3+\frac{h_y^5}{8}\right) \tag{3.16}$$

$$\frac{R_2}{R_0}=1+\frac{\kappa}{2}+\kappa\left(h_y+h_xh_y+h_x^2h_y-\frac{h_y^3}{2}+h_x^3h_y-h_xh_y^3+h_x^4h_y-h_x^2h_y^3-\frac{h_y^5}{8}\right) \tag{3.17}$$

$$\frac{R_3}{R_0}=1+\frac{\kappa}{2}+\kappa\left(h_y-h_xh_y+h_x^2h_y-\frac{h_y^3}{2}-h_x^3h_y+h_xh_y^3+h_x^4h_y-h_x^2h_y^3-\frac{h_y^5}{8}\right) \tag{3.18}$$

$$\frac{R_4}{R_0}=1+\frac{\kappa}{2}+\kappa\left(-h_y+h_xh_y-h_x^2h_y+\frac{h_y^3}{2}+h_x^3h_y-h_xh_y^3-h_x^4h_y+h_x^2h_y^3+\frac{h_y^5}{8}\right) . \tag{3.19}$$

In the Wheatstone bridge, denoting i_b the input current of the bridge,

$$\begin{aligned} V_y &= \left(\frac{R_3}{R_3+R_4}-\frac{R_1}{R_1+R_2}\right)\text{VBRIDGE} \\ &= \frac{\kappa}{1+\frac{\kappa}{2}}\left(h_y+h_x^2h_y-\frac{h_y^3}{2}+h_x^4h_y-h_x^2h_y^3-\frac{h_y^5}{8}\right)\text{VBRIDGE} , \end{aligned} \tag{3.20}$$

where

$$\begin{aligned} \text{VBRIDGE} &= \left(\frac{1}{R_1+R_2}+\frac{1}{R_3+R_4}\right)^{-1} i_b \\ &= \left(1+\frac{\kappa}{2}\right)R_0 i_b . \end{aligned} \tag{3.21}$$

Thus, denoting $v_y \doteq \frac{V_y}{R_0 i_b \kappa}$ (dimensionless), using formal calculation software, the following series expansion for v_y up to order 5 is obtained,

$$v_y = h_y + h_x^2h_y - \frac{h_y^3}{2} + h_x^4h_y - h_x^2h_y^3 - \frac{h_y^5}{8} . \tag{3.22}$$

All non-linearities of even-order have simplified without resorting to flipping (see e.g. Ref. [Mohamadabadi, 2013, Sec. 3.4]). This Wheatstone bridge configuration is already sufficient to reduce the cross-axis effect significantly.

Calibration model of an orthogonal tri-axis magnetometer

Let us consider

- A first single-axis magnetometer with e_x as sensitive axis, and e_y as easy axis. Its dimensionless output is denoted v_x;
- A second magnetometer with e_y as sensitive axis, and e_x as easy axis. Its dimensionless output is denoted v_y;

- A third magnetometer with e_z as sensitive axis, and e_x as easy axis. Its dimensionless output is denoted v_z.

Eq. (3.22) represents the measurement model of the second magnetometer. Measurement models for the other two can be deduced from Eq. (3.22) by relabeling. The calibration model must then invert the resulting equations system in order to recover (h_x, h_y, h_z) from (v_x, v_y, v_z). Under the above assumptions and using formal calculation software, the following series expansion up to order 5 can be obtained by injection and identification of unknown series expansion

$$\begin{cases} h_x &= v_x - v_x v_y^2 + \frac{v_x^3}{2} - v_x v_y^4 + v_x^3 v_y^2 + \frac{7v_x^5}{8} \\ h_y &= v_y - v_y v_x^2 + \frac{v_y^3}{2} - v_y v_x^4 + v_y^3 v_x^2 + \frac{7v_y^5}{8} \\ h_z &= v_z - v_z v_x^2 + \frac{v_z^3}{2} - v_z v_x^4 - v_z^3 v_x^2 + 2v_x^2 v_y^2 v_z + \frac{7v_z^5}{8} \ . \end{cases} \tag{3.23}$$

It can be noticed that before accounting for sensors non-orthogonality, the only unknown parameters are linked to the constants used to express the dimensionless quantities, that is to say, scale factors $(R_0 i_b \kappa)$ and the anisotropy field (H_k).

Assuming that the anisotropy field H_k is identical for all barber pole elements, one can denote $u_x \doteq H_k v_x$, $u_y \doteq H_k v_y$, $u_z \doteq H_k v_z$ and use Eq. (3.13) such that the magnetic field can be recovered as

$$\begin{cases} H_x &= u_x - \frac{u_x u_y^2}{H_k^2} + \frac{u_x^3}{2H_k^2} - \frac{u_x u_y^4}{H_k^4} + \frac{u_x^3 u_y^2}{H_k^4} + \frac{7u_x^5}{8H_k^4} \\ H_y &= u_y - \frac{u_y u_x^2}{H_k^2} + \frac{u_y^3}{2H_k^2} - \frac{u_y u_x^4}{H_k^4} + \frac{u_y^3 u_x^2}{H_k^4} + \frac{7u_y^5}{8H_k^4} \\ H_z &= u_z - \frac{u_z u_x^2}{H_k^2} + \frac{u_z^3}{2H_k^2} - \frac{u_z u_x^4}{H_k^4} - \frac{u_z^3 u_x^2}{H_k^4} + \frac{2u_x^2 u_y^2 u_z}{H_k^4} + \frac{7u_z^5}{8H_k^4} \ . \end{cases} \tag{3.24}$$

Eq. (3.24) can then be used to identify the anisotropy field H_k in calibration, or compensate the effect of non-linearity to recover (H_x, H_y, H_z) from (u_x, u_y, u_z).

3.2.5. Nonlinear calibration experiment

Let us refine the linear model described in Sec. 3.2.2 that accounts for sensor non-orthogonality and biases, by using the non-linear model described in Sec. 3.2.4 which does not. A single scalar parameter, H_k, is added to the model to account for non-linearity. This refinement is then validated with a calibration experiment.

Let us denote c the function such that Eq. (3.24) reads

$$\begin{pmatrix} H_x \\ H_y \\ H_z \end{pmatrix} = c\left(\begin{bmatrix} u_x \\ u_y \\ u_z \end{bmatrix}, H_k\right) . \tag{3.25}$$

The proposed calibration model reads

$$\mathbf{B^b}_0(t) = \begin{pmatrix} 1 & a_{xy} & a_{xz} \\ 0 & 1 & a_{yz} \\ 0 & 0 & 1 \end{pmatrix} c\left(\begin{bmatrix} d_x({}_1y(t) - b_x) \\ d_y({}_2y(t) - b_y) \\ d_z({}_3y(t) - b_z) \end{bmatrix}, H_k\right) , \tag{3.26}$$

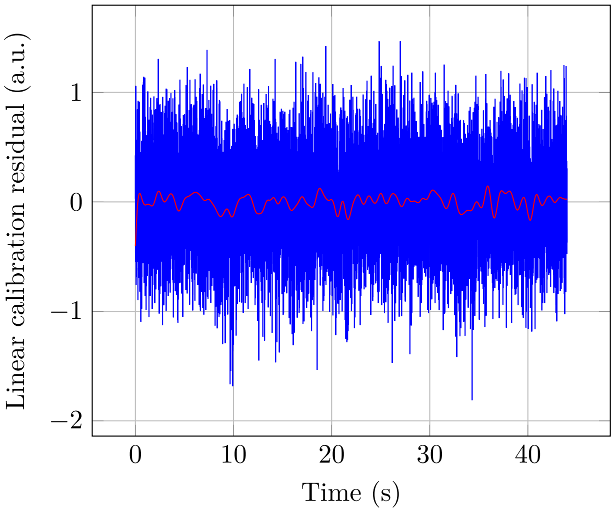

Figure 3.9: Nonlinear calibration residuals (in arbitrary units) with respect to time during a nonlinear calibration trial, on the same data and in the same units as Fig. 3.5a. The solid red line represents the solid blue line filtered by a low pass filter with 2Hz cutoff frequency. Residuals bear a much closer resemblance to a white noise.

where b_x, b_y and b_z represent sensor bias, d_x, d_y and d_z represent individual scale factors, a_{xy}, a_{xz} and a_{yz} represent sensors non-orthogonality, and H_k represents a common anisotropy field. This model neglects the effect of sensor non-orthogonality on nonlinear corrections.

Identification of H_k is achieved using an iterative gradient-based algorithm aiming at minimizing linear calibration residuals at fixed H_k. The experimental results are plotted in Fig. 3.9 and 3.10, showing a successful compensation at fixed temperature and homogeneous field conditions (Earth's magnetic field over a small volume). One can reasonably conclude that measurement noise and inherent sensor non-linearity are the main sources of error in these calibration experiments and in these experimental conditions.

3.2.6. Gradient measurement and calibration issues

Linear interpolation scheme

Since the sensor board does not directly measure the gradient of the magnetic field, it must be deduced from measurements. Let us assume that the sensor board is equipped with ideal linear single-axis magnetometers described by Eq. (3.1). Assumptions 3.2.1 and 3.2.2 are made (see Sec. 3.2.1). If the magnetic field in body frame can be described

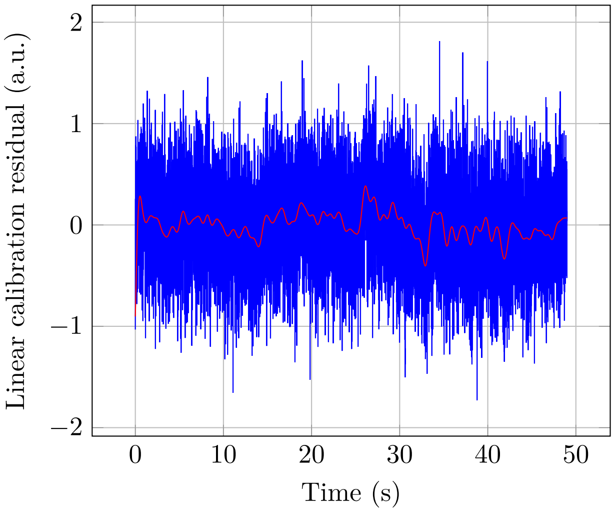

Figure 3.10: Same as Fig. 3.9 on another dataset. The noise pattern is slightly different. Once non-linearities have been removed, other sources of error remain.

by a linear dependency on the spatial variables,

$$\mathbf{B}^{\mathrm{b}}(\mathbf{P}^{\mathrm{b}}, t) = \mathbf{B}^{\mathrm{b}}({\mathbf{P}^{\mathrm{b}}}_0, t) + \nabla\mathbf{B}^{\mathrm{b}}({\mathbf{P}^{\mathrm{b}}}_0, t)(\mathbf{P}^{\mathrm{b}} - {\mathbf{P}^{\mathrm{b}}}_0) \ , \tag{3.27}$$

then estimating the 9 components of $\nabla{\mathbf{B}^{\mathrm{b}}}_0$ and the 3 components of ${\mathbf{B}^{\mathrm{b}}}_0$ can be seen as a 3D linear interpolation problem using sensor measurements at the n_{mag} different known sensor positions ${}_j\mathbf{p}^{\mathrm{b}}$. This also requires the knowledge of parameters ${}_j\mathbf{a}^{\mathrm{b}}$ and ${}_jb$, with $j \in \{1, ..., n_{\mathrm{mag}}\}$. In other words, in order to be able to compute the magnetic field gradient:

- All single axis sensors must be calibrated so that at least their effective positions, scale factors, and biases are known in the same reference frame $\mathfrak{R}_{\mathrm{b}}$
- The interpolation problem must be solvable, which imposes constraints on its conditioning. (For example, sensors cannot be aligned in a straight line)

Ellipsoid fitting calibration techniques *do not provide any way of ensuring a predefined calibration reference frame* and *do not provide any information about sensor effective positions*. However, Ref. Dorveaux et al. [2010] provides three methods for calibrating an array of tri-axis magnetometers, proving that this problem can be partially solved, by calibrating scale factors and biases in a *common unknown* reference frame fixed with respect to $\mathfrak{R}_{\mathrm{b}}$, using the same type of data as for ellipsoid fitting techniques. The problem of calibrating sensors effective positions *cannot be solved under homogeneous field conditions*, since they have no influence on sensor measurements in the underlying model.

In Chapters 5 and 6, two replacement calibration methods are proposed in order to fully calibrate an array of magnetometers. In case magnetometer effective positions are known in $\mathfrak{R}_\mathrm{b}$, a method is proposed in Sec. 3.3.1 in order to express magnetometer calibration parameters in $\mathfrak{R}_\mathrm{b}$.

Measuring the gradient with a planar arrangement of sensors

Combining Eq. (3.1) with Eq. (3.27) yields

$$\forall j \in \{1, ..., n_\mathrm{mag}\},\ \forall t,\ {}_j y(t) - {}_j b = {}_j\mathbf{a}^\mathrm{b} \left(\mathbf{B}^\mathrm{b}(\mathbf{P}^\mathrm{b}{}_0, t) + \nabla\mathbf{B}^\mathrm{b}(\mathbf{P}^\mathrm{b}{}_0, t)({}_j\mathbf{p}^\mathrm{b} - \mathbf{P}^\mathrm{b}{}_0)\right). \tag{3.28}$$

From this equation, it becomes visible that interpolating $\mathbf{B}^\mathrm{b}(\mathbf{P}^\mathrm{b}{}_0, t)$ and $\nabla\mathbf{B}^\mathrm{b}(\mathbf{P}^\mathrm{b}{}_0, t)$ would require at least $n_\mathrm{mag} \geqslant 3 + 9$ and a 3-dimensional arrangement of sensors. But in fact, if the magnetic field is assumed to satisfy Maxwell's equations for a source-free region of space, then $\nabla\mathbf{B}^\mathrm{b}(\mathbf{P}^\mathrm{b}{}_0, t)$ can be described with only 5 degrees of freedom. Denoting $\mathbf{B}^\mathrm{b}(\mathbf{P}^\mathrm{b}{}_0, t) = \begin{pmatrix} B^\mathrm{b}_1 \\ B^\mathrm{b}_2 \\ B^\mathrm{b}_3 \end{pmatrix}$, $\nabla\mathbf{B}^\mathrm{b}(\mathbf{P}^\mathrm{b}{}_0, t) = \begin{pmatrix} \partial_1 B^\mathrm{b}_1 & \partial_2 B^\mathrm{b}_1 & \partial_3 B^\mathrm{b}_1 \\ \partial_1 B^\mathrm{b}_2 & \partial_2 B^\mathrm{b}_2 & \partial_3 B^\mathrm{b}_2 \\ \partial_1 B^\mathrm{b}_3 & \partial_2 B^\mathrm{b}_3 & \partial_3 B^\mathrm{b}_3 \end{pmatrix}$, then Maxwell's equations imply that the gradient of the magnetic field is symmetric and traceless,

$$\begin{cases} \partial_1 B^\mathrm{b}_1 + \partial_2 B^\mathrm{b}_2 + \partial_3 B^\mathrm{b}_3 = 0 \\ \forall i, j \in \{1, 2, 3\},\ \partial_i B^\mathrm{b}_j = \partial_j B^\mathrm{b}_i \ . \end{cases} \tag{3.29}$$

Therefore, the third column of $\nabla\mathbf{B}^\mathrm{b}(\mathbf{P}^\mathrm{b}{}_0, t)$ can be recovered from the first two columns. In other words, a 2 dimensional arrangement of sensors is sufficient to recover the full magnetic field gradient by finite differences (or interpolation).

Planar arrangements of sensors: more than the gradient is accessible

One may argue that the baseline limits the above-mentioned finite differences scheme, that is to say, the distance between sensors, since variations of the magnetic field on a smaller scale cannot be measured (see Ref. [Dorveaux, 2011, Sec. 3.4]). One way to address this problem is to use a higher order spatial interpolation of the magnetic field. Is such an interpolation possible using a planar arrangement of sensors?

Let us assume that all components of the magnetic field are of class $\mathcal{C}^n$. Because of Eq. (3.29) and thanks to Schwarz's theorem, the following Lemma holds

Lemma 3.2.2. *Let ρ be a function from $\{1, 2, ..., n\}$ to $\{1, 2, 3\}$, and σ any permutation on $\{1, 2, .., n\}$, with $n > 1$, then*

$$\partial_{\rho(1)}\partial_{\rho(2)}...\partial_{\rho(n-1)} B^\mathrm{b}_{\rho(n)} = \partial_{\rho(\sigma(1))}\partial_{\rho(\sigma(2))}...\partial_{\rho(\sigma(n-1))} B^\mathrm{b}_{\rho(\sigma(n))} \ .$$

Proof. This result can be proven by recurrence on n. It is true for $n = 2$ because of Maxwell's equations or Eq. (3.29). Let us assume that the result holds for $n - 1$. Then if σ' is any permutation on $\{2, ..., n\}$,

$$\partial_{\rho(1)}\partial_{\rho(2)}...\partial_{\rho(n-1)} B^\mathrm{b}_{\rho(n)} = \partial_{\rho(1)}\partial_{\rho(\sigma'(2))}...\partial_{\rho(\sigma'(n-1))} B^\mathrm{b}_{\rho(\sigma'(n))} \ .$$

Assuming that components of B^{b} are regular enough, then Schwarz's theorem applies, and

$$\partial_{\rho(1)}\partial_{\rho(\sigma'(2))}...\partial_{\rho(\sigma'(n-1))}B^{\mathrm{b}}_{\rho(\sigma'(n))} = \partial_{\rho(\sigma'(2))}\partial_{\rho(1)}...\partial_{\rho(\sigma'(n-1))}B^{\mathrm{b}}_{\rho(\sigma'(n))}.$$

From the above, all indexes after the first can be swapped with the first index. Also all indexes after the first index can be swapped with each other without changing the result, which concludes the proof. ☐

Finally, because of Eq. (3.29) and Lemma 3.2.2, the following Lemma holds,

Lemma 3.2.3. *Any expression of the form* $\partial_{\rho(1)}\partial_{\rho(2)}...\partial_{\rho(n-1)}B^{\mathrm{b}}_{\rho(n)}$ *with* ρ *a function from* $\{1,2,...,n\}$ *to* $\{1,2,3\}$ *can be expressed as a linear combination of such terms, such that any of them admits at most one index equal to 3.*

Proof. Let us assume that ρ evaluates to 3, $m \geqslant 2$ times. Without loss of generality, because of Lemma 3.2.2, we can assume that $\rho(n-1) = \rho(n) = 3$. Then, because of Eq. 3.29,

$$\begin{aligned}\partial_{\rho(1)}\partial_{\rho(2)}...\partial_{\rho(n-1)}B^{\mathrm{b}}_{\rho(n)} &= \partial_{\rho(1)}\partial_{\rho(2)}...\partial_3 B^{\mathrm{b}}_3\\ &= -\partial_{\rho(1)}\partial_{\rho(2)}...\partial_2 B^{\mathrm{b}}_2 - \partial_{\rho(1)}\partial_{\rho(2)}...\partial_1 B^{\mathrm{b}}_1\end{aligned} \tag{3.30}$$

Which means that $\partial_{\rho(1)}\partial_{\rho(2)}...\partial_{\rho(n-1)}B^{\mathrm{b}}_{\rho(n)}$ is a linear combination of elements whose indexes evaluate to 3, $m-2$ times. This operation can be repeated until there is at most one index equal to 3 in every term. ☐

For example, with $m = 2$, we have

$$\begin{aligned}\partial_2\partial_3\partial_3 B^{\mathrm{b}}_1 &= \partial_1\partial_2\partial_3 B^{\mathrm{b}}_3\\ &= \partial_1\partial_2(-\partial_1 B^{\mathrm{b}}_1 - \partial_2 B^{\mathrm{b}}_2)\ .\end{aligned}$$

Therefore, Lemmas 3.2.2 and 3.2.3 imply that all spatial derivatives of order n can be computed if spatial derivatives are known up to order n only along the first two spatial coordinates. In other words, interpolating all 3 components of the magnetic field in a plane at order n, with a planar arrangement of sensors, is sufficient to deduce a three-dimensional interpolation of the magnetic field at the same order.

Admissible planar arrangements of magnetometers

A sufficient number of tri-axis magnetometers needed for a spatial interpolation of order n can be deduced from the above result, because it corresponds to the minimum number of 2D monomials of degree lower than or equal to n: 1 for $n = 0$, 3 for $n = 1$, 6 or $n = 2$... [4]

All planar arrangements are not suitable, and the position of tri-axis magnetometers must be chosen accordingly, which is expected from any interpolation grid. Should the need arise, tri-axis magnetometers could be arranged in a sparse interpolation grid (with, e.g., Ref. Smolyak [1963], using a 1-dimensional interpolation grid such as Chebyshev nodes as a starting point).

---

[4] see `https://oeis.org/A000217`

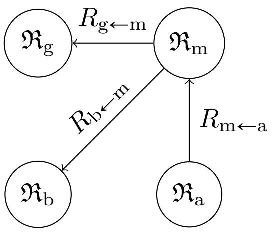

Figure 3.11: Various sensor calibration frames

3.3. A common frame of reference for all sensors

The issue Because the considered calibration techniques treat the different types of sensors independently, each sensor can be considered to have been calibrated in its own frame of reference, that is fixed with respect to the body frame $\mathfrak{R}_\mathrm{b}$. However, Table 3.1 lists physical quantities expressed in the same reference frame $\mathfrak{R}_\mathrm{b}$. Therefore, there is a need to investigate how all sensors can be calibrated in the same reference frame, that can later be defined as $\mathfrak{R}_\mathrm{b}$.

Notations and assumptions Let us denote $\mathfrak{R}_\mathrm{m}$, $\mathfrak{R}_\mathrm{a}$ and $\mathfrak{R}_\mathrm{g}$ the frames of reference in which magnetometers, accelerometers and gyrometers are calibrated respectively. They are all assumed fixed with respect to $\mathfrak{R}_\mathrm{b}$. To denote changes of frames, the notation $R_{\mathrm{g}\leftarrow\mathrm{m}} \in \mathrm{SO}(3)$ is used to refer to the rotation matrix such that coordinate transformations from $\mathfrak{R}_\mathrm{m}$ to $\mathfrak{R}_\mathrm{g}$ read

$$\mathbf{P}^\mathrm{g} = R_{\mathrm{g}\leftarrow\mathrm{m}}\mathbf{P}^\mathrm{m}. \tag{3.31}$$

Other changes of reference frames are denoted in a similar way (see Fig. 3.11).

For the sake of simplicity, in this section, we assume that effective positions are known by construction and expressed in $\mathfrak{R}_\mathrm{b}$; this simplifying assumption is dropped in Chapters 5 and 6, were means of calibrating them are provided.

Outline The problem of identifying $R_{\mathrm{b}\leftarrow\mathrm{m}}$ is investigated in Sec. 3.3.1, and the problem of identifying $R_{\mathrm{g}\leftarrow\mathrm{m}}$ and $R_{\mathrm{m}\leftarrow\mathrm{a}}$ is briefly explained in Sec. 3.3.2.

3.3.1. Magnetometers scale factors and effective positions

In order for the spatial gradient of the magnetic field to be correctly estimated, all magnetometers must be fully calibrated in the same frame of reference, including sensors effective positions. However, measurements models in homogeneous field do not give access to sensor effective positions, as discussed in Sec. 3.2.6. Even assuming that sensor effective positions are known in some reference frame, there is no way to know whether scale factors and biases are expressed in that same reference frame in a homogeneous field. However, it might be possible to recover this change of frame *a posteriori* using a specific trial that would not, in principle, require any expensive setup.[5]

Principle

Let us assume that magnetometers are calibrated in $\mathfrak{R}_\mathrm{m}$ with methods such that those proposed in Ref. Dorveaux et al. [2010] and that sensors effective positions are known in $\mathfrak{R}_\mathrm{b}$. Let us denote $R_{m\leftarrow b} \in \mathrm{SO}(3)$ the rotation matrix such that coordinate transformations from $\mathfrak{R}_\mathrm{b}$ to $\mathfrak{R}_\mathrm{m}$ read

$$\mathbf{P}^\mathrm{m} = R_{\mathrm{m}\leftarrow\mathrm{b}}\mathbf{P}^\mathrm{b} \ . \tag{3.32}$$

Then, using Eq. (3.28), with a planar arrangement of magnetometers along the first two spatial coordinates in $\mathfrak{R}_\mathrm{b}$, the first two columns of the matrix M such that

$$M \doteq \begin{pmatrix} m_{11} & m_{12} & m_{13} \\ m_{21} & m_{22} & m_{23} \\ m_{31} & m_{32} & m_{33} \end{pmatrix} = R^\top_{\mathrm{m}\leftarrow\mathrm{b}}\nabla\mathbf{B}^\mathrm{b} = \nabla\mathbf{B}^\mathrm{m} R_{\mathrm{m}\leftarrow\mathrm{b}} \tag{3.33}$$

can be interpolated.

Let us denote $\Theta = \begin{pmatrix} \phi \\ \theta \\ \psi \end{pmatrix}$, $[\Theta\times] = \begin{pmatrix} 0 & -\psi & \theta \\ \psi & 0 & -\phi \\ -\theta & \phi & 0 \end{pmatrix}$, $R_{\mathrm{m}\leftarrow\mathrm{b}} = \mathbf{1} + [\Theta\times] + o(\|\theta\|)$. We want $\widehat{R_{\mathrm{b}\leftarrow\mathrm{m}}}$ such that the spatial gradient of the magnetic field

$$\nabla\mathbf{B}^\mathrm{m} \approx \nabla\mathbf{B}^\mathrm{m} R_{\mathrm{m}\leftarrow\mathrm{b}}\widehat{R_{\mathrm{b}\leftarrow\mathrm{m}}} = M\widehat{R_{\mathrm{b}\leftarrow\mathrm{m}}}$$

satisfies Maxwell's equations.

The equation $\nabla\mathbf{B}^\mathrm{m} = \nabla\mathbf{B}^{\mathrm{m}\top}$ yields:

$$\begin{pmatrix} m_{32} - m_{23} \\ m_{13} - m_{31} \\ m_{21} - m_{12} \end{pmatrix} + \begin{pmatrix} m_{22} + m_{33} & -m_{21} & -m_{31} \\ -m_{12} & m_{11} + m_{33} & -m_{32} \\ -m_{31} & -m_{23} & m_{11} + m_{22} \end{pmatrix} \Theta = 0 \ . \tag{3.34}$$

The equation $\mathrm{Tr}(\nabla\mathbf{B}^\mathrm{m}) = 0$ (the sum of diagonal elements is zero) yields

$$m_{11} + m_{22} + m_{33} + \begin{pmatrix} m_{23} - m_{32} & m_{31} - m_{13} & m_{12} - m_{21} \end{pmatrix} \Theta = 0 \ . \tag{3.35}$$

If M could be interpolated from a 3-dimensional arrangement of magnetometers, these equations would suffice. However, with a planar arrangement of magnetometers, M cannot be entirely recovered.

Let us assume that m_{i3} with $i \in \{1, 2, 3\}$ and Θ are unknown. Identifying the terms m_{i3} is equivalent to solving the following equation

$$\begin{pmatrix} 0 & -1 & \phi & m_{32} - m_{21}\theta + m_{22}\phi - m_{31}\psi \\ 1 & 0 & \theta & -m_{31} + m_{11}\theta - m_{12}\phi - m_{32}\psi \\ -\phi & -\theta & 0 & -m_{12} + m_{21} + m_{11}\psi + m_{22}\psi \\ -\theta & \phi & 1 & m_{11} + m_{22} + m_{31}\theta - m_{32}\phi + m_{12}\psi - m_{21}\psi \end{pmatrix} \begin{pmatrix} m_{13} \\ m_{23} \\ m_{33} \\ 1 \end{pmatrix} = 0 \ . \tag{3.36}$$

---

[5] The paternity of this idea is owed to D. Caruso

This system has a solution if and only if the determinant of the system is equal to 0,

$$\begin{vmatrix} 0 & -1 & \phi & m_{32} - m_{21}\theta + m_{22}\phi - m_{31}\psi \\ 1 & 0 & \theta & -m_{31} + m_{11}\theta - m_{12}\phi - m_{32}\psi \\ -\phi & -\theta & 0 & -m_{12} + m_{21} + m_{11}\psi + m_{22}\psi \\ -\theta & \phi & 1 & m_{11} + m_{22} + m_{31}\theta - m_{32}\phi + m_{12}\psi - m_{21}\psi \end{vmatrix} = 0\ , \tag{3.37}$$

which is equivalent to

$$\begin{aligned}&(1+\theta^2+\phi^2)\big(m_{12} - m_{21} + m_{32}\theta + m_{31}\phi - (m_{11}+m_{22})\psi \\ &\quad -m_{21}\theta^2 + (-m_{11}+m_{22})\theta\phi + m_{12}\phi^2 - m_{31}\theta\psi + m_{32}\phi\psi\big) = 0\ .\end{aligned} \tag{3.38}$$

Since $(1+\theta^2+\phi^2) > 0$, this factor can be equivalently omitted from Eq. (3.38). At first order approximation in Θ, we have

$$m_{12} - m_{21} + \begin{pmatrix} m_{31} & m_{32} & -m_{11} - m_{22} \end{pmatrix} \Theta \approx 0 \tag{3.39}$$

This equation characterizes the possibility of completing the matrix M in such a way that $M\widehat{R_{\mathrm{b}\leftarrow\mathrm{m}}}$ satisfies Maxwell's equations. It must be approximately true for every sampled measurement, which gives us one equation per sample. The equation system resulting from the concatenation of all measurements can be solved for Θ with a least-square method. An iterative identification algorithm can then be designed in order to find $\widehat{R_{\mathrm{b}\leftarrow\mathrm{m}}}$: at each iteration, the estimated $[\Theta\times]$ is exponentiated to obtain a rotation matrix, which is used to update $\widehat{R_{\mathrm{b}\leftarrow\mathrm{m}}}$, rotate scale factors and biases into a new $\mathfrak{R}_{\mathrm{m}}$ representing the current estimate of $\mathfrak{R}_{\mathrm{b}}$, and interpolate a new M.

Simulation results

In a first simulation trial, random gradients are fed into the algorithm with small rotations (angles smaller than $^{1}/_{10}$ rad). Without noise, convergence is obtained up to machine precision.

A more realistic simulation needs to take into account sensor noise and the impact of spatial discretization since the spatial gradient of the magnetic field is not constant. The choice is made to simulate the relative motion of a sensor board around a magnetic dipole, only because this situation is easy to reproduce in real-world experiments with permanent magnets; any other source of magnetic field could have been used instead.

Let us denote $\mathbf{m}^{\mathrm{n}}$ the vector representing coordinates of a magnetic dipole placed at the origin of $\mathfrak{R}_{\mathrm{n}}$. The following formula is used in order to compute the generated magnetic field $\mathbf{B}^{\mathrm{n}}$ at the position $\mathbf{P}^{\mathrm{n}}$ (see Ref. [Jackson, 1998, (5.56)]),

$$\mathbf{B}^{\mathrm{n}}(\mathbf{P}^{\mathrm{n}}) = \left(\frac{\mu_0}{4\pi}\right)\left(\frac{3\mathbf{P}^{\mathrm{n}}(\mathbf{m}^{\mathrm{n}}\cdot\mathbf{P}^{\mathrm{n}})}{\|\mathbf{P}^{\mathrm{n}}\|^5} - \frac{\mathbf{m}^{\mathrm{n}}}{\|\mathbf{P}^{\mathrm{n}}\|^3}\right)\ . \tag{3.40}$$

Magnetometer measurements are simulated for our planar sensor board configuration at various positions and attitudes around the magnetic dipole, in such a way that the frame $\mathfrak{R}_{\mathrm{m}}$ in which calibration is expressed differs from the frame $\mathfrak{R}_{\mathrm{b}}$ in which effective

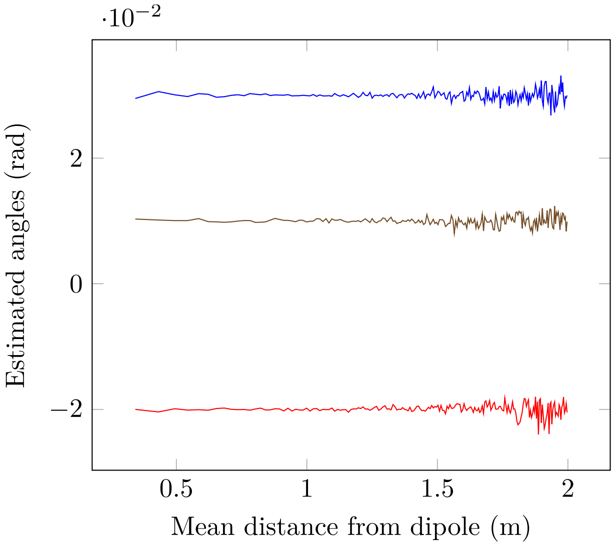

Figure 3.12: Estimated angles with respect to the mean distance to the dipole with the algorithm of Sec. 3.3.1 in simulation. The true values are $\{0.01, -0.02, 0.03\}$. Very close distances (not plotted) do not yield good results. Further away, the magnetic gradient is too small compared to the noise. Overall, the algorithm yields the correct angles.

positions are expressed by an arbitrary value of $R_{\mathrm{m}\leftarrow\mathrm{b}}$. Noise is added to magnetometer measurements, and the identification algorithm is run on clusters of data simulated at various distances of the dipole. The result is plotted Fig. 3.12, showing a good performance on simulated data. However, there seems to exist an ideal distance at which the magnetic dipole must be placed. Too close, the algorithm does not yield good results, probably because the interpolation model is not representative. Too far, data is dominated by noise, and the algorithm becomes imprecise.

Experimental results

An experimental protocol has been tested mimicking the simulation mentioned above, but instead of moving the sensor board around a magnetic dipole, the sensor board is fixed, and a magnetic dipole is moved around the sensor in various orientations. Despite promising behavior on simulated data, *no consistent experimental results have been obtained with this protocol.* It is not clear where the problem lies. More work seems necessary in order to design an experiment for which the identification problem is well-conditioned, and for which the interpolation model is representative enough. Moreover, sensitivity to other calibration errors has not been tested.

3.3.2. Magnetometers and inertial sensors

Identifying the change of frame between inertial and magnetic sensors is a known issue, see Refs. Kok et al. [2012], Kok and Schön [2016], Li et al. [2015], Yang et al. [2017] and references therein. The impact of a wrong identification of this change of frame in the context of MIDR was studied together with a calibration procedure relying on this impact in Ref. Dorveaux and Petit [2011a].

Internally, SYSNAV has methods for inertial sensor calibration at its disposal. It is interesting to notice that once magnetic sensors and inertial sensors are calibrated in their respective frames, two straightforward methods can be used in order to identify the change of frame between magnetometers and gyrometers, and between magnetometers and accelerometers.

Gyrometers Using Eqs. (2.5), (2.8) and (2.11) and notations from the previous chapter in a homogeneous stationary magnetic field yields

$$R_{\mathrm{g}\leftarrow\mathrm{m}}\frac{d}{dt}\mathbf{B}^{\mathrm{m}} = -\boldsymbol{\omega}^{\mathrm{g/n}} \times \left(R_{\mathrm{g}\leftarrow\mathrm{m}}\mathbf{B}^{\mathrm{m}}\right) \ . \tag{3.41}$$

The sampled version of this equation can be used directly in a Maximum Likelihood estimator of $R_{\mathrm{g}\leftarrow\mathrm{m}}$.

Accelerometers Estimating $R_{\mathrm{a}\leftarrow\mathrm{m}}$ can be done using data collected in static conditions in an homogeneous stationary field, exploiting the fact that in such conditions the dot-product between the calibrated magnetic field and the calibrated proper acceleration vector is invariant if and only if $\mathfrak{R}_{\mathrm{m}}$ and $\mathfrak{R}_{\mathrm{g}}$ are identical (see Ref. Li et al. [2015]). Actually, according to Ref. Li et al. [2015], more calibration parameters are accessible using this invariant.

3.4. Theoretical effect of measurement uncertainty on motion estimation

The previous sections highlight that the quantities needed in MIDR, cf. Table 3.1 are known at least up to a calibration uncertainty and measurement noise. In this section, the impact of the latter on trajectory estimation is studied.

Outline The effect of measurement (uncorrelated / white) noise is investigated in Sec. 3.4.1. The effect of systematic gradient measurement errors related to calibration issues is investigated in Sec. 3.4.2. Finally, some effects of inertial sensors calibration uncertainty are discussed in Sec. 3.4.3.

3.4.1. Measurement noise

All measurements are noisy. Those of the magnetic gradient are no exception, since they are interpolated from magnetic measurements. To understand the effect of gyrometer, accelerometer and magnetic measurement noise on attitude and velocity estimation, let us study the simplified linear discrete-time stochastic toy state-space model (3.42), which is a simplified 1-dimensional version of Eqs. (2.28)-(2.31) from Ch. 2. The following model is constructed by considering a 3-dimensional model in a simplified case, and “freezing” surplus dimensions for the movement and the magnetic field,

$$\begin{cases} x_B[k+1] &= x_B[k] + T(G[k] + \eta_G[k])x_v[k] + T\alpha\eta_{\omega'}[k] \\ x_v[k+1] &= x_v[k] + Tgx_r[k] + T\eta_\gamma[k] \\ x_r[k+1] &= x_r[k] + T\eta_\omega[k] \\ y[k] &= x_B[k] + \nu_y[k] \end{cases} \tag{3.42}$$

At each time-step k, the state vector of dimension 3, $x[k] = \begin{pmatrix} x_B[k] \\ x_v[k] \\ x_r[k] \end{pmatrix}$, represents the magnetic field $x_B[k]$, velocity $x_v[k]$, and attitude $x_r[k]$. The role of the spatial gradient of the magnetic field is played by the scalar $G[k]$, g represents gravity, and α represents a component of the magnetic field different from x_B that interacts with gyrometer noise. The sampling period is represented by T. Gyrometer noise is represented by η_ω and $\eta_{\omega'}$, accelerometer noise by η_γ, and gradiometer noise by η_G. The output y is the magnetic field.

In order to simplify the model, all noises are assumed to be zero-mean, white, Gaussian and uncorrelated. We remark that the noise term $\eta_G[k]$ is multiplicative since it multiplies the estimated state $x_v[k]$. This justifies the following study of the impact of gyrometer, accelerometer and magnetic measurement noise by first assuming that $\eta_G[k] \equiv 0$, then removing this assumption.

Case without gradient measurement noise

Without gradient measurement noise ($\forall k,\ \eta_G[k] = 0$), the linear system (3.42) can be studied using discrete-time linear Kalman filtering tools (see e.g. Refs. Alazard [2005], Barker et al. [1995]). The discrete-time system reads

$$\begin{aligned} x[k+1] &= A[k]x[k] + B[k]\eta[k] \\ y[k] &= C[k]x[k] + \nu_y[k]\ , \end{aligned}$$

with

$$A[k] = \begin{pmatrix} 1 & TG[k] & 0 \\ 0 & 1 & Tg \\ 0 & 0 & 1 \end{pmatrix},\ B[k] = \begin{pmatrix} T\alpha & 0 & 0 \\ 0 & T & 0 \\ 0 & 0 & T \end{pmatrix},\ C[k] = \begin{pmatrix} 1 & 0 & 0 \end{pmatrix},\ \eta[k] = \begin{pmatrix} \eta_{\omega'} \\ \eta_\gamma \\ \eta_\omega \end{pmatrix},$$

and

$$\mathrm{Cov}(\eta[k], \eta[k+l]) = \delta_{0l} \begin{pmatrix} \sigma^2_{\omega'} & 0 & 0 \\ 0 & \sigma^2_\gamma & 0 \\ 0 & 0 & \sigma^2_\omega \end{pmatrix},\ \mathrm{Cov}(\nu_y[k], \nu[k+l]) = \delta_{0l} \left(\sigma^2_y\right).$$

If we assume that the density probability $p(x[0])$ is Gaussian, then for all k, conditional probability densities $p(x[k] \mid y[k], y[k-1], ..., y[1], x[0])$ are Gaussian. Let us denote multivariate Gaussian probability density functions of mean μ and covariance Σ as $\mathcal{N}(\mu, \Sigma)$, and let us denote for all $k \geqslant 1$

$$\begin{aligned} p(x[k] \mid y[k], y[k-1], ..., y[1], x[0]) &= \mathcal{N}(\hat{x}[k]^+, \Sigma[k]^+) \\ p(x[k+1] \mid y[k], y[k-1], ..., y[1], x[0]) &= \mathcal{N}(\hat{x}[k+1]^-, \Sigma[k+1]^-) \end{aligned}$$

Let us denote $Q \doteq \begin{pmatrix} \sigma_{\omega'}^2 & 0 & 0 \\ 0 & \sigma_\gamma^2 & 0 \\ 0 & 0 & \sigma_\omega^2 \end{pmatrix}$, and $R \doteq \left(\sigma_y^2\right)$. Then, we have the classical Kalman filtering formulas (see Refs. Alazard [2005], Barker et al. [1995])

$$\begin{aligned} \Sigma[k+1]^- &= A[k]\Sigma[k]^+ A[k]^\top + B[k]QB[k]^\top \\ \Sigma[k+1]^+ &= (\mathbf{1} - K[k+1]C[k+1])\Sigma[k+1]^- \\ K[k+1] &\doteq \Sigma[k+1]^- C[k+1]^\top S[k+1]^{-1} \\ S[k+1] &\doteq R + C[k+1]\Sigma[k+1]^- C[k+1]^\top \end{aligned}$$

If $G[k]$ is constant and non-zero, it can be proven that the system is observable, by, e.g., using Kalman's criterion for observability (see Ref. Alazard [2005]). The process is stationary and the sequence $(\Sigma[k]^+)$ for $k \geqslant 1$ converges asymptotically towards a limit that we denote $\Sigma[\infty]^+$, which represents uncertainty associated with measurement noise under conditions where the magnetic gradient $G[k]$ is perfectly known. Asymptotic variances of marginal laws for x_r and x_v can be read on the diagonal of $\Sigma[\infty]^+$. Their square root are standard deviations, which are plotted on Fig. 3.13 and Fig. 3.14.

Without considering gradient measurement noise, velocity uncertainty is mainly driven by gyrometer and accelerometer noise: in Fig. 3.13a, whose limits represent realistically expectable noise levels, error grow approximately linearly with respect to σ_ω, and slower with respect to σ_y; in Fig. 3.14a, whose limits are chosen likewise, σ_y has little influence compared with σ_ω. Only requirements on accelerometer noise decrease significantly together with magnetometer noise (Fig. 3.15). Attitude uncertainty is mainly dependent on gyrometer noise, with other parameters having little effect (Fig. 3.13b and 3.14b). These results are consistent with cases where magnetometers are not used, such as in Ref. Woodman [2007], which considers gyrometer noise as the primary source of error in MEMS inertial navigation.

The reader must be careful that the effect of inertial sensor bias instability (see Ref. IEEE [2003]) is not considered, and neither is magnetic gradient measurement noise. The latter is discussed hereafter.

Case with gradient measurement noise

The magnetic field gradient is interpolated from noisy magnetometer measurements. It follows that it is affected by noise. In this simplified model, $\eta_G[k]$ plays the role

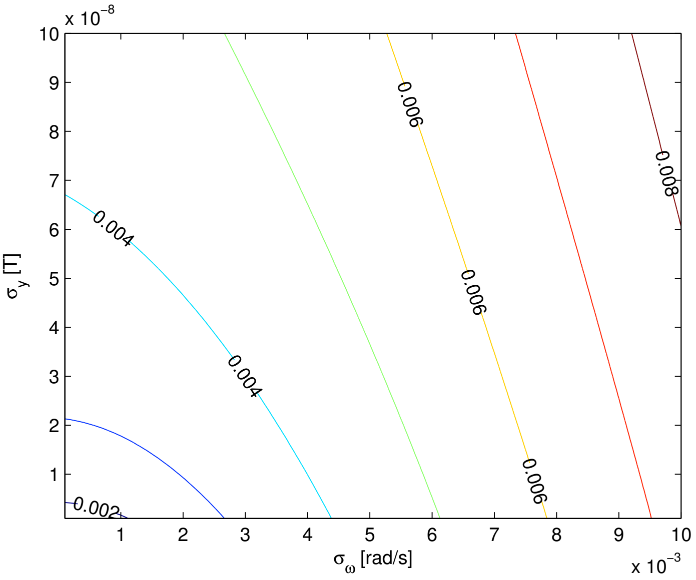

(a) Velocity (x_v) standard deviation [m/s], with respect to magnetometer and gyrometer noise

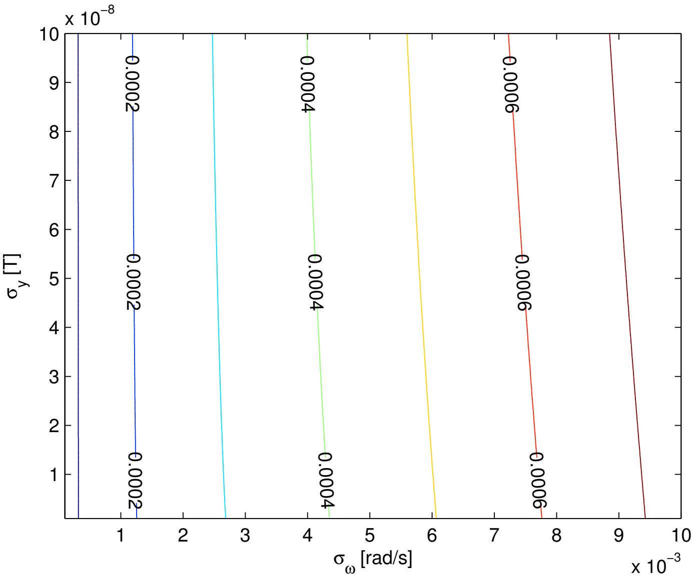

(b) Attitude (x_r) standard deviation [rad], with respect to magnetometer and gyrometer noise

Figure 3.13: Asymptotic behavior of the standard deviation of marginal probability densities for x_v and x_r deduced from approaching $\Sigma[\infty]^+$ for different values of σ_ω and σ_y, with $\sigma'_\omega = \sigma_\omega$, $G[k] = 5\mu\text{T/m}$, $\alpha = 50\mu\text{T}$, $\sigma_\gamma = 0.1\text{m/s}^2$ and $T = 3.072\text{ms}$, and assuming perfect knowledge of the magnetic gradient.

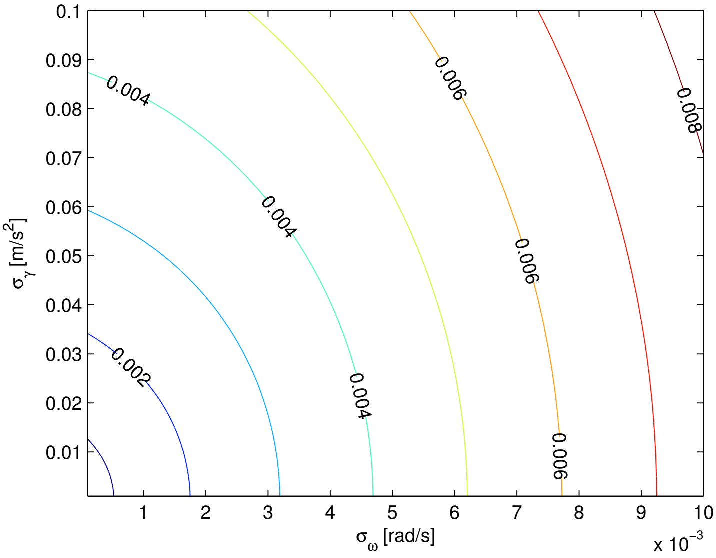

(a) Velocity (x_v) standard deviation [m/s], with respect to accelerometer and gyrometer noise

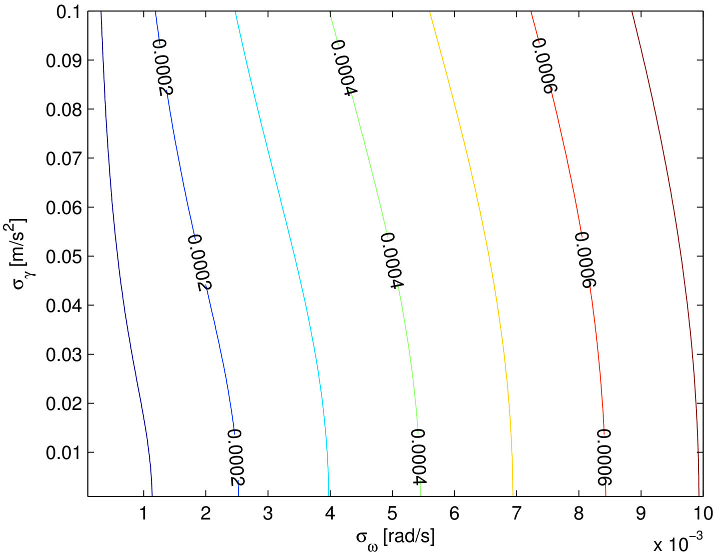

(b) Attitude (x_r) standard deviation [rad], with respect to accelerometer and gyrometer noise

Figure 3.14: Asymptotic behavior of the standard deviation of marginal probability densities for x_v and x_r deduced from approaching $\Sigma[\infty]^+$ for different values of σ_ω and σ_γ, with $\sigma'_\omega = \sigma_\omega$, $G[k] = 5\mu\text{T/m}$, $\alpha = 50\mu\text{T}$, $\sigma_y = 100\text{nT}$, and $T = 3.072\text{ms}$, and assuming perfect knowledge of the magnetic gradient.

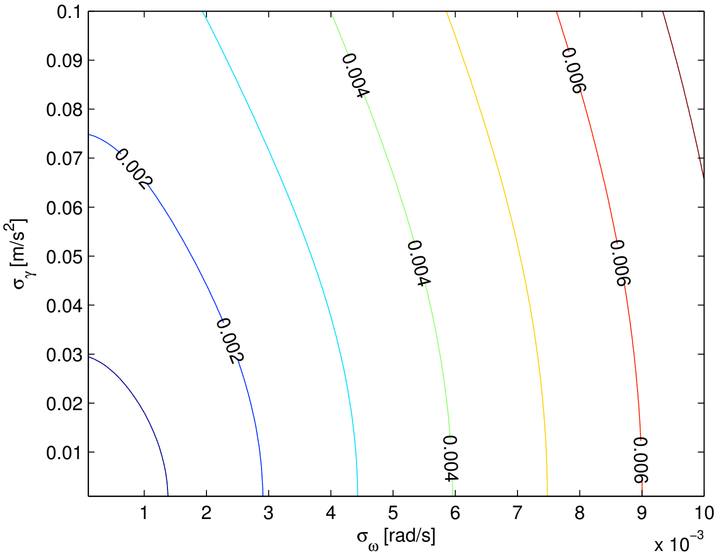

(a) Velocity (x_v) standard deviation [m/s]

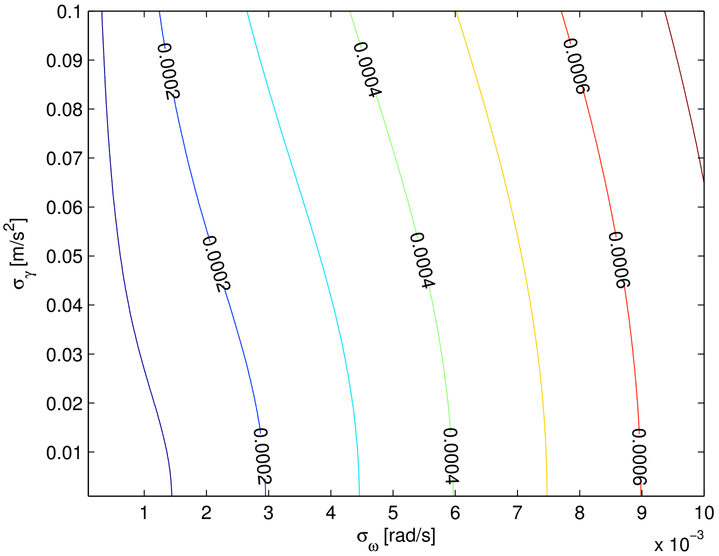

(b) Attitude (x_r) standard deviation [rad]

Figure 3.15: Same as Fig. 3.14 but with $\sigma_y = 10$nT, ten times smaller. Only requirements on σ_γ, accelerometer noise, decreased significantly.

of this noise. Since magnetometer noise is modeled as a zero-mean white Gaussian random variable, likewise, $\eta_G[k]$ must be a zero-mean white Gaussian random variable whose standard deviation denoted σ_G depends linearly on σ_y in order to get an accurate representation.

Since our simplified model is 1D, let us assume an array of 3 equally spaced magnetometers. The magnetic field is measured by the central magnetometer to obtain $y[k]$, and $G[k]$ the difference between the readings of the two remaining sensors divided by their relative distance ℓ. This way, uncertainty on $\nu_y[k]$ and $\eta_G[k]$ are independent, and we have

$$\sigma_G^2 = \frac{2\sigma_y^2}{\ell^2}. \tag{3.43}$$

We can choose $\ell = 5\text{cm}$ in order to model the sensor board illustrated in Fig. 3.1a.

Eq. (3.42) involves the product of $x_v[k]$ and $\eta_G[k]$. If probability densities for $x_v[k]$ and $\eta_G[k]$ are Gaussian, then the probability density for their product is not Gaussian. In order to circumvent this problem and assess the effect of gradient measurement noise, we proceed by separating the effect of gradient measurement noise from the rest.

The posterior conditional probability density

$$p(x[k] \mid y[k], \eta_G[k-1], ..., y[1], \eta_G[1], x[0], \eta_G[0])$$

is a normal distribution since it is conditioned on the multiplicative gradient noise, and it can be evaluated using the earlier-mentioned Kalman formulas. Since we have

$$\begin{aligned} &p(x[k] \mid y[k], ..., y[1], x[0]) \\ &= \int p(x[k] \mid y[k], \eta_G[k], ..., y[1], \eta_G[1], x[0], \eta_G[0]) p(\eta_G[k], ..., \eta_G[0]) \mathrm{d}\eta_G[k] ... \mathrm{d}\eta_G[0] \ , \end{aligned}$$

it is possible get an approximation of the probability density $p(x[k] \mid y[k], ..., y[1], x[0])$ with a Monte-Carlo approach by randomly sampling $\eta_G[k], ..., \eta_G[0]$.

Gradient measurement noise has two noticeable effects. The first one, concerning the increased estimation uncertainty, is illustrated in Fig. 3.16. Figures 3.13 and 3.16 are drawn in such a way that they represent the same variations of σ_ω and σ_y (using Eq. (3.43) to get the corresponding values of σ_G), in order to highlight the additional uncertainty brought by gradient measurement noise. However, color scales are different. Velocity uncertainty grows much faster with gradient measurement noise, with a milder effect on attitude uncertainty. The second effect is that if the magnetic gradient is small compared with σ_G, the posterior density for x_v shifts towards 0, in a sort of "damping" effect, see Fig. 3.17. This so-called damping does not appear if the gradient noise is approximated as additive in Eq. (3.42). Although the model considered is heavily simplified, this damping effect may be observed in a real situation whenever the magnetic gradient is close to being singular, and the uncertainty on velocity along the unobservable direction grows large enough that the effect of multiplicative noise may be observed.[6]

---

[6] If $G = 0$, although the true values of x_r and x_v should not be observable, the final probability

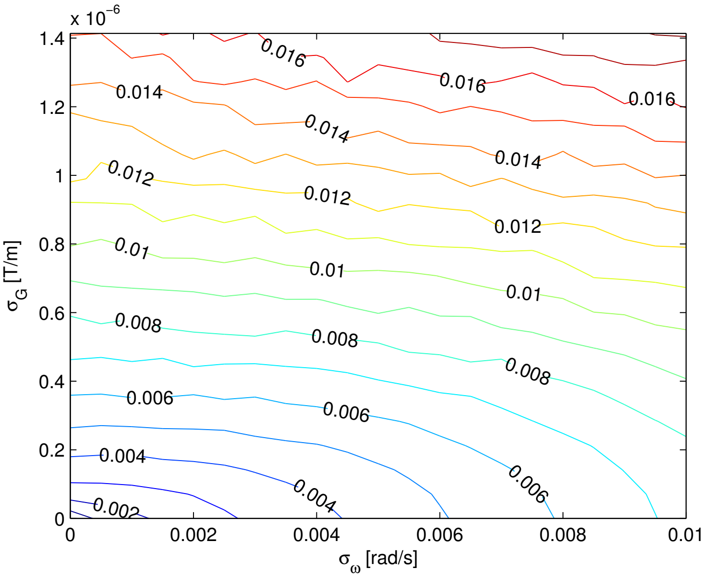

(a) Velocity (x_v) standard deviation [m/s]

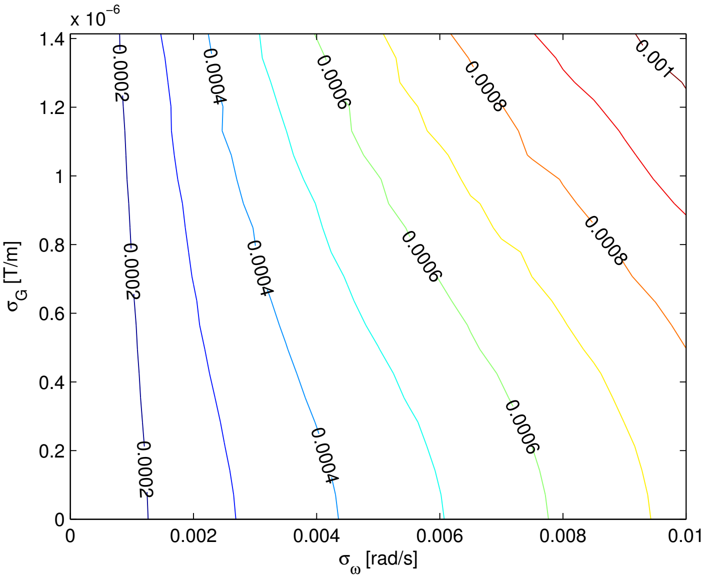

(b) Attitude (x_r) standard deviation [rad]

Figure 3.16: Approximate asymptotic marginal probability density standard deviations of x_v and x_r for different values of σ_G and σ_ω, with $\sigma_y = \frac{\ell}{\sqrt{2}}\sigma_G$ (3.43), $\ell = 5\text{cm}$, $\sigma_\gamma = 0.1\text{m/s}^2$, $\sigma_{\omega'} = \sigma_\omega$, $\alpha = 50\mu\text{T}$ $G[k] = 5\mu\text{T}$, with measurement corresponding to a velocity of 1m/s.

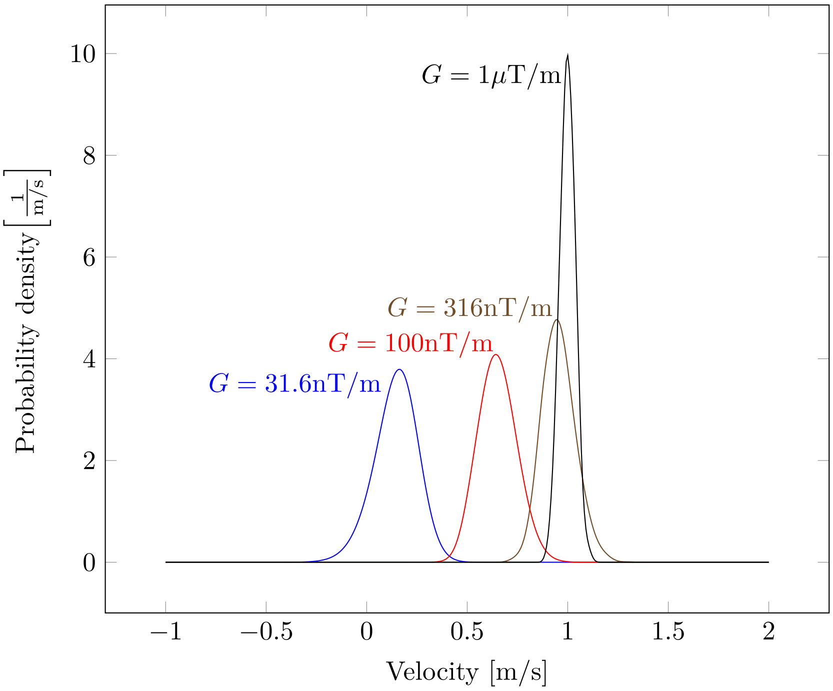

Figure 3.17: Approximate asymptotic marginal probability densities for x_v using a Monte-Carlo approach, with $\sigma_\omega = \sigma'_\omega = 0.005$rad/s, $\sigma_\gamma = 0.1$m/s, $\sigma_G = 1\mu$T/m, $\alpha = 50\mu$T, $\sigma_y = \frac{\ell}{\sqrt{2}}\sigma_G$, and $\ell = 5$cm, with measurements corresponding to a velocity of 1m/s with different gradient values.

3.4.2. Gradiometer calibration uncertainty

PCB frame uncertainty

Calibration techniques in homogeneous field are insensitive to magnetometer effective positions (the equivalent position at which magnetometers are assumed to measure the ambient magnetic field, cf. Sec. 3.2.1). Even when those positions are known in $\mathfrak{R}_{\mathrm{b}}$, there remains uncertainty about the change of frame between $\mathfrak{R}_{\mathrm{b}}$, and $\mathfrak{R}_{\mathrm{m}}$ in which the magnetometers' calibration is expressed.

We wish to know the effect of such an uncertainty. To understand its impact, let us consider that the gradient of the interpolated field has not been projected onto the space of Maxwell's equations solutions. Reusing notations of Sec. 3.3.1, in place of the actual gradient of the magnetic field $\nabla\mathbf{B}^{\mathrm{b}}$, what is actually interpolated is (see Eq. (3.33))

$$M = R_{\mathrm{m}\leftarrow\mathrm{b}}^{\top}\nabla\mathbf{B}^{\mathrm{b}} = \nabla\mathbf{B}^{\mathrm{m}}R_{\mathrm{m}\leftarrow\mathrm{b}} \ .$$

We assume that all sensors are calibrated in $\mathfrak{R}_{\mathrm{m}}$ using techniques of the previous section.

Using the notations of Sec. 2.2.1, considering the model proposed in Sec. 2.4, and substituting $\nabla\mathbf{B}^{\mathrm{b}}$ with M, $\boldsymbol{\omega}^{\mathrm{b/n}}$ by $\boldsymbol{\omega}^{\mathrm{m/n}}$, and $\mathbf{B}^{\mathrm{b}}$ by $\mathbf{B}^{\mathrm{m}}$, the estimated velocity in $\mathfrak{R}_{\mathrm{m}}$, that we denote $\widehat{\mathbf{v}^{\mathrm{m}}}$, must then read

$$\begin{aligned}\widehat{\mathbf{v}^{\mathrm{m}}} &= M^{-1}\left(\frac{d}{dt}\mathbf{B}^{\mathrm{m}} + \boldsymbol{\omega}^{\mathrm{m/n}} \times \mathbf{B}^{\mathrm{m}}\right)\\ &= R_{\mathrm{m}\leftarrow\mathrm{b}}^{\top}(\nabla\mathbf{B}^{\mathrm{m}})^{-1}\left(\frac{d}{dt}\mathbf{B}^{\mathrm{m}} + \boldsymbol{\omega}^{\mathrm{m/n}} \times \mathbf{B}^{\mathrm{m}}\right)\end{aligned} \tag{3.44}$$

While the true velocity in $\mathfrak{R}_{\mathrm{m}}$ reads

$$\begin{aligned}\mathbf{v}^{\mathrm{m}} &= R_{\mathrm{m}\leftarrow\mathrm{b}}\widehat{\mathbf{v}^{\mathrm{m}}}\\ &= R_{\mathrm{m}\leftarrow\mathrm{b}}\mathbf{v}^{\mathrm{b}}\end{aligned} \tag{3.45}$$

The estimated velocity in $\mathfrak{R}_{\mathrm{m}}$ is rotated, which results in a systematic "crabbing error" because velocity is actually estimated in the frame in which magnetometer effective positions are expressed. If accelerometers are also calibrated in $\mathfrak{R}_{\mathrm{m}}$, then accelerations will not be coherent with the velocity expected from angular velocity and magnetic measurements. This results in the same type of errors as described in Ref. Dorveaux and Petit [2011a], when inertial sensors and magnetic sensors are not calibrated in the same frame of reference, even though in our case all sensors *are* calibrated in the same frame of reference $\mathfrak{R}_{\mathrm{m}}$ except for magnetometer effective positions.

---

density clearly yields an estimate. This is a case of "false observability" which is different from the one studied in Ref. Barrau [2015]. It is similarly caused by a wrong linearization, in that the wrong linear model is used, but the model was already state-affine. In fact, this probability density is representative of trajectories where the magnetic gradient actually looks like a white noise. Unfortunately, a non-linear error state will not remove the issue.

Inter-magnetometer distance

Even if the change of frame between $\mathfrak{R}_\mathrm{b}$ and $\mathfrak{R}_\mathrm{m}$ is known, manufacturing variability can lead to uncertainty in the placement of sensors.

To illustrate the issue, in Eq. (3.28), replacing effective positions $({}_j\mathbf{p}^\mathrm{b} - \mathbf{P}^\mathrm{b}{}_0)$ with $\lambda({}_j\mathbf{p}^\mathrm{b} - \mathbf{P}^\mathrm{b}{}_0)$ amounts to rescaling $\nabla\mathbf{B}^\mathrm{b}$ as $\lambda\nabla\mathbf{B}^\mathrm{b}$, where $\lambda \in \mathbb{R}$. The effect of rescaling $\nabla\mathbf{B}^\mathrm{b}$ as $\lambda\nabla\mathbf{B}^\mathrm{b}$ in Eq. (2.36) is that the estimated velocity is multiplied by λ. On a baseline of, e.g., 5 cm, moving all sensors towards the center of the array by 0.25 mm is enough to cause velocity to be systematically underestimated by 1%. However, as explained hereafter, it is wrong to conclude that in general, errors of 0.25 mm lead to relative velocity errors no higher than 1%.

Let us consider the case of a planar disposition of magnetometer along the first two coordinates in $\mathfrak{R}_\mathrm{b}$, as described in Sec. 3.2.6. The last column of the magnetic field gradient is computed by using Maxwell's equations. As explained in Sec. 3.2.6, $\nabla\mathbf{B}^\mathrm{b}$ is a real symmetric matrix, therefore is diagonalizable. Considering the case where the magnetic gradient is diagonal in $\mathfrak{R}_\mathrm{b}$, that is to say,

$$\nabla\mathbf{B}^\mathrm{b} = \begin{pmatrix} d_1 & 0 & 0 \\ 0 & d_2 & 0 \\ 0 & 0 & d_3 \end{pmatrix} = \begin{pmatrix} d_1 & 0 & 0 \\ 0 & d_2 & 0 \\ 0 & 0 & -d_1 - d_2 \end{pmatrix} ,$$

Let us transform effective positions in such a way that the first spatial coordinate is multiplied by $(1 + \epsilon_1)$, the second by $(1 + \epsilon_2)$, and the third is left unchanged. The estimated gradient M becomes

$$M \doteq \begin{pmatrix} d'_1 & 0 & 0 \\ 0 & d'_2 & 0 \\ 0 & 0 & d'_3 \end{pmatrix} = \begin{pmatrix} (1+\epsilon_1)d_1 & 0 & 0 \\ 0 & (1+\epsilon_2)d_2 & 0 \\ 0 & 0 & -(1+\epsilon_1)d_1 - (1+\epsilon_2)d_2 \end{pmatrix} ,$$

since the third column is recovered using Maxwell's equations. Now, let us denote the ratio

$$\begin{aligned}(1+\epsilon_3) &\doteq \frac{d'_3}{d_3} \\ &= \frac{-(1+\epsilon_1)d_1 - (1+\epsilon_2)d_2}{-d_1 - d_2} \\ &= 1 + \frac{\epsilon_1 d_1 + \epsilon_2 d_2}{d_1 + d_2} .\end{aligned}$$

If $d_1 + d_2 = -d_3$ decreases to zero (the magnetic gradient becomes singular) and if $\epsilon_1 \neq \epsilon_2$, then $(1 + \epsilon_3)$ diverges towards $\pm\infty$. To make it clearer, assuming $\epsilon_1 + \epsilon_2 = 0$, we have

$$\epsilon_3 = \epsilon_1 \frac{d_1 - d_2}{d_1 + d_2} .$$

We have proven that the use of a planar array of magnetometers whose effective positions are known with an *arbitrarily small error* can lead to *arbitrarily large velocity estimation relative errors.*

Remark regarding scale factors Similar reasoning leads to the same conclusion regarding scale factors that with a planar arrangement of sensors, arbitrarily small scale factor errors can lead to arbitrarily large velocity estimation relative errors close to singular gradient conditions.

General case

In the general case, if all sensors are calibrated in $\mathfrak{R}_{\mathrm{b}}$, and are without noise, denoting $\widehat{\mathbf{v}^{\mathrm{b}}}$ the velocity estimated from the wrong magnetic gradient M and $\mathbf{v}^{\mathrm{b}}$ the true value of the velocity in $\mathfrak{R}_{\mathrm{b}}$, we have in first order approximation in $\nabla\mathbf{B}^{\mathrm{b}} - M$ near 0,

$$\begin{aligned}
\widehat{\mathbf{v}^{\mathrm{b}}} - \mathbf{v}^{\mathrm{b}} &= \left(M^{-1} - \nabla\mathbf{B}^{\mathrm{b}^{-1}}\right) \cdot \left(\frac{d}{dt}\mathbf{B}^{\mathrm{b}} + \boldsymbol{\omega}^{\mathrm{b/n}} \times \mathbf{B}^{\mathrm{b}}\right) \\
&= \left(M^{-1} - \nabla\mathbf{B}^{\mathrm{b}^{-1}}\right) M\widehat{\mathbf{v}^{\mathrm{b}}} \\
&= \left(M^{-1} - (M + \nabla\mathbf{B}^{\mathrm{b}} - M)^{-1}\right) M\widehat{\mathbf{v}^{\mathrm{b}}} \\
&= \left(M^{-1} - \left[\mathbf{1} + M^{-1}(\nabla\mathbf{B}^{\mathrm{b}} - M)\right]^{-1} M^{-1}\right) M\widehat{\mathbf{v}^{\mathrm{b}}} \\
&= \left(M^{-1} - \sum_{k=0}^{\infty}(-1)^k \left[M^{-1}(\nabla\mathbf{B}^{\mathrm{b}} - M)\right]^k M^{-1}\right) M\widehat{\mathbf{v}^{\mathrm{b}}} \\
&\approx \left(M^{-1}\left[\nabla\mathbf{B}^{\mathrm{b}} - M\right] M^{-1}\right) M\widehat{\mathbf{v}^{\mathrm{b}}} \\
&\approx M^{-1}\left[\nabla\mathbf{B}^{\mathrm{b}} - M\right]\widehat{\mathbf{v}^{\mathrm{b}}}
\end{aligned} \tag{3.46}$$

From this equation, it can be seen that velocity errors are preferably expressed as relative errors, because they are proportional to the estimated velocity with the coefficient of proportionality $M^{-1}\left[\nabla\mathbf{B}^{\mathrm{b}} - M\right]$. However, since in practice M can be infinitesimally close to a singular matrix and calibration errors are not zero, this coefficient is *unbounded in the general case*, even without taking measurement noise into account, since systematic calibration errors are sufficient to cause this unbounded growth. While biases can cause such errors, it is also the case with the other calibration parameters (sensor effective positions and scale factors) when using a planar arrangement of sensors (see above).

3.4.3. Other inertial sensors uncertainties

Frame of reference uncertainty

The case in which magnetometers are calibrated in $\mathfrak{R}_{\mathrm{b}}$ (including magnetometer effective positions) and inertial sensors are calibrated in $\mathfrak{R}_{\mathrm{g}} = \mathfrak{R}_{\mathrm{a}} \neq \mathfrak{R}_{\mathrm{b}}$ is investigated in Ref. Dorveaux and Petit [2011a]. The most visible effect is a vertical drift for trajectories combining forward movements and turns around the vertical axis, which is typical of standing pedestrian or car use cases. Velocity is computed in $\mathfrak{R}_\mathrm{b}$ and incorrectly projected in $\mathfrak{R}_\mathrm{n}$ by using the change of frame between $\mathfrak{R}_\mathrm{n}$, and $\mathfrak{R}_\mathrm{a}$ erroneously instead of $\mathfrak{R}_\mathrm{b}$. Other errors are expected whenever angular velocity is different from zero, leading to a biased velocity estimate. This effect will not be detailed here.

Inertial sensor bias uncertainty

In Sec. 2.5, inertial sensor biases led to the existence of a set of indistinguishable trajectories including static ones. In static cases, accelerometer biases are expected to induce an attitude error, and gyrometer biases are expected to induce a drift if they are only vertical. Other situations will cause incoherent measurements.

3.5. Conclusion

Magnetometer measurement model At constant temperature, an accurate measurement model of our magnetometers has been verified, proving that high precision calibration of AMR is achievable at low hardware cost in homogeneous fields. Thus the validity of linear measurement models can be predicted on this hardware.

Limits of available calibration techniques Mentioned available calibration techniques are suitable for use in homogeneous fields, but not suitable for gradiometer calibration used in inhomogeneous fields. In particular, Assumption 3.2.3 is broken in inhomogeneous fields and Assumption 3.2.2 is broken in presence of soft-iron materials close to magnetometers. This makes the case for a different calibration approach, suitable for use in inhomogeneous field and in presence of soft-iron materials. At least, the issue of identifying the magnetometers calibration frame remains partially unsolved in the context of this chapter. Note that even in homogeneous fields, the mentioned calibration techniques are not suitable in the presence of soft-iron materials with significant hysteresis.

Calibration frame issues Identification algorithms have been used or proposed in order to ensure that all sensors are calibrated in the same reference frame. In particular, an algorithm has been proposed in order to express all magnetometer calibration parameters in the same reference frame including their effective position, however real-world experiments have not been conclusive. The difficulty of calibrating a gradiometer is addressed in later chapters.

Planar magnetometer arrays Ignoring the issue of calibrating a magnetic gradiometer, exploiting Maxwell's equations enables the use of planar magnetometer arrays to compute to any spatial derivative of the magnetic field in 3 dimensions, in a hardware configuration that was never going to be available during this work as mentioned in Sec. 2.6.

Effect of measurement uncertainty on movement estimation Finally, the effects of measurement uncertainty have been explored. In particular, uncertainties on the magnetic field gradient play an important role. Even arbitrarily small calibration errors can cause *unbounded velocity estimation errors* close to singular gradient conditions. Measurement noise sharply increases estimation uncertainty and prevents proper function in low gradient conditions, leading to a damping effect, which manifests in overconfident and underestimated velocity estimates. On the other hand, the damping effect of magnetic gradient measurement noise might actually be helpful in preventing velocity estimates from diverging along low-gradient directions.

4. Using Extended Kalman Filters for Magneto-Inertial Dead-Reckoning

Contents

4.1. Introduction

Context The aim is to estimate the trajectory of a system equipped with Microelectromechanical Systems (MEMS) inertial sensors and an array of magnetometers as described in Ch. 3. The first step towards this goal has been modeling the problem in the form of a state-space model, hence the fact that in Ch. 2, several such Magneto-Inertial Dead-Reckoning (MIDR) models have been proposed and studied. The second step has been studying how to obtain the necessary inputs from our hardware, and understanding and mitigating measurement uncertainty. This work is documented in Ch. 3. The third and last step is the actual implementation and test of a navigation algorithm.

In order to better understand the contributions in this chapter, the main previous publications on the subject are recalled hereafter:

- Ref. Vissière et al. [2007a], relying on a model whose reasons for not keeping are explained in Sec. 2.4;
- Ref. Dorveaux [2011], relying on a two-independent-observers structure (see Ref. [Dorveaux, 2011, Fig. 2.3], reproduced in Fig. 2.2), an approach whose disadvantages are explained in Sec. 2.3.

Therefore, we use the candidate models described in Sec. 2.4.1 and Sec. 2.5.1 as starting points of this Chapter.

Outline Implementing a navigation algorithm would require first to choose an appropriate class of estimation algorithm and an adequate architecture. A promising initial experiment was successfully conducted with a monolithic Extended Kalman Filter (EKF) early in this work, built on the model in Sec. 2.4.1, leading SYSNAV to demand that this early choice be maintained; while Sec. 2.3.3 justifies a monolithic observer, inputs for discussion, and justifications of the choice of an EKF are nevertheless provided *a posteriori* in Sec. 4.2.

Since an EKF has been chosen, principles implementation of discrete-time Kalman filtering are recalled in Sec. 4.3. Afterward, two issues are studied: the handling of power-line interference in Sec. 4.4, and of heading estimation in Sec. 4.5. In both cases, justifications for modeling choices are provided, and the resulting observer is evaluated in experiments.

4.2. About the choice of observer

The choice of estimation algorithm depends on three criteria. First, navigation algorithms must be able to provide a converging estimate of observable states, in such a way that in absence of measurement errors, the estimated state converges towards its true value. Under this condition, the choice of algorithm depends, among others, on the type of dynamical system that must be observed. Secondly, navigation algorithms must be able to provide information about the uncertainty of computed estimates.

Finally, and in our specific case, the hardware was designed as an autonomous navigation system as small as possible, leading to the design constraint that estimation algorithm must be able to run on a low-power microcontroller with an Floating-Point Unit (FPU), with a computing power that is decent but small compared with modern microprocessors. In the following, the choice of observer is discussed in view of these elements.

The choice of observer in light of the first criterion is discussed in Sec. 4.2.1. It is then discussed in light of the second criterion in Sec. 4.2.3, in light of the third criterion in Sec. 4.2.3, and Sec. 4.2.4 concludes the discussion.

4.2.1. Convergence and class of dynamical system

Monolithic Kalman observers are poorly adapted to our model candidates

Two model candidates have been proposed in Ch. 2, in Sec. 2.4 and Sec. 2.5. In both cases, observability depends on the input, especially on the magnetic field gradient $\nabla \mathbf{B}^{\mathrm{b}}$. Therefore, neither of these systems is uniformly observable in the sense of Ref. [Besançon, 2007, Defs. 8 and 9], that are recalled thereafter.

Definition 7 (Universal inputs (resp. on $[0,t]$) Ref. [Besançon, 2007, Sec. 1.2.2, Def. 8])**.** *An input u is universal (resp. on $[0,t]$) for system* (2.9) *if* $\forall x_0 \neq x_0'$, $\exists \tau \geqslant 0$ *(resp.* $\exists \tau \in [0,t]$*) s.t.* $h(\chi_u(\tau, x_0)) \neq h(\chi_u(\tau, x_0'))$.

An input u is a singular input if it is not universal.

Definition 8 (Uniformly observable systems (resp. locally) Ref. [Besançon, 2007, Sec. 1.2.2, Def. 9])**.** *A system is uniformly observable (UO) if every input is universal (resp. on* $[0,t]$*).*

Therefore, possible observers will also depend on the inputs, which tips the choice of observers towards *Kalman-like* observers (Ref. Besançon [2007]).[1]

The Kalman filter, Ref. Kalman [1960], is designed for linear systems for which the state-space representation (2.9) has the following form,

$$\begin{aligned} \dot{x}(t) &= A(t)x(t) + Bu(t) \\ y(t) &= C(t)x(t) \ . \end{aligned} \tag{4.1}$$

For the system studied in Sec. 2.4, namely (2.28)-(2.29), the system is not linear.

- Strictly speaking, the Jacobian $\frac{\partial \dot{x}}{\partial x}$ depends on the input. However, one can consider $A(t)$ separately as if it were known independently of an input. After all, there is no controllable input in our navigation problem.
- To know whether the dependency of $\dot{x}(t)$ with respect to $x(t)$ is linear, that is to say, whether the system is state-affine, one must decide on what attitude parameterization to consider. For the sake of readability, in Ch. 2, elements of

---

[1] In Ref. Dorveaux [2011], an ad-hoc converging observer is proposed that depends on the input but is not a Kalman-like observer. Therefore, Kalman-like observers are not the only possible candidates.

> SO(3) have been parameterized with orthogonal 3x3 matrices. In this particular parameterization, the dependency is linear. However, it is so in the space of all 3x3 matrices, not in SO(3). Many other choices could have been made in order to represent attitude, that lead either to singular representations (such as Euler angles), or to over-parameterization (the use of more than 3 numbers to represent an element of the 3-dimensional manifold SO(3), such as rotation matrices or quaternions), (see Refs. Lefferts et al. [1982], Markley [2003] and references therein). Moreover, in an approach known as the Multiplicative EKF (MEKF), attitude is represented by a quaternion (or equivalently any other non-singular representation), and *errors* are represented by a three-component vector. Therefore, in such an implementation, *one cannot count on the model used in Kalman filtering being state-affine in general.*

The use of a monolithic EKF is a possible choice motivated by the non-linearity of the complete model. However, the convergence of such an observer is not guaranteed in general.

A bi-observer approach might help only for one of them

Instead, another possible architecture is to estimate *the gravity vector instead of the attitude*, in which case a state-affine model is obtained, for which tools such as in Ref. Besançon et al. [1996] are appropriate; the velocity and the estimated gravity vector can then be injected into a connected converging attitude observer, in such a way that after convergence, both dynamic models remain correct in the presence of accelerations in light of Sec. 2.3.3. The difference with the structure illustrated in Fig. 2.2 is that in Ref. Dorveaux [2011], the attitude observer is presented as *independent* from the velocity and magnetic field observer. There is no interconnection between the two observers, and therefore the use of accelerometers in velocity estimation is hindered, because integrating the strapdown navigation equation (2.30) requires an attitude estimate and the attitude estimate is disturbed by accelerations (see Sec. 2.3.3). However, compared to a monolithic EKF, such an architecture is more difficult to augment to account for inertial sensor biases.

For the system studied in Sec. 2.5 that accounts for inertial sensor biases, the problem is made harder by gyrometer biases. Each term in which they appear in the dynamical model, namely in Eqs. (2.40),(2.41) and (2.42), is bilinear in the state, thus making tools designed for state-affine models theoretically inadequate.

4.2.2. Uncertainty awareness

Kalman filters cannot model gradient measurement uncertainty

To a concerned end-user, information about estimation uncertainty is valuable. Providing such information requires appropriate error modeling. Formulated in these terms, one may lean in favor of probabilistic, set-oriented, or game-theory approaches.

The Kalman Filter carries a covariance matrix which accurately represents such an uncertainty *under its derivation assumptions* (see Ref. Barker et al. [1995]). However, as seen in Ch. 3, these derivation assumptions are not valid in the context of MIDR. Gradient measurement uncertainties constitute a significant source of error, and cannot be modeled in the Kalman Filtering framework alone. Moreover, these uncertainties can cause unbounded errors or cause inconsistency. Because of this unboundedness, no generic performance guarantee can be provided for all possible trajectories: one can always find a trajectory causing an arbitrarily large error.[2]

There is plenty of literature about this shortcoming

For the above-mentioned reasons, many other estimation tools that extend Kalman filtering in order to take into account and be robust to modeling uncertainty seem more appropriate than an EKF in order to tackle MIDR specifically, given our design specifications; ignoring the problem of nonlinearity, see Ref. Theodor et al. [1994] or Dong and You [2006] (see also Refs. Einicke and White [1999], Liu et al. [2008], Lu et al. [2007], Ra et al. [2004] and references therein).

4.2.3. Computing power

Compared to modern processors, embedded microcontrollers with FPUs have far less computing power, and only a few KiloBytes of RAM are available. Memory is a very limiting factor in the choice of algorithm. Approaches such that finite horizon observation tools or optimization based techniques (see Ref. [Besançon, 2007, Ch. 5]) risk requiring more computing power and being unusable on this hardware. Kalman filtering, however, can still run on a microcontroller with an FPU provided that the dimensions of the problem not be too high (number of states, inputs, measurements).

4.2.4. Conclusion

A monolithic EKF is an approximately appropriate choice for the criteria of convergence, uncertainty awareness and computing power. It can nevertheless provide qualitatively meaningful, but quantitatively wrong error bounds in this context. It is also a reasonable compromise regarding computing power constraints. However, in order to meet the design constraints of convergence or uncertainty modeling, another tool would be needed. This direction has not been explored.

4.3. Discrete-time Kalman filtering implementation

Process and issues EKFs are simply Kalman filters on a linearized system. One can then separate the problem into two parts:

1. Implementing Kalman filtering formulas,

---

[2] Let us remark that the effect of modeling error in Kalman filtering has been studied in, e.g., Ref. Toda and Patel [1980]

2. Implementing the equations of the state-space model in discrete-time.

Sec. 4.4 and 4.5 focus on the second item. Concerning the first item, early after Kalman's seminal publication Ref. Kalman [1960], many papers have documented numerical stability issues of the strict implementation of Kalman's formulas and made a strong case for alternative numerical implementations (see Refs. Bierman and Thornton [1977], Thornton and Bierman [1980], Verhaegen and Dooren [1986]). For the sake of simplicity, the full discrete-time version of the Kalman filter is implemented; it is derived from a discretized dynamic model, with a discrete-time update. Kalman filtering formulas are discussed in Ref. Anderson and Moore [2005], the square-root covariance-based algorithms described in Ref. Kaminski et al. [1971] are implemented.

Outline In Sec. 4.3.1, discrete-time Extended Kalman filtering with an error-state is described. The actual numerical implementation of Kalman formulas is described in Sec. 4.3.2. Then, the implementation process is summarized in Sec. 4.3.3.

4.3.1. Extended Kalman filtering

Kalman filtering formulas are already introduced in Sec. 3.4.1 with the goal of studying the effect of measurement noise, see also Refs. Alazard [2005], Barker et al. [1995]. Here, they are introduced in the context of discrete-time Extended Kalman filtering with an error state.[3]

Linearized state-space model with an error state

Let us consider a discrete-time system of the form

$$\left\{ \begin{array}{lcl} x[k+1] & = & f(x[k], u[k]) \ , \\ y[k] & = & h(x[k]) \ , \end{array} \right. \tag{4.2}$$

with $k \in \mathbb{N}$. The variable $x[k]$ denotes the true state at time-step k, and $y[k]$ denotes the system's output vector. Let us define $\hat{u}[k]$ and $\hat{y}[k]$ such that

$$\begin{aligned} u[k] &= \hat{u}[k] + \tilde{u}[k] \ , \\ y[k] &= \hat{y}[k] + \tilde{y}[k] \ , \end{aligned}$$

where $\tilde{u}[k]$ and $\tilde{y}[k]$ are unknown independent zero-mean Gaussian variables whose known covariance matrices at each time-step k are respectively $Q[k]$ and $R[k]$,

$$\begin{aligned} \tilde{u}[k] &\sim \mathcal{N}(0, Q[k]) \ , \\ \tilde{y}[k] &\sim \mathcal{N}(0, R[k]) \ . \end{aligned}$$

---

[3] While the presented approach allows writing an MEKF, see Refs. Lefferts et al. [1982], Markley [2003], and is similar to the invariant approach Ref. Barrau and Bonnabel [2017], no invariance property is meant to be exploited in this chapter. This is a research direction that has not been explored in this work.

Only the state estimate $\hat{x}[k]$ is known with an error that we denote $\tilde{x}[k]$. The error parameterization is such that

$$x[k] = \xi(\hat{x}[k], \tilde{x}[k]) \ , \tag{4.3}$$

where ξ is a differentiable mapping such that for all $\hat{x}[k]$, the mapping

$$\tilde{x}[k] \mapsto \xi(\hat{x}[k], \tilde{x}[k]) \doteq \xi_{\hat{x}[k]}(\tilde{x}[k])$$

is locally bijective around the value 0 of $\tilde{x}[k]$ representing "no error", that is to say

$$x[k] = \xi_{\hat{x}[k]}(0) \Leftrightarrow x[k] = \hat{x}[k] \ .$$

Combining Eq. (4.2) and (4.3) yields

$$\xi_{\hat{x}[k+1]}(\tilde{x}[k+1]) = f\left(\xi_{\hat{x}[k]}(\tilde{x}[k]), \hat{u}[k] + \tilde{u}[k]\right) \ , \tag{4.4}$$

or,

$$\tilde{x}[k+1] = \xi^{-1}_{\hat{x}[k+1]} \left(f\left(\xi_{\hat{x}[k]}(\tilde{x}[k]), \hat{u}[k] + \tilde{u}[k]\right)\right) \ . \tag{4.5}$$

Linearizing this system around $\tilde{x}[k] = 0$ and $\tilde{u}[k] = 0$, yields

$$\tilde{x}[k+1] \approx F[k]\tilde{x}[k] + G[k]\tilde{u}[k] \ , \tag{4.6}$$

where

$$F[k] = \left.\frac{\partial}{\partial \tilde{x}[k]}\right|_{\tilde{x}[k]=0,\ \tilde{u}[k]=0} \xi^{-1}_{\hat{x}[k+1]} \left(f\left(\xi_{\hat{x}[k]}(\tilde{x}[k]), \hat{u}[k] + \tilde{u}[k]\right)\right) \ ,$$

and

$$G[k] = \left.\frac{\partial}{\partial \tilde{u}[k]}\right|_{\tilde{x}[k]=0,\ \tilde{u}[k]=0} \xi^{-1}_{\hat{x}[k+1]} \left(f\left(\xi_{\hat{x}[k]}(\tilde{x}[k]), \hat{u}[k] + \tilde{u}[k]\right)\right) \ .$$

The measurement equation can also be linearized similarly,

$$\begin{aligned} y[k+1] &= h(\xi_{\hat{x}[k+1]}(\tilde{x}[k+1])) \\ &\approx h(\hat{x}[k+1]) + H[k]\tilde{x}[k+1] \ , \end{aligned}$$

where

$$H[k] = \left.\frac{\partial}{\partial \tilde{x}[k]}\right|_{\tilde{x}[k]=0} \left(h\left(\xi_{\hat{x}[k]}(\tilde{x}[k])\right)\right) \ .$$

Thus,

$$y[k+1] - h(\hat{x}[k+1]) \approx H[k]\tilde{x}[k+1] \ . \tag{4.7}$$

A classical discrete-time Kalman filter can now be implemented on the linearized model

$$\left\{ \begin{array}{ll} \tilde{x}[k+1] & \approx F[k]\tilde{x}[k] + G[k]\tilde{u}[k] \ , \\ y[k+1] - h(\hat{x}[k+1]) & \approx H[k]\tilde{x}[k+1] \ . \end{array} \right. \tag{4.8}$$

Kalman prediction and update with an error state

Kalman prediction and update algorithms with an error state are described thereafter. Let us denote for $k \in \mathbb{N}$,

$$\hat{U}[k] = \{\hat{u}[0], ..., \hat{u}[k]\} \ ,$$
$$\hat{Y}[k] = \{\hat{y}[0], ..., \hat{y}[k]\} \ .$$

Let us assume that at time-step $k \in \mathbb{N}$, we have an estimate $\hat{x}[k]$ of $x[k]$ such that

$$x[k] = \xi(\hat{x}[k], \tilde{x}[k]) \ ,$$

where $\tilde{x}[k]$ denotes the error state vector, and $\Sigma[k]^+$ denotes the covariance matrix such that

$$p\left(\tilde{x}[k] \mid \hat{Y}[k], \hat{U}[k-1]\right) = \mathcal{N}\left(0, \Sigma[k]^+\right) \ . \tag{4.9}$$

Then, using Eq. (4.6), the prior prediction error is obtained with the classical Kalman filtering formulas (see Refs. Barker et al. [1995], Alazard [2005]),

$$p\left(\tilde{x}[k+1] \mid \hat{U}[k], \hat{Y}[k]\right) = \mathcal{N}\left(0, F[k]\Sigma[k]^+ F[k]^\top + G[k]Q[k]G[k]^\top\right) \ , \tag{4.10}$$

with, because of Eq. (4.4) and under the approximation that $\tilde{u}[k] \approx 0$,

$$\hat{x}[k+1] \approx f(\hat{x}[k], \hat{u}[k]) \ . \tag{4.11}$$

Eq. (4.11) is the state prediction equation, which is simply an iteration of the discrete-time model, while Eq. (4.10) predicts the covariance of the error state vector, which concludes the prediction step.

Let us denote for $k \in \mathbb{N}$

$$\Sigma[k+1]^- = F[k]\Sigma[k]^+ F[k]^\top + G[k]Q[k]G[k]^\top \tag{4.12}$$

Then, we have the classical Kalman filtering formulas (see Refs. Barker et al. [1995], Alazard [2005])

$$\Sigma[k+1]^+ = (\mathbf{1} - K[k+1]H[k+1])\Sigma[k+1]^- \tag{4.13}$$
$$K[k+1] \doteq \Sigma[k+1]^- H[k+1]^\top S[k+1]^{-1} \tag{4.14}$$
$$S[k+1] \doteq R[k+1] + H[k+1]\Sigma[k+1]^- H[k+1]^\top \tag{4.15}$$

with the posterior error state estimate

$$\begin{aligned} & p\left(\tilde{x}[k+1] \mid \hat{Y}[k+1], \hat{U}[k]\right) \\ & \qquad = \mathcal{N}\left(K[k+1]\{y[k+1] - h(\hat{x}[k+1])\}, \Sigma[k+1]^+\right) \ . \end{aligned} \tag{4.16}$$

Following this computation, the predicted value of the state $\hat{x}[k+1]$ can be updated to

$$\xi_{\hat{x}[k+1]}(K[k+1]\{y[k+1] - h(\hat{x}[k+1])\}) \ ,$$

and $\tilde{x}[k+1]$ be reset to zero, which concludes an iteration.

4.3.2. Square-root filtering

The strict numerical implementation of Eqs. (4.12)-(4.15) leads to stability problems as documented in Refs. Bierman and Thornton [1977], Thornton and Bierman [1980], Verhaegen and Dooren [1986]. The first observation that can be made when implementing these formulas is that the computed values of $\Sigma[k]^+$ and $\Sigma[k]^-$ do not remain numerically symmetric, positive definite, because of the effect of rounding errors and numerical instability. One possible alternative proposed by these references is to avoid computing $\Sigma[k]^+$ and $\Sigma[k]^-$ explicitly, and to compute their respective "*square roots*" (in the sense of Cholesky factorization) instead. Doing so results in an improved numerical stability, and square root representations require half the number of bytes for the same numerical precision.[4]

Let M be any symmetric positive definite matrix. Let us denote $M^{1/2}$ one of its square roots, in the sense that

$$M^{1/2}(M^{1/2})^\top = M \; . \tag{4.17}$$

This square root is not unique; if T is any orthogonal matrix of compatible dimensions, $M^{1/2}T$ is also a square root of M,

$$\left[M^{1/2}T\right]\left[M^{1/2}T\right]^\top = M^{1/2}(M^{1/2})^\top = M$$

By QR factorization, any square matrix M can be written as the product of an orthogonal matrix Q by an upper triangular matrix R such that $M = QR$.

The square root of $\Sigma[k+1]^-$ can be computed by noticing that there exists an orthogonal matrix T such that

$$\begin{pmatrix} [(\Sigma[k]^+)^{1/2}]^\top F[k]^\top \\ [Q[k]^{1/2}]^\top G[k]^\top \end{pmatrix} = T \begin{pmatrix} [(\Sigma[k+1]^-)^{1/2}]^\top \\ 0 \end{pmatrix} \; , \tag{4.18}$$

where $(\Sigma[k+1]^-)^{1/2}$ is an upper triangular square root of $\Sigma[k+1]^-$. Eq. (4.18) can then be replaced by the QR factorization implied by Eq. (4.12) to directly compute a triangular square root of $\Sigma[k+1]^-$.

Then, the square root of $\Sigma[k+1]^+$ can be computed by noticing that there exists another orthogonal matrix $\widetilde{T}$ such that

$$\begin{aligned} &\begin{pmatrix} (R[k]^{1/2})^\top & 0 \\ [(\Sigma[k+1]^-)^{1/2}]^\top [H[k]^{1/2}]^\top & [(\Sigma[k+1]^-)^{1/2}]^\top \end{pmatrix} \\ &\qquad\qquad = \widetilde{T} \begin{pmatrix} [S[k+1]^{1/2}]^\top & \tilde{K}[k+1]^\top \\ 0 & [(\Sigma[k+1]^+)^{1/2}]^\top \end{pmatrix} \; , \end{aligned}$$

---

[4] The Cholesky factorization is described thereafter, but other decompositions exist and may even be preferred, see, e.g., Ref. Thornton and Bierman [1980] for the so-called $UDU^\top$ covariance factorization algorithm. This algorithm avoids computing square roots and was advertised at the time to be faster than Cholesky factorization-based algorithms.

where $(\Sigma[k+1]^+)^{1/2}$ is an upper triangular square root of $\Sigma[k+1]^+$, and where

$$\tilde{K}[k+1] = K[k+1]S[k+1]^{1/2} \ ,$$

see Refs. Anderson and Moore [2005], Kaminski et al. [1971] and references therein. Thus, Eqs. (4.12)-(4.15) can be entirely replaced by two successive QR factorizations, allowing the computation of the square roots of covariance matrices along with the Kalman gain, without ever computing covariance matrices explicitly.

4.3.3. Practical implementation

Now that a numerically stable Kalman filtering implementation is chosen, the design of an EKF consists in the following steps,

1. Choosing and implementing the discrete-time model Eq. (4.2)
2. Choosing an error parameterization Eq. (4.3)
3. Computing the linearized system Eqs. (4.6), (4.7)
4. Tuning the observer by the appropriate choice of matrices $Q[k]$ and $R[k]$ for each time-step k.

Once done, only the initialization of the filter is left at the discretion of the engineer. Thereafter, Step 1 is sufficiently outlined, and Step 2 is described. Steps 3 and 4, that mainly consist in lengthy model-specific computations and know-how, are omitted.

4.4. Velocity and attitude estimation

The starting point of this section is the model proposed in Sec. 2.4.1. This model has been slightly adapted in this Section.

Motivations for its adaptation are provided in Sec. 4.4.1. The actual model is described in Sec. 4.4.2. The EKF implementation is described in Sec. 4.4.3. Then, performance is evaluated on indoor closed paths in Sec. 4.4.4, and in motion capture experiments in Sec. 4.4.5. Finally, Sec. 4.4.6 concludes this Section.

4.4.1. Motivations

Power-line interference The model described in Sec. 2.4.1 relies on the hypothesis that the magnetic field $\mathbf{B}^{\mathrm{n}}$ be stationary in $\mathfrak{R}_{\mathrm{n}}$. However, this hypothesis is in general not true in indoor and urban environment because of power-line interference. Such periodic interference can be as strong as 1 μT in amplitude in SYSNAV's office, located near a train station. During this work, early experiments showed that in some cases, power-line interference could cause significant drift. Therefore, it was deemed necessary to take those disturbances into account.

Sensors effective positions On our hardware, considering magnetometers' and accelerometer's measurements separately leads to computing their values at different effective positions in $\mathfrak{R}_{\mathrm{b}}$. Therefore, the models described in Ch. 2 are modified in this Chapter in order to take the corresponding lever arm into account. The model is chosen to avoid taking time derivatives of inputs. Let us remark that this lever arm is then a new calibration parameter.

Trajectory integration As discussed in Ch. 2, the position is not observable in the proposed dead-reckoning models. However, it can be argued that by using the EKF as a recursive Bayesian estimator, integrating this unobservable state into the filter

- can be numerically achieved without influencing the estimation of other states;
- is beneficial if one desires optimal *a posteriori* corrections of the estimated position from the starting point, in ideal cases where linearization and modeling errors are negligible.

4.4.2. Model

Continuous-time dynamic model

Let us assume that the magnetic field is the sum of a stationary field that is still denoted $\mathbf{B}^{\mathrm{n}}$ in the navigation frame, and disturbance field that only depends on time in the navigation frame and that is denoted ${\mathbf{B}^{\mathrm{n}}}_{\mathrm{pli}}$, as in "power-line interference". With this assumption, it follows that the measured gradient of the total field is the gradient of the stationary field $\nabla\mathbf{B}^{\mathrm{b}}$, and the measured total magnetic field is the sum of both fields.

As in Ch. 2, the goal is to track the 6-D position of the sensor board $(R, \mathbf{M}^{\mathrm{n}}) \in \mathrm{SE}(3)$ with time. Let us assume that $\mathbf{M}$ denotes the percussion point of accelerometers.

Let us denote $\mathbf{N}$ the point at which the magnetic field and its gradient are measured. In this Chapter, shortened notations are used,

$$\mathbf{B}^{\mathrm{b}} = \mathbf{B}^{\mathrm{b}}(\mathbf{N}^{\mathrm{b}}, t) \tag{4.19}$$

$$\nabla\mathbf{B}^{\mathrm{b}} = \nabla\mathbf{B}^{\mathrm{b}}(\mathbf{N}^{\mathrm{b}}, t)\ . \tag{4.20}$$

Velocity $\mathbf{v}^{\mathrm{b}}$ is still defined according to Eqs. (2.3) and (2.4).

Lastly, let us denote ω_{pli} the pulsation of power-line interference. The continuous-time dynamic model can now be written,

$$\left\{\begin{aligned}
\frac{d\mathbf{B}^{\mathrm{b}}}{dt} &= -\boldsymbol{\omega}^{\mathrm{b/n}} \times \mathbf{B}^{\mathrm{b}} + \nabla\mathbf{B}^{\mathrm{b}}\left(\mathbf{v}^{\mathrm{b}} + \boldsymbol{\omega}^{\mathrm{b/n}} \times \overrightarrow{\mathbf{M}^{\mathrm{b}}\mathbf{N}^{\mathrm{b}}}\right) && (4.21)\\
\frac{d\mathbf{v}^{\mathrm{b}}}{dt} &= -\boldsymbol{\omega}^{\mathrm{b/n}} \times \mathbf{v}^{\mathrm{b}} + \boldsymbol{\gamma}^{\mathrm{b}} + R^{\top}\mathbf{g}^{\mathrm{n}} && (4.22)\\
\frac{dR}{dt} &= R[\boldsymbol{\omega}^{\mathrm{b/n}}\times] && (4.23)\\
\frac{d^2{\mathbf{B}^{\mathrm{n}}}_{\mathrm{pli}}}{dt^2} &= -\omega_{\mathrm{pli}}^2{\mathbf{B}^{\mathrm{n}}}_{\mathrm{pli}} && (4.24)\\
\frac{d\mathbf{M}^{\mathrm{n}}}{dt} &= R\mathbf{v}^{\mathrm{b}}\ . && (4.25)
\end{aligned}\right.$$

The output is then the sum of the stationary field and the disturbance field,

$$y = \mathbf{B}^{\mathrm{b}} + R^{\top}{\mathbf{B}^{\mathrm{n}}}_{\mathrm{pli}}\ . \tag{4.26}$$

Discrete-time dynamic model

Discrete-time integration of $\frac{d\mathbf{v}^{\mathrm{b}}}{dt}$, $\frac{d\mathbf{M}^{\mathrm{n}}}{dt}$ and $\frac{dR}{dt}$ can be found in various references such as Ref. Savage [2000], therefore, they are not detailed here.

An ingenious way of integrating $\frac{d^2{\mathbf{B}^{\mathrm{n}}}_{\mathrm{pli}}}{dt^2}$ in discrete-time is to use a trigonometric identity (see Ref. Sameni [2012]),

$${\mathbf{B}^{\mathrm{n}}}_{\mathrm{pli}}[k+1] + {\mathbf{B}^{\mathrm{n}}}_{\mathrm{pli}}[k-1] = 2\cos(\omega_{\mathrm{pli}}T){\mathbf{B}^{\mathrm{n}}}_{\mathrm{pli}}[k]\ , \tag{4.27}$$

where T represents the sampling period, which means that

$$\begin{pmatrix}{\mathbf{B}^{\mathrm{n}}}_{\mathrm{pli}}[k+1]\\ {\mathbf{B}^{\mathrm{n}}}_{\mathrm{pli}}[k]\end{pmatrix} = \begin{pmatrix}2\cos(\omega_{\mathrm{pli}}T)\ \mathbf{1} & -\mathbf{1}\\ \mathbf{1} & \mathbf{0}\end{pmatrix}\begin{pmatrix}{\mathbf{B}^{\mathrm{n}}}_{\mathrm{pli}}[k]\\ {\mathbf{B}^{\mathrm{n}}}_{\mathrm{pli}}[k-1]\end{pmatrix}\ . \tag{4.28}$$

The discrete-time model Eq. (4.2) is then defined using

$$x[k] = \begin{pmatrix}\mathbf{B}^{\mathrm{b}}[k]\\ \mathbf{v}^{\mathrm{b}}[k]\\ R[k]\\ {\mathbf{B}^{\mathrm{n}}}_{\mathrm{pli}}[k]\\ {\mathbf{B}^{\mathrm{n}}}_{\mathrm{pli}}[k-1]\\ \mathbf{M}^{\mathrm{n}}[k]\end{pmatrix}\ ,\ y[k] = \mathbf{B}^{\mathrm{b}}[k] + R[k]^{\top}{\mathbf{B}^{\mathrm{n}}}_{\mathrm{pli}}[k]\ , \tag{4.29}$$

with an input $u[k]$ corresponding to the discrete-time versions of $\boldsymbol{\omega}^{\mathrm{b/n}}$, $\boldsymbol{\gamma}^{\mathrm{b}}$, $\nabla\mathbf{B}^{\mathrm{b}}$, and with a dynamic model of the form Eq. (4.2). The discrete-time variable $\mathbf{B}^{\mathrm{b}}[k]$ is chosen in order to accurately model the magnetic measurement process, and the discrete-time model is written accordingly.

4.4.3. EKF implementation

An error representation is chosen such that the implemented algorithm is an MEKF, that is to say, the attitude error parameterization is multiplicative,

$$\tilde{x}[k] \doteq \begin{pmatrix} \widetilde{\mathbf{B}}^{\mathrm{b}}[k] \\ \tilde{\mathbf{v}}^{\mathrm{b}}[k] \\ \tilde{\Phi}[k] \\ \widetilde{\mathbf{B}}^{\mathrm{n}}_{\mathrm{pli}}[k] \\ \widetilde{\mathbf{B}}^{\mathrm{n}}_{\mathrm{pli}}[k-1] \\ \widetilde{\mathbf{M}}^{\mathrm{n}}[k] \end{pmatrix}, \ \xi(\hat{x}[k], \tilde{x}[k]) \doteq \begin{pmatrix} \widehat{\mathbf{B}}^{\mathrm{b}}[k] + \widetilde{\mathbf{B}}^{\mathrm{b}}[k] \\ \hat{\mathbf{v}}^{\mathrm{b}}[k] + \tilde{\mathbf{v}}^{\mathrm{b}}[k] \\ \exp\left[\tilde{\Phi}[k]\times\right] \hat{R}[k] \\ \widehat{\mathbf{B}}^{\mathrm{n}}_{\mathrm{pli}}[k] + \widetilde{\mathbf{B}}^{\mathrm{n}}_{\mathrm{pli}}[k] \\ \widehat{\mathbf{B}}^{\mathrm{n}}_{\mathrm{pli}}[k-1] + \widetilde{\mathbf{B}}^{\mathrm{n}}_{\mathrm{pli}}[k-1] \\ \widehat{\mathbf{M}}^{\mathrm{n}}[k] + \widetilde{\mathbf{M}}^{\mathrm{n}}[k] \end{pmatrix}.$$

The derivation of the linearized system and the tuning of the EKF are not detailed here.

Remark In practice, the attitude matrices $\exp\left[\tilde{\Phi}[k]\times\right]$ and $R[k]$ are numerically represented by associated unit quaternions, using formulas similar to those used for rotation matrices.[5].

4.4.4. Evaluation on indoor closed path

Choice of criterion In indoor dead-recknoning, the variable of interest is the position $\mathbf{M}^{\mathrm{n}}$. Therefore, in indoor experimental performance evaluation, the quality of position estimates needs to be evaluated, although in the model formed by Eqs. (4.21)-(4.26), it can be shown that heading and the position $\mathbf{M}^{\mathrm{n}}$ are not observable. Both estimates are then initialized arbitrarily at the start of each experiment, and a criterion is chosen that is mainly sensitive to estimation drift, and not to an absolute positioning error which would be meaningless without precise knowledge of the starting point and initial heading.

Let us recall the discussion in Sec. 3.4.2, that velocity errors are preferably expressed as relative errors, see Eq. (3.46). In light of this discussion, let us denote $s[k]$ the estimated traveled distance at time-step k,

$$s[k+1] \doteq s[k] + \left\| \widehat{\mathbf{M}}^{\mathrm{n}}[k+1] - \widehat{\mathbf{M}}^{\mathrm{n}}[k] \right\| , \tag{4.30}$$

---

[5] Ref. Chesneau et al. [2016], however, describes an EKF where attitude is simply represented by a unit quaternion without mentioning an error representation such as in Sec. 4.3.1

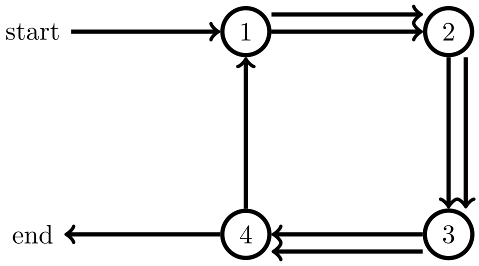

Figure 4.1: Sketch of a closed path benchmark trajectory with 4 landmarks and two cycles.

with $s[0] \doteq 0$. Whenever in reality the path is closed, that is to say, $\|\mathbf{M}^{\mathrm{n}}[k] - \mathbf{M}^{\mathrm{n}}[k_0]\| = 0$ between two time-steps k_0 and $k > k_0$, the (dimensionless) drifting error can be defined as

$$\epsilon[k, k_0] = \frac{\left\|\widehat{\mathbf{M}}^{\mathrm{n}}[k] - \widehat{\mathbf{M}}^{\mathrm{n}}[k_0]\right\|}{s[k] - s[k_0]} \ . \tag{4.31}$$

Criticism of the criterion It is important to remark that from a probabilistic point of view, Eqs. (4.30) and (4.31) do not make any sense. The sequence of $\widehat{\mathbf{M}}^{\mathrm{n}}[k]$ is causal; $\widehat{\mathbf{M}}^{\mathrm{n}}[k]$ is defined as the most probable position at time-step k knowing all measurements only in its past, up to time-step k only. Thus, computing $s[k]$ leads to an incoherent use of information. Instead, it would be appropriate to compute $s[k]$ on the output of a *smoothing* algorithm providing each position with the knowledge of all measurements until the end of the trajectory. The sequence of positions from which the criterion is computed would then be deduced from the same information. Moreover, periodic disturbances that may cause oscillations in $\widehat{\mathbf{M}}^{\mathrm{n}}[k]$ may lead to an overestimation of traveled distance, causing optimistic results. Finally, small closed paths are less sensitive to heading drift than long straight lines.

Experiments The protocol consists in choosing more or less than four landmarks in SYSNAV's office, and doing several cycles through them, see Fig. 4.1. Most experiments are performed by "neutral" colleagues in SYSNAV, who did not take part in designing the navigation algorithms. Some of the resulting trajectories are reproduced in Fig. 4.2 from Ref. Chesneau et al. [2016]. The overall computed relative drift errors on 18 benchmark trajectories done by 13 different persons are reproduced in an histogram Fig. 4.3. Computable relative drift errors all lay between 0.13% and 3.3% of the travelled distance, the majority laying under 2%, which is a level of performance which used to be comparable with pedestrian dead-reckoning systems (see Refs. Jiménez et al. [2009], Nilsson et al. [2010]). In light of the conclusions of Chapters 2 and 3, these are encouraging results.

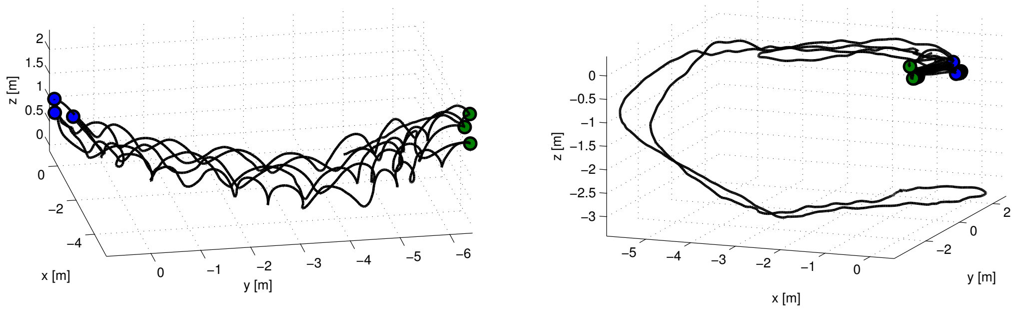

(a) Relative drift errors lay between 0.89 and 1.79% (b) Relative drift errors lay between 0.28 and 2.84%

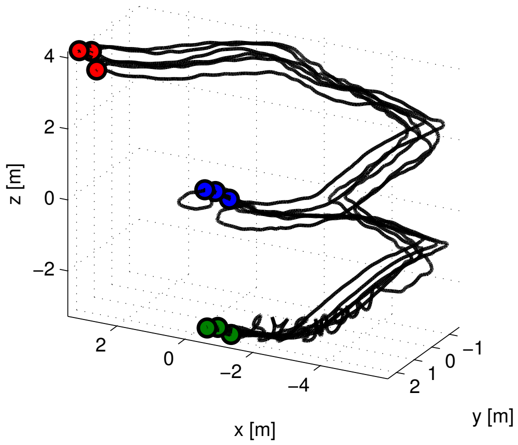

(c) Relative drift errors lay between 0.57 and 0.79%

Figure 4.2: From Ref. Chesneau et al. [2016], examples of computed benchmark trajectories

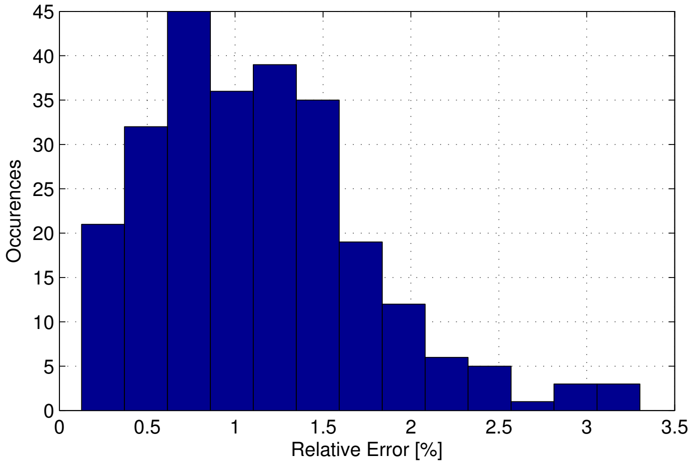

Figure 4.3: From Ref. Chesneau et al. [2016], experimental closed path relative error occurrences

Conclusion Compared with results from Ref. Dorveaux [2011], the obtained long-distance performance is similarly a few percents of the total traveled distance. Thus, the EKF has not improved this particular situation. However, the noticeable difference is that the short-term performance allows a much more accurate reconstruction of the path, as can be seen in Fig. 4.2c, where the word "SYSNAV" was drawn in the middle of the trajectory with the sensor board.[6] Writing the problem as one of strapdown inertial navigation has removed the issue of convergence speed that existed on accelerated trajectories with the previous bi-independent-observer architecture.

4.4.5. Evaluation in motion capture experiments

The evaluation method in Sec. 4.4.4 suffers from several disadvantages.

- The experimental protocol does not allow any precise evaluation of the estimation accuracy of the observable states;
- No absolute comparison is possible using the trajectory itself as a reference.

To solve this problem, an evaluation was undertaken using the optical tracking equipment of GIPSA-lab, in Grenoble, see Fig. 4.4.

Comparison method with an optical tracking system

Frames of reference A *direct* comparison of a trajectory with the output of an optical tracking equipment is not meaningful. Each calibration of this equipment defines an

---

[6] A synchronized video demonstration is also available here: `https://youtu.be/lnDEXiztIUk`, August 2018

(a) Picture of the VICON equipment in GIPSA-lab

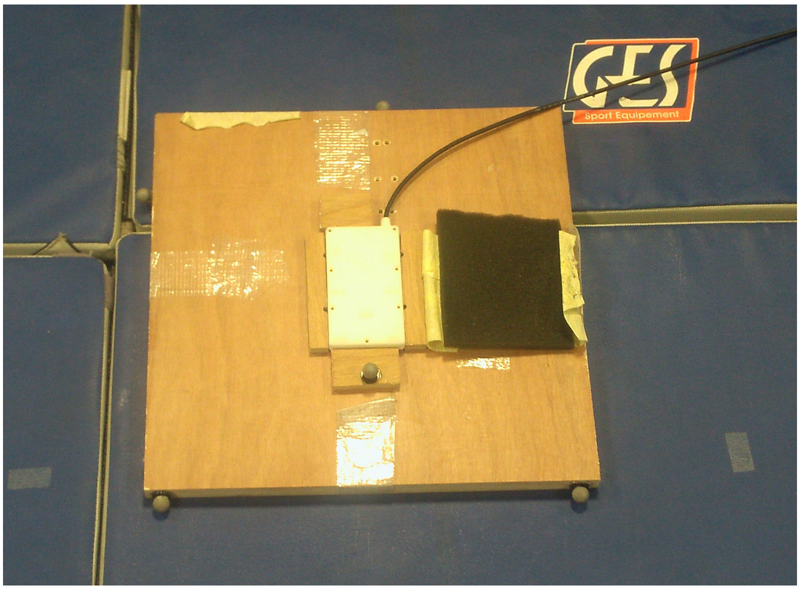

(b) Picture of the sensor board, on a 40cm x 40cm wooden board, with markers. The self-locking cable binders securing the sensor board are removed for the picture.

Figure 4.4: Optical tracking setup in GIPSA-lab, Grenoble

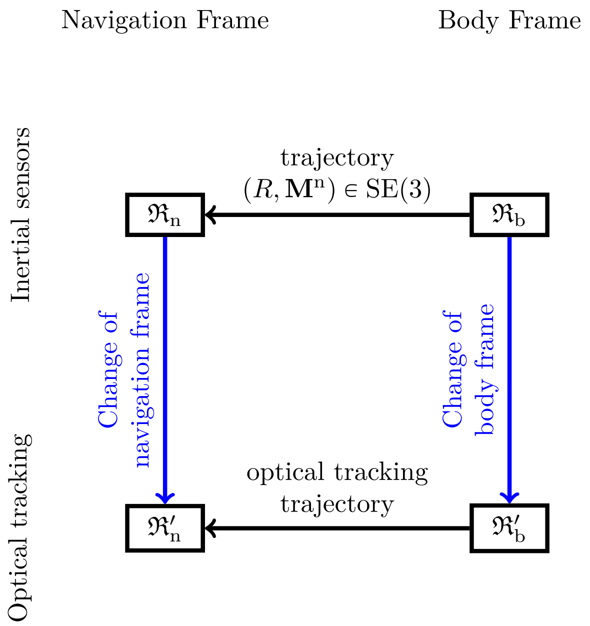

Figure 4.5: Reference frames of interest when comparing a trajectory with an optical tracking system

optical navigation frame $\mathfrak{R}'_{\mathrm{n}}$. Each assembling of markers defines an optical body frame $\mathfrak{R}'_{\mathrm{b}}$ associated with the relative position of markers. The trajectory that is provided by the optical tracking system is none other than the change of frame between $\mathfrak{R}'_{\mathrm{n}}$ and $\mathfrak{R}'_{\mathrm{b}}$ (see Fig. 4.5), while the trajectory that is computed using strapdown inertial and magnetic sensors corresponds to the change of frame between two different reference frames $\mathfrak{R}_{\mathrm{n}}$ and $\mathfrak{R}_{\mathrm{b}}$. Moreover, each trajectory is computed using a different time reference. Comparing the two trajectories requires at least the identification of the changes of frame between $\mathfrak{R}_{\mathrm{n}}$ and $\mathfrak{R}'_{\mathrm{n}}$, between $\mathfrak{R}_{\mathrm{b}}$ and $\mathfrak{R}'_{\mathrm{b}}$, and between the two time references. Once this identification is made, the trajectories can be compared by, for example, interpolating one trajectory on the sampling times of the other trajectory.

Velocity and attitude estimates Since optical tracking does not provide any velocity estimate, it is also necessary to deduce one from optical tracking. The VICON optical tracking system used in GIPSA-lab samples at 500Hz, with sub-millimeter accuracy, notwithstanding the occasional loss of tracking caused by temporary camera masking. Therefore, computing a velocity by direct differentiation results in an unacceptably high level of noise (A few cm/s up to 10-20cm/s).

This is why a partial identification of the changes of frame and time reference is proposed, with a smoothing of optical tracking outputs exploiting inertial sensor outputs and taking inertial sensor biases into account. The estimated trajectory of the accelerometer is then used as a reference. The smoothing algorithm consists of

1. The synchronization of the two datasets using attitude and gyrometer data, followed by the estimation of the rotation matrix $R_{\mathrm{b}' \leftarrow \mathrm{b}}$
2. The unified maximum likelihood estimation of the sequence of positions, attitudes, velocities and inertial sensor biases, along with the accelerometers' percussion point and the gravity vector and dataset synchronization parameters.

This smoothing algorithm has been improved and used in Ch. 6.

The attitude output of the VICON optical tracking system is deduced from individual computed positions of markers. Therefore, the farther they are from each other, the more accurate attitude reconstruction can be. Hence the 40cm x 40cm wooden board illustrated in Fig. 4.4b, that allows a greater separation of markers. At this distance, the attitude ground truth provided by optical tracking should have a precision better than around $\pm 2 \times \frac{1 \text{ mm}}{40 \text{ cm}} = \pm 5$ mrad.

Corrections introduced by the smoothing algorithm are submillimetric (see Fig. 4.6a) and smaller than 3.2 mrad (see Fig. 4.6b) 99% of the time. This is consistent with the expected precision of the reference system. In the following, the ground truth is the output of the smoothing algorithm.

Environment The experimental conditions have been hostile to navigation algorithms, since

- The magnetic field gradient is close to singular in almost the entire room
- The 50Hz power-line interference caused by neighboring electrical appliances is irregular (pulsating every second)
- Experiments are designed to deliberately test some edge cases (high dynamic, high magnetic field curvature).

Overall attitude and velocity errors

Results of a trial of several minutes are described thereafter. The system is moved in circles in the room at low speed at first, then at a faster pace. Then, it is moved above a metallic stool in a cross-shaped path (see Fig. 4.7). The ground truth is computed using the above mentioned smoothing algorithm, and compared with the output of the EKF described in Sec. 4.4.2 - 4.4.3.

Attitude error Attitude errors are typically under 10 mrad, (see Fig. 4.8), lower when the system is moving (5 mrad), and higher when the system is static or whenever the first order interpolation model used for gradient computation (see Eq. (3.27)) is not valid. These results, which are close to the expected precision of the ground truth, are more than compatible with those of state-of-the-art attitude estimation algorithms using MEMS inertial sensors without relying on MIDR to compensate the effect of accelerations (see Refs. Michel et al. [2015], Makni [2016]), considering the simplicity of

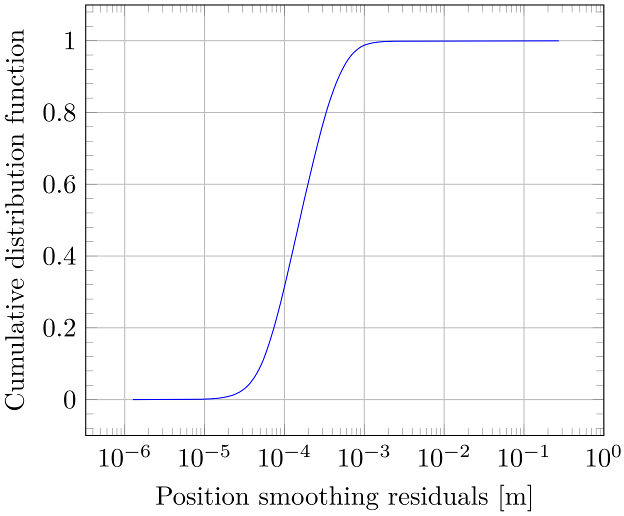

(a)

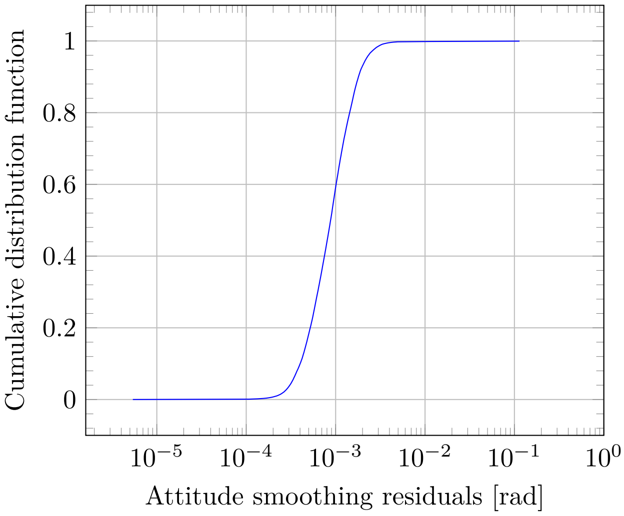

(b)

Figure 4.6: Cumulative distribution functions of smoothing residuals of motion capture data. This corresponds to the distance between smoothed and raw interpolated position estimates from the VICON optical tracking system (Fig. 4.6a), and the angle between smoothed and raw interpolated attitude estimates from the tracking system (Fig. 4.6b). After taking into account the change of frame between $\mathfrak{R}_\mathrm{b}$ and $\mathfrak{R}_{\mathrm{b}'}$, corrections introduced by the smoothing algorithm are smaller than 1 mm and 3.2 mrad, 99% of the time.

Figure 4.7: Metallic stool used during the evaluation trial with a VICON optical tracking system

the approach. According to these references, experimental error bounds obtained from these algorithms are closer to 5 degrees, one order of magnitude higher.[7] However, a fair comparison would imply implementing and running these algorithms on the same data, since a difference in experimental conditions can explain the apparent improvement such that the quality and calibration of inertial sensors, the accuracy of the reference system, or the alignment and synchronization issues that Fig. 4.5 is about. This comparison has not been made in this work.

Velocity estimation error Velocity estimates are compared in $\mathfrak{R}_b$ with the reference. During the trial, 95% of the time, velocity estimation errors are below 15 cm/s (see Fig. 4.10), which is surprisingly high considering the experimental results obtained on indoor closed path Sec. 4.4.4, or even the output trajectory (see Fig. 4.9), that display a drift of only a few meters during the 10 minutes long experiment. Errors as high as 1 m/s are visible when the system is moved close to the stool, where the first-order spatial interpolation of the magnetic field Eq. (3.28) is not valid. Let us notice that in the room in which the evaluation experiments are made, the gradient of the magnetic field is most of the time close to singular, which may explain this level of error in light of Sec. 3.4.

Effect of gyrometer biases

Gyrometer biases are not part of the state vector of the EKF currently being tested. Therefore, to evaluate their contribution to estimation errors, their approximate value is identified over the trial, and removed from data before rerunning the navigation algorithms. The result is plotted in Fig. 4.11. In the trial, errors are now most of

---

[7] 5 degrees is around 87 mrad

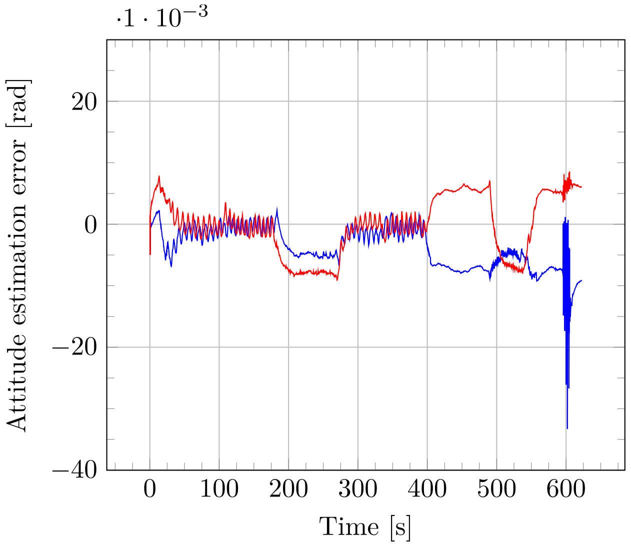

(a) Tilt errors during the evaluation experiment

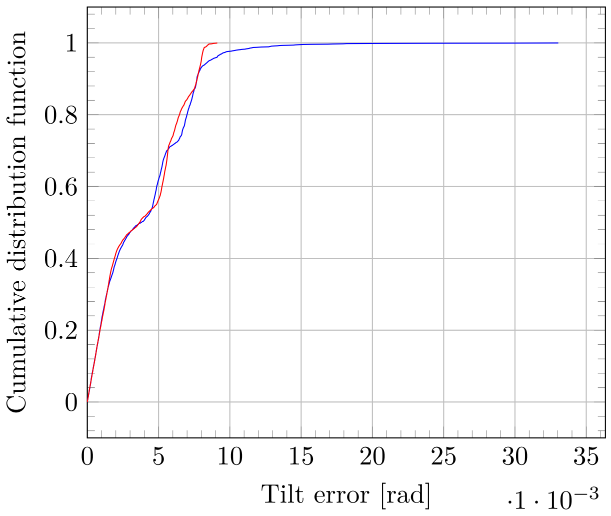

(b) Tilt errors cumulative distribution function

Figure 4.8: Experimental tilt errors of the EKF of Sec. 4.4 (or Ref. Chesneau et al. [2016]).
Each line represents a different tilt angle.
From 30 to 180s, the system is moved around at low pace, errors lay between ±5 mrad.
From 270 to 400s, the system is shaken with a high dynamic while the user tries his best at running in circles in the small volume of the room, errors lay between ±5 mrad.
From 180 to 270s and from 400 to 490s, the system is not moving. errors lay between ∓10 mrad. During the last stage, the system is moved close to the stool, whose highly curved magnetic field causes large attitude estimation errors, up to 35 mrad.

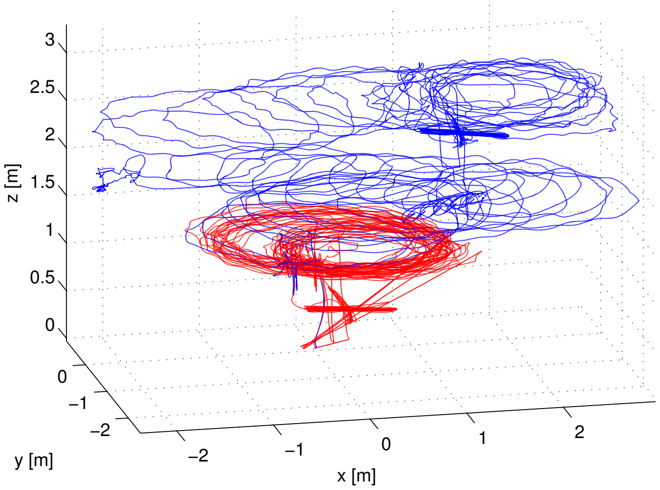

Figure 4.9: Navigation algorithm output and ground truth on the optical tracking evaluation experiment. The ground truth is in red, and computed trajectory in blue.

the time under 5 mrad even in static cases compared with 10 mrad before removing gyrometer biases. This parameter is then a major source of tilt estimation error. The observed improvement motivates online estimation of gyrometer biases (model Sec. 2.5.1).

The removal of gyrometer biases has improved the best velocity estimation performance to a few mm/s instead of a few cm/s, see Fig. 4.12.

Effect of accelerometer biases

Accelerometer biases are not part of the state vector of the EKF being tested either. Therefore, the approximate value of gyrometer and accelerometer biases are identified over the trial and removed from data before rerunning the navigation algorithms. The result is plotted in Fig. 4.13. An improvement can be observed in tilt errors, but it is comparable with the precision of the reference system. The distribution of velocity estimation errors is practically identical before and after removing accelerometer biases.

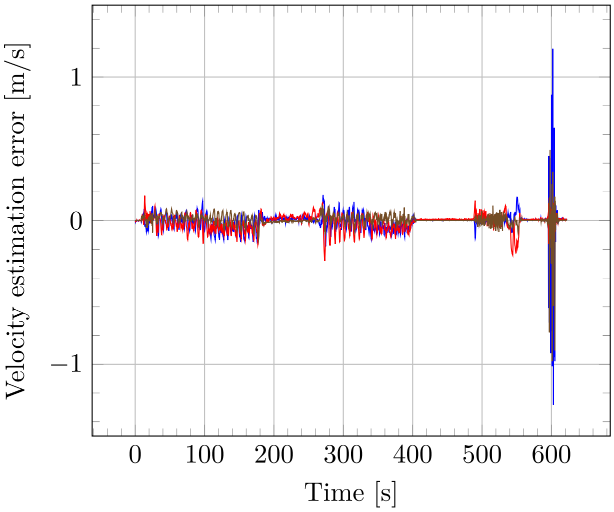

(a) Velocity estimation errors during the evaluation experiment (one line for each component). High errors around 600s correspond to movements close to the metallic stool Fig. 4.7.

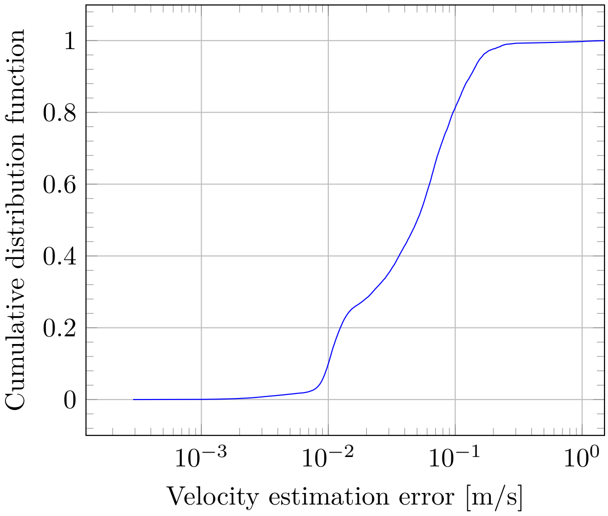

(b) Velocity estimation errors cumulative distribution function.

Figure 4.10: Velocity estimation errors of the EKF of Sec. 4.4 (or Ref. Chesneau et al. [2016])

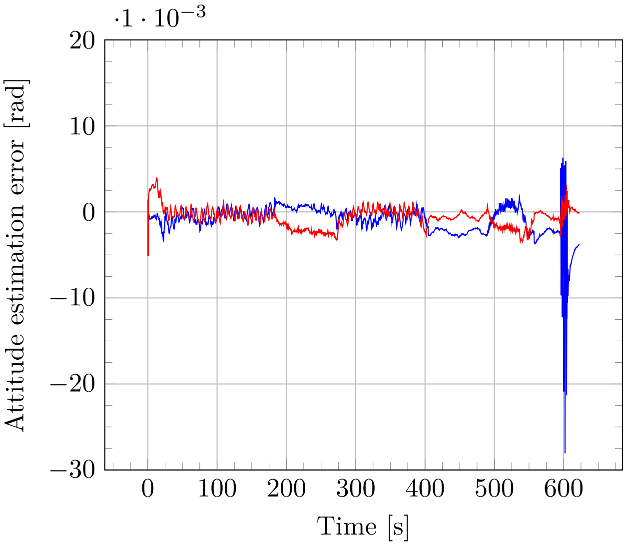

(a) Tilt errors during the evaluation experiment

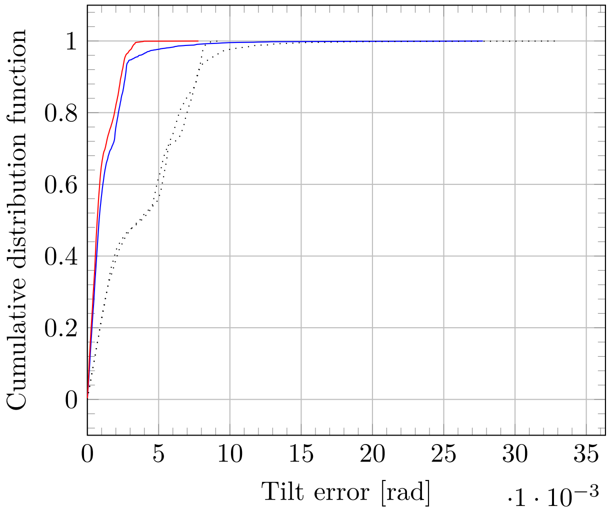

(b) Tilt errors cumulative distribution function (one line for each tilt angle)

Figure 4.11: Experimental tilt errors from Fig. 4.8 corrected for gyrometer biases. Cumulative distribution fonctions from Fig. 4.8 are reproduced in dotted lines.

Removing gyrometer biases has significantly improved the result.

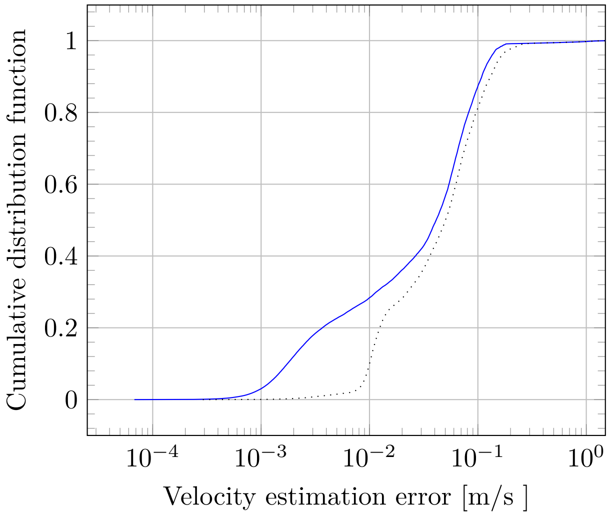

Figure 4.12: Velocity estimation errors from Fig. 4.10, corrected for gyrometer biases. Velocity estimation errors from Fig. 4.10 are reproduced in dotted line.

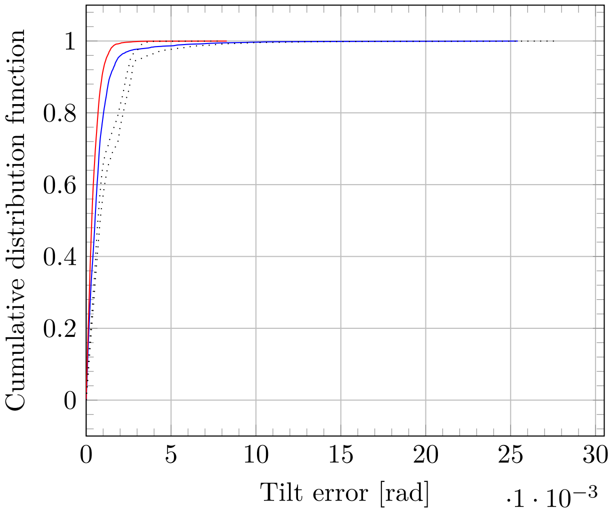

(a) Tilt estimation errors (one line for each tilt angle)

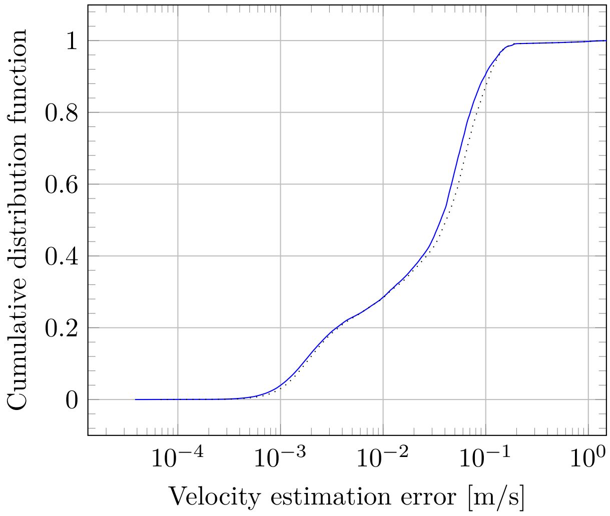

(b) Velocity estimation errors

Figure 4.13: Experimental tilt and velocity estimation errors, after removing gyrometer and accelerometer biases. Errors with only gyrometer biases removed are reproduced in dotted lines.
An improvement in attitude estimation accuracy can be observed, even though errors are already comparable with the precision of the reference system. However, the effect on velocity estimation error is insignificant.

4.4.6. Conclusion

EKF design The dynamic model described in Sec. 2.4.1 has been modified to take power-line interference into account in Sec. 4.4.2. An EKF has been designed in order to estimate the trajectory in an arbitrary navigation frame, and the performance of the resulting navigation algorithm has been evaluated in experiments.

Closed path performance The obtained error in closed-path is typically under 3% of the traveled distance in SYSNAV's office. In motion capture experiments, tilt errors have been evaluated to be under 10 mrad except in situations where the spatial gradient of the magnetic field is not constant enough for the spatial interpolation model (high curvature). Velocity estimation errors seem to be between 1 cm/s and 15 cm/s in high dynamic conditions and can be higher in high curvature situations.

Motion capture experiments The main sources of tilt estimation errors have been identified to be mainly gyrometer bias, with accelerometer bias seemingly playing a minor role. Removing inertial sensor biases improves the best performance, typically when the system is not moving, but do little to reduce velocity errors in high dynamic or singular gradient conditions. It is suspected that the cause of this level of error is simply the use of Eq. (2.11), the central equation of MIDR, in close to singular gradient conditions. Such difficulties have been anticipated in Sec. 3.4.2 in relationship with calibration errors. However, this equation is what the observer relies upon in order to observe the velocity.

Possible improvements Although this has not been shown, all motion capture experiments display a heading drift, which is normal since heading is not observable in the underlying model. In Sec. 4.5, another observer is proposed, aiming at solving this issue, along with the estimation of gyrometer and accelerometer biases which have been identified as sources of errors. Calibration errors will be addressed in Part. II.

4.5. Heading estimation, inertial sensor biases, and disturbances

4.5.1. Motivation

Inertial sensor biases In Sec. 4.4.5 it has been made apparent in experiments that inertial sensor biases are significant causes of attitude and velocity estimation error in MIDR. This difficulty has been anticipated in a previous chapter, Sec. 2.5, by including gyrometer and accelerometer biases into the dynamic model; doing so may help reducing trajectory estimation error, under the condition that biases are observable. However, a set of trajectories has been exhibited for which this is not the case.

Heading Heading is unobservable in all of the previously considered non-rotating Earth models. This implies an inevitable drift, which is worsened by gyrometer biases. This issue is already a significant source of positioning error in indoor pedestrian dead-reckoning with low-cost MEMS sensors and motivates various solutions of the state of the art. Some of them rely on the magnetic field (see Refs. Faulkner et al. [2010], Afzal et al. [2011b]), while other approaches rely on assumptions about the shape of the building, that is to say its dominant directions (see Refs. Borenstein and Ojeda [2010], Abdulrahim et al. [2010], Jiménez et al. [2011], Jiménez et al. [2012]). The magnitude of magnetic disturbances in indoor environments (quite often, a magnetic compass will show ±50° of error, and sometimes an utterly incoherent value) is a valid reason not to use the magnetic field at all. Alternatively, it is also possible to use map-matching algorithms in environments where all obstacles or paths are known, an apparent practical difficulty being how to deal with the obsolescence of mapping information. The goal, here, is to prevent heading from drifting without using any map.

Computing-power requirements Requirements include being able to compute heading using a recursive, lightweight and generic algorithm capable of being run on a microcontroller with an FPU inside of the operation unit (Fig. 3.1b p. 35). Therefore, it was deemed necessary to provide a recursive heading estimator. These requirements leave very little freedom except using the magnetic field.

The starting point of the following work[8] is the EKF described in Sec. 4.4.[9]

---

[8] The following work presents an updated version of what has already been published in Ref. Chesneau et al. [2017]regarding these issues of gyrometer and accelerometer estimation and heading computation.

[9] Sec. 4.4 presents an updated version of what has already been published in Ref. Chesneau et al. [2016]

4.5.2. Inertial sensor biases

Let us consider that accelerometer and gyrometer measurements are biased according to Eqs. (2.38)-(2.39),

$$\begin{aligned}\boldsymbol{\gamma}_{\mathrm{meas}} &\doteq \boldsymbol{\gamma}^{\mathrm{b}} + \mathbf{b}_{\gamma}\\ \boldsymbol{\omega}_{\mathrm{meas}} &\doteq \boldsymbol{\omega}^{\mathrm{b/n}} + \mathbf{b}_{\omega},\end{aligned}$$

The dynamic model of accelerometer and gyrometer biases from Eq. (2.43) and (2.44) is replaced by

$$\frac{d\mathbf{b}_{\gamma}}{dt} \approx -\frac{\mathbf{b}_{\gamma}}{\tau_{\mathbf{b}_{\gamma}}}\ , \tag{4.32}$$

$$\frac{d\mathbf{b}_{\omega}}{dt} \approx -\frac{\mathbf{b}_{\omega}}{\tau_{\mathbf{b}_{\omega}}}\ , \tag{4.33}$$

where $\tau_{\mathbf{b}_{\gamma}} > 0$ and $\tau_{\mathbf{b}_{\omega}} > 0$ are two time constants. This model ensures that inertial sensor biases are at least detectable, if not observable because this is a stable model. Thus, in the absence of external information, the “best guess” for biases is zero with some uncertainty.

4.5.3. Magnetic field instationarity

We assumed in Ch. 2 a magnetic field stationary in the navigation frame. In Sec. 4.4.2, the total magnetic field has been modeled as the sum of a stationary magnetic field and a homogeneous power-line interference of known frequency (In Europe, 50Hz).

Let us drop the assumption of a stationary magnetic field, and replace it with an assumption on its spectrum. The resulting model reads

$$\frac{d\mathbf{B}^{\mathrm{b}}}{dt} \approx -(\boldsymbol{\omega}_{\mathrm{meas}} - \mathbf{b}_{\omega}) \times \mathbf{B}^{\mathrm{b}} + \nabla\mathbf{B}^{\mathrm{b}}\left[\mathbf{v}^{\mathrm{b}} + (\boldsymbol{\omega}_{\mathrm{meas}} - \mathbf{b}_{\omega}) \times \overrightarrow{\mathbf{M}^{\mathrm{b}}\mathbf{N}^{\mathrm{b}}}\right] + R^{\top}{\mathbf{B}_{\mathrm{p}}}^{\mathrm{n}} \tag{4.34}$$

$$\frac{d{\mathbf{B}_{\mathrm{p}}}^{\mathrm{n}}}{dt} \approx -\frac{{\mathbf{B}_{\mathrm{p}}}^{\mathrm{n}}}{\tau_{\mathbf{B}_{\mathrm{p}}}} \tag{4.35}$$

$$\frac{d^2{\mathbf{B}^{\mathrm{n}}}_{\mathrm{pli}}}{dt^2} \approx -\omega_{\mathrm{pli}}^2{\mathbf{B}^{\mathrm{n}}}_{\mathrm{pli}} \tag{4.36}$$

$$y_{\mathbf{B}} \approx \mathbf{B}^{\mathrm{b}} + R^{\top}{\mathbf{B}^{\mathrm{n}}}_{\mathrm{pli}}\ . \tag{4.37}$$

Eqs. (4.34)-(4.35) mean that the typical settling time of a (detectable) magnetic instationarity is $\tau_{\mathbf{B}_{\mathrm{p}}}$, while the total measured field accounts for an additive power-line interference ${\mathbf{B}^{\mathrm{n}}}_{\mathrm{pli}}$ of pulsation ω_{pli} that is homogeneous in the navigation frame. This model allows a better rejection of lower frequency disturbances.

4.5.4. Recursive magnetic field-based heading estimation model

In all of the previously considered non-rotating Earth models, the heading is unobservable. All of them are invariant with respect to a change of heading. Therefore, heading drift is inevitable with these models.

Our goal is to prevent the heading from drifting by using a recursive algorithm running on a microcontroller with an FPU. One way to achieve this result is to modify the dynamic model in a way that breaks the problematic symmetry. With low-cost gyrometers, there is not much choice except relying on the magnetic field.

First, how this can be done without disturbances is discussed. Then, it is shown that with disturbances, this approach is unusable, and a model is proposed in order to solve the magnetic heading estimation problem. Finally, the tuning of the resulting observer is explained, first in one dimension, then in 3 dimensions.

Without disturbances

Pure heading estimation with a Kalman filter is a rather straightforward problem. In discrete-time, this leads to the one-state, one measurement model of the form:

$$\psi[k+1] \approx \psi[k] + \Delta\psi[k] \tag{4.38}$$

$$y_\psi[k] \approx \psi[k] \tag{4.39}$$

where $\psi[k]$ represents the heading at time-step k, $\Delta\psi[k] \approx \psi[k+1] - \psi[k]$ its variation between time-steps k and $k+1$ that can be typically estimated from gyrometer measurements, and $y_\psi[k]$ a noisy measurement of heading, using for example the horizontal projection of the magnetic field as a heading reference.

With disturbances

In our case, heading measurement is affected by spatially correlated disturbances from magnetic materials in the environment. Illustrating the issue, a first try at modeling the dynamics of the disturbance to

$$\psi_\mathrm{d}[k+1] \approx \psi_\mathrm{d}[k] + u[k] \ , \tag{4.40}$$

where $\psi_\mathrm{d}[k]$ denotes the magnetic heading disturbance at time-step k, and where an approximate value of $u[k]$ is assumed to be be provided by an external mean. The heading measurement is redefined as,

$$y_\psi[k] \approx \psi[k] + \psi_\mathrm{d}[k] \ , \tag{4.41}$$

where ψ_d is the disturbance. Because $u[k]$ is the variation of the magnetic heading disturbance between time-steps k and $k+1$, its value can be predicted with an approximate value of the velocity and the gradient of the magnetic field by using a discrete-time version of Eq. (2.11) p. 17 (This is done explicitly in Eq. (4.77) p. 110). However, the model formed by Eqs. (4.38), (4.40) and (4.41) is unobservable, because it shares the same structural problem as all of the non-rotating earth MIDR models that have previously been defined. The problem is obvious even without using Kalman's criterion for observability, by considering the following change of variables,

$$
\begin{aligned}
x_1[k] &\doteq \psi[k] + \psi_{\mathrm{d}}[k] \ , && (4.42)\\
x_2[k] &\doteq \psi[k] - \psi_{\mathrm{d}}[k] \ , && (4.43)\\
u_1[k] &\doteq \Delta\psi[k] + u[k] \ , && (4.44)\\
u_2[k] &\doteq \Delta\psi[k] - u[k] \ , && (4.45)
\end{aligned}
$$

which yields the equivalent state-space model,

$$
\begin{aligned}
x_1[k+1] &\approx x_1[k] + u_1[k] && (4.46)\\
x_2[k+1] &\approx x_2[k] + u_2[k] && (4.47)\\
y_\psi[k] &\approx x_1[k] \ . && (4.48)
\end{aligned}
$$

The variable x_2 evolves independently from x_1 and the output, so recovering information on x_2 is impossible. By noticing that

$$\psi[k] = \frac{1}{2}\left(x_1[k] + x_2[k]\right) \ ,$$

it is clear that recovering the heading is impossible with this model. Therefore, another model that breaks the problematic symmetry is needed.

The issue

Let us consider the problem of heading estimation from a disturbed magnetic field from a Bayesian filtering viewpoint. What is needed is a model that captures

- Correlations between magnetic heading disturbances the system is subjected to;
- Prior information about the magnitude of the local magnetic disturbance.

Gyrometers provide variations of heading between successive time-steps. If the velocity is known, variations of disturbances between successive time-steps can be inferred from the primary equation of MIDR, Eq. (2.11), but the actual value of magnetic disturbances depends mainly on position with regularity conditions dictated by the laws of physics.

The structure of the inference problem can be modeled as a Bayesian network as depicted in Fig. 4.14. Without the "disturbance model" $\mathcal{D}$, this is the above-mentioned unobservable system. The "disturbance model" must provide prior information on the amplitude and/or value of $\psi_{\mathrm{d}}[l]$, $l \leqslant k$, and should be able to reproduce spatial correlations. It can be built, for example, by using Gaussian processes (see, e.g., Refs. Wahlström et al. [2013], Kok and Solin [2018], that propose the use of this type of model for magnetic Simultaneous Localization and Mapping (SLAM)), or parametric models. However, this would not conform to the design constraint of using solely an EKF, nor does it seem to be tractable on a microcontroller with an FPU, which prevents us from benefiting from this area of work. The structure that would fit

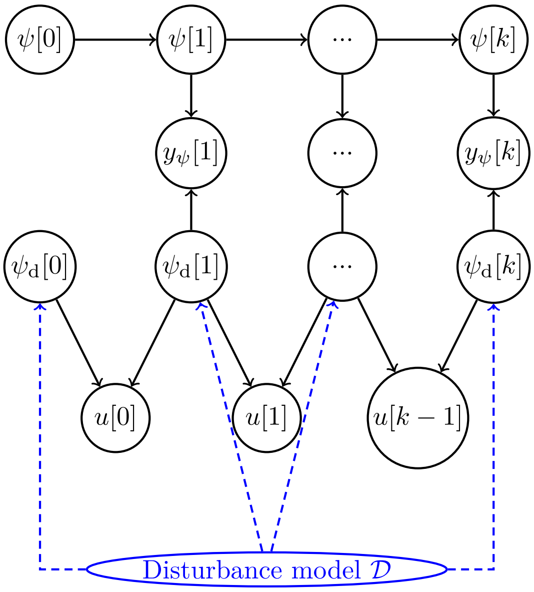

Figure 4.14: Structure of the magnetic heading computation problem seen as a Bayesian network.
The sequence $\psi[l]$, $l \leqslant k$ representing the heading variable can be interpreted as a Markov chain. The sequence $\psi_\mathrm{d}[l]$, $l \leqslant k$ representing the disturbance is not, strictly speaking, a Markov chain, but realizations in space of a "disturbance model" $\mathcal{D}$. The input $u[k]$ connects its successive values, thanks to the gradient of the magnetic field. Without $\mathcal{D}$, the heading is unobservable. With an accurate disturbance model, to fit into a recursive scheme, $\mathcal{D}$ would need to be represented by, e.g., a state variable.

a recursive algorithm is described in, e.g., Ref. Barker et al. [1995], as a Markov Chain. With a Kalman filter, this would lead to making $\mathcal{D}$ a parametric model whose parameters would then be carried with the state vector, or lead to use a non-parametric model in a finite-horizon observer for example.

In order to respect the design constraints, the proposed solution is to give up entirely on a "disturbance model" $\mathcal{D}$ that would take spatial correlations into account properly, and to rely only on $u[l],\ l < k$ to model them. More formally, the assumption is that

$$p(\psi_\mathrm{d}[0], \psi_\mathrm{d}[1], ..., \psi_\mathrm{d}[k] \mid \mathcal{D}) = \prod_{l=0}^{k} p(\psi_\mathrm{d}[l] \mid \mathcal{D}) \ . \tag{4.49}$$

The advantage of doing so is that it will avoid increasing the dimension of the state-space model by too much, resulting in a tractable problem. The disadvantage is that for example, on periodic movements, one will fail to model correlations between magnetic disturbances from each loop, because the fact that the disturbance has already been seen will be forgotten.

Proposed model

To fit into a Kalman filtering scheme, let us consider the graph in Fig. 4.14, and find an appropriate state-space model. The followed method is to express a probabilistic discrete-time model in a form close to the one described Ref. Barker et al. [1995]. Let us represent a state-vector at time-step k

$$x[k] \doteq \begin{pmatrix} \psi[k] \\ \psi_\mathrm{d}[k] \end{pmatrix} \ . \tag{4.50}$$

Let us denote

$$X[k] \doteq \{x[0], ..., x[k]\} \tag{4.51}$$

$$U[k] \doteq \{u[0], ..., u[k]\} \tag{4.52}$$

$$Y_\psi[k] \doteq \{y_\psi[1], ..., y_\psi[k]\} \ , \tag{4.53}$$

and denote the estimate at time-step k

$$\hat{x}[k] \doteq \begin{pmatrix} \hat{\psi}[k] \\ \hat{\psi}_\mathrm{d}[k] \end{pmatrix} \ , \tag{4.54}$$

such that the recursively estimated state be

$$p(x[k] \mid Y[k], U[k-1], \mathcal{D}) = \mathcal{N}\left(\hat{x}[k], \Sigma[k]\right) \ , \tag{4.55}$$

with $\Sigma[k]$ denoting a corresponding covariance matrix. Let us derive a prediction model

$$p(x[k+1] \mid Y[k], U[k], \mathcal{D}, X[k]) \ , \tag{4.56}$$

with the following assumptions,

$$p(u[k] \mid \psi_{\mathrm{d}}[k+1], \psi_{\mathrm{d}}[k]) = \mathcal{N}\left(\psi_{\mathrm{d}}[k+1] - \psi_{\mathrm{d}}[k], \sigma_u[k]^2\right) \ , \tag{4.57}$$

and

$$p(\psi_{\mathrm{d}}[k] \mid \mathcal{D}) = \mathcal{N}(0, a[k]^2) \ , \tag{4.58}$$

where $\sigma_u[k]^2$ and $a[k]^2$ denote the respective variances of these two normal distributions. On the one hand, we have the Bayes identity

$$\begin{aligned} &p(\psi_{\mathrm{d}}[k+1], Y[k], U[k], \mathcal{D}, X[k]) \\ &\qquad = p(\psi_{\mathrm{d}}[k+1] \mid Y[k], U[k], \mathcal{D}, X[k]) p(Y[k], U[k], \mathcal{D}, X[k]) \ . \end{aligned} \tag{4.59}$$

On the other hand, we have the Bayes identity

$$\begin{aligned} &p(\psi_{\mathrm{d}}[k+1], Y[k], U[k], \mathcal{D}, X[k]) \\ &\qquad = p(u[k] \mid \psi_{\mathrm{d}}[k+1], Y[k], U[k-1], \mathcal{D}, X[k]) \\ &\qquad\quad p(\psi_{\mathrm{d}}[k+1] \mid Y[k], U[k-1], \mathcal{D}, X[k]) \\ &\qquad\qquad p(Y[k], U[k-1], \mathcal{D}, X[k]) \ . \end{aligned} \tag{4.60}$$

Let us introduce the inverse variance

$$\lambda[k]^2 \doteq \left(\frac{1}{\sigma_u[k]^2} + \frac{1}{a[k+1]^2}\right) \ , \tag{4.61}$$

and the correlation coefficient

$$\alpha[k] \doteq \frac{1}{\left(1 + \frac{\sigma_u[k]^2}{a[k+1]^2}\right)} = 1 - \frac{\sigma_u[k]^2}{a[k+1]^2 + \sigma_u[k]^2} = \frac{1/\lambda[k]^2}{\sigma_u[k]^2} \ . \tag{4.62}$$

Combining Eqs. (4.59) and (4.60) and simplifying the result yields

$$\begin{aligned} &p(\psi_{\mathrm{d}}[k+1] \mid Y[k], U[k], \mathcal{D}, X[k]) \\ &\quad \propto p(u[k] \mid \psi_{\mathrm{d}}[k+1], \psi_{\mathrm{d}}[k]) \ p(\psi_{\mathrm{d}}[k+1] \mid \mathcal{D}) \qquad \text{(Bayes' rule)} \\ &\quad \propto \exp\left(\frac{(\psi_{\mathrm{d}}[k+1] - \psi_{\mathrm{d}}[k] - u[k])^2}{\sigma_u[k]^2}\right) \exp\left(\frac{\psi_{\mathrm{d}}[k+1]^2}{a[k+1]^2}\right) \quad \text{(Eqs. (4.57) and (4.58))} \\ &\quad \propto \exp\left[\lambda[k]^2 \left(\psi_{\mathrm{d}}[k+1]^2 - 2\alpha[k]\psi_{\mathrm{d}}[k+1](\psi_{\mathrm{d}}[k] + u[k]) + \alpha[k](\psi_{\mathrm{d}}[k] + u[k])^2\right)\right] \\ &\quad \propto \exp\left[\lambda[k]^2 \left(\psi_{\mathrm{d}}[k+1] - \alpha[k](\psi_{\mathrm{d}}[k] + u[k])\right)^2\right] \\ &\quad \propto \mathcal{N}\left(\alpha[k]\left(\psi_{\mathrm{d}}[k] + u[k]\right), 1/\lambda[k]^2\right) \ . \end{aligned} \tag{4.63}$$

Therefore, the following state-space model is obtained

$$\begin{cases} \psi[k+1] = \psi[k] + \Delta\psi[k] + \eta_\psi[k] & (4.64) \\ \psi_{\mathrm{d}}[k+1] = \alpha[k]\left(\psi_{\mathrm{d}}[k] + u[k]\right) + \eta_{\psi_{\mathrm{d}}}[k] & (4.65) \\ y_\psi[k] \approx \psi[k] + \psi_{\mathrm{d}}[k] \ , & (4.66) \end{cases}$$

where $\eta_{\psi_\mathrm{d}}[k]$ represents zero-mean random Gaussian variable of variance $1/\lambda[k]^2$.

The resulting disturbance model we end up with is an autoregressive process of order 1 with normal errors, which is the introductory example in Ref. [Rue and Held, 2005, Sec. 1.1.1], and possibly one of the most straightforward Gaussian processes that can be dealt with recursively.

By construction, $0 \leqslant \alpha[k] \leqslant 1$. As long as $\alpha[k]$ is not identically 0 or 1, the system is now observable. The behavior of a steady-state Kalman filter on this model would be the separation of higher frequencies of y_ψ into ψ_d and of lower frequencies into ψ. The parameter $\alpha[k]$ can be chosen by using Eq. (4.62), such that now, we have a constructive method to tune a Kalman filter that solves the heading estimation problem.

Tuning

Tuning parameters are computed using the following heuristics. The variable $\sigma_u[k]$ is chosen such that

$$\sigma_u[k] \propto \|\mathbf{v}[k]\| \ , \tag{4.67}$$

in order to model a spatial regularity condition[10], and $a[k]$ models the expected magnitude of the local disturbance, in a way that is discussed later on. This scheme is illustrated in Fig. 4.15, where $u[k]$ is deduced from the gradient of the magnetic field and the current velocity $\mathbf{v}[k]$ with the help of Eq. (2.11).

The case $\alpha[k] = 0$ reduces to the classical Attitude and Heading Reference System (AHRS) model, represented by Eqs. (4.38)-(4.39). The case where $\alpha[k]$ is close to 1 corresponds to $\sigma_u[k]^2$, or $\|\mathbf{v}\|$, close to 0, for which $\eta_{\psi_\mathrm{d}}[k] \approx 0$. If gyrometer biases were also modeled in this one-dimensional case, the behavior of such a model would be comparable to the quasi-static field approach (see Ref. Afzal et al. [2011b]).

Let us remark that, if $\sigma_u[k]^2 \ll a[k]^2$,

$$\alpha[k] \approx 1 - \frac{\sigma_u[k]^2}{a[k]^2} \ , \tag{4.68}$$

approximation which does not ensure that $0 \leqslant \alpha[k] \leqslant 1$.

The magnetic gradient as a variable of interest

This section reproduces Ref. [Chesneau et al., 2017, Sec. II.D]

In practice, tuning $\sigma_u[k]$ may lead to a static proportionality coefficient with respect to velocity. However, tuning $a[k]$ reveals slightly more problematic. A small value leads to a faster convergence but poor disturbance rejection, while a high value leads to poor convergence rates but good disturbance rejection with respect to magnetic disturbances. A heuristic would be useful in order to choose a pertinent tuning for

---

[10] In fact, should one consistently model the disturbance as a *spatial* first-order autoregressive process, a more logical choice would ignore $u[k]$, and ensure that $\log(\alpha[k]) \propto -\|\mathbf{v}\|$. Instead, for small velocities the choice of Eq. (4.67) leads to $\log(\alpha[k]) \propto -\|\mathbf{v}\|^2$, which is closer to a second-order spatial autoregressive process. This choice is motivated by the predictability of $u[k]$.

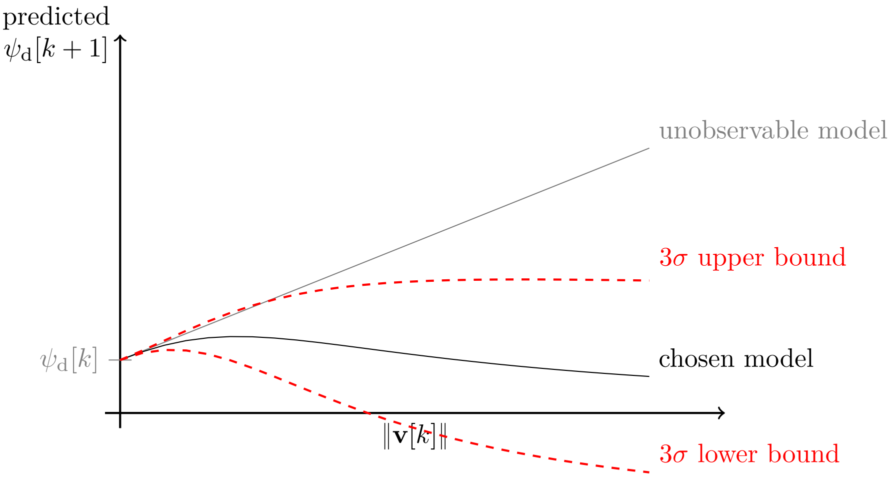

Figure 4.15: Magnetic heading disturbance prediction model. With increasing velocity, the traveled distance between time-steps k and $k+1$ increases. The first order interpolated magnetic model becomes less relevant, which is captured by our model, that smoothly falls back to a zero-mean prior with relatively large uncertainty.

$a[k]$ from measurements, that is to say, increasing with the expected amplitude of the local magnetic disturbance.

Among trajectories used in Ref. Chesneau et al. [2016], one of them is chosen for its relatively small heading drift and large swept volume (Fig. 4.16). Magnetic declination can be computed for each time-step in an arbitrary navigation frame (Fig. 4.17). Data is then sorted by magnetic gradient norm, clustered, and the standard deviation is computed for each cluster (Fig. 4.18). One can notice that, while the magnitude of magnetic disturbances remains somewhat high, its distribution matches noticeably well with an affine model with respect to the magnetic gradient. This suggests the following empirical model:

$$a[k] = a_0 + a_1 N[k], \tag{4.69}$$

where

$$N[k] = \left\| \nabla \mathbf{B}^\text{b}[k] \right\|. \tag{4.70}$$

Other publications such as Refs. Faulkner et al. [2010], Afzal et al. [2011a] suggest comparing the magnetic norm and dip to a geomagnetic model. However, on the same data, these variables do not seem to provide a reliable prior about the magnitude of the local disturbance of the magnetic declination. Empirical data instead suggest that in general, the local declination, norm, and dip of the magnetic field behave like independent variables. This observation is an argument against using these properties to compute a value for $a[k]$.

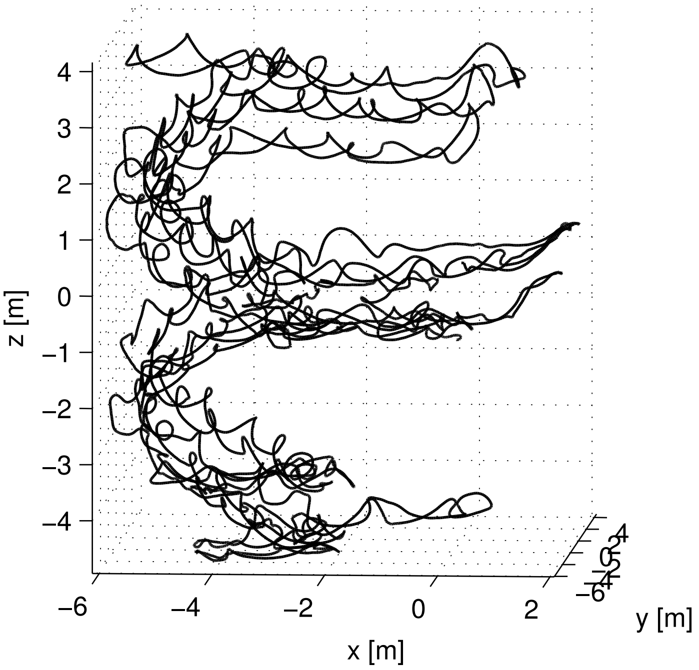

Figure 4.16: Reference multi-floor trajectory for magnetic heading model calibration

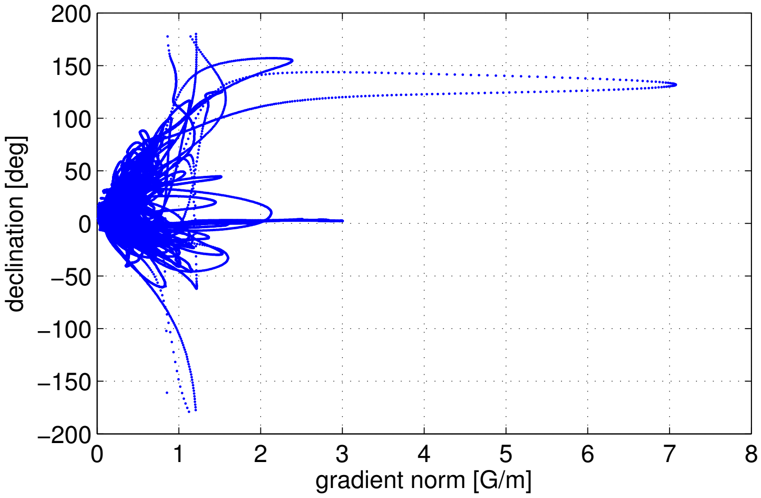

Figure 4.17: Estimated magnetic declination in the navigation frame with respect to the gradient norm

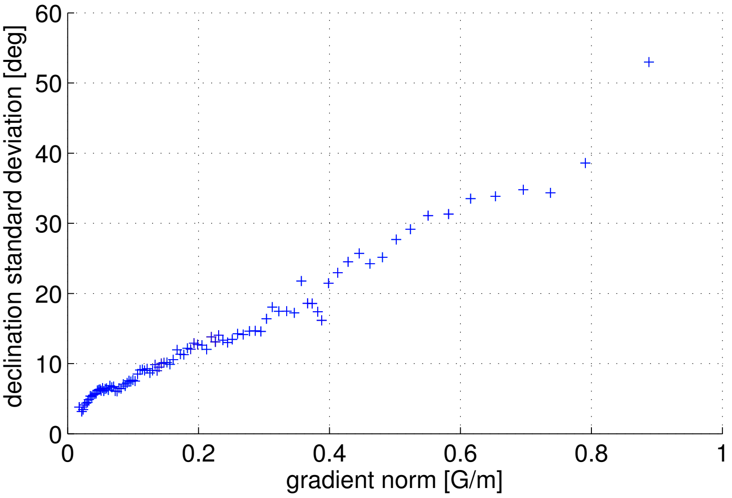

Figure 4.18: Declination standard deviation with respect to gradient norm

We have no data to assert that Eq. (4.69) is an accurate model for other buildings apart from SYSNAV's office in Vernon. This has not been checked for lack of resources and time. It would certainly be useful to verify these results from magnetic maps such as in Ref. Wahlström et al. [2013] and with the help of an external reference.

Heading estimation in the full 3D problem

This section reproduces Ref. [Chesneau et al., 2017, Sec. II.C].

In the full 3-dimensional problem, we propose adding two variables to the state vector, namely ψ_{init} and ψ_{d} and one scalar measurement y_ψ.

To appropriately use multivariate Gaussian distributions to represent uncertainties, attitude and trajectory are then represented in a navigation frame with arbitrary heading $\mathfrak{R}_{\text{n}}$, and the additional scalar variable ψ_{init} is added to the error state in order to represent the arbitrary initial heading. Since ψ_{init} is constant by definition, we have, with no process noise,

$$\forall k,\ \psi_{\text{init}}[k+1] = \psi_{\text{init}}[k]\ . \tag{4.71}$$

With ψ_{d} also added to the state vector, equations (4.65) and (4.71) are then combined to get the full discrete-time model.

Let $\mathfrak{R}_{\text{e}}$ be a frame of reference whose *north* is defined by the geomagnetic field. Let us define ψ_{init} such that

$$\begin{aligned}
R_{\text{init}} &\doteq \begin{pmatrix} \cos\psi_{\text{init}} & -\sin\psi_{\text{init}} & 0 \\ -\sin\psi_{\text{init}} & \cos\psi_{\text{init}} & 0 \\ 0 & 0 & 1 \end{pmatrix} && (4.72)\\
\mathbf{g}_1^{\text{n}} &= 0 && (4.73)\\
\mathbf{g}_2^{\text{n}} &= 0 && (4.74)\\
\mathbf{B}^{\text{e}} &\doteq R_{\text{init}}\left(R\mathbf{B}^{\text{b}}\right) && (4.75)\\
\psi_{\text{d}} &\doteq \arctan\left(\frac{B_1^{\text{e}}}{B_2^{\text{e}}}\right) \doteq \phi(\mathbf{B}^{\text{e}}) && (4.76)
\end{aligned}$$

In absence of magnetic distortions in $\mathfrak{R}_{\text{e}}$, $B_1^{\text{e}} = 0$, $B_2^{\text{e}} > 0$, and $\psi_{\text{d}} = 0$.

The value of $u[k]$ from Eq. (4.65) is computed using the discrete-time prediction equation stemming from Eq. (4.34),

$$u[k] = \phi(R[k+1]\mathbf{B}^{\text{b}}[k+1]) - \phi(R[k]\mathbf{B}^{\text{b}}[k]) \tag{4.77}$$

Then (4.76) can be used as a scalar measurement equation for Kalman filtering in the 3D problem, by substituting $\mathbf{B}^{\text{e}}$ with its expression in (4.75), then substituting $R\mathbf{B}^{\text{b}}$ with a function of $y_{\mathbf{B}}$ and ${\mathbf{B}^{\text{b}}}_{\text{pli}}$ by using (4.37),

$$\begin{aligned}
y_\psi[k] &\doteq \phi\left(R_{\text{init}}[k](R[k]y_{\mathbf{B}}[k] - {\mathbf{B}^{\text{n}}}_{\text{pli}}[k])\right) - \psi_{\text{d}}[k]\\
&= \phi\left(R[k]y_{\mathbf{B}}[k] - {\mathbf{B}^{\text{n}}}_{\text{pli}}[k]\right) - \psi_{\text{d}}[k] \qquad (4.78)\\
&= 0\ .
\end{aligned}$$

Since $y_{\mathbf{B}}[k]$ is not precisely known, neither is $y_\psi[k]$, which must then be visible in the measurement noise covariance matrix of the Kalman filter.

The chosen error parameterization for ψ_{init} and ψ_{d} is additive.

Let us remark that adding ψ_{init} to the state vector leads to an over-parameterization of heading, and therefore, to an unobservable model. An alternative solution is to identify $\mathfrak{R}_{\mathrm{e}}$ with the arbitrary initial navigation frame $\mathfrak{R}_{\mathrm{n}}$ and to modify the error parameterization function ξ such that a circular correction is correctly applied when heading is corrected. However, this parameterization is preferred in order to avoid ugly trajectory corrections during the convergence phase of heading estimation.

4.5.5. EKF implementation

An error representation is chosen such that the implemented algorithm is a MEKF, that is to say,

$$\tilde{x}[k] \doteq \begin{pmatrix} \widetilde{\mathbf{B}}^{\mathrm{b}}[k] \\ \widetilde{\mathbf{v}}^{\mathrm{b}}[k] \\ \tilde{\Phi}[k] \\ \widetilde{\mathbf{B}}^{\mathrm{n}}_{\mathrm{pli}}[k] \\ \widetilde{\mathbf{B}}^{\mathrm{n}}_{\mathrm{pli}}[k-1] \\ \widetilde{\mathbf{B}}^{\mathrm{n}}_{\mathrm{p}}[k] \\ \widetilde{\mathbf{b}}_\gamma[k] \\ \widetilde{\mathbf{b}}_\omega[k] \\ \tilde{\psi}_{\mathrm{init}}[k] \\ \tilde{\psi}_{\mathrm{d}}[k] \\ \widetilde{\mathbf{M}}^{\mathrm{n}}[k] \end{pmatrix} , \xi(\hat{x}[k], \tilde{x}[k]) \doteq \begin{pmatrix} \widehat{\mathbf{B}}^{\mathrm{b}}[k] + \widetilde{\mathbf{B}}^{\mathrm{b}}[k] \\ \widehat{\mathbf{v}}^{\mathrm{b}}[k] + \widetilde{\mathbf{v}}^{\mathrm{b}}[k] \\ \exp\left[\tilde{\Phi}[k]\times\right] \hat{R}[k] \\ \widehat{\mathbf{B}}^{\mathrm{n}}_{\mathrm{pli}}[k] + \widetilde{\mathbf{B}}^{\mathrm{n}}_{\mathrm{pli}}[k] \\ \widehat{\mathbf{B}}^{\mathrm{n}}_{\mathrm{pli}}[k-1] + \widetilde{\mathbf{B}}^{\mathrm{n}}_{\mathrm{pli}}[k-1] \\ \widehat{\mathbf{B}}^{\mathrm{n}}_{\mathrm{p}}[k] + \widetilde{\mathbf{B}}^{\mathrm{n}}_{\mathrm{p}}[k] \\ \hat{\mathbf{b}}_\gamma[k] + \widetilde{\mathbf{b}}_\gamma[k] \\ \hat{\mathbf{b}}_\omega[k] + \widetilde{\mathbf{b}}_\omega[k] \\ \hat{\psi}_{\mathrm{init}}[k] + \tilde{\psi}_{\mathrm{init}}[k] \\ \hat{\psi}_{\mathrm{d}}[k] + \tilde{\psi}_{\mathrm{d}}[k] \\ \widehat{\mathbf{M}}^{\mathrm{n}}[k] + \widetilde{\mathbf{M}}^{\mathrm{n}}[k] \end{pmatrix} .$$

The output vector is

$$y[k] = \begin{pmatrix} y_{\mathbf{B}}[k] \\ y_\psi[k] \end{pmatrix} ,$$

where $y_{\mathbf{B}}[k]$ depends on the state according to Eq. (4.37), and $y_\psi[k]$ depends on the state according to Eq. (4.78). The derivation of the linearized system and the tuning of the EKF are not detailed here.

With this parameterization, the trajectory is computed in an initially unknown navigation frame $\mathfrak{R}_{\mathrm{n}}$, and the change of frame to express the position in a frame whose north is defined by the magnetic field $\mathfrak{R}_{\mathrm{e}}$ is represented by ψ_{init}.

After convergence of ψ_{init}, this over-parameterization should be dropped either in favor of the simple removal of the state or an error parameterization for $\mathbf{M}^{\mathrm{n}}$ that is independent of the navigation frame.

4.5.6. Experimental results

These experimental results have been published in Ref. Chesneau et al. [2017]

Two data sets are chosen in order to illustrate the effect of magnetic heading estimation on the accuracy of the trajectory. In each case, the sensor board is strapped to the user's trunk.

IPIN 2016 competition, Track 2

The first data set was acquired during an *unofficial* trial at the IPIN 2016 competition in Alcalá de Henares, Spain, on the actual path of the pedestrian dead reckoning competition.[11] The path included 57 geo-referenced waypoints. The described observer is compared with the one published in Ref. Chesneau et al. [2016] (or equivalently the one described in Sec. 4.4) in the following manner: algorithms are started on the first waypoint with no initialization procedure beforehand. Since trajectories are computed in the same arbitrary initial reference frame, both are rotated by the final estimate of ψ_{init} computed by the new algorithm, corrected by a magnetic declination of -0.93 degrees obtained from the World Magnetic Model (WMM) and displayed on the same map (see Fig. 4.19-4.22). The solid blue trajectory is computed with the new algorithm, the dotted green one is computed with the old algorithm, and solid red bars are plotted between waypoints and their corresponding estimate according to the new algorithm. A clear improvement in performance is observed (see Fig. 4.23a-4.23b) comparing the algorithm in Ref. Chesneau et al. [2016] with the current one. The output heading of the old algorithm drifts clockwise, which seems to cause most of the error growth after waypoints number 20-25. The new algorithm that includes magnetic heading estimation does not display this behavior.

Indoor trial with a heading reference

The second data set is acquired in a building with a heading reference. The heading reference consists of two georeferenced landmarks materializing a known geographical direction. An experimental trajectory is made by repeatedly traveling between these two references, 55 times, and marking the passage in front of each landmark in the same position, with a probable precision of ±30 cm. The estimated distance between the two landmarks is 22.9 m.

After compensating for the local declination according to a geomagnetic model, heading error is inferred from computing the traveling direction between the two references from the estimated trajectory (see Fig. 4.24), and comparing it with the direction of the heading reference. Results are compiled in Table 4.1. Between marks 49 and 50, movement is almost stopped during 10 minutes in front of a ferromagnetic structure, resulting in a strong magnetic disturbance. Heading drifts slowly during these 10 minutes, and recovers after a few round trips.

The maximum estimated heading error immediately after initialization is 6.2 degrees, 4.8 degrees excluding the first measurement. The standard deviation of the estimated

---

[11] The sensor board carries barometers that are sensitive to light. See, e.g., the datasheet of another barometer `https://www.nxp.com/docs/en/data-sheet/MPL115A2.pdf`. Barometers measurements were used in navigation algorithms during the two official runs of this competition without properly protecting the barometer of the prototype, severely degrading the estimation performance.

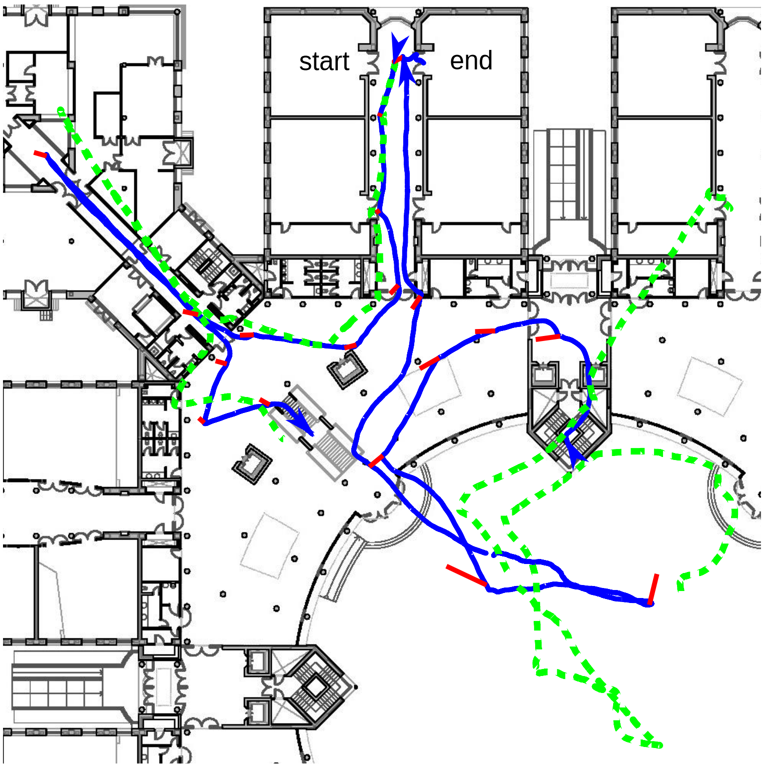

Figure 4.19: Computed trajectory on the path of IPIN 2016 Track 2, ground floor. The blue solid line is the output of the EKF published in Ref. Chesneau et al. [2017] (or Sec. 4.5). The green dashed line is the output of the EKF published in Ref. Chesneau et al. [2016] (or Sec. 4.4). Solid red bars are plotted between waypoints and their corresponding estimate according to the former algorithm.

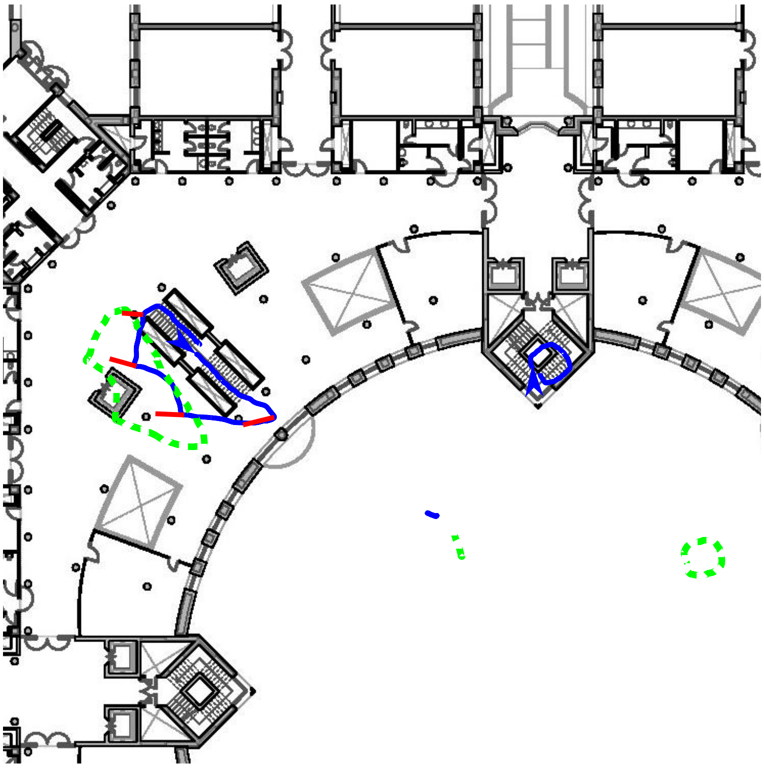

Figure 4.20: Computed trajectory on the path of IPIN 2016 Track 2, first floor. The blue solid line is the output of the EKF published in Ref. Chesneau et al. [2017] (or Sec. 4.5). The green dashed line is the output of the EKF published in Ref. Chesneau et al. [2016] (or Sec. 4.4). Solid red bars are plotted between waypoints and their corresponding estimate according to the former algorithm.

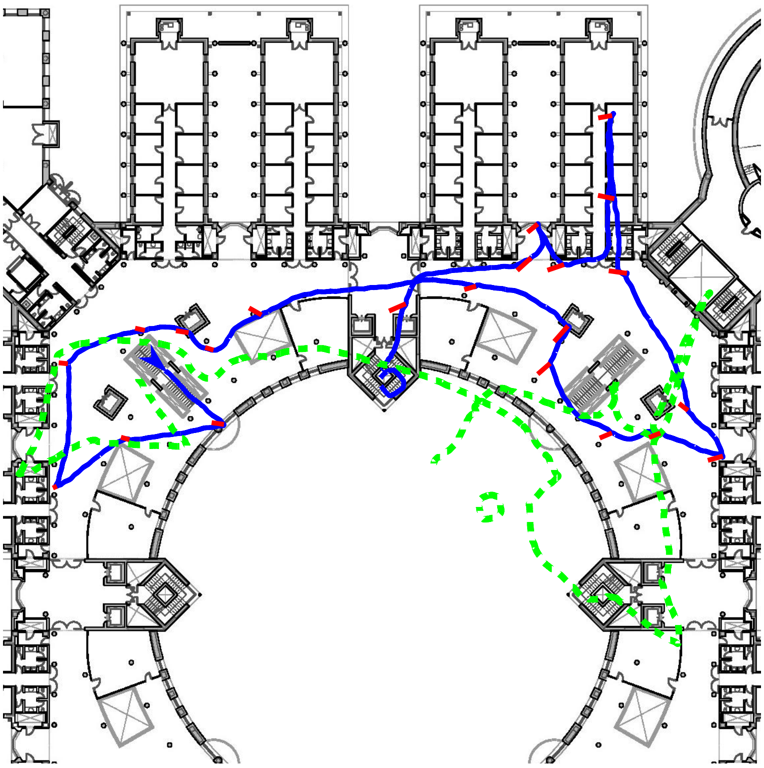

Figure 4.21: Computed trajectory on the path of IPIN 2016 Track 2, second floor. The blue solid line is the output of the EKF published in Ref. Chesneau et al. [2017] (or Sec. 4.5). The green dashed line is the output of the EKF published in Ref. Chesneau et al. [2016] (or Sec. 4.4). Solid red bars are plotted between waypoints and their corresponding estimate according to the former algorithm.

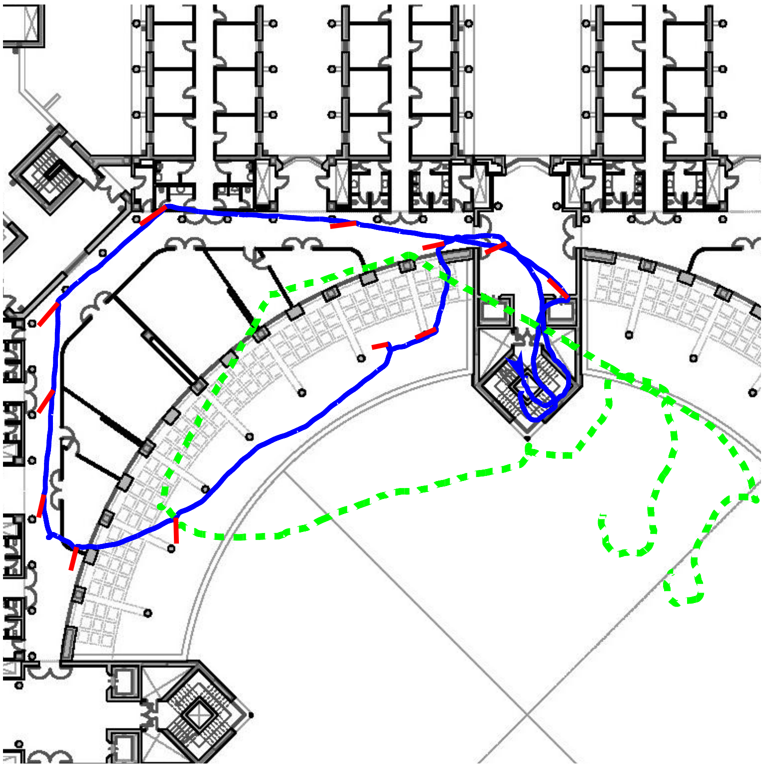

Figure 4.22: Computed trajectory on the path of IPIN 2016 Track 2, third floor. The blue solid line is the output of the EKF published in Ref. Chesneau et al. [2017] (or Sec. 4.5). The green dashed line is the output of the EKF published in Ref. Chesneau et al. [2016] (or Sec. 4.4). Solid red bars are plotted between waypoints and their corresponding estimate according to the former algorithm.

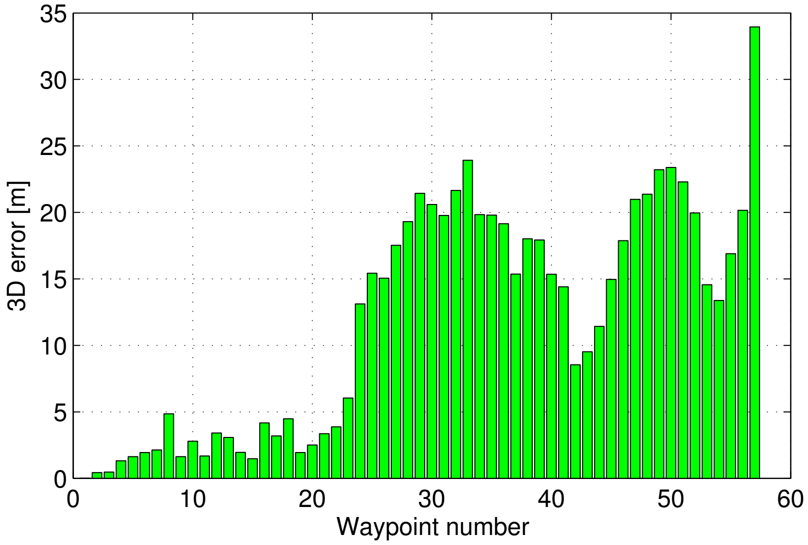

(a) Distance from ground truth with the algorithm from Sec. 4.4 (or Ref. Chesneau et al. [2016]). The third quartile of error is 19.76m

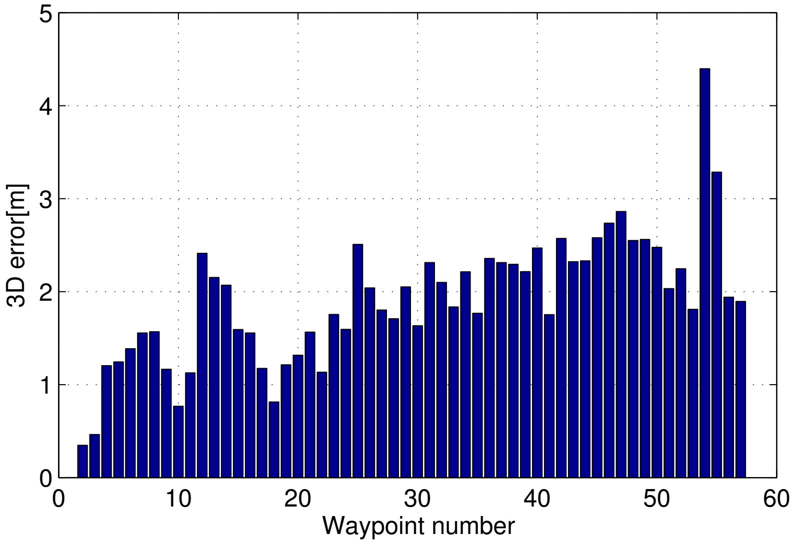

(b) Distance from ground truth with the algorithm from Sec. 4.5 (or Ref. Chesneau et al. [2017]). The third quartile of error is 2.32m

Figure 4.23: Comparison of distance from ground truth between algorithms

Table 4.1.: Estimated direction of travel during the indoor trial with a heading reference

South landmark	North landmark	Estimated direction of travel [deg]	Heading error [deg]
1	2	307.7	6.2
4	5	303.1	1.6
6	5	302.2	0.7
6	7	302.9	1.4
8	7	302.4	0.8
8	9	303.1	1.5
10	9	302.9	1.4
10	11	303.1	1.5
17	18	303.5	2.0
19	18	303.0	1.4
19	20	303.6	2.1
21	20	303.0	1.5
41	42	306.3	4.8
43	42	304.2	2.7
43	44	304.9	3.4
45	44	303.6	2.1
45	46	305.0	3.5
47	46	303.7	2.2
47	48	304.1	2.6
49	48	303.1	1.6
50	51	297.9	-3.6
52	51	297.1	-4.4
52	53	298.8	-2.7
54	55	301.8	0.2
56	55	301.0	-0.5
56	57	301.8	0.3
58	57	301.3	-0.2
58	59	302.3	0.8
60	59	301.7	0.1
60	61	303.1	1.6
62	61	302.5	1.0
62	63	303.0	1.5
64	63	302.3	0.8
64	65	303.2	1.7
66	65	301.9	0.3
66	67	303.0	1.5
68	67	302.0	0.5
68	69	303.2	1.7
70	69	302.1	0.6
70	71	303.5	1.9

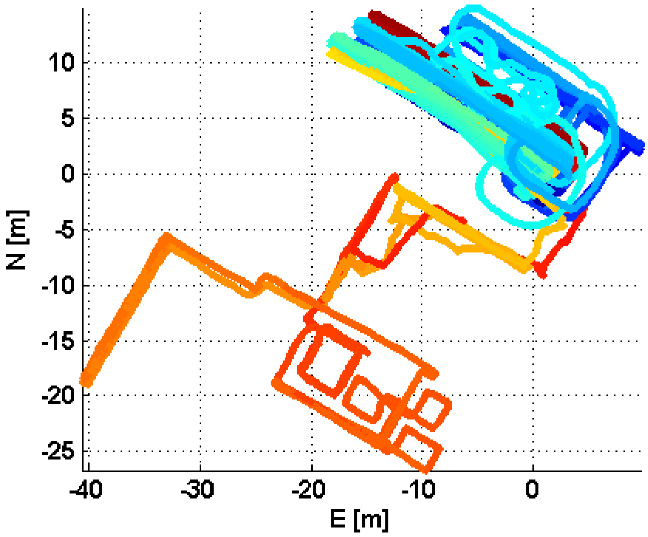

Figure 4.24: A 2.5km, 56 min long benchmark trajectory

heading error is 1.9 degrees.

A few other trials have been made without a heading reference (see Fig. 4.26). Heading remains generally stable with a few degrees of accuracy. However, in some cases, performance can be degraded. In one instance, a metallic swing gate has had to be open after climbing a caged ladder, resulting in a strong magnetic disturbance. This type of disturbance is poorly managed by the EKF and heading estimator, since it leads to wrong velocity estimates, wrong heading disturbance predictions, and wrong heading estimation tuning. This explains the visible a slowly recovering heading error in Fig. 4.26b. Moreover, the fact that the EKF carries an unobservable state in its parameterization of heading leads to poor recovery of such disturbances. Another compromise needs to be found to replace this parameterization, depending on the use case of the navigation algorithms.

4.5.7. Conclusion

Compliance In this Section, the state-space model of an EKF has been described, aiming at taking into account inertial sensor biases, power-line interference, some lower frequency magnetic disturbances, and tackling the problem of heading drift. This complies with the motivations enumerated in Sec. 4.5.1.

Performance Performance has been evaluated using data collected during the IPIN 2016 Conference, with results that are comparable, on this trial, with those achievable with Pedestrian Dead Reckoning (PDR) algorithms with high-performance foot-

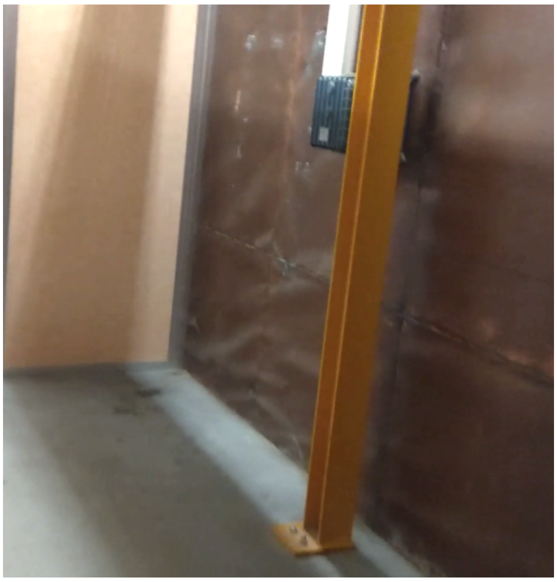

Figure 4.25: Beam in front of which the user is sitting for 10 min in the middle of the benchmark trajectory

mounted Inertial Measurement Units (IMUs).

In contrast with PDR algorithms, this performance is obtained without making assumptions about the nature of the movement. Sensors do not need to be foot-mounted, and can be carried by hand, to draw cursive text with the trajectory, for example.

The long-distance performance has been improved since the first observer (Described in Sec. 4.4), often leading to relative drift errors well under 1% of the traveled distance. Illustrating this fact, on the IPIN 2016 - Track 2, errors stay under a few meters for a trajectory several hundreds of meters long (Fig. 4.23b). In Fig. 4.28, a test trajectory of more than 550 m shows a closed path drift of under 42cm. In Fig. 4.26 are displayed trajectories of one to several kilometers, 20 to 60 minutes walks. This was done without compromising the short term accuracy observed with the previous algorithm.

Remaining work The short-term performance has not been evaluated in motion capture experiments like for the previous observer. Moreover, despite its fulfilling its intended purpose in practice, the heading estimation model suffers from a representativeness problem.

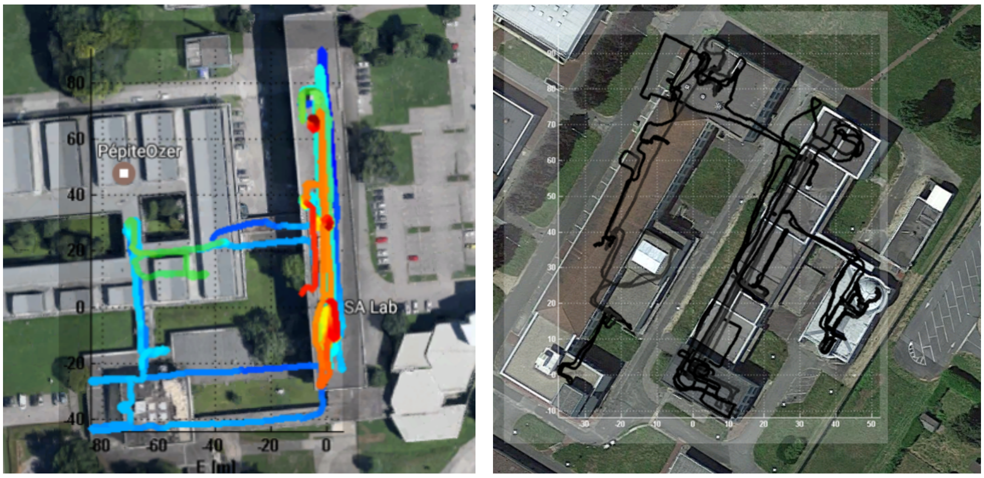

(a) Trajectory computed during a 20 min walk in GIPSA-lab, Grenoble

(b) Trajectery computed during a 50 min indoor walk

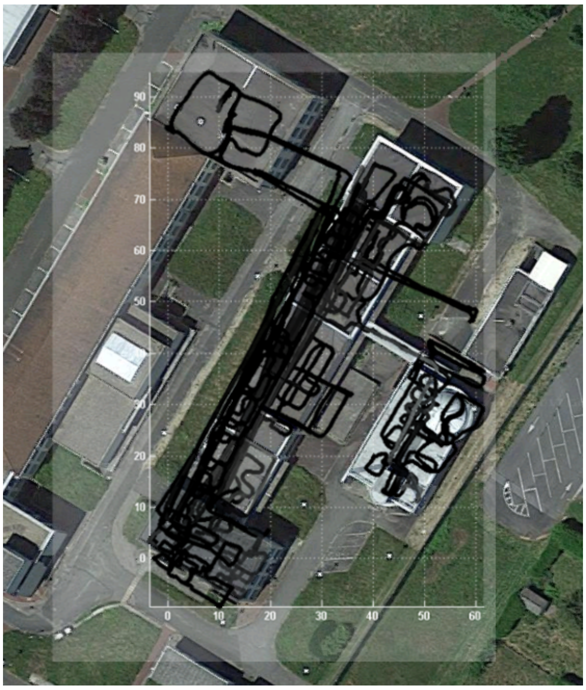

(c) Trajectory computed during a 1h indoor walk

Figure 4.26: A few more trajectories computed during indoor trials, without heading reference.

Figure 4.27: A metallic swing gate has been opened during the trial from Fig. 4.26b

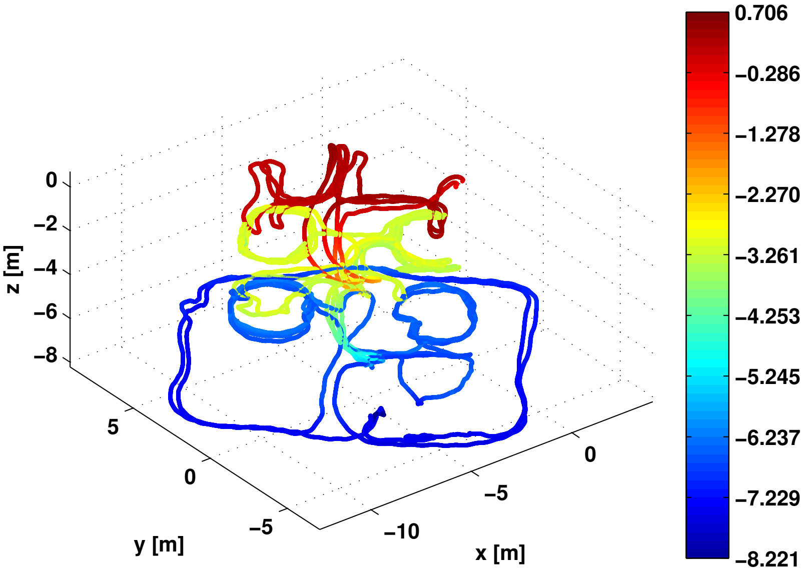

Figure 4.28: Test trajectory in SYSNAV's office (Fig. 4.29) with the navigation algorithms described in Sec. 4.5. Colors represent height. The starting point and the ending point are the same. On the estimated trajectory, they are 42 cm apart, for a total estimated traveled distance of more than 550 m. Many colleagues have been bothered during its realization by the repeated circling around their desks. Several loops are also made around the building.

Figure 4.29: Picture of SYSNAV's office in Vernon

4.6. Conclusion

Performance Experimental results show that with MIDR, a performance under 1% of traveled distance is accessible in practice. At this point, a large part of the reason seems to stem from considerations in Sec. 3.4 rather than from navigation algorithms since the proposed discrete-time model is mainly phenomenological. This justifies the work undertaken in Part. II aiming at improving the calibration process, and reducing measurement uncertainty.

Heading Regarding heading estimation, the proposed solution allows a pretty robust filtering solution in practice regarding the amplitude of disturbances usually observed in indoor environments. However, it rests on shaky theoretical foundations. Computing the heading by relying on the direction of the magnetic field does not seem to be a problem solvable using a recursive algorithm, all the more with a recursive Bayesian filtering algorithm such as the Kalman filter.

Power-line interference The main source of subjective uncertainty with regards to MIDR is the validity of the stationarity assumption of the magnetic field. Experiments show that this assumption is in general not true. However, the main offender is power-line interference, which is a pretty predictable disturbance. An observer accounting for this disturbance has been designed and evaluated on experimental data successfully (evaluation in simulation is not reported in this document but in Ref. Chesneau et al.

[2016].)

Inertial sensor biases Experimental evaluation has shown the sensitivity of attitude and velocity estimation to inertial sensor errors, especially to biases. This problem, anticipated in Ch. 2, is solved in practice in Sec. 4.5. The successful recovery of inertial sensor biases shows that the hope of recovering them, formulated in Sec. 2.6 was well-founded.

Theoretical shortcomings The designed EKF is used successfully, but without proof of convergence, and is not adapted to yield valid error estimates in the presence of modeling errors such as those of the magnetic field gradient. This issue, which is not a surprise, is an inherent characteristic of MIDR, which motivates finding another tool.

Future work Let us remark that the MIDR approach we have described in discrete-time mainly consists in interpolating a linear local map of the magnetic field at a time-step k, then measuring the magnetic field at time-step $k+1$, and computing the position of the sensor at time-step $k+1$ in the frame of time-step k. The same approach is presented in Ref. Skog et al. [2018] using interpolations of higher order spatial derivatives of the magnetic field, allowing direct estimation of the angular velocity. Assuming a proper array of magnetometers has been designed (see Sec. 3.2.6), then it can be combined with the current one (see Sec. 2.2.2). Better estimates of inertial sensor biases can be expected with this approach.

Part II.

Calibration techniques for magnetometer arrays

5. Calibration of a magnetometer array using Helmholtz coils

Contents

5.1. Introduction

In Part. I, particularly in Ch. 3, it is shown that the reachable accuracy of Magneto-Inertial Dead-Reckoning (MIDR) depends heavily on magnetometer calibration. The magnetometer calibration techniques discussed in Ch. 3 are based on ellipsoid fitting techniques (see the relevant chapter and references therein). However, these techniques are limiting in several aspects.

Completeness In the context of magnetometer array calibration, ellipsoid fitting techniques provide incomplete calibrations, since they are insensitive to magnetometer effective positions and the choice of sensor reference frame. This weakness is shared by all techniques that rely upon homogeneous magnetic fields.

Scaling-up the production process The magnetic calibration process of the Magneto-Inertial Measurement Unit (MIMU) device discussed in Ch. 3 relies on manual outdoor data collection. Difficulties naturally arise with the scaling-up of the production, that needs to be reliable, repeatable and efficient. As is, because the many sources of error must be controlled during data collection, the process requires careful and painstaking work of a trained operator.

Mechanization Mechanization of ellipsoid fitting data collection is indeed possible and was demonstrated in several publications, but requires non-magnetic materials and actuators (see Ref. Pang et al. [2013]). Depending on the desired accuracy, this can be a limiting factor. The use of actuators can be avoided by relying on calibrated Helmholtz coils to simulate an outdoor trial with the technique described in Ref. Mohamadabadi and Hillion [2014], Díaz-Michelena et al. [2015]. In that case, magnetometer calibration accuracy requires sizeable and precisely assembled Helmholtz coils (see, e.g., Ref. Le Contel et al. [2016]), the size of the coils depending on the size of the MIMU device that must be contained into the zone in which the generated magnetic field is homogeneous. Nevertheless, the size of the coils can be decreased by the use of additional coils, e.g., in the so-called Maxwell or Braunbeck configurations. However, because the generated field is meant to be homogeneous, many calibration problems listed in Ch. 3 remain unsolved. Such coil systems also require calibration (see Refs. Dinale [2013], Zikmund et al. [2015]).

State of the art Ref. Turner et al. [2015], Hall et al. [2012] describe single-axis Helmholtz antiparallel coils, enabling the precise calibration of a magnetic gradiometer. The described technique requires precise placement of the device inside of the coils. Avoiding this kind of requirement was one of the motivations for the use of ellipsoid fitting techniques.

Refs. Adachi et al. [2014], Yoshida et al. [1994] solve this issue, at the cost of a precise arrangement of magnetic sources, for Superconducting QUantum Interference Device (SQUID) magnetometer arrays. Magnetic sources are small coils whose generated field is similar to magnetic dipoles. This solution is not convenient for use with Anisotropic Magneto-Resistance (AMR) magnetometers, because of their lower sensitivity. In our case, it is preferable to work inside rather than outside of coils, because it is possible to generate much stronger magnetic fields with little current this way.

Requirements Since magnetometer biases can be calibrated with dedicated passive hardware such as a mu-metal box (see Ref. Mohamadabadi [2013]), an accurate, mechanizable calibration process is investigated for *unbiased* magnetometer arrays, using an arrangement of coils (such as Helmholtz, Maxwell, Braunbeck configurations...). The solution must be sensitive to magnetometer effective positions. It must also avoid the need for precise placement of the device, as is the case with ellipsoid fitting techniques. The process must give access to coil calibration with the lowest possible requirements on their manufacturing process or any potential reference magnetometer.

Idea An arrangement of coils is used, such as tri-axis Helmholtz coils (Fig. 5.1), in a non-standard way, by driving each of the six individual coils independently instead of by pairs, in order to generate an unknown, inhomogeneous magnetic field. The magnetometer array is placed anywhere inside of the coils in several, different unknown positions, while independent and known currents are supplied to each coil. It is shown that in practice, the simultaneous knowledge of currents and measurements is enough in order to calibrate both the coil system and the array of magnetic sensors, up to unknown units of length and magnetic field, and to precisely compute the different positions in which the array has been placed. While the unit of magnetic field is unimportant in MIDR, the unit of length is important and may be recovered with a specific experiment. When calibrating the coil system, rather than its geometric characteristics, the generated magnetic field in an open simply connected space enclosed by the coils is identified instead. Prior knowledge of the geometry of both the coil system and the magnetometer array is only used to initialize computations. Alignment with inertial sensors is made possible by simultaneously using the setup as a localization system. Using Helmholtz coils as an example, the process can be extended to any configuration of at least six coils.

Outline The problem of localizing the magnetometer array inside of the coils while calibrating both the generated magnetic field and the sensor array is stated in Sec. 5.2. Since the arrangement of coils is assumed to be Helmholtz coils, discussion on the practical implications of this configuration is provided in Sec. 5.3; this discussion must be adapted to whatever other configuration is desired. Calibration is undertaken in simulation in Sec. 5.4. A proof of concept experiment is undertaken in Sec. 5.5. Then, Sec. 5.6 concludes this chapter.

Figure 5.1: Tri-axis Ferronato® BH-600 Helmholtz coils used for this work

5.2. Problem statement

Let us consider a rigid body strapped with an array of (unbiased) linear single-axis point-magnetometers (as defined in Sec. 3.2.1). The rigid body is associated with a reference frame $\mathfrak{R}_{\mathrm{b}}$. Let us also consider three pairs of Helmholtz coils arranged orthogonally as in Fig. 5.1, fixed with respect to a navigation frame $\mathfrak{R}_{\mathrm{n}}$.[1] Currents through each of the six coils are assumed to be controlled and measured independently from each other. It is also assumed that the rigid body can be moved inside of the volume enclosed by the coils. The problem under consideration is to determine the trajectory of the system inside of the coils, along with the calibration of both the coils and of the array of magnetometers, from simultaneous measurements of currents in the coils and magnetometers output. The trajectory, although not considered a calibration parameter, is useful for alignment purposes with inertial sensors (see Sec. 3.3.2).

5.2.1. Notations and definitions

Magnetometers Linear single-axis point-magnetometers are defined in Sec. 3.2.1. Based on Eq. (3.1), the unbiased measurement model assumption for the j-th sensor is then

$$\forall j \in \{1, ..., n_{\mathrm{mag}}\},\ \forall t,\ Y^j(t) = {}_j\mathbf{a}^{\mathrm{b}}\ \mathbf{B}^{\mathrm{b}}({}_j\mathbf{p}^{\mathrm{b}}, t)\ , \tag{5.1}$$

where ${}_j\mathbf{a}^{\mathrm{b}}$ is the co-vector representing the j-th magnetometer scale factor and sensitive axis in body frame, ${}_j\mathbf{p}^{\mathrm{b}}$ the vector representing its effective position in body frame, and $\mathbf{B}^{\mathrm{b}}$ represents the magnetic field vector in body frame $\mathfrak{R}_{\mathrm{b}}$.

Let us also denote $\forall i, j,\ \mathfrak{a}^j{}_i \doteq {}_j a^{\mathrm{b}}_i$ (see notations p. 38) the coordinates of ${}_j\mathbf{a}^{\mathrm{b}}$, and ${}_j\mathfrak{p}^i$ those of ${}_j\mathbf{p}^{\mathrm{b}}$ such that ${}_j\mathbf{p}^{\mathrm{b}} = ({}_j\mathfrak{p}^1, {}_j\mathfrak{p}^2, {}_j\mathfrak{p}^3)^\top$.

Change of frame Let us assume that at any point $\mathbf{P}$ in space, the change of frame between $\mathfrak{R}_{\mathrm{b}}$ and $\mathfrak{R}_{\mathrm{n}}$ can be expressed according to Eq. (2.8),

$$\mathbf{B}^{\mathrm{n}}(\mathbf{P}^{\mathrm{n}}, t) = R\mathbf{B}^{\mathrm{b}}(\mathbf{P}^{\mathrm{b}}, t)\ ,$$

where for any point $\mathbf{P}$ whose coordinates are $\mathbf{P}^{\mathrm{b}}$ in $\mathfrak{R}_{\mathrm{b}}$ and $\mathbf{P}^{\mathrm{n}}$ in $\mathfrak{R}_{\mathrm{n}}$, the change of coordinates between $\mathfrak{R}_{\mathrm{n}}$ and $\mathfrak{R}_{\mathrm{b}}$ reads Eq. (2.1),

$$\mathbf{P}^{\mathrm{n}} = R(\mathbf{P}^{\mathrm{b}} - \mathbf{M}^{\mathrm{b}}) + \mathbf{M}^{\mathrm{n}}\ ,$$

where $\mathbf{M}$ is a fixed point of the rigid body, $\mathbf{M}^{\mathrm{n}}$ (resp. $\mathbf{M}^{\mathrm{b}}$) represents its coordinates in $\mathfrak{R}_{\mathrm{n}}$ (resp. in $\mathfrak{R}_{\mathrm{b}}$), and the trajectory of the rigid body is defined as the evolution of $(R, \mathbf{M}^{\mathrm{n}}) \in \mathrm{SE}(3)$ with time, where SE(3) denotes the special Euclidean group that represents rigid body motion. To later simplify notations, let us define

$$\mathbf{M}^{\mathrm{b}} \doteq 0\ . \tag{5.2}$$

In the following, coefficients of the matrix R are denoted $R^i{}_j$ where i is the line number and j the column number. We denote $S \doteq R^\top = R^{-1}$ such that

$$\forall i, j,\ S^j{}_i \doteq R^i{}_j\ .$$

---

[1] The same work can be done with other arrangements of *at least* six coils.

Coils Let us assume that the magnetic field is only produced by electric currents in the coils and that these currents vary slowly enough that magnetic field propagation times are negligible. The magnetic field in the navigation frame $\mathfrak{R}_\mathrm{n}$ can then be expressed as a linear function of the $n_\mathrm{coils} = 6$ currents in the coils $I^m(t),\ 1 \leqslant m \leqslant 6$,

$$\mathbf{B}^\mathrm{n}(\mathbf{P}^\mathrm{n}) = \sum_m \mathbf{T}^\mathrm{n}_m(\mathbf{P}^\mathrm{n})\ I^m(t)\ , \tag{5.3}$$

where

$$\mathbf{T}^\mathrm{n}_m(\mathbf{P}^\mathrm{n}) \doteq \begin{pmatrix} {T^1}_m(\mathbf{P}^\mathrm{n}) \\ {T^2}_m(\mathbf{P}^\mathrm{n}) \\ {T^3}_m(\mathbf{P}^\mathrm{n}) \end{pmatrix} \tag{5.4}$$

represents the magnetic field in the navigation frame, generated by the m-th coil, divided by the current I^m going through it. The functions $\mathbf{T}^\mathrm{n}_m$ represent the calibration of the coils. They are assumed to be time-independent in $\mathfrak{R}_\mathrm{n}$.

Magnetic field, set of possible positions The magnetic field, in an open simply connected space enclosed by the coils, is assumed to satisfy Maxwell's equations for a source-free region of space. This property must also be respected by the functions $\mathbf{T}^\mathrm{n}_m$, that are therefore only defined on this simply connected space. Conversely, possible values of $(R, \mathbf{M}^\mathrm{n}) \in \mathrm{SE}(3)$ must be limited into an open, simply connected subset $\mathcal{X} \subset \mathrm{SE}(3)$ enclosed by the coils, that is assumed to contain the origin of $\mathfrak{R}_\mathrm{b}$.

The calibration of the coils is then local, in the sense that the magnetic field is identified only in a bounded region of space.

Measured transfer matrices Combining Eq. (5.1) with Eq. (5.3) together with change of frame equations, i.e. Eqs. (2.1) and (2.8), yields

$$Y^j(t) = \sum_m {}_j\mathbf{a}^\mathrm{b} R^\top \mathbf{T}^\mathrm{n}_m(R\ {}_j\mathbf{p}^\mathrm{b} + \mathbf{M}^\mathrm{n})\ I^m(t)\ . \tag{5.5}$$

Let us assume that $Y^j(t)$ and $I^m(t)$ can be measured at fixed position $(R, \mathbf{M}^\mathrm{n}) \in \mathrm{SE}(3)$ for a time during which all currents $I^m(t)$ are linearly independent. Then, because of Eq. (5.5), the knowledge of $Y^j(t)$ and $I^m(t)$ for a given position can be condensed into a transfer matrix that depends on $(R, \mathbf{M}^\mathrm{n}) \in \mathrm{SE}(3)$. In other words, there exists a transfer matrix $\mathbf{H}(R, \mathbf{M}^\mathrm{n})$ whose coefficients ${H^i}_j(R, \mathbf{M}^\mathrm{n})$ are such that, following Einstein summation convention[2],

$$Y^i = {H^i}_m(R, \mathbf{M}^\mathrm{n})\ I^m\ , \tag{5.6}$$

where coefficients ${H^i}_m$ can be expressed as

$${H^i}_m(R, \mathbf{M}^\mathrm{n}) = {\mathfrak{a}^i}_j {S^j}_k {T^k}_m(R\ {}_i\mathbf{p}^\mathrm{b} + \mathbf{M}^\mathrm{n})\ . \tag{5.7}$$

Finally, let us denote

$$\mathcal{H} \subset \mathbb{R}^{n_\mathrm{mag} \times n_\mathrm{coils}}\ ,$$

the manifold spanned by $\mathbf{H}(R, \mathbf{M}^\mathrm{n})$ when $(R, \mathbf{M}^\mathrm{n})$ varies in $\mathcal{X} \subset \mathrm{SE}(3)$.

---

[2] See Ref. [Appel, 2007, Sec. 16.1.b] summation is implied whenever an index appears in a term once as a subscript and only once as a superscript.

5.2.2. Problem formulation

The problem can be formulated as,

P1 Given (a possibly finite subset of) the manifold $\mathcal{H}$, are magnetometer calibration parameters ${}_j\mathbf{a}^{\mathrm{b}}$ and ${}_j\mathbf{p}^{\mathrm{b}}$ identifiable, along with coil calibration functions $\mathbf{T}^{\mathrm{n}}_m$?

P2 Given (a possibily finite subset of) the manifold $\mathcal{H}$, is it possible to recover the corresponding position of the magnetometer array for each possible point on the manifold? That is to say, is it possible to recover the inverse of

$$\begin{aligned} \mathcal{X} &\to \mathcal{H} \\ (\mathbf{M}^{\mathrm{n}}, R) &\mapsto \mathbf{H}(R, \mathbf{M}^{\mathrm{n}}) \ . \end{aligned}$$

5.2.3. Theoretical considerations and reformulation

Problems P1 and P2, as such, are ambiguously defined. The following theoretical aspects must be considered before attempting to solve them.

Notion of identifiability in Problem P1

Parameter space Let us denote θ the tuple of magnetometers and coils calibration parameters,

$$\theta \doteq \left(({}_j\mathbf{p}^{\mathrm{b}}), ({}_j\mathbf{a}^{\mathrm{b}}), (\mathbf{T}^{\mathrm{n}}_m)\right) \ , \tag{5.8}$$

where the notation $({}_j\mathbf{p}^{\mathrm{b}}) = ({}_j\mathbf{p}^{\mathrm{b}})_{j=1,\dots,n_{\mathrm{mag}}}$ represents the tuple of effective position vectors for all n_{mag} magnetometers (the same applies to $({}_j\mathbf{a}^{\mathrm{b}})$), and the notation $(\mathbf{T}^{\mathrm{n}}_m) = (\mathbf{T}^{\mathrm{n}}_m)_{m=1,\dots,n_{\mathrm{coils}}}$ represents the tuple of coil calibration functions as defined in Sec. 5.2.1. The space of all such θ will be denoted Θ. Each element $\theta \in \Theta$ indirectly defines an image manifold $\mathcal{H}$, through Eq. (5.7).

Notion of identifiability For Problem P1, the notion of identifiability is interpreted as the ability to distinguish tuples of parameters by their corresponding manifold $\mathcal{H}$. This means that if two tuples of parameters θ and θ' in the parameter space Θ are different, $\theta \neq \theta'$, then their corresponding manifolds $\mathcal{H}$ and $\mathcal{H}'$ spanned by the corresponding measured transfer matrices $\mathbf{H}$ and $\mathbf{H}'$, when $(R, \mathbf{M}^{\mathrm{n}})$ varies in $\mathcal{X} \subset \mathrm{SE}(3)$, should be different too. This is equivalent to guaranteeing that the symmetric difference $\mathcal{H}\Delta\mathcal{H}'$ should not be the empty set $\varnothing$, where

$$\mathcal{H}\Delta\mathcal{H}' \doteq (\mathcal{H} \cup \mathcal{H}')\backslash(\mathcal{H} \cap \mathcal{H}') \ . \tag{5.9}$$

Distinguishing θ from θ' can then consist in finding at least one element of $\mathcal{H}\Delta\mathcal{H}'$; it is then unnecessary to always fully know $\mathcal{H}$ and $\mathcal{H}'$.

Reference frame and scaling ambiguity This notion of identifiability is too strong to hold because the manifold $\mathcal{H}$ is invariant by redefinition of body and navigation frame and by distance and magnetic field rescaling. Indeed, with $\lambda, \mu > 0$, $U, V \in \mathrm{SO}(3)$ and $\mathbf{C}, \mathbf{D} \in \mathbb{R}^3$,

$$\begin{aligned}
&H^j{}_m(R, \mathbf{M}^{\mathrm{n}}) \\
&= {}_j\mathbf{a}^{\mathrm{b}} R^\top \mathbf{T}^{\mathrm{n}}_m(R\ {}_j\mathbf{p}^{\mathrm{b}} + \mathbf{M}^{\mathrm{n}}) \\
&= \lambda\ {}_j\mathbf{a}^{\mathrm{b}} V V^\top R^\top U U^\top \frac{1}{\lambda} \\
&\qquad \mathbf{T}^{\mathrm{n}}_m \left(U U^\top R V V^\top \frac{\mu}{\mu} \left[{}_j\mathbf{p}^{\mathrm{b}} + \frac{1}{\mu} V(\mathbf{C} - \mathbf{C}) \right] + \frac{\mu}{\mu} U U^\top \mathbf{M}^{\mathrm{n}} + \frac{1}{\mu} U(\mathbf{D} - \mathbf{D}) \right) \\
&= \left(\lambda\ {}_j\mathbf{a}^{\mathrm{b}} V\right) \left(U^\top R V\right)^\top \frac{1}{\lambda} U^\top \\
&\qquad \mathbf{T}^{\mathrm{n}}_m \left(\frac{1}{\mu} U \left\{ (U^\top R V)[\mu V^\top ({}_j\mathbf{p}^{\mathrm{b}} + \frac{1}{\mu} V(\mathbf{C} - \mathbf{C}))] + \mu U^\top \mathbf{M}^{\mathrm{n}} + \mathbf{D} - \mathbf{D} \right\} \right) \\
&= {}_j\mathbf{a}^{\mathrm{b}'} R'^\top \mathbf{T}^{\mathrm{n}'}_m \left(R'\ {}_j\mathbf{p}^{\mathrm{b}'} + \mathbf{M}^{\mathrm{n}'} \right) \ ,
\end{aligned} \tag{5.10}$$

where

$$R' \doteq U^\top R V \ , \tag{5.11}$$

$$\mathbf{M}^{\mathrm{n}'} \doteq \mu U^\top \mathbf{M}^{\mathrm{n}} + R'\mathbf{C} + \mathbf{D} \ , \tag{5.12}$$

$${}_j\mathbf{a}^{\mathrm{b}'} \doteq \lambda\ {}_j\mathbf{a}^{\mathrm{b}} V \ , \tag{5.13}$$

$${}_j\mathbf{p}^{\mathrm{b}'} \doteq \mu\ V^\top {}_j\mathbf{p}^{\mathrm{b}'} - \mathbf{C} \ , \tag{5.14}$$

$$\forall \mathbf{P}^{\mathrm{n}'} \in \mathbb{R}^3,\ \mathbf{T}^{\mathrm{n}'}_m(\mathbf{P}^{\mathrm{n}'}) \doteq \frac{1}{\lambda} U^\top \mathbf{T}^{\mathrm{n}}_m \left(\frac{1}{\mu} U(\mathbf{P}^{\mathrm{n}'} - \mathbf{D}) \right) \ . \tag{5.15}$$

It can then be checked that $\mathbf{T}^{\mathrm{n}'}_m$ also follows Maxwell's equations for a source-free region of space. This invariance motivates the definition of an equivalence relation "$\sim$" on Θ, which identifies two elements $\theta, \theta' \in \Theta$ if and only if there exists $\lambda, \mu > 0$, $U, V \in \mathrm{SO}(3)$ and $\mathbf{C}, \mathbf{D} \in \mathbb{R}^3$ such that

$$\theta' \doteq \left(({}_j\mathbf{p}^{\mathrm{b}'}), ({}_j\mathbf{a}^{\mathrm{b}'}), (\mathbf{T}^{\mathrm{n}'}_m) \right)$$

can be deduced from θ with Eqs. (5.13)-(5.15). In this case, we write $\theta \sim \theta'$. In terms of the equivalence relation "$\sim$", identifiability for Problem P1 corresponds to the injectivity of the mapping $[\theta] \mapsto \mathcal{H}$ on the *identification space* $\Theta/\sim$ (see Ref. Willard [2004], Def. (9.11) p. 62), where the notation $[\theta]$ denotes the equivalence class in $\Theta/\sim$ of the particular representative θ.

Reformulation of the localization problem P2

By construction, there exists at least one coordinatization of $\mathcal{H}$ by a subset of SE(3), namely $\mathcal{X}$. However, because of the above considerations, such a coordinatization is not unique. A whole family of them can be deduced from Eqs. (5.11)-(5.12). Therefore, to obtain a meaningful answer to Problem P2, let us reformulate it as such: Given $\theta \in \Theta$, is the application

$$\begin{aligned} \mathcal{X} &\to \mathcal{H} \\ (\mathbf{M}^{\mathrm{n}}, R) &\mapsto \mathbf{H}(R, \mathbf{M}^{\mathrm{n}}) \ . \end{aligned}$$

injective? If so, since it is surjective by definition of $\mathcal{H}$, then it is bijective. Thus its inverse can be recovered. Localization is then dependent on the ability to choose a unique representative θ in its equivalence class $[\theta]$, in a way that defines $\mathfrak{R}_{\mathrm{n}}$ and $\mathfrak{R}_{\mathrm{b}}$ along with the distance scale factor unambiguously.

Missing assumptions?

Proofs of identifiability and of injectivity of $(\mathbf{M}^{\mathrm{n}}, R) \mapsto \mathbf{H}(R, \mathbf{M}^{\mathrm{n}})$ have not been found, and assumptions are certainly missing for these results to hold (for example, regarding the minimal number of sensors and the space of admissible calibrations). Finally, let us remark that while the problem is stated in a Helmholtz coils configuration, this assumption has not yet been used.

5.3. Approach with Helmholtz coils

Until now, the fact that the coils were Helmholtz coils has not been used. Let us look at the practical implications of using this specific arrangement.

5.3.1. Magnetic field parameterization in ideal Helmholtz coils

Parallel (classic) configuration

The Helmholtz coils configuration is illustrated in Fig. 5.2. Let us consider an orthonormal frame of reference. Let us consider a 1-turn coil of radius 1, axis z and center $z = -1/2$, crossed by a current 1 spinning in counter-clockwise around z. Let us consider an identical coil placed at $z = 1/2$. Denoting the dimensionless variable $X = \begin{pmatrix} x \\ y \\ z \end{pmatrix}$ with $r = \sqrt{x^2 + y^2 + z^2}$ it can be show that the (dimensionless) magnetic field generated by this configuration reads

$$B_z^{\uparrow\uparrow}(X) = \begin{pmatrix} \frac{1}{125}\left(-216x^3z - 216xy^2z + 288xz^3\right) + O(r^5) \\ \frac{1}{125}\left(-216y^3z - 216x^2yz + 288yz^3\right) + O(r^5) \\ 1 - \frac{1}{125}\left(-54x^4 - 108x^2y^2 + 432x^2z^2 - 54y^4 + 432y^2z^2 - 144z^4\right) + O(r^5) \end{pmatrix} \tag{5.16}$$

Denoting ℓ the radius of the coils, μ_0 the magnetic constant and $I_z^{\uparrow\uparrow}$ the current in the coils, to link the dimensionless variables with the dimensional variables,

- x, y, z are obtained by division of a length by ℓ

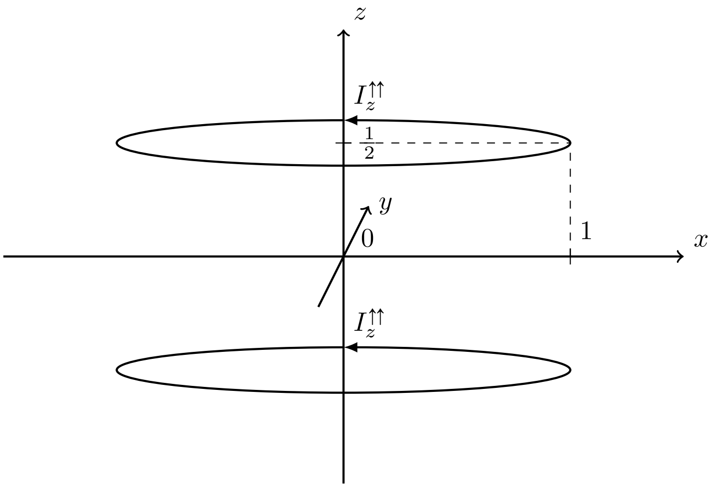

Figure 5.2: Parallel (classic) Helmholtz coils configuration along the z axis.

- $B_z^{\uparrow\uparrow}(X)$ is obtained by division of a magnetic field by $\dfrac{8\mu_0 I_z^{\uparrow\uparrow}}{5\sqrt{5}\ell}$.

The magnetic field is then parallel to the z axis up to order 4 around the origin.

Antiparallel (gradient) configuration

The antiparallel Helmholtz coils configuration is illustrated in Fig. 5.3. It is obtained by reversing the current in the coil placed at $z = -1/2$. With the same notations as above,

$$B_z^{\uparrow\downarrow}(X) = \begin{pmatrix} -x + \frac{1}{5}\left(-4x^3 - 4xy^2 + 16xz^2\right) + O(r^5) \\ -y + \frac{1}{5}\left(-4x^2y - 4y^3 + 16yz^2\right) + O(r^5) \\ 2z + \frac{1}{5}\left(16x^2z + 16y^2z\right) - \frac{32}{15}z^3 + O(r^5) \end{pmatrix} . \tag{5.17}$$

- x, y, z are still obtained by division of a length by ℓ,
- $B_z^{\uparrow\downarrow}$ is obtained by division of a magnetic field by $\dfrac{24\mu_0 I_z^{\uparrow\downarrow}}{25\sqrt{5}\ell}$. This coefficient is different from the one of the parallel configuration.

3-axis coil configuration

The above parameterization can be generalized to an orthogonal 3-axis configuration by axes relabeling. In the following, it is assumed that in the ideal configuration, the three axes are aligned with those of $\mathfrak{R}_\mathrm{n}$.

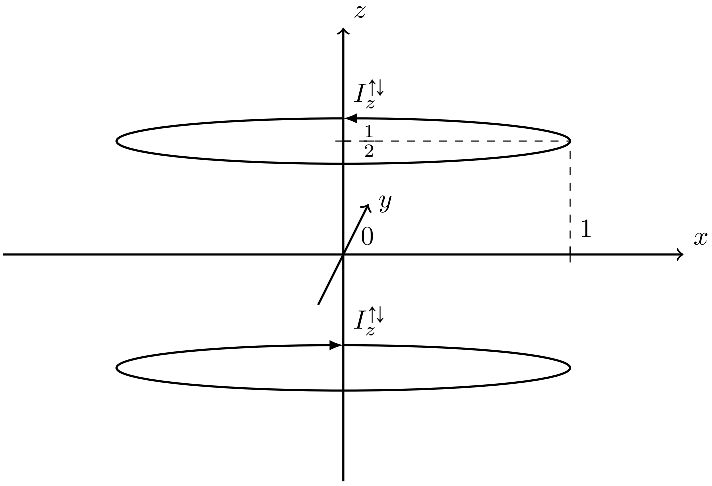

Figure 5.3: Antiparallel (gradient) Helmholtz coils configuration along the z axis.

5.3.2. Localization principle

Let us consider 3 ideal identical Hemholtz coils mounted to form 3-axis coils such as in Fig. 5.1.[3] The (dimensional) magnetic field around the center of the coils reads

$$\mathbf{B}^{\mathrm{n}}(X,t) = \frac{8\mu_0}{5\sqrt{5}\ell}\begin{pmatrix}1 & 0 & 0\\ 0 & 1 & 0\\ 0 & 0 & 1\end{pmatrix}\begin{pmatrix}I_x^{\uparrow\uparrow}\\ I_y^{\uparrow\uparrow}\\ I_z^{\uparrow\uparrow}\end{pmatrix} + \frac{24\mu_0}{25\sqrt{5}\ell}\begin{pmatrix}2x & -x & -x\\ -y & 2y & -y\\ -z & -z & 2z\end{pmatrix}\begin{pmatrix}I_x^{\uparrow\downarrow}\\ I_y^{\uparrow\downarrow}\\ I_z^{\uparrow\downarrow}\end{pmatrix} + O(r^3) \tag{5.18}$$

From the above equation, it can be seen that it is possible to deduce the position of a calibrated 3-axis magnetometer placed around the origin. Indeed, in this case,

$$\begin{aligned}\begin{pmatrix}Y^1\\ Y^2\\ Y^3\end{pmatrix} &= R^\top \mathbf{B}^{\mathrm{n}}(X,t)\\ &= \frac{8\mu_0}{5\sqrt{5}\ell}R^\top\begin{pmatrix}I_x^{\uparrow\uparrow}\\ I_y^{\uparrow\uparrow}\\ I_z^{\uparrow\uparrow}\end{pmatrix} + \frac{24\mu_0}{25\sqrt{5}\ell}R^\top\begin{pmatrix}2x & -x & -x\\ -y & 2y & -y\\ -z & -z & 2z\end{pmatrix}\begin{pmatrix}I_x^{\uparrow\downarrow}\\ I_y^{\uparrow\downarrow}\\ I_z^{\uparrow\downarrow}\end{pmatrix} + O(r^3)\ .\end{aligned} \tag{5.19}$$

The attitude matrix R can then be directly deduced from the transfer matrix $\mathbf{H}$. Once R is known, position variables x, y, z can be obtained by solving an over-determined system from the knowledge of the transfer matrix $\mathbf{H}$.

Basis for the expression of currents The basis in which the current vector is expressed as $\begin{pmatrix}I^1 & I^2 & \dots & I^6\end{pmatrix}^\top = \begin{pmatrix}I_x^{\uparrow\uparrow} & I_y^{\uparrow\uparrow} & I_z^{\uparrow\uparrow} & I_x^{\uparrow\downarrow} & I_y^{\uparrow\downarrow} & I_z^{\uparrow\downarrow}\end{pmatrix}^\top$ is shown to be es-

---

[3] Let us ignore the fact that such a configuration is physically impossible, because otherwise, coils would go through each other. This issue is later addressed in calibration.

pecially convenient. Unless specified otherwise, this will be the default choice in the rest of this chapter.

Conclusion In the case of ideal 3-axis Helmholtz coils and an ideal 3-axis magnetometer, the answer to Problem P2 is positive, in that it is possible to determine the position of the 3-axis magnetometer around the origin.

Remark The computation of attitude and position involves solving an overdetermined system (18 equations for only 6 degrees of freedom).

5.3.3. Finite dimensional parameterization with uncalibrated systems

In Sec. 5.3.1, the particular case of ideal Helmholtz coils with an ideal 3-axis magnetometer has been considered. Addressing the calibration problem P1 involves generalizing to uncalibrated coils with an uncalibrated magnetometer array, and taking into account the invariance issue raised in Sec. 5.2.3. This generalization is discussed thereafter.

Uncalibrated coils

As mentioned above, let us assume that currents are expressed in the basis where

$$\begin{pmatrix} I^1 & I^2 & \dots & I^6 \end{pmatrix}^\top = \begin{pmatrix} I_x^{\uparrow\uparrow} & I_y^{\uparrow\uparrow} & I_z^{\uparrow\uparrow} & I_x^{\uparrow\downarrow} & I_y^{\uparrow\downarrow} & I_z^{\uparrow\downarrow} \end{pmatrix}^\top \ . \tag{5.20}$$

Each function $\mathbf{T}^{\mathrm{n}}_m$, $1 \leqslant m \leqslant 6$ must, by assumption, follow Maxwell's equations for a source-free region of space on a subset $\mathcal{X} \subset \mathrm{SE}(3)$. The space of such functions is infinite-dimensional. On this subset, representing each $\mathbf{T}^{\mathrm{n}}_m$ by its coordinates in a finite-dimensional subspace of solution to Maxwell's equations (see Ref. Jackson [1998]), written with the dimensionless variables x, y, z yields

$$T^k{}_m(\ell X) = J^k{}_l(X)\alpha^l{}_m \ , \tag{5.21}$$

where functions $J^k{}_l(X)$ represent basis vectors of this space of solutions, and $\alpha^l{}_m$ are dimensionless coordinates representing the function $T^k{}_m$ in this space. Working in a finite-dimensional subspace of solutions, however, reduces the size of the set on which it is representative of actual possible solutions, making the coils' calibration more "local".

Solving the ambiguities of navigation frame, distance rescaling, and magnetic field rescaling can be achieved by imposing restrictions on the space of solutions. To that end, let us admit that the coordinate system of $\mathfrak{R}_{\mathrm{n}}$ can always be chosen (using

Eqs. (5.11)-(5.15)) in such a way that for example, at its origin,

$$T^2{}_1(0) = 0 \tag{5.22}$$

$$T^3{}_1(0) = 0 \tag{5.23}$$

$$T^3{}_2(0) = 0 \tag{5.24}$$

$$T^1{}_4(0) = 0 \tag{5.25}$$

$$T^2{}_5(0) = 0 \tag{5.26}$$

$$T^3{}_6(0) = 0 \tag{5.27}$$

$$T^1{}_1(0) = \frac{8\mu_0}{5\sqrt{5}\ell} \tag{5.28}$$

$$\frac{\partial}{\partial x}\, T^1{}_4(X)\big|_{X=0} = -2\frac{24\mu_0}{25\sqrt{5}\ell}\ . \tag{5.29}$$

Eqs. (5.22)-(5.24) determine the orientation of $\mathfrak{R}_\mathrm{n}$, Eqs. (5.25)-(5.27) determine the origin of R_n, Eq. (5.28) determines the magnetic field scale factor, and Eq. (5.29) determines the distance scale factor. The last two equations are arbitrary choices relying on the precision of the manufacturing of the coils of axis x and can be modified whenever a more accurate value can be defined for given hardware. These relationships can be transformed into conditions on coefficients $\alpha^l{}_m$.

Remark Functions $T^k{}_m$ can be entirely dimensionless if coefficients $H^i{}_m$ are also dimensionless. It is then possible to simply define, for example

$$T^1{}_1(0) = 1 \tag{5.30}$$

$$\frac{\partial}{\partial x}\, T^1{}_4(X)\big|_{X=0} = -2\ . \tag{5.31}$$

and make $H^i{}_m$ coefficients dimensionless by dividing them by $\frac{8\mu_0}{5\sqrt{5}\ell}$ if $m \leqslant 3$ or $\frac{24\mu_0}{25\sqrt{5}\ell}$ by if $m > 3$. This way, identification algorithms can be executed on dimensionless quantities.

Uncalibrated magnetometer arrays

There are several ways to define $\mathfrak{R}_\mathrm{b}$ from a choice of parameters. One such a way (others are possible) is to assert that

$$\mathfrak{a}^1{}_2 = 0 \tag{5.32}$$

$$\mathfrak{a}^1{}_3 = 0 \tag{5.33}$$

$$\mathfrak{a}^2{}_3 = 0 \tag{5.34}$$

$${}_1\mathbf{p}^\mathrm{b} = 0\ . \tag{5.35}$$

Finally, for an uncalibrated array of magnetometers, coefficients $H^i{}_m$ can be expressed as

$$H^i{}_m(R, \ell X) = \mathfrak{a}^i{}_j S^j{}_k J^k{}_l(R\ {}_i\mathbf{p}^\mathrm{b}/\ell + X)\ \alpha^l{}_m\ . \tag{5.36}$$

Following the same remarks as above, all computations can be achieved on dimensionless versions of $H^i{}_m$, along with using $\frac{8\mu_0 I_0}{5\sqrt{5}\ell}\mathfrak{a}^i{}_j$ and ${}_i\mathbf{p}^\mathrm{b}/\ell$ as dimensionless calibration parameters in place of $\mathfrak{a}^i{}_j$ and ${}_i\mathbf{p}^\mathrm{b}$, where I_0 denotes a constant reference current (e.g. 1 A).

5.4. Calibration simulation

Identifiability is assessed in simulation on numerical experiments. A first experiment consists in, given a random set of parameters

$$\theta \doteq \big(({}_j\mathbf{p}^\mathrm{b}), ({}_j\mathbf{a}^\mathrm{b}), (\alpha^l{}_m)_{1\leqslant m\leqslant 6,\ 1\leqslant l\leqslant \ldots}\big) \ ,$$

and a random set of 6D positions

$$(R[k], \mathbf{M}^\mathrm{n}[k]) \in \mathcal{X} \subset \mathrm{SE}(3) \ , \ 1 \leqslant k \leqslant n_\mathrm{pos} \ ,$$

deducing the exact theoretical values of $H^i{}_m(R[k], \mathbf{M}^\mathrm{n}[k])$ for each value of $(R[k], \mathbf{M}^\mathrm{n}[k])$, then, given the set of generated $H^i{}_m(R[k], \mathbf{M}^\mathrm{n}[k])$, numerically computing estimates of the corresponding starting parameters

$$\hat{\theta} \doteq \big(({}_j\hat{\mathbf{p}}^\mathrm{b}), ({}_j\hat{\mathbf{a}}^\mathrm{b}), (\hat{\alpha}^l_m)_{1\leqslant m\leqslant 6,\ 1\leqslant l\leqslant \ldots}\big)$$

and the corresponding estimated values $(\hat{R}[k], \widehat{\mathbf{M}}^\mathrm{n}[k])$. The desired outcome is that the result must be identical to the starting parameters up to machine precision, for initial conditions in a plausible range of values.

A second experiment consists in, instead of generating a random set of parameters

$$\theta \doteq \big(({}_j\mathbf{p}^\mathrm{b}), ({}_j\mathbf{a}^\mathrm{b}), (\mathbf{T}^\mathrm{n}_m)\big) \ ,$$

by expressing $(\mathbf{T}^\mathrm{n}_m)$ as a finite element simulation of imperfect Helmholtz coils. Each coils is represented by a broken line forming 40 loops of around 200 line segments, and the magnetic field is computed with the Biot-Savart law (see Ref. Jackson [1998]). In order to simulate imperfections, they are scaled by at most a thousandth, translated by at most a thousandth of their radius, and rotated by at most tenth of a degree. The same identification as above is undertaken using the finite dimensional parameterization $(\alpha^l{}_m)_{1\leqslant m\leqslant 6,\ 1\leqslant l\leqslant \ldots}$ to represent the magnetic field. Identification errors are expected for scale factors and effective positions. The quality of magnetic field estimation is not evaluated.

Both experiments rely on an identification algorithm that must be described. The one used thereafter is the Gauss-Newton algorithm, but any other non-linear least-square solver could have been chosen.

Outline The Gauss-Newton identification algorithm is briefly described in Sec. 5.4.1, and the results of the two identification experiments are explained in Sec. 5.4.2.

5.4.1. Identification algorithm

Denoting $H^i{}_m(R[k], \ell X[k])$ and $\hat{H}^i_m(\hat{\theta}, \hat{R}[k], \ell\hat{X}[k])$ the measured transfer matrix coefficients and their theoretical value using Eq. (5.36) respectively, the identification algorithm aims at minimizing

$$\Lambda(\hat{\theta}, (\hat{R}[k], \hat{X}[k])_{1 \leqslant k \leqslant n_{\mathrm{pos}}}) = \sum_i \sum_m \sum_k [H^i{}_m(R[k], \ell X[k]) - \hat{H}^i_m(\hat{\theta}, \hat{R}[k], \ell\hat{X}[k])]^2 \ . \tag{5.37}$$

Because $\hat{R} \in \mathrm{SO}(3)$, the exponential mapping described p. 25 in Sec. 2.4.2 is used to parameterize SO(3) locally, around each $\hat{R}[k]$. The iterative optimization algorithm used is then a straightforward Gauss-Newton algorithm. The new estimate is obtained by linearizing each $\hat{H}^i_m(\hat{\theta}, \hat{R}[k], \ell\hat{X}[k])$ for all variables, solving the linearized least-squares system thus obtained, replacing $(\hat{\theta}, (\hat{R}[k], \hat{X}[k])_{1 \leqslant k \leqslant n_{\mathrm{pos}}})$ by the obtained values, and iterating.

5.4.2. Numerical results

First numerical experiment In the first numerical experiment, a planar arrangement of 12 single axis magnetometers is simulated with randomly chosen calibration parameters. Let us denote

$$\varepsilon_{\mathbf{p}} = \sqrt{\sum_{j,k} \frac{1}{\ell^2} ({}_j\hat{\mathfrak{p}}^k - {}_j\mathfrak{p}^k)^2} \ , \tag{5.38}$$

$$\varepsilon_{\mathbf{a}} = \sqrt{\sum_{i,j} \left(\frac{8\mu_0 I_0}{5\sqrt{5}\ell}\right)^2 (\hat{\mathfrak{a}}^i{}_j - \mathfrak{a}^i{}_j)^2} \ , \tag{5.39}$$

$$\varepsilon_{\boldsymbol{\alpha}} = \sqrt{\sum_{l,m} (\hat{\alpha}^l_m - \alpha^l{}_m)^2} \ . \tag{5.40}$$

These three norms of estimation errors can be evaluated after each Gauss-Newton iteration and plotted in Fig. 5.4, that shows a convergence up to machine precision after 6 iterations. The identification algorithm systematically converges to the correct parameter values up to machine precision. The same convergence is observed on trajectory parameters (not illustrated).

Second numerical experiment In the second numerical experiment, the magnetic field is computed with a finite-elements simulation representing imperfect coils. Since coils are imperfect and since dimension factors are defined from magnetic field parameters; parameters must be optimally rescaled for distance and magnetic field units in order to minimize $\varepsilon_{\mathbf{p}}$ and $\varepsilon_{\mathbf{a}}$. These two norms of estimation errors are evaluated after each Gauss-Newton iteration and plotted in Fig. 5.5, that shows a convergence up to machine precision after five iterations. The identification algorithm converges towards a value that is close to the actual parameters. This small error can be explained by

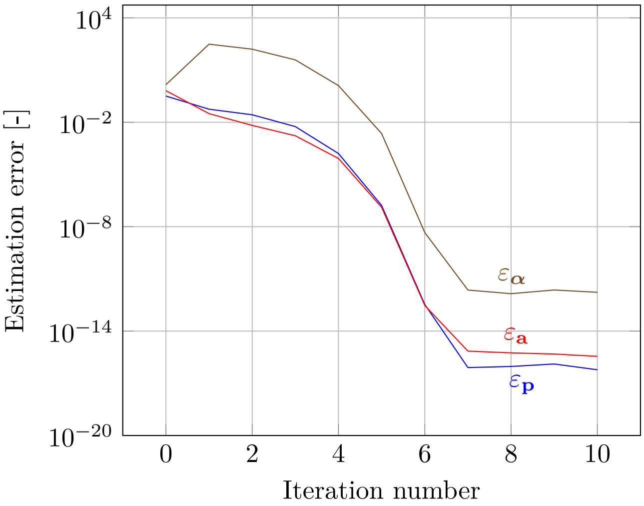

Figure 5.4: Evolution of calibration parameters estimation error, with respect to iteration number for simulated data for Problem P1. Iteration number 0 corresponds to initial conditions.

the distance between the parameter space used to simulate measurements and the lower-dimensional one in which the identification takes place.

5.4.3. Conclusion

In simulation, the answer to Problem P1 has been positive in all tested cases where coil calibration functions have been restricted to a finite-dimensional space. This restriction can be used as an approximation of more general cases at the cost of a small identification error.

The number of distinct positions required for convergence depends on the parameter space. In particular, if effective positions and coil calibration parameters are known[4] scale factors can be identified in simulation from a manifold $\mathcal{X}$ containing a single element.

5.5. Calibration experiments

Experiments have been carried out using two 3-axis magnetometers fixed onto a board, 10 cm apart, whose calibration parameters have been individually estimated using a different technique. The six Helmholtz coils are powered using independent signals, enabling the computation of transfer coefficients $\hat{H}_m^i$.

---

[4] Knowledge of effective positions defines $\mathfrak{R}_{\mathrm{b}}$ unambiguously, which imply not using Eqs. (5.32)-(5.34).

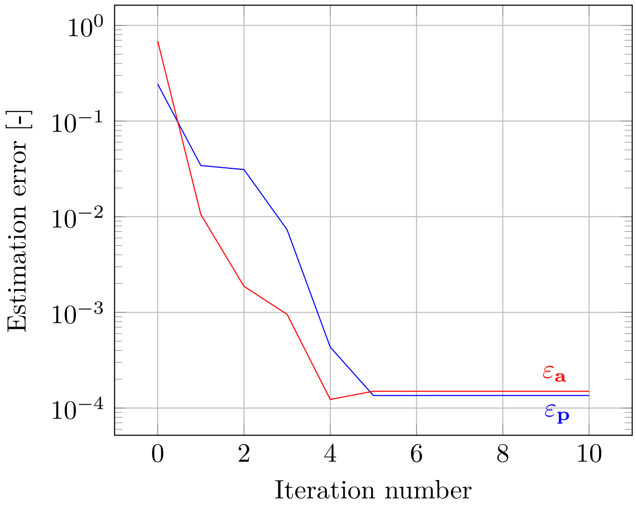

Figure 5.5: Evolution of calibration parameters estimation error, with respect to iteration number *for finite-elements simulated data* for Problem P1. Iteration number 0 corresponds to initial conditions. The identification algorithm converges close to the true parameter values, albeit not to machine precision.

Estimated scale factors reproduce the ones obtained with a different technique with a precision that is coherent with the accuracy of the measurement system, validating the two calibration techniques against each-other (see Table. 5.1). The distance between the two three-axis magnetometers is correctly estimated as 10 cm ±1 mm, which is expected considering the precision of the assembly.

5.6. Conclusion

This chapter has demonstrated a method by which a magnetometer array can be precisely calibrated using 3-axis Helmholtz coils. This method has the same advantage as ellipsoid fitting techniques that no precision is required when placing the magnetometer array inside of the coils, the byproduct of the calibration process is an estimate of the array's trajectory. The main advantage of this technique over ellipsoid fitting is that it gives access to effective positions, thus allowing the full calibration of a magnetometer array. This method preserves calibration accuracy when the size of the system is close to the size of the zone in which the magnetic field is considered homogeneous, in the center of the coils. Moreover, it provides a simple way to characterize this zone.

Numerical results show that with marginal changes, this approach may be generalized to arbitrary arrangements of at least six coils with at least two single-axis magnetometers.

The main disadvantage of this technique is that accurate synchronized measurements

Table 5.1.: Experimental scale factor estimation errors.
The function $f_{\mathbf{a}}$ denotes an increasing function. The error $\varepsilon_{\mathbf{a}}$ is evaluated by comparing normalized scale factors obtained with the described technique and normalized reference scale factors obtained with another technique. The function $f_{\mathbf{a}}$ is chosen such that, considering the measurement system's accuracy, the comparison between calibrated values must yield a negative number.

	$f_{\mathbf{a}}(\varepsilon_{\mathbf{a}})$, 3-axis #1	$f_{\mathbf{a}}(\varepsilon_{\mathbf{a}})$, 3-axis #2
before calibration	12.96	12.97
trial #1	-3.51	-2.61
trial #2	-3.84	-2.34
trial #3	-3.21	-2.40
trial #4	-4.27	-2.32

of currents inside of the coils are necessary. This disadvantage has implications for hardware design.

6. Calibration of a magnetometer array using motion information

Contents

This chapter is a transcript of an article submitted to the Special Issue of the Asian Journal of Control on Recent Advances on Data Fusion, Estimation in Navigation and Control, entitled *Calibration of a magnetometer array using motion capture equipment* (C.-I. Chesneau, R. Robin, H. Meier, M. Hillion and C. Prieur), to be published in 2019.

6.1. Introduction

Precise calibration of micro-electronic single-axis point-magnetometers is often required for practical applications. This is especially true for Magneto-Inertial Dead-Reckoning (MIDR), described in Part. I, a technique which is rather demanding regarding magnetometer calibration accuracy. As stated in Ch. 3 and Ch. 5 the problem of precisely calibrating an array of single-axis magnetometers is still not satisfactorily solved in order to be applicable in so-called MIDR applications. This observation motivates the research of a calibration technique that is less demanding on the environment and dedicated setups than existing techniques, including the one introduced in Ch. 5.

In parallel with this work, several frameworks have been provided, in which magnetic sensor information can be combined with visual odometry (see Refs. Caruso et al. [2016, 2017b,c]), resulting in a robust dead-reckoning navigation solution. In such setups, positioning is often achievable without relying on magnetometers. It is then of interest that a precise magnetometer calibration technique is available to leverage positioning information, thereby enabling their on-the-field self-calibration.

This chapter presents a calibration technique for magnetometer arrays solving a problem inverse to MIDR. Whereas the latter, applicable for an indoor stationary (inhomogeneous) magnetic field (see Ref. Chesneau et al. [2017]), allows us to obtain positions and attitudes as a function of the calibration parameters (and the raw magnetic data), the present method builds on raw magnetic data paired with motion capture data, i.e. position and attitude of the array of the moving sensor device, in order to estimate calibration parameters as well as the magnetic field. The only parameter that is not accessible through our method is the global scale factor that defines the unit of the magnetic field (and may be adjusted to Tesla or Gauss in a separate experiment if desired); in any case, the choice of such a unit does not intervene in magneto-inertial dead-reckoning.

The chapter is organized as follows. In Sec. 6.2, we state the explicit problem addressed by this article. In Sec. 6.3, we mathematically prove the identifiability of calibration parameters. Section 6.4 shows, using simulated data, that calibration parameters are in practice identifiable. Finally, Section 6.5 shows the results of applying this technique in real-world experiments, and Sec. 6.6 contains some concluding remarks and points out a natural perspective. The appendices collect some proofs of intermediate results.

6.2. Problem statement

The problem under consideration is the calibration of an array of linear-response single-axis point magnetometers strapped on a rigid body using motion information.

Let $\mathbf{M}$ be a fixed point of the rigid body defining the origin of the body frame $\mathfrak{R}_b$; by definition, its coordinates in body frame are $\mathbf{M}^{\mathrm{b}} \doteq 0$. Let R be the attitude matrix belonging to the special orthogonal group SO(3), defined in the same way as in previous chapters. The rigid body motion is defined by the time-evolution of $\mathbf{M}^{\mathrm{n}}(t)$ and $R(t)$ during an experiment.

Let $\mathbf{B}$ denote the magnetic field, which is assumed static in $\mathfrak{R}_n$. This means that $\mathbf{B}^{\mathrm{n}}$ varies only as a function of the position $\mathbf{M}^{\mathrm{n}}$,

$$\begin{aligned} \mathbf{B}^{\mathrm{n}} : \mathbb{R}^3 &\to \mathbb{R}^3 \\ \mathbf{M}^{\mathrm{n}} &\mapsto \mathbf{B}^{\mathrm{n}}(\mathbf{M}^{\mathrm{n}}). \end{aligned}$$

Let ${}_j\mathbf{p}^{\mathrm{b}}$ denote the position of the j-th single-axis magnetic sensor in the moving reference frame $\mathfrak{R}_b$. The magnetic field at this point, and in $\mathfrak{R}_b$, is related to the magnetic field in the navigation frame $\mathfrak{R}_n$ as[1].

$$\mathbf{B}^{\mathrm{b}}\left({}_j\mathbf{p}^{\mathrm{b}}, t\right) = R(t)^\top \mathbf{B}^{\mathrm{n}}\left(\mathbf{M}^{\mathrm{n}}(t) + R(t)_j\mathbf{p}^{\mathrm{b}}\right) \ . \tag{6.1}$$

As $\mathbf{M}^{\mathrm{n}}$ and R vary as a function of time, so does in general $\mathbf{B}^{\mathrm{b}}$.

To complete our measurement model, we specify the direction and scale factor of the j-th single-axis magnetic sensor by a co-vector ("row vector") ${}_j\mathbf{a}^{\mathrm{b}}$ and add a (scalar) bias ${}_jb$. The full model for a measurement with result ${}_jy$ then reads

$${}_jy = {}_j\mathbf{a}^{\mathrm{b}} R^\top \mathbf{B}^{\mathrm{n}}\left(\mathbf{M}^{\mathrm{n}} + R\ {}_j\mathbf{p}^{\mathrm{b}}\right) + {}_jb \tag{6.2}$$

for each magnetic single-axis sensor j. It is implied that the co-vector ${}_j\mathbf{a}^{\mathrm{b}}$, the bias ${}_jb$, and the position vector ${}_j\mathbf{p}^{\mathrm{b}}$ (which is a usual "column vector") are time-independent.

The magnetic field $\mathbf{B}^{\mathrm{n}}$ lives in an infinite-dimensional vector space — the space of solutions to Maxwell's equations. In practice, it is typically possible to describe this field with sufficient accuracy in a finite-dimensional subspace, using only a finite number of coordinates that we denote α_i.

During a calibration, $\mathbf{M}^{\mathrm{n}}(t)$ and $R(t)$ are varied as a function of time t with $t_i \leqslant t \leqslant t_f$. The time-dependency of these (6D) coordinates inflicts a time-dependency on the measurement functions ${}_jy$. In the situation of an experiment that allows us to measure all these quantities, $\mathbf{M}^{\mathrm{n}}(t)$, $R(t)$, and ${}_jy(t)$ at each time t, $t_i \leqslant t \leqslant t_f$, we consider the following problems:

P1 Are parameters ${}_j\mathbf{a}^{\mathrm{b}}$, ${}_jb$, and magnetic field coordinates α_i identifiable if the effective position parameters ${}_j\mathbf{p}^{\mathrm{b}}$ are given?

P2 Are parameters ${}_j\mathbf{a}^{\mathrm{b}}$, ${}_jb$, ${}_j\mathbf{p}^{\mathrm{b}}$, and magnetic field coordinates α_i identifiable?

---

[1] In fact, Eq. (6.1) is merely a (Galilean) transformation between the two reference frames (see Ref. [Jackson, 1998, 6.10.A, 11.10])

Problem P1 implies that we have to know the effective position of each individual sensor in both $\mathfrak{R}_b$ and $\mathfrak{R}_n$. Problem P2 does not require us to possess this information, a situation that is closer to what is obtained in a motion capture experiment: such a setup locates visual markers, while sensors are typically hidden inside of a package, and their position is not precisely known with respect to markers. Furthermore, effective positions are needed in order to calibrate a magnetic gradiometer built from an array of sensors. Proving that parameters are identifiable in Problems P1 and P2 would be equivalent to proving that any parameterization to (6.2) is unique — a notion we clarify in the next section. At the same time, the mere existence of such a parameterization is guaranteed in experiments by the physics behind the measurement model.

6.3. Identifiability

In this section, we prove the identifiability of calibration parameters under "mathematically controlled" conditions that, as we argue, represent the situation in realistic experiments nevertheless.

6.3.1. Notion of identifiability and assumptions

We adopt the setting of Sec. 6.2 and consider a set of m single-axis magnetometers that measure the projection of the magnetic field $\mathbf{B}$. The field $\mathbf{B}$ is assumed time-independent in our navigation frame $\mathfrak{R}_n$. The measurement of each magnetometer is physically modeled by a function ${}_jy$, $j \in \{1, 2, \ldots, m\}$, that assigns to a 6D position $(\mathbf{M}^\mathrm{n}, R)$ of the rigid body the magnetic field component along the axis of the j-th magnetometer,

$$\begin{aligned} {}_jy :\ & \mathbb{R}^3 \times \mathrm{SO}(3) \to \mathbb{R} \\ & (\mathbf{M}^\mathrm{n}, R) \mapsto {}_j\mathbf{a}^\mathrm{b} R^\top \mathbf{B}^\mathrm{n}\left(\mathbf{M}^\mathrm{n} + R\ {}_j\mathbf{p}^\mathrm{b}\right) + {}_jb\ . \end{aligned} \tag{6.3}$$

We note that for a reasonable sensor, ${}_j\mathbf{a}^\mathrm{b} \neq 0$, which is what we thus assume in the following. The magnetic field $\mathbf{B}^\mathrm{n}$ is assumed to satisfy Maxwell's equations for a source-free region of space (which in particular implies analyticity). Furthermore, $\mathbf{B}^\mathrm{n}$ is assumed not to vanish identically and to feature at least one position in which all eigenvalues of its derivative (Jacobian matrix) are different from each other. Any realistic magnetic field verifies this assumption. [2]

---

[2] In Eqs. (6.1) and (6.3), we consider for the sake of simple notations $\mathbb{R}^3$ as domain of our fields. We could also restrict ourselves to a bounded open subset without any loss of validity of our statement. In an actual experiment, the position $\mathbf{M}^\mathrm{n}$ is restricted to vary within some (bounded) open subset $V \subset \mathbb{R}^3$. Also, it is sufficient to consider position vectors ${}_j\mathbf{p}^\mathrm{b}$ within a ball whose radius r is of the order of the linear size of the device that contains all magnetometers. Then, the domain of the magnetic field $\mathbf{B}^\mathrm{n}$ can also be restricted to an open bounded subset $\subset \mathbb{R}^3$, for instance, the interior of the union of the balls of radius r around all $\mathbf{M}^\mathrm{n} \in V$. Physical source currents of the magnetic field are assumed to be outside this subset.

In experiment, all the parameters and the magnetic field are *a priori* unknown and need to be determined in calibration. Let us unite these parameters into one tuple θ,

$$\theta \doteq \left(({}_j b), ({}_j \mathbf{p}^{\mathrm{b}}), ({}_j \mathbf{a}^{\mathrm{b}}), \mathbf{B}^{\mathrm{n}} \right) \ , \tag{6.4}$$

where the notation $({}_j b) = ({}_j b)_{j=1,\ldots,m}$ represents the tuple of biases for all m magnetometers (and the same applies to $({}_j \mathbf{p}^{\mathrm{b}})$ and $({}_j \mathbf{a}^{\mathrm{b}})$). The space of all such θ will be denoted Θ. Each element $\theta \in \Theta$ defines a set of m measurement functions ${}_j y$, Eq. (6.3).

We interpret identifiability as the ability to distinguish different tuples of parameters by their corresponding measurement functions. This means that if two tuples of parameters θ and θ' in the parameter space Θ are different, $\theta \neq \theta'$, then their corresponding measurement functions $({}_j y)$ and $({}_j y')$ should be different too. In other words, there should be at least one 6D position $\mathbf{M}^{\mathrm{n}}, R$ of the rigid body for which at least one of the m magnetometers, say magnetometer j, produces a different measurement result, i.e. ${}_j y(\mathbf{M}^{\mathrm{n}}, R) \neq {}_j y'(\mathbf{M}^{\mathrm{n}}, R)$.

However, this notion of identifiability is a little too strong to hold, as revealed by a quick inspection of Eq. (6.3). In fact, the functions $({}_j y)$ are invariant under simultaneous rescaling ${}_j \mathbf{a}^{\mathrm{b}} \mapsto \lambda_j \mathbf{a}^{\mathrm{b}}$ and $\mathbf{B}^{\mathrm{n}} \mapsto \mathbf{B}^{\mathrm{n}}/\lambda$ for $\lambda \in \mathbb{R}\backslash\{0\}$, which corresponds just to the global scale factor that, as we mentioned in Sec. 6.1, we cannot calibrate.

This invariance motivates the definition of an equivalence relation "$\sim$" on Θ, which identifies two elements $\theta, \theta' \in \Theta$ if and only if there exists a $\lambda \in \mathbb{R}\backslash\{0\}$ such that

$$\begin{gathered} \mathbf{B}^{\mathrm{n}\prime} \equiv \mathbf{B}^{\mathrm{n}}/\lambda \ , \\ \forall\ j,\ {}_j b' = {}_j b \ , {}_j \mathbf{p}^{\mathrm{b}\prime} = {}_j \mathbf{p}^{\mathrm{b}} \ , {}_j \mathbf{a}^{\mathrm{b}\prime} = \lambda \ {}_j \mathbf{a}^{\mathrm{b}}. \end{gathered}$$

In this case, we write $\theta \sim \theta'$. In terms of the equivalence relation "$\sim$", we aim to prove identifiability in the sense that for two tuples $\theta, \theta' \in \Theta$, that are not equivalent, $\theta \nsim \theta'$, the measurement functions are able to distinguish them from each other at least at one 6D position for at least one magnetometer, i.e. if $\theta \nsim \theta'$, there exists a tuple $(j, \mathbf{M}^{\mathrm{n}}, R)$ such that ${}_j y(\mathbf{M}^{\mathrm{n}}, R) \neq {}_j y'(\mathbf{M}^{\mathrm{n}}, R)$.

In a more formal reformulation, the notion of identifiability we wish to prove is injectivity of the mapping $\theta \mapsto ({}_j y)$ on the *identification space* $\Theta/\sim$, see, e.g., Ref. Willard [2004], Def. (9.11) p. 62. The mapping is defined by inserting a representative θ into Eq. (6.3). Here and in the following, we use the notation θ for a particular representative of equivalent parameter tuples also for its equivalence class in $\Theta/\sim$.

6.3.2. Theorems of identifiability

Adopting the assumptions and notations of the previous sections, we formulate the following theorem of identifiability that addresses the problem P2 raised in Sec. 6.2:

Theorem 6.3.1. *For each tuple of parameters $\theta \in \Theta/\sim$, there exists an open neighborhood $T \subset \Theta/\sim$, $\theta \in T$, on which the mapping $\theta \mapsto ({}_j y)$, defined by inserting θ into Eq. (6.3), is injective.*

The restriction to an open neighborhood applies only to the effective sensor positions $({}_j \mathbf{p}^{\mathrm{b}})$. For biases $({}_j b)$, injectivity holds globally. For the scale factors ${}_j \mathbf{a}^{\mathrm{b}}$ and *the magnetic field* $\mathbf{B}^{\mathrm{n}}$*, no restriction of locality is imposed beyond the required properties discussed in the preceding section.*

In special situations, for instance, if an affine mapping fully describes the magnetic field, our proof allows immediately to lift the restriction to an open neighborhood of $({}_j\mathbf{p}^{\mathrm{b}})$ and the theorem holds globally.

As a corollary to Theorem 6.3.1, we find

Corollary 6.3.2. *The mapping* $\theta \mapsto ({}_j y)$*, defined by inserting* θ *into Eq. (6.3), is injective on any subset of* $\Theta/\sim$ *in which the sensor positions* $({}_j\mathbf{p}^{\mathrm{b}})$ *are constant.*

We note that this corollary, which addresses Problem P1, is, in fact, valid for arbitrary magnetic fields as long as they do not vanish identically. No requirement on its gradient is necessary. (In particular, the gradient would be allowed to be identically zero.)

6.3.3. Proof of Theorem 6.3.1

We proceed by proving parameter by parameter that changes in any parameter of a given $\theta \in \Theta/\sim$ result in a different measurement ${}_j y(\mathbf{M}^{\mathrm{n}}, R)$ for at least one 6D position $(\mathbf{M}^{\mathrm{n}}, R)$, regardless of possible simultaneous changes of other parameters whose identifiability has not yet been proven.

The proof is built on the (theoretical) availability of a trajectory that traverses the entire 6D position manifold while we can expect a suitably designed experimental trajectory to cover a large-enough and sufficiently diverse subset that is representative for the entire manifold.

Biases

The identifiability of the biases ${}_j b$ follows from the following lemma.

Lemma 6.3.3. *Let* $j \in \{1, 2, \ldots, m\}$*. Using the notation of the previous sections, for all* $\mathbf{M}^{\mathrm{n}}$*, the integral of* ${}_j y(\mathbf{M}^{\mathrm{n}}, R)$ *over* $R \in \mathrm{SO}(3)$ *yields*

$$\oint_{R \in \mathrm{SO}(3)} {}_j y(\mathbf{M}^{\mathrm{n}}, R)\ \mathrm{d}R = {}_j b, \tag{6.5}$$

where $\mathrm{d}R$ *denotes the Haar measure of* $\mathrm{SO}(3)$ *that normalizes its volume to unity.*

Proof See Appendix B.1.

Lemma 6.3.3 implies that if two tuples of parameters θ and θ' that contain different biases ${}_j b$ and ${}_j b'$ for the j-th magnetometer, then the integral of Lemma 6.3.3 on their respective measurement functions will yield different results, regardless of other parameters. Inevitably, the measurement functions must thus differ for at least one position. Therefore, biases are identifiable.

Effective sensor positions

Let $j \in \{1, 2, \ldots, m\}$. Since the bias ${}_j b$ has been proven identifiable (see the preceding Sec. 6.3.3), we can assume it to be zero, ${}_j b = 0$, without loss of generality.

As noted in the statement of Theorem 6.3.1, we refrain from trying to prove global injectivity with respect to the sensor positions $({}_j\mathbf{p}^{\mathrm{b}})$ and content ourselves with local injectivity around its true value.

Let $\theta_j = ({}_j\mathbf{p}^{\mathrm{b}}, {}_j\mathbf{a}^{\mathrm{b}}, \mathbf{B}^{\mathrm{n}})$ denote the tuple of the true parameters of the physical model. The reader may assume that we have already "guessed" the true ${}_j\mathbf{p}^{\mathrm{b}}$, yet we are still unaware of its (local) uniqueness.

As to the scale factor ${}_j\mathbf{a}^{\mathrm{b}}$ and the magnetic field $\mathbf{B}^{\mathrm{n}}$, the only information we need (and have) is that by assumption, ${}_j\mathbf{a}^{\mathrm{b}} \neq 0$ and that there is at least one position ${\mathbf{M}^{\mathrm{n}}}_0$ in which the gradient of the magnetic field (Jacobian matrix),

$$\nabla \mathbf{B}^{\mathrm{n}}\Big|_{{\mathbf{M}^{\mathrm{n}}}_0} = \frac{\partial(\mathbf{B}^{\mathrm{n}})}{\partial(\mathbf{M}^{\mathrm{n}})}\Big|_{\mathbf{M}^{\mathrm{n}} = {\mathbf{M}^{\mathrm{n}}}_0} ,$$

possesses eigenvalues that are all mutually different.

If, using only the knowledge of the measurement function ${}_j y$, we can construct an injective mapping ζ from the effective positions space $\mathbb{R}^3$ into some other vector space such that $\zeta({}_j\mathbf{p}^{\mathrm{b}}) = 0$ (independently from ${}_j\mathbf{a}^{\mathrm{b}}$ and $\mathbf{B}^{\mathrm{n}}$ as long as the assumptions stated above hold), uniqueness and thus identifiability of ${}_j\mathbf{p}^{\mathrm{b}}$ is proven.

Lemma 6.3.4. *Under the assumptions made for* ${}_j\mathbf{a}^{\mathrm{b}}$ *and* $\mathbf{B}^{\mathrm{n}}$*, the construction of a mapping* ζ *as described above is possible in an open neighborhood of* ${}_j\mathbf{p}^{\mathrm{b}}$*.*

Proof In Appendix B.2, we present an explicit construction of a mapping $\zeta : \mathbb{R}^3 \to \mathbb{R}^6$ using only knowledge of ${}_j y$.

Remarks In the special case that the Jacobian matrix of the magnetic field is constant, i.e. if the magnetic field is affine, the arguments provided in Appendix B.2 are sufficient to prove global identifiability.

Scale factors and magnetic field

Without loss of generality, θ is such that biases ${}_j b$ are zero and that effective sensor positions $({}_j\mathbf{p}^{\mathrm{b}})$ are known. Also, by assumption, there exists a position ${\mathbf{M}^{\mathrm{n}}}_0$ at which the magnetic field is non-zero, $\mathbf{B}^{\mathrm{n}}({\mathbf{M}^{\mathrm{n}}}_0) \neq 0$. In this situation, we can place any sensor, say the j-th, at this position ${\mathbf{M}^{\mathrm{n}}}_0$ (in navigation frame) for an arbitrary orientation R. This is possible by choosing

$$\mathbf{M}^{\mathrm{n}} = {\mathbf{M}^{\mathrm{n}}}_0 - R\, {}_j\mathbf{p}^{\mathrm{b}} . \tag{6.6}$$

As a result, a (theoretical) calibration experiment allows us to gain full knowledge of the auxiliary measurement function

$$\begin{aligned} {}_j Y(\mathbf{M}^{\mathrm{n}}{}_0) : R \mapsto {}_j y(\mathbf{M}^{\mathrm{n}}{}_0 - R\ {}_j\mathbf{p}^{\mathrm{b}}, R) \\ = \operatorname{Tr}\left[R^\top \mathbf{B}^{\mathrm{n}}(\mathbf{M}^{\mathrm{n}}{}_0) \otimes {}_j\mathbf{a}^{\mathrm{b}}\right], \end{aligned} \tag{6.7}$$

where ${}_j\mathbf{a}^{\mathrm{b}}$ and $\mathbf{B}^{\mathrm{n}}(\mathbf{M}^{\mathrm{n}}{}_0)$ denote the true (yet until now unknown to be unique) values for the scale vector and the magnetic field at $\mathbf{M}^{\mathrm{n}}{}_0$; the symbol Tr is the trace.

We observe that

$$A \mapsto \operatorname{Tr}\left[A^\top \mathbf{B}^{\mathrm{n}}(\mathbf{M}^{\mathrm{n}}{}_0) \otimes {}_j\mathbf{a}^{\mathrm{b}}\right] \tag{6.8}$$

defines a linear form on the space of real 3×3 matrices $\mathbb{R}^{3\times 3}$ whose uniquely defined (standard) gradient is the matrix $\mathbf{B}^{\mathrm{n}}(\mathbf{M}^{\mathrm{n}}{}_0) \otimes {}_j\mathbf{a}^{\mathrm{b}}$. Since SO(3) as generating set in $\mathbb{R}^{3\times 3}$ spans the entire matrix space, the knowledge of ${}_j Y(\mathbf{M}^{\mathrm{n}}{}_0)$ for matrices $R \in \mathrm{SO}(3)$ is sufficient to uniquely determine $\mathbf{B}^{\mathrm{n}}(\mathbf{M}^{\mathrm{n}}{}_0) \otimes {}_j\mathbf{a}^{\mathrm{b}}$.

The rank of $\mathbf{B}^{\mathrm{n}}(\mathbf{M}^{\mathrm{n}}{}_0) \otimes {}_j\mathbf{a}^{\mathrm{b}}$ is 1, lines are proportional to (the row vector) ${}_j\mathbf{a}^{\mathrm{b}}$, columns are proportional to (the column vector) $\mathbf{B}^{\mathrm{n}}(\mathbf{M}^{\mathrm{n}}{}_0)$, which means that ${}_j\mathbf{a}^{\mathrm{b}}$ is identifiable up to an unknown scale factor λ while the magnetic field at $\mathbf{M}^{\mathrm{n}}{}_0$ is identifiable up to an unknown scale factor $1/\lambda$.

Once $\mathbf{B}^{\mathrm{n}}(\mathbf{M}^{\mathrm{n}}{}_0)$ is identified up to the unknown scale factor $1/\lambda$, all scale factors of the other sensors ${}^{\mathrm{b}}_{j'}\mathbf{a}$ for $j' \neq j$ are identifiable (relatively to a chosen scale factor for ${}^{\mathrm{b}}_{j'}\mathbf{a}$), using the same construction.

Since this construction works at all positions $\mathbf{M}^{\mathrm{n}}{}_0$ with a non-zero magnetic field, the magnetic field itself is identifiable as well (up to an unknown scale factor $1/\lambda$). This concludes the proof of Theorem 6.3.1.

6.3.4. Conclusion of the proof and discussion

The above reasoning proves that Theorem 6.3.1 and its Corollary 6.3.2 hold. Theorem 6.3.1 states that unknown parameters corresponding to Problem P2 (defined in Sec. 6.2) are locally identifiable, as long as there exists at least one place where the magnetic gradient is non-singular, and if all magnetometer scale factors ${}_j\mathbf{a}^{\mathrm{b}}$ are different from zero. According to the remark at the end of Sec. 6.3.3, we are aware of at least one important special case in which identifiability holds globally in all of the parameter space.

Corollary 6.3.2 states that unknown parameters corresponding to Problem P1 (defined in Sec. 6.2) are globally identifiable, if the magnetic field is different from zero in at least one place, with no requirement about gradient. In both cases, magnetometer scale factors ${}_j\mathbf{a}^{\mathrm{b}}$ are only identifiable up to an unknown global scale factor λ, while the magnetic field ($\mathbf{B}^{\mathrm{n}}$) is identifiable up to the unknown global scale factor $1/\lambda$.

In practical applications, measurements are not known for all 6D positions: only a finite set of sampled measurements are provided. In the following, we show that in practice, identifiability is preserved in this situation.

6.4. Practical identifiability of parameters for simulated data

In this section, we want to check if for a given realistic input, the above calibration problem can be solved. We proceed by collecting motion capture data in order to get a realistic sampled trajectory. We denote $\mathbf{M}^{\mathrm{n}}[k]$ the sampled positions, and $R[k]$ the sampled attitudes, where k is the sample number. For the purpose of the simulation, we choose at random a realistic set of parameters $\big(({}_j b), ({}_j \mathbf{p}^{\mathrm{b}}), ({}_j \mathbf{a}^{\mathrm{b}}), (\alpha_i)\big)$, describing magnetometer calibration parameters and the magnetic field in the volume of the trajectory. Then we generate sampled values of measurements ${}_j y[k]$ according to (6.2) at each trajectory sample,

$$ {}_j y[k] = {}_j \mathbf{a}^{\mathrm{b}} R[k]^{\top} \mathbf{B}^{\mathrm{n}}{}_{(\alpha_i)} \left(\mathbf{M}^{\mathrm{n}}[k] + R[k]\ {}_j \mathbf{p}^{\mathrm{b}}\right) + {}_j b. \tag{6.9}$$

Problem P2 is rewritten as: given the set of sampled measurements ${}_j y[k]$ and the sampled trajectory $\mathbf{M}^{\mathrm{n}}[k]$, $R[k]$, find the exact set of parameters that has been used as input.

6.4.1. Scale factor ambiguity

Let us assume that there exists a tuple of parameters $\big(({}_j b), ({}_j \mathbf{p}^{\mathrm{b}}), ({}_j \mathbf{a}^{\mathrm{b}}), (\alpha_i)\big)$ satisfying (6.9). Let $\lambda > 0$. Then,

$$ {}_j y[k] = \lambda\ {}_j \mathbf{a}^{\mathrm{b}} R[k]^{\top} \frac{1}{\lambda} \mathbf{B}^{\mathrm{n}}{}_{(\alpha_i)} \left(\mathbf{M}^{\mathrm{n}}[k] + R[k]\ {}_j \mathbf{p}^{\mathrm{b}}\right) + {}_j b. \tag{6.10}$$

Thus a tuple of parameters containing $\frac{1}{\lambda}\mathbf{B}^{\mathrm{n}}{}_{(\alpha_i)}$ and $\lambda_j \mathbf{a}^{\mathrm{b}}$ is indistinguishable from the former tuple using only measurements ${}_j y[k]$, as discussed in Sec. 6.3. Therefore, in the rest of the document, we impose the global scale factor by setting the first coefficient of the scale factor of the first magnetometer to unity, ${}_1 a_1^{\mathrm{b}} = 1$.

6.4.2. Least-square parameter estimation model

Let us denote magnetic measurement residuals ${}_j r[k]$ such that for all j and k,

$$ {}_j r[k] \doteq {}_j \mathbf{a}^{\mathrm{b}} R[k]^{\top} \mathbf{B}^{\mathrm{n}}{}_{(\alpha_i)} \left(\mathbf{M}^{\mathrm{n}}[k] + R[k]_j \mathbf{p}^{\mathrm{b}}\right) + {}_j b - {}_j y[k] \tag{6.11}$$

By Eq. (6.9) for all j, k, ${}_j r[k] = 0$, and is equivalent to

$$ J_{\mathrm{mag}} \doteq \sum_{j,k} \left({}_j r[k]\right)^2 = 0. \tag{6.12}$$

It follows that the problem could be seen as a generic non-linear least-square problem. Identifiability of parameters $\big(({}_j b), ({}_j \mathbf{p}^{\mathrm{b}}), ({}_j \mathbf{a}^{\mathrm{b}}), (\alpha_i)\big)$ can be assessed on a specific trajectory by computing the rank of the Hessian matrix of the cost function J_{mag} with respect to these unknown variables. Parameter estimation can be attempted by running a non-linear least-square numerical solver.

We propose using Ceres-Solver, Ref. Agarwal et al. [2010], and its implementation of the Levenberg-Marquardt algorithm in order to solve this calibration problem, taking advantage of its auto-differentiation framework. Doing so, we successfully show that the solver converges toward the correct parameter values, and numerically obtain that the Hessian of J_{mag} with respect to all estimated parameters is full rank in tested cases.

6.4.3. Convergence of the Levenberg-Marquardt algorithm for simulated data

Using an input trajectory, after choosing a set of calibration and magnetic field parameters and simulating corresponding measurements without noise, we choose a starting point at random, different from the set of calibration and magnetic field parameters used to simulate magnetic measurements, and run our non-linear least-square solver Ref. Agarwal et al. [2010] implementing the Levenberg-Marquardt algorithm (see Refs. Levenberg [1944], Marquardt [1963]). This numerical algorithm is a common choice for solving non-linear least-square problems. In order to impose the global scale factor corresponding to the unit of the magnetic field, ${}_1a_1^{\mathrm{b}} = 1$ is excluded from the algorithm. Figure 6.1 shows the evolution of calibration parameter estimation errors at each iteration for all calibration parameters in both Problem P1 and Problem P2. In both cases, the solver converges successfully toward the correct solution and stops iterating after the seventh iteration upon reaching its convergence criteria. Final errors are at most one-millionth of initial errors.

6.4.4. Conclusion of simulation experiments

The above experiments confirm that in practice, identifiability holds for simulated sampled data, along a realistic input trajectory.

6.5. Real-world experiments

We use an Optitrack™ motion capture equipment, see Fig. 6.2, providing trajectory data at $\sim$ 240Hz, to track the movement of a sensor board carrying magnetometers and micro-electro-mechanical inertial sensors. The sensor board is the same that was used in Refs. Chesneau et al. [2016, 2017], Caruso et al. [2017c,b]. All sensors are sampled at $f \approx 325$Hz. No synchronization information between motion capture data and sensor board data is available in our setup.

Motion capture data is noisy and not synchronized with sensor board data. Also, body frames are not necessarily defined in the same way for each type of information (gyrometer, accelerometer, magnetometer and motion capture). To account for different measurement uncertainties, we use three sets of equations: integrated discrete-time strapdown IMU navigation equations, as can be found in Ref. [Savage, 2000, Ch. 7], simplified motion capture measurement equations, and magnetic measurement equations corresponding to (6.9). The augmented problem is then reformulated as a

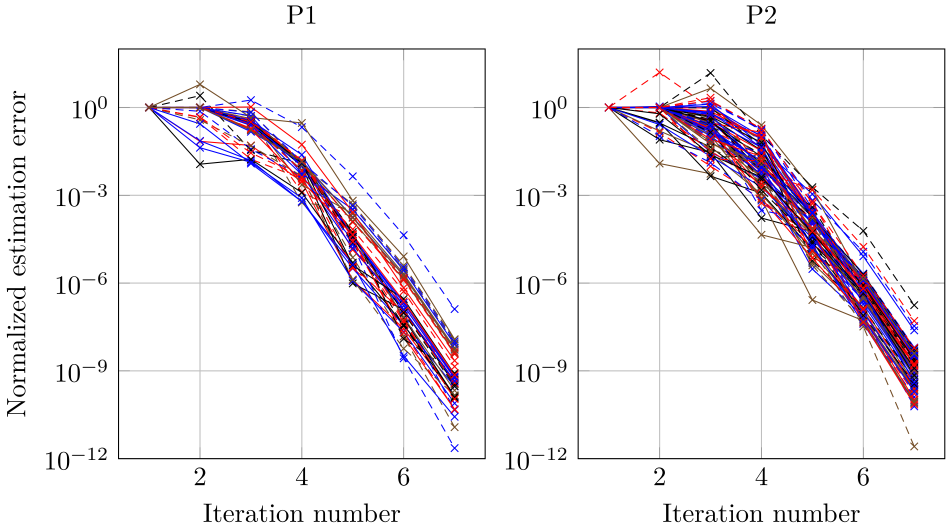

Figure 6.1: Evolution of calibration parameters estimation error, with respect to iteration number for simulated data for Problem P1 (left) and Problem P2 (right). Errors converge toward 0. The solver reaches its convergence criteria and stops iterating at the seventh iteration in both cases.

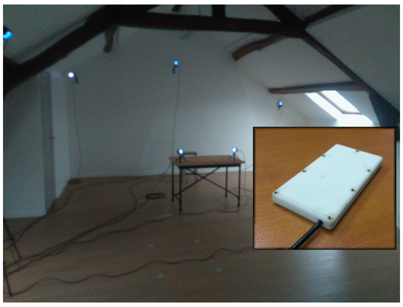

Figure 6.2: Picture of the optitrack setup. The sensor board package is displayed in the insert.

non-linear least-squares identification problem in the same manner as in (6.11) and (6.12). Moreover, magnetic measurements are filtered in order to remove power-line interference.

The sensor board is moved around in a space covered by the motion capture setup. A sufficiently diverse arbitrary trajectory is chosen, with enough rotations and translations, in an indoor magnetic field satisfying identifiability hypotheses for Problem P2 (defined in Sec. 6.2). Sensor and motion capture data is collected, and injected into the optimization problem that is solved using Ceres-Solver Ref. Agarwal et al. [2010] as described in Sec 6.4.

The solver converges toward a set of scale factors and biases that are in agreement with those obtained using the technique in Ref. Dorveaux et al. [2009a]. The estimated positions are coherent with sensor-sensor distances expected by construction (see Fig. 6.3). With these results, we have verified that identifiability also holds in real-world experiments.[3]

6.6. Conclusion

This chapter has demonstrated that magnetic data together with position and attitude information suffices to identify calibration parameters of linear-response single-axis point magnetometers, including their effective positions within the device. Experimental data has confirmed the identifiability we have proven with a mathematical theory in real situations. This approach makes it possible to calibrate arrays of magnetometers in magnetic fields within unknown environments, provided that the magnetic field is stationary and not specifically homogeneous, and that positioning information is available. For instance, the underlying concept could be used to extend tools such as Ref. Furgale et al. [2013] to calibrate visual-inertial setups coupled with magnetic sensor arrays such as in Refs. Caruso et al. [2016, 2017c,b]. Finally, experimental results suggest that some positioning information might be redundant. In a subsequent study, we intend to understand what minimal information is needed in order to identify calibration parameters.

---

[3] A patent is pending on the whole calibration process.

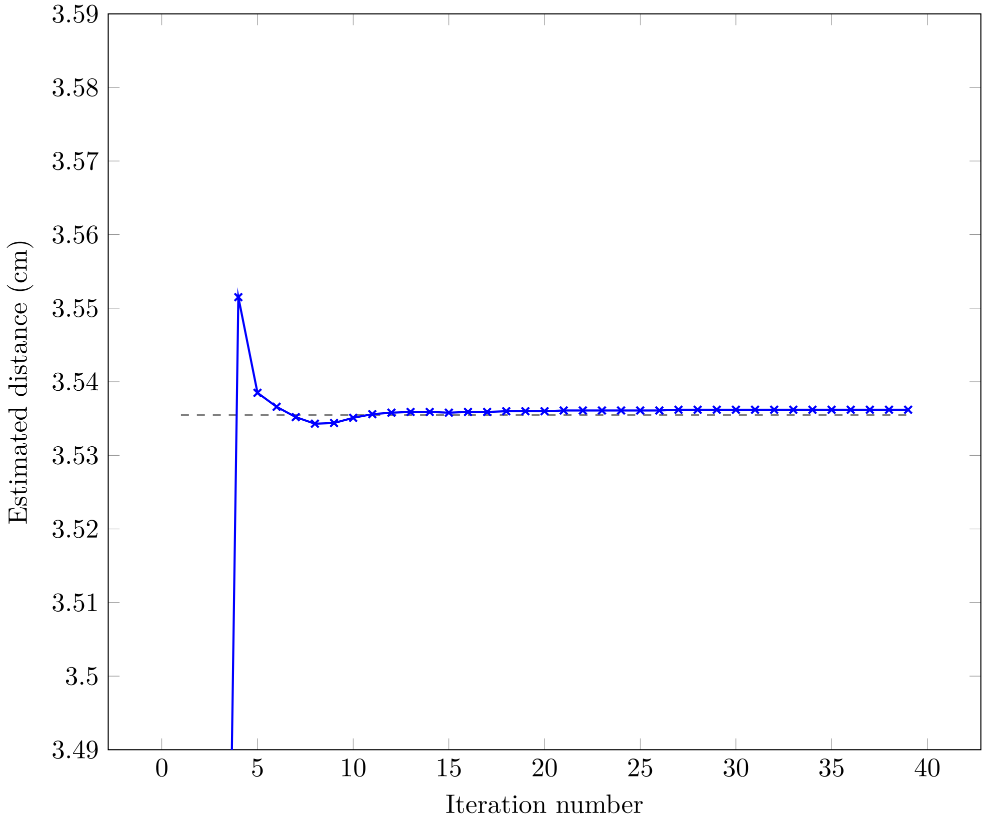

Figure 6.3: Evolution of the estimated distance between two magnetic sensors of the array as a function of algorithm iteration number (blue solid line). All positions are initialized as 0cm. The distance by construction can be expected to be 35.4mm ±0.2mm (gray dashed line). The final estimated distance is 35.36mm.

7. General conclusion

Contents

7.1. Summary of main contributions

7.1.1. Navigation models

A pragmatic approach has been proposed to model MIDR, summarizing all the advantages of previously published models on the subject. This approach consists in using classical strapdown inertial navigation equations in combination with Eq. (2.11), p. 17, to build a state-space model whose design principle is to be as representative of physics as possible, while remaining as simple as possible. Studying these models have raised the following important issues:

- In indoor navigation, the assumption that the navigation frame is inertial is usually made. Under this assumption, the heading is not observable in MIDR. This issue becomes a major source of error, as for any other indoor dead-reckoning technique.
- If inertial sensor biases are taken into account, static trajectories always belong to an unobservable set to which some helical trajectories also belong.

Previous studies in the state of the art mostly focused on observability issues associated with singular gradient conditions. However, these conditions can only be determined as accurately as measurements themselves, which has motivated the modeling and study of the array of sensors itself.

7.1.2. Measurement errors

A simple model of the array of magnetometer provided by SYSNAV has been described and verified; experimental data is consistent with what is recalled from the literature on barber-pole Anisotropic Magneto-Resistance (AMR) magnetometers in Ch. 3.

The computation of the magnetic field gradient from calibrated magnetometer outputs can be interpreted as an interpolation problem. As such, it has been proven that a planar array of magnetometers is sufficient to access any spatial derivative of the magnetic field thanks to Maxwell's equations. However, this can only be done under the assumption that all sensors have been calibrated, that is to say, all parameters of the calibration models have been identified.

The effect of measurement errors on trajectory estimation has thus been studied both regarding (white) noise and regarding calibration parameter uncertainty. Among other results, it has been shown that

- With planar arrays of magnetometers, any uncertainty on any calibration parameter (bias, scale-factor, effective position) can cause an unbounded velocity estimation errors close to singular gradient conditions. Thus, the issue of velocity estimation through singular gradient conditions is also an issue of robustness to calibration uncertainty.
- Gradient measurement noise can lead to a damping effect in close to singular gradient conditions, biasing velocity estimates. Together with the previous

point, measurement noise may instead be helpful in avoiding divergent velocity estimates in this case.

- Existing calibration techniques often neglect the frame of reference in which magnetometer arrays are calibrated and their effective position parameters. While the former problem may be solved using straightforward methods, the latter requires the development of processes introduced in the later chapters of this document.

7.1.3. Performance evaluation

Two Extended Kalman Filters (EKF) have been presented and evaluated on experimental data, highlighting some sources of estimation errors. Performance comparable to previous Pedestrian Dead Reckoning (PDR) techniques has been obtained with pure MIDR on long-term trajectories. Besides, a recursive magnetic heading estimation algorithm has also been introduced and successfully tested.

7.1.4. Calibration techniques for magnetometer arrays

Following the previous study, two complete calibration techniques have been introduced in light of what has been written in Ch. 3. A calibration technique relying on coils such as Helmholtz coils has been introduced, whose advantages are

- No theoretical dependency on magnetic field homogeneity in the center of the coils.
- No need for precise placement of the sensors inside of the coils.
- The possibility of a precise calibration of the magnetic field generated by the coils during the process.
- As a side effect, the usability of this technique to make an accurate magnetic tracker, as shown in experiments. Thus, inertial sensors can be calibrated in the same frame of reference as magnetometers.

Furthermore, this technique can be optimized for use in factory calibration processes.

A second technique has also been presented, based on a problem that is inverse of MIDR. A theoretical proof has been provided that a magnetometer array can be wholly calibrated from the knowledge of the trajectory of the rigid body that carries the array, and calibration has been successful in experiments. This technique is usable in an inhomogeneous magnetic field and allows the onboard calibration of magnetometer arrays on setups that can compute their absolute trajectory, such as Visual Inertial Navigation (VIN) systems.

7.2. Why so little attention? Clues towards a wider adoption

Going back to the question asked in the introduction, why has this navigation technique attracted so little attention? This work provides several possible answers.

7.2.1. The definition of MIDR

Voluntary adoption of a technique is difficult without an explicit and brief definition or several different examples providing it by induction. Thus the definition of MIDR attempted in Ch. 2. However, this definition is still perfectible, because expressed in terms of choice of state-space model suggesting tools from observation/control theory.

7.2.2. Interdisciplinarity

The above remark raises the problem of interdisciplinarity. The seminal paper Ref. Vissière et al. [2007a] was published in a conference on decision and control. However, navigation is profoundly interdisciplinary and involves physics, electronics, applied mathematics, information theory, robotics... It is comprehensible for the magnetic navigation community to have missed the information entirely. Interdisciplinary conferences such as the IPIN conference partly solve this problem by gathering these communities around the practical problems of indoor navigation.

An interdisciplinary flow of information does not prevent, however, different communities from misunderstanding each other. Ref. Skog et al. [2018], which describes a magnetic odometry technique relying on measurement of second and higher order spatial derivatives, mentioned state of the art techniques as the direct inversion of the magnetic gradient, which is already not the case in the seminal paper or Dorveaux [2011].

Finally, standardized benchmarks and trustable competitions results are an excellent way to compare navigation techniques which each other. This justifies participations to the IPIN 2016 and IPIN 2017 using pure MIDR, albeit using a barometer for the vertical coordinate.

7.2.3. An unusual hardware configuration

Arrays of at least three 3-axis magnetometers, especially used together with inertial sensors, do not exist off-the-shelf to the author's knowledge; even though other works have been carried out on hardware using multiple magnetometers and on which MIDR can be performed (e.g., Ref. Afzal et al. [2010], Skog et al. [2018]) the usual configuration features only a single 3-axis magnetometer. The necessary investment hinders experiments or benchmarks. Purely theoretical studies remain possible, but risk focusing on secondary issues without conclusive answers on performance and feasibility (e.g., the theoretical problem of observability under singular gradient conditions, Ref. Batista et al. [2013]).

Besides, carrying out experiments requires resources and know-how. MIDR experiments in Ch. 4, and the work in Ch. 5 and Ch. 6 have all relied on SYSNAV's hardware, and SYSNAV's and the GIPSA-lab's infrastructures. Without those, this work would not have been possible or greatly hindered.

7.2.4. Patents

Patents are designed with the protection of inventions in mind before the sharing of the associated knowledge. Their secondary effect is that further improvements are less readily shared, and can discourage teams to continue working on patented technologies without clear expected benefits. Yet, MIDR systems were patented very early in Ref. Vissière et al. [2008].

7.2.5. Technical challenges

MIDR still has many technical challenges.

- Working with magnetic measurements is not simple nor necessarily intuitive (see Ch. 3),
- The stationarity assumption is a challenge (internal and external disturbances),
- Observability issues remain in low gradient / outdoor conditions and static trajectories,
- Heading estimation is not satisfactorily solved, in particular, a converging estimator of true north is missing, but seems theoretically plausible.
- Calibration is a challenge which is taken up in Part. II, however, work remains on this subject.

These problems are not necessarily insurmountable, and addressing them may either convince in favor of the more general adoption of this technique or bury it forever.

7.3. Future work

Future work may focus on

- Extensions of Ch. 2 and 4 with robust observers,
- Exploitation of higher order spatial derivatives of the magnetic field and non-stationary signals for navigation,
- Detection of- and robustness to internal and external magnetic disturbances,
- Extensions of Ch. 6 with the goal of minimizing the amount of necessary information,

- Proofs and extensions of the work in Ch. 5 for general coils configurations
- Extension of all chapters to more sophisticated/ specific magnetometer models (than the linear single-axis point-magnetometer model, e.g., non-linear models), gyrometer and accelerometer models.

Appendices

A. High-end IMU MIDR

The models proposed in Sec. 2.4.1 and Sec. 2.5.1 both suffer from heading unobservability stemming from a symmetry in the model. If unbiased high-end gyrometers are sensitive enough to measure the earth's angular velocity, then it is justified to take it into account and remove the simplifying assumption that $\mathfrak{R}_\mathrm{n}$ is inertial.

Let us remove this assumption from the model of Sec. 2.4.1. The angular velocity $\boldsymbol{\omega}^{\mathrm{n/i}}$ is a constant parameter in the same way as $\mathbf{g}^\mathrm{n}$. If we denote $R(t)$ and $R'(t)$ two solutions of Eq. (2.6), and define $\delta R \doteq R' R^\top$, we have

$$\frac{d}{dt}\delta R = \delta R[\boldsymbol{\omega}^{\mathrm{n/i}}\times] - [\boldsymbol{\omega}^{\mathrm{n/i}}\times]\delta R\ .$$

It follows that the only way for $\mathbf{g}^\mathrm{n}$ to always remain invariant by δR is to have $\mathbf{g}^\mathrm{n}$ and $\boldsymbol{\omega}^{\mathrm{n/i}}$ aligned, as can be the case at the poles, or that δR be the identity matrix. One may expect that the direction of $\mathbf{g}^\mathrm{n}$ be observable in this model in the same way as in Sec. 2.4.1. While it is not sufficient in order to prove that this model is observable, it shows that the symmetry by change of heading is broken when the assumption of an inertial $\mathfrak{R}_\mathrm{n}$ is dropped, and the earth's angular velocity is taken into account.

B. Proofs of Lemmas from Ch. 6

B.1. Proof of Lemma 6.3.3

We adopt the assumptions and notations of Sec. 6.3.3. Let $j \in \{1, 2, \ldots, m\}$, and $\mathbf{M}^{\mathrm{n}} \in \mathbb{R}^3$. Inserting Eq. (6.3) into the integral and subtracting the bias ${}_jb$ from it, we find

$$\begin{aligned} &\oint\limits_{R \in \mathrm{SO}(3)} {}_jy(\mathbf{M}^{\mathrm{n}}, R)\ \mathrm{d}R - {}_jb \\ &= \oint\limits_{R \in \mathrm{SO}(3)} {}_j\mathbf{a}^{\mathrm{b}} R(t)^\top \mathbf{B}^{\mathrm{n}} \left(\mathbf{M}^{\mathrm{n}} + R_j\mathbf{p}^{\mathrm{b}}\right) \mathrm{d}R\ , \end{aligned} \tag{B.1}$$

as $\mathrm{d}R$ is normalized such that the volume of SO(3) is unity. In order to prove the lemma, it suffices to show that the expression (B.1) vanishes.

To do so, we recall that any element $R \in \mathrm{SO}(3)$ can be decomposed (see also Fig. B.1) into two rotations, $R = R_2.R_1$, such that the first rotation R_1 in $\mathcal{S}^1$ ($\cong$ SO(2)) is around ${}_j\mathbf{p}^{\mathrm{b}}$ and the second rotation R_2 in $\mathcal{S}^2$ ($\cong$ SO(3)/SO(2)) around an axis orthogonal to ${}_j\mathbf{p}^{\mathrm{b}}$. The first rotation leaves the sensor position constant, which means that $\mathbf{M}^{\mathrm{n}} + R_j\mathbf{p}^{\mathrm{b}} = \mathbf{M}^{\mathrm{n}} + R_{2j}\mathbf{p}^{\mathrm{b}}$ does not depend on R_1. Then,

$$\begin{aligned} &\oint\limits_{R \in \mathrm{SO}(3)} {}_j\mathbf{a}^{\mathrm{b}} R(t)^\top \mathbf{B}^{\mathrm{n}} \left(\mathbf{M}^{\mathrm{n}} + R_j\mathbf{p}^{\mathrm{b}}\right) \mathrm{d}R \\ &= \oint\limits_{R_2 \in \mathcal{S}^2} \left[\oint\limits_{R_1 \in \mathcal{S}^1} {}_j\mathbf{a}^{\mathrm{b}} R_1^\top \mathrm{d}R_1 \right] R_2^\top \mathbf{B}^{\mathrm{n}} \big(\mathbf{M}^{\mathrm{n}} + R_{2j}\mathbf{p}^{\mathrm{b}}\big) \mathrm{d}R_2 \end{aligned}$$

By construction (cf. also Fig. B.1), the integral over R_1 is proportional to ${}_j\mathbf{p}^{\mathrm{b}\top}$. Thus, the expression (B.1) is proportional to

$$\oint\limits_{R_2 \in \mathcal{S}^2} \big(R_{2j}\mathbf{p}^{\mathrm{b}}\big)^\top \mathbf{B}^{\mathrm{n}} \big(\mathbf{M}^{\mathrm{n}} + R_{2j}\mathbf{p}^{\mathrm{b}}\big) \mathrm{d}R_2\ . \tag{B.2}$$

This expression is just the magnetic flux through the surface of a sphere of radius $\|{}_j\mathbf{p}^{\mathrm{b}}\|$. According to Gauss' theorem for magnetism, it must vanish. As a result, the expression (B.1) vanishes indeed, which concludes the proof. □

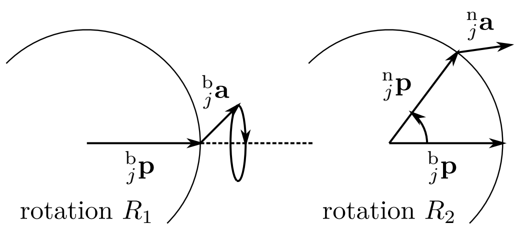

Figure B.1: A rotation $R \in \mathrm{SO}(3)$ can be decomposed as $R = R_2 R_1$ where R_1 rotates around ${}_{j}\mathbf{p}^{\mathrm{b}}$, and R_2 rotates around an axis orthogonal to ${}_{j}\mathbf{p}^{\mathrm{b}}$.

B.2. Proof of Lemma 6.3.4

We adopt assumptions and notations of Sec. 6.3.3. Without loss of generality , we may put

$$ {}_{j_0}\mathbf{p}^{\mathrm{b}} = 0 \ , \tag{B.3} $$

which can always be achieved by redefining the center of the moving frame $\mathfrak{R}_b$. In this case, the injective mapping ζ to be constructed has to satisfy $0 = \zeta^{-1}(0)$.

In order to facilitate the construction, let

$$ S_\phi \doteq \begin{pmatrix} \cos\phi & -\sin\phi & 0 \\ \sin\phi & \cos\phi & 0 \\ 0 & 0 & 1 \end{pmatrix} \ , \tag{B.4} $$

$$ T_\phi \doteq \begin{pmatrix} \cos\phi & 0 & \sin\phi \\ 0 & 1 & 0 \\ -\sin\phi & 0 & \cos\phi \end{pmatrix} \ , \tag{B.5} $$

$$ U_\phi \doteq \begin{pmatrix} 1 & 0 & 0 \\ 0 & \cos\phi & -\sin\phi \\ 0 & \sin\phi & \cos\phi \end{pmatrix} \tag{B.6} $$

with $\phi \in [0, 2\pi]$. For fixed $\mathbf{M}^{\mathrm{n}} \in \mathbb{R}^3$, $R \in \mathrm{SO}(3)$ and given measurement function ${}_{j}y$, we define the mapping

$$ \begin{aligned} \zeta : \mathbb{R}^3 &\to \mathbb{R}^6 \\ \mathbf{q} &\mapsto \frac{1}{2}\sum_{k=0}^{3}(-1)^k \begin{pmatrix} ({}_{j}y \circ f)(\mathbf{q}, \mathbf{M}^{\mathrm{n}}, R S_{\frac{k\pi}{2}}) \\ ({}_{j}y \circ f)(\mathbf{q}, \mathbf{M}^{\mathrm{n}}, R S_{\frac{k\pi}{2}+\frac{\pi}{4}}) \\ ({}_{j}y \circ f)(\mathbf{q}, \mathbf{M}^{\mathrm{n}}, R T_{\frac{k\pi}{2}}) \\ ({}_{j}y \circ f)(\mathbf{q}, \mathbf{M}^{\mathrm{n}}, R T_{\frac{k\pi}{2}+\frac{\pi}{4}}) \\ ({}_{j}y \circ f)(\mathbf{q}, \mathbf{M}^{\mathrm{n}}, R U_{\frac{k\pi}{2}}) \\ ({}_{j}y \circ f)(\mathbf{q}, \mathbf{M}^{\mathrm{n}}, R U_{\frac{k\pi}{2}+\frac{\pi}{4}}) \end{pmatrix} \end{aligned} \tag{B.7} $$

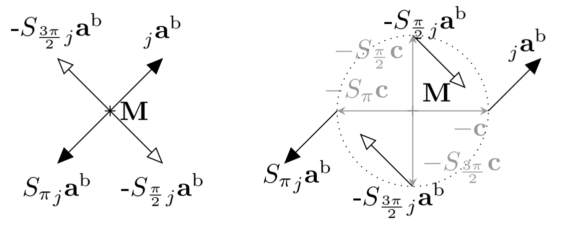

$\mathbf{c} = 0$ $\qquad$ $\mathbf{c} \neq 0$

Figure B.2: (left) The first component of $\zeta(0)$ can be expressed as an inner product between the magnetic field at $\mathbf{M}$ and $_j\mathbf{a}^{\mathrm{b}}\left(\sum_{k=0}^{3}(\text{-}1)^k S_{\frac{k\pi}{2}}\right)^{\top} = 0$, which is always 0. (right) At $\mathbf{q} \neq 0$, $\zeta(\mathbf{q})$ becomes dependent on spatial variations of the magnetic field around $\mathbf{M}$. The construction is analogous for other components.

with

$$\begin{aligned} f : \mathbb{R}^3 \times \mathbb{R}^3 \times \mathrm{SO}(3) &\to \mathbb{R}^3 \times \mathrm{SO}(3) \\ (\mathbf{q}, \mathbf{M}^{\mathrm{n}}, R) &\mapsto (\mathbf{M}^{\mathrm{n}} - R\mathbf{q}, R) \end{aligned} . \tag{B.8}$$

By definition of f and $_jy$, i.e. (6.3) and (B.8), and using assumption (B.3),

$$({}_jy \circ f)(\mathbf{q}, \mathbf{M}^{\mathrm{n}}, R) = \left(R_j\mathbf{a}^{\mathrm{b}}\right) \cdot \mathbf{B}^{\mathrm{n}}(\mathbf{M}^{\mathrm{n}} - R\mathbf{q}).$$

To prove the lemma, we first show that $\zeta(0) = 0$ independently of scale factors and the magnetic field. For $\mathbf{q} = 0$, we find that the first component of $\zeta(\mathbf{q})$ is proportional to $\sum_{k=0}^{3}(\text{-}1)^k S_{\frac{k\pi}{2}}^{\top} = 0$, cf. also Fig. B.2. A completely analogous calculation shows that in fact all components of $\zeta(q)$ vanish for $\mathbf{q} = 0$, independently of other parameters.

In order to show injectivity, consider the linear approximation in $\mathbf{q}$,

$$({}_jy \circ f)(\mathbf{q}, \mathbf{M}^{\mathrm{n}}, R) \simeq {}_j\mathbf{a}^{\mathrm{b}} R^{\top}\mathbf{B}^{\mathrm{n}}(\mathbf{M}^{\mathrm{n}}) - {}_j\mathbf{a}^{\mathrm{b}} R^{\top} \left.\nabla\mathbf{B}^{\mathrm{n}}\right|_{\mathbf{M}^{\mathrm{n}}} R\mathbf{q}\ . \tag{B.9}$$

By assumption, there exists a position ${\mathbf{M}^{\mathrm{n}}}_0$ such that the magnetic gradient's eigenvalues are different from each other. Also, since Ampere's law in the absence of source currents implies that $\left.\nabla\mathbf{B}^{\mathrm{n}}\right|_{{\mathbf{M}^{\mathrm{n}}}_0}$ is symmetric, its matrix can be diagonalized by an orthogonal matrix. Thus, there exists $R_0 \in$ SO(3) such that

$$\begin{pmatrix} d_1 & 0 & 0 \\ 0 & d_2 & 0 \\ 0 & 0 & d_3 \end{pmatrix} = R_0^{\top} \left.\nabla\mathbf{B}^{\mathrm{n}}\right|_{\mathbf{M}^{\mathrm{n}}} R_0, \tag{B.10}$$

with mutually different $d_1, d_2, d_3 \in \mathbb{R}$.

We now specialize the construction of the mapping ζ, Eq. (B.7), by inserting the 6D position $({\mathbf{M}^{\mathrm{n}}}_0, R_0)$ for $\mathbf{M}^{\mathrm{n}}$ and R. Using the notation ${}_j\mathbf{a}^{\mathrm{b}} = \begin{pmatrix} {}_ja_1^{\mathrm{b}} & {}_ja_2^{\mathrm{b}} & {}_ja_3^{\mathrm{b}} \end{pmatrix}$, we find that the Jacobian matrix of the mapping ζ, Eq. (B.7), at $\mathbf{q} = 0$ takes the form

$$\nabla\zeta\Big|_0 = \begin{pmatrix} -(d_1 - d_2)\,{}_j a_1^{\mathrm{b}} & (d_1 - d_2)\,{}_j a_2^{\mathrm{b}} & 0 \\ (d_1 - d_2)\,{}_j a_2^{\mathrm{b}} & (d_1 - d_2)\,{}_j a_1^{\mathrm{b}} & 0 \\ (d_3 - d_1)\,{}_j a_1^{\mathrm{b}} & 0 & -(d_3 - d_1)\,{}_j a_3^{\mathrm{b}} \\ (d_3 - d_1)\,{}_j a_3^{\mathrm{b}} & 0 & (d_3 - d_1)\,{}_j a_1^{\mathrm{b}} \\ 0 & -(d_2 - d_3)\,{}_j a_2^{\mathrm{b}} & (d_2 - d_3)\,{}_j a_3^{\mathrm{b}} \\ 0 & (d_2 - d_3)\,{}_j a_3^{\mathrm{b}} & (d_2 - d_3)\,{}_j a_2^{\mathrm{b}} \end{pmatrix} .$$

Since by assumption, the d_1, d_2, d_3 are mutually different and ${}_j\mathbf{a}^{\mathrm{b}} \neq 0$, the 6×3 Jacobian matrix $\nabla\zeta\big|_0$ contains necessarily a non-zero minor determinant of order 3, and thus is injective. As a result, the mapping ζ itself is an immersion in $\mathbf{q} = 0$, and thus injective, at least locally, around $\mathbf{q} = 0$. □

Bibliography

Procédé de calibration d'un magnétomètre. *Patent Application B250148FR*, 2017a.

Procédé et dispositif de caractérisation d'un cap déterminé à partir de la mesure du champ magnétique. *Patent Application B250150FR*, 2017b.

Procédé de calibration d'un magnétomètre. *Patent Application B250151FR*, 2017c.

Détermination de cap à partir du champ mesuré par des capteurs magnétiques. *Patent Application B250181FR*, 2017d.

K. Abdulrahim, C. Hide, T. Moore, and C. Hill. Aiding MEMS IMU with building heading for indoor pedestrian navigation. *2010 Ubiquitous Positioning Indoor Navigation and Location Based Service*, Oct 2010. doi: 10.1109/upinlbs.2010.5653986.

Y. Adachi, M. Higuchi, D. Oyama, Y. Haruta, S. Kawabata, and G. Uehara. Calibration for a multichannel magnetic sensor array of a magnetospinography system. *IEEE Transactions on Magnetics*, 50(11):1–4, Nov 2014. doi: 10.1109/tmag.2014.2326869.

M. H. Afzal, V. Renaudin, and G. Lachapelle. Assessment of indoor magnetic field anomalies using multiple magnetometers. In *ION GNSS*, volume 10, pages 21–24, 2010.

M. H. Afzal, V. Renaudin, and G. Lachapelle. Magnetic field based heading estimation for pedestrian navigation environments. In *2011 International Conference on Indoor Positioning and Indoor Navigation*, Guimaraes, Portugal, Sep 2011a. ISBN http://id.crossref.org/isbn/978-1-4577-1805-2. doi: 10.1109/ipin.2011.6071947.

M. H. Afzal, V. Renaudin, and G. Lachapelle. Use of Earth's magnetic field for mitigating gyroscope errors regardless of magnetic perturbation. *Sensors*, 11(12): 11390–11414, 2011b. doi: doi:10.3390/s111211390.

S. Agarwal, K. Mierle, and Others. Ceres solver. `http://ceres-solver.org`, 2010.

D. Alazard. Introduction to Kalman filtering. *SUPAERO*, 2005.

R. Alonso and M. D. Shuster. Complete linear attitude-independent magnetometer calibration. *Journal of the Astronautical Sciences*, 50(4):477–490, 2002a.

R. Alonso and M. D. Shuster. TWOSTEP: A fast robust algorithm for attitude-independent magnetometer-bias determination. *Journal of the Astronautical Sciences*, 50(4):433–452, 2002b.

B. D.O. Anderson and J.B. Moore. *Optimal filtering.* Dover Books on Electrical Engineering. Mineola, N.Y., Dover Publications, 2005.

W. Appel. *Mathematics for Physics and Physicists.* Princeton University Press, 2007. ISBN 0691131023.

A.L. Barker, D.E. Brown, and W.N. Martin. Bayesian estimation and the Kalman filter. *Computers & Mathematics with Applications*, 30(10):55 – 77, 1995. ISSN 0898-1221. doi: https://doi.org/10.1016/0898-1221(95)00156-S.

A. Barrau. *Non-linear state error based extended Kalman filters with applications to navigation.* PhD thesis, Mines Paristech, 2015.

A. Barrau and S. Bonnabel. The invariant extended kalman filter as a stable observer. *IEEE Transactions on Automatic Control*, 62(4):1797–1812, April 2017. ISSN 0018-9286. doi: 10.1109/TAC.2016.2594085.

P. Batista, N. Petit, C. Silvestre, and P. Oliveira. Further results on the observability in magneto-inertial navigation. In *American Control Conference (ACC)*, pages 2503–2508, Washington DC, 2013. doi: 10.1109/ACC.2013.6580210.

G. Besançon. *Nonlinear Observers and Applications*, volume 636 of *Lecture Notes in Control and Information Sciences.* Springer-Verlag Berlin Heidelberg, 2007. doi: 10.1007/978-3-540-73503-8.

G. Besançon, G. Bornard, and H. Hammouri. Observer synthesis for a class of nonlinear control systems. *European Journal of Control*, 2(3):176 – 192, 1996. ISSN 0947-3580. doi: 10.1016/S0947-3580(96)70043-2.

G. J. Bierman and C. L. Thornton. Numerical comparison of Kalman filter algorithms: Orbit determination case study. *Automatica*, 13(1):23 – 35, 1977. ISSN 0005-1098. doi: 10.1016/0005-1098(77)90006-1.

J. Borenstein and L. Ojeda. Heuristic drift elimination for personnel tracking systems. *Journal of Navigation*, 63(04):591–606, Sep 2010. ISSN 1469-7785. doi: 10.1017/s0373463310000184.

D. Caruso, A. Eudes, M. Sanfourche, G. Le Besnerais, and D. Vissière. Infrastructure-less indoor navigation with an hybrid magneto-inertial and depth sensor system. In *2016 International Conference on Indoor Positioning and Indoor Navigation (IPIN)*, Alcalá de Henares, Spain, Oct 2016. doi: 10.1109/ipin.2016.7743690.

D. Caruso, A. Eudes, M. Sanfourche, D. Vissière, and G. Le Besnerais. An inverse square root filter for robust indoor/outdoor magneto-visual-inertial odometry. In *2017 International Conference on Indoor Positioning and Indoor Navigation (IPIN)*, Sapporo, Japan, Sep 2017a. doi: 10.1109/ipin.2017.8115888.

D. Caruso, A. Eudes, M. Sanfourche, D. Vissière, and G. Le Besnerais. Robust indoor/outdoor navigation through magneto-visual-inertial optimization-based estimation. In *2017 IEEE/RSJ International Conference on Intelligent Robots and Systems (IROS)*, Vancouver, Canada, Sep 2017b. doi: 10.1109/iros.2017.8206304.

D. Caruso, A. Eudes, M. Sanfourche, D. Vissière, and G. Le Besnerais. A robust indoor/outdoor navigation filter fusing data from vision and magneto-inertial measurement unit. *Sensors*, 17(12):2795, Dec 2017c. doi: 10.3390/s17122795.

C.-I. Chesneau, M. Hillion, and C. Prieur. Motion estimation of a rigid body with an EKF using magneto-inertial measurements. In *2016 International Conference on Indoor Positioning and Indoor Navigation (IPIN)*, Alcalá de Henares, Spain, Oct 2016. doi: 10.1109/ipin.2016.7743702.

C.-I. Chesneau, M. Hillion, J.-F. Hullo, G. Thibault, and C. Prieur. Improving magneto-inertial attitude and position estimation by means of a magnetic heading observer. In *2017 International Conference on Indoor Positioning and Indoor Navigation (IPIN)*, Sapporo, Japan, Sep 2017. doi: 10.1109/ipin.2017.8115862.

C.-I. Chesneau, R. Robin, H. Meier, M. Hillion, and C. Prieur. Calibration of a magnetometer array using motion capture equipment (to appear). *Asian Journal of Control*, 2019.

W.H.K. de Vries, H.E.J. Veeger, C.T.M. Baten, and F.C.T. van der Helm. Magnetic distortion in motion labs, implications for validating inertial magnetic sensors. *Gait & Posture*, 29(4):535 – 541, 2009. ISSN 0966-6362. doi: 10.1016/j.gaitpost.2008.12.004.

M. Díaz-Michelena, R. Sanz, M. F. Cerdán, and A. B. Fernández. Calibration of qmmoura three-axis magnetometer and gradiometer. *Geoscientific Instrumentation, Methods and Data Systems*, 4(1):1–18, 2015. doi: 10.5194/gi-4-1-2015.

J. P. Dinale. Magnetic test facility-sensor and coil calibrations. Technical report, Defense Science and Technology Organization Victoria (Australia) Maritime Platforms Div, 2013.

Zhe Dong and Zheng You. Finite-horizon robust Kalman filtering for uncertain discrete time-varying systems with uncertain-covariance white noises. *IEEE Signal Processing Letters*, 13(8):493–496, Aug 2006. ISSN 1070-9908. doi: 10.1109/LSP.2006.873148.

E. Dorveaux. *Magneto-inertial navigation: principles and application to an indoor pedometer.* PhD thesis, Ecole Nationale Supérieure des Mines de Paris, France, 2011.

E. Dorveaux and N. Petit. Harmonization of a multi-sensor navigation system. In *2011 International Conference on Indoor Positioning and Indoor Navigation*, pages 1–7, Sept 2011a. doi: 10.1109/IPIN.2011.6071944.

E. Dorveaux and N. Petit. Presentation of a magneto-inertial positioning system: navigating through magnetic disturbances. In *International Conference on Indoor Positioning and Indoor Navigation (IPIN)*, Guimarães, Portugal, 2011b.

E. Dorveaux, D. Vissière, A.-P. Martin, and N. Petit. Iterative calibration method for inertial and magnetic sensors. In *Proceedings of the 48h IEEE Conference on Decision and Control (CDC) held jointly with 2009 28th Chinese Control Conference*, pages 8296–8303, Shanghai, China, Dec 2009a. doi: 10.1109/cdc.2009.5399503.

E. Dorveaux, D. Vissiere, A.P. Martin, and N. Petit. Timestamping for an array of low-cost sensors. *IFAC Proceedings Volumes*, 42(1):86 – 91, 2009b. ISSN 1474-6670. doi: https://doi.org/10.3182/20090210-3-CZ-4002.00020. 9th IFAC Workshop on Programmable Devices and Embedded Systems.

E. Dorveaux, D. Vissière, and N. Petit. On-the-field calibration of an array of sensors. In *Proceedings of the 2010 American Control Conference*, pages 6795–6802, June 2010. doi: 10.1109/ACC.2010.5531632.

E. Dorveaux, T. Boudot, M. Hillion, and N. Petit. Combining inertial measurements and distributed magnetometry for motion estimation. In *American Control Conference (ACC)*, pages 4249–4256, San Francisco, CA, 2011.

G. A. Einicke and L. B. White. Robust extended kalman filtering. *IEEE Transactions on Signal Processing*, 47(9):2596–2599, Sep 1999. ISSN 1053-587X. doi: 10.1109/78.782219.

W. T. Faulkner, R. Alwood, W.A. T. David, and J. Bohlin. GPS-Denied pedestrian tracking in indoor environments using an IMU and magnetic compass. In *Proceedings of the 2010 International Technical Meeting of The Institute of Navigation*, pages 198 – 204, San Diego, CA, Jan 2010.

C. C. Foster and G. H. Elkaim. Extension of a two-step calibration methodology to include nonorthogonal sensor axes. *IEEE Transactions on Aerospace and Electronic Systems*, 44(3):1070–1078, July 2008. ISSN 0018-9251. doi: 10.1109/TAES.2008.4655364.

E. Foxlin. Pedestrian tracking with shoe-mounted inertial sensors. *Computer Graphics and Applications*, 25(6):38–46, 2005. doi: 10.1109/MCG.2005.140.

P. Furgale, J. Rehder, and R. Siegwart. Unified temporal and spatial calibration for multi-sensor systems. In *Intelligent Robots and Systems (IROS), 2013 IEEE/RSJ International Conference on*, pages 1280–1286, 2013.

B. Gozick, K. P. Subbu, R. Dantu, and T. Maeshiro. Magnetic maps for indoor navigation. *IEEE Transactions on Instrumentation and Measurement*, 60(12):3883–3891, Dec 2011. ISSN 0018-9456. doi: 10.1109/TIM.2011.2147690.

J.P.J. Groenland, C.J.M. Eijkel, J.H.J. Fluitman, and R.M. de Ridder. Permalloy thin-film magnetic sensors. *Sensors and Actuators A: Physical*, 30(1):89 – 100, 1992. ISSN 0924-4247. doi: https://doi.org/10.1016/0924-4247(92)80201-D.

M. J. Hall, S. A. C. Harmon, and S. Turner. Magnetic environment and magnetic field standards at npl for the calibration of low noise magnetometers and gradiometers for cleanliness studies. In *2012 ESA Workshop on Aerospace EMC*, pages 1–6, May 2012.

J. Haverinen. Utilizing magnetic field based navigation, August 5 2014. US Patent 8,798,924.

J. Haverinen and A. Kemppainen. Global indoor self-localization based on the ambient magnetic field. *Robotics and Autonomous Systems*, 57(10):1028 – 1035, 2009. ISSN 0921-8890. doi: 10.1016/j.robot.2009.07.018. 5th International Conference on Computational Intelligence, Robotics and Autonomous Systems (5th CIRAS).

IEEE. *IEEE Std 952-1997 (R2003) IEEE Standard Specification Format Guide and Test Procedure for Single-Axis Interferometric Fiber Optic Gyros.* 2003.

J.D. Jackson. *Classical Electrodynamics, Third Edition.* John Wiley & Sons, Inc., 1998.

Yeon Fuh Jiang and Yu Ping Lin. On the rotation vector differential equation. *IEEE Transactions on Aerospace and Electronic Systems*, 27(1):181–183, Jan 1991. ISSN 0018-9251. doi: 10.1109/7.68165.

A. R. Jiménez, F. Seco, F. Zampella, and J. Prieto J.C.and Guevara. Improved heuristic drift elimination with magnetic-aided dominant directions (mihde) for pedestrian navigation in complex buildings. *Journal of Location Based Services*, 6(3):186–210, 2012. doi: 10.1080/17489725.2012.687779.

A. R. Jiménez, F. Seco, C. Prieto, and J. Guevara. A comparison of pedestrian dead-reckoning algorithms using a low-cost MEMS IMU. In *IEEE International Symposium on Intelligent Signal Processing (WISP)*, pages 37–42, Budapest, 2009. ISBN http://id.crossref.org/isbn/978-1-4244-5057-2. doi: 10.1109/wisp.2009.5286542.

A. R. Jiménez, F. Seco, F. Zampella, J. C. Prieto, and J. Guevara. Improved heuristic drift elimination (iHDE) for pedestrian navigation in complex buildings. In *2011 International Conference on Indoor Positioning and Indoor Navigation*, Guimaraes, Portugal, Sep 2011. ISBN http://id.crossref.org/isbn/978-1-4577-1805-2. doi: 10.1109/ipin.2011.6071923.

R. E. Kalman. A new approach to linear filtering and prediction problems. *Journal of basic Engineering*, 82(1):35–45, 1960.

P. Kaminski, A. Bryson, and S. Schmidt. Discrete square root filtering: A survey of current techniques. *IEEE Transactions on Automatic Control*, 16(6):727–736, Dec 1971. ISSN 0018-9286. doi: 10.1109/TAC.1971.1099816.

M. Kok and T. B. Schön. Magnetometer calibration using inertial sensors. *IEEE Sensors Journal*, 16(14):5679–5689, July 2016. ISSN 1530-437X. doi: 10.1109/JSEN.2016.2569160.

M. Kok and A. Solin. Scalable magnetic field slam in 3d using gaussian process maps. arXiv:1804.01926, June 2018.

M. Kok, J. D. Hol, T. B. Schön, F. Gustafsson, and H. Luinge. Calibration of a magnetometer in combination with inertial sensors. In *2012 15th International Conference on Information Fusion*, pages 787–793, July 2012.

K. Kuijk, W. van Gestel, and F. Gorter. The barber pole, a linear magnetoresitive head. *IEEE Transactions on Magnetics*, 11(5):1215–1217, Sep 1975. doi: 10.1109/TMAG.1975.1058886.

E.J. Lefferts, F.L. Markley, and M.D. Shuster. Kalman filtering for spacecraft attitude estimation. *Journal of Guidance, Control, and Dynamics*, 5(5):417–429, Sep 1982. doi: 10.2514/3.56190.

K. Levenberg. A method for the solution of certain non-linear problems in least squares. *Quarterly of Applied Mathematics*, 2(2):164–168, Jul 1944. doi: 10.1090/qam/10666.

O. Le Contel, P. Leroy, A. Roux, C. Coillot, D. Alison, A. Bouabdellah, L. Mirioni, L. Meslier, A. Galic, M. C. Vassal, R. B. Torbert, J. Needell, D. Rau, I. Dors, R. E. Ergun, J. Westfall, D. Summers, J. Wallace, W. Magnes, A. Valavanoglou, G. Olsson, M. Chutter, J. Macri, S. Myers, S. Turco, J. Nolin, D. Bodet, K. Rowe, M. Tanguy, and B. de la Porte. The search-coil magnetometer for mms. *Space Science Reviews*, 199(1):257–282, Mar 2016. ISSN 1572-9672. doi: 10.1007/s11214-014-0096-9.

Xiang Li, Yongjun Wang, and Zhi Li. Calibration of tri-axial magnetometer in magnetic compass using vector observations. In *2015 IEEE 28th Canadian Conference on Electrical and Computer Engineering (CCECE)*, May 2015. doi: 10.1109/ccece.2015.7129172.

Yurong Liu, Zidong Wang, and Xiaohui Liu. Robust h∞ filtering for discrete nonlinear stochastic systems with time-varying delay. *Journal of Mathematical Analysis and Applications*, 341(1):318 – 336, 2008. ISSN 0022-247X. doi: https://doi.org/10.1016/j.jmaa.2007.10.019.

F. J. Lowes. Do magnetometers measure B or H? *Geophysical Journal of the Royal Astronomical Society*, 37(1):151–155, April 1974. doi: 10.1111/j.1365-246X.1974.tb02449.x.

X. Lu, L. Xie, H. Zhang, and W. Wang. Robust Kalman filtering for discrete-time systems with measurement delay. *IEEE Transactions on Circuits and Systems II: Express Briefs*, 54(6):522–526, June 2007. ISSN 1549-7747. doi: 10.1109/TCSII.2007.892223.

R. Mahony, T. Hamel, and J. M. Pflimlin. Complementary filter design on the special orthogonal group SO(3). In *Proceedings of the 44th IEEE Conference on Decision and Control*, pages 1477–1484, Dec 2005. doi: 10.1109/CDC.2005.1582367.

R. Mahony, T. Hamel, and J. M. Pflimlin. Nonlinear complementary filters on the special orthogonal group. *IEEE Transactions on Automatic Control*, 53(5):1203–1218, June 2008. ISSN 0018-9286. doi: 10.1109/TAC.2008.923738.

A. Makni. *Fusion de données inertielles et magnétiques pour l'estimation de l'attitude sous contrainte énergétique d'un corps rigide accéléré*. PhD thesis, Université Grenoble Alpes, 2016.

F. Landis Markley. Attitude error representations for Kalman filtering. *Journal of Guidance, Control, and Dynamics*, 26(2):311–317, Mar 2003. doi: 10.2514/2.5048.

I. Markovsky, A. Kukush, and S. Van Huffel. Consistent least squares fitting of ellipsoids. *Numerische Mathematik*, 98(1):177–194, Jul 2004. ISSN 0945-3245. doi: 10.1007/s00211-004-0526-9.

D. W. Marquardt. An algorithm for least-squares estimation of nonlinear parameters. *Journal of the Society for Industrial and Applied Mathematics*, 11(2):431–441, Jun 1963. doi: 10.1137/0111030.

T. Matolcsi and P. Ván. Can material time derivative be objective? *Physics Letters A*, 353(2):109 – 112, 2006. ISSN 0375-9601. doi: 10.1016/j.physleta.2005.12.072.

T. Michel, H. Fourati, P. Genevès, and N. Layaïda. A comparative analysis of attitude estimation for pedestrian navigation with smartphones. In *2015 International Conference on Indoor Positioning and Indoor Navigation (IPIN)*, pages 1–10, Oct 2015. doi: 10.1109/IPIN.2015.7346767.

K. Mohamadabadi. *Anisotropic Magnetoresistance Magnetometer for inertial navigation systems*. PhD thesis, Ecole Polytechnique X, 2013.

K. Mohamadabadi and M. Hillion. An automated indoor scalar calibration method for three-axis vector magnetometers. *IEEE Sensors Journal*, 14(9):3076–3083, Sep 2014. doi: 10.1109/jsen.2014.2322396.

K. Mohamadabadi, C. Coillot, and M. Hillion. New compensation method for cross-axis effect for three-axis amr sensors. *IEEE Sensors Journal*, 13(4):1355–1362, April 2013a. ISSN 1530-437X. doi: 10.1109/JSEN.2012.2236511.

K. Mohamadabadi, A. Jeandet, M. Hillion, and C. Coillot. Autocalibration method for anisotropic magnetoresistive sensors using offset coils. *IEEE Sensors Journal*, 13(2):772–776, Feb 2013b. ISSN 1530-437X. doi: 10.1109/JSEN.2012.2227595.

J.-O. Nilsson, I. Skog, and P. Handel. Performance characterisation of foot-mounted ZUPT-aided INSs and other related systems. In *International Conference on Indoor Positioning and Indoor Navigation (IPIN)*, pages 1 – 7, Zurich, 2010. ISBN http://id.crossref.org/isbn/978-1-4244-5862-2. doi: 10.1109/ipin.2010.5646939.

Hongfeng Pang, Shitu Luo, Qi Zhang, Ji Li, Dixiang Chen, Mengchun Pan, and Feilu Luo. Calibration of a fluxgate magnetometer array and its application in magnetic object localization. *Measurement Science and Technology*, 24(7):075102, May 2013. doi: 10.1088/0957-0233/24/7/075102.

N. Praly, P-J Bristeau, J. Laurent-Varin, and N. Petit. Using distributed magnetometry in navigation of heavy launchers and space vehicles. In *Progress in Flight Dynamics, Guidance, Navigation, Control, Fault Detection, and Avionics*, volume 6, pages 45–54. EDP Sciences, 2013.

Won-Sang Ra, Seung-Hee Jin, Tae-Sung Yoon, and Jin-Bae Park. Recursive robust h_∞ filtering within the framework of set-valued estimation. In *2004 43rd IEEE Conference on Decision and Control (CDC) (IEEE Cat. No.04CH37601)*, volume 5, pages 5182–5187 Vol.5, Dec 2004. doi: 10.1109/CDC.2004.1429630.

J.-C. Radix and B. de Cremiers. *Systemes inertiels à composant liés: "Strap-down"*. Cépaduès, 1991.

V. Renaudin and C. Combettes. Magnetic, acceleration fields and gyroscope quaternion (magyq)-based attitude estimation with smartphone sensors for indoor pedestrian navigation. *Sensors*, 14(12):22864–22890, 2014.

V. Renaudin, M.H. Afzal, and G. Lachapelle. Complete triaxis magnetometer calibration in the magnetic domain. *Journal of Sensors*, 2010:1–10, 2010. doi: 10.1155/2010/967245.

P. Ripka. *Improving the Accuracy of Magnetic Sensors*, pages 45–60. Springer Berlin Heidelberg, Berlin, Heidelberg, 2008. ISBN 978-3-540-69033-7. doi: 10.1007/978-3-540-69033-7_3.

P. Ripka and M. Butta. Origin of the crossfield effect in amr sensors. *Sensor Letters*, 7(3):259–262, 2009. ISSN 1546-198X. doi: doi:10.1166/sl.2009.1036.

P Ripka, M Janosek, M Butta, SW Billingsley, and E Wakefield. Crossfield effect in magnetic sensors. In *Sensors, 2009 IEEE*, pages 1860–1863, 2009.

H. Rue and L. Held. *Gaussian Markov random fields: theory and applications*. Number 104 in Monographs on Statistics and Applied Probability. CRC press, 2005.

R. Sameni. A linear Kalman notch filter for power-line interference cancellation. In *16th CSI International Symposium on Artificial Intelligence and Signal Processing*, pages 604–610, Shirez, Iran, 2012. doi: 10.1109/AISP.2012.6313817.

Paul G. Savage. *Strapdown Analytics by Paul G. Savage*. Strapdown Associates, 2000. ISBN 0971778604.

Guobin Jacky Shen, Chunshui Zhao, and Feng Zhao. Indoor location-finding using magnetic field anomalies, April 26 2016. US Patent 9,326,103 B2.

I. Skog, G. Hendeby, and F. Gustafsson. Magnetic odometry - a model-based approach using a sensor array. In *21st International Conference on Information Fusion (FUSION)*, pages 794–798, Cambridge, United Kingdom, July 2018. doi: 10.23919/ICIF.2018.8455430.

S. A. Smolyak. Quadrature and interpolation formulas for tensor products of certain classes of functions. In *Soviet. Math. Dokl.*, volume 4, pages 240–243, 1963.

W. Storms, J. Shockley, and J. Raquet. Magnetic field navigation in an indoor environment. *Ubiquitous Positioning Indoor Navigation and Location Based Service*, pages 1–10, 2010. doi: 10.1109/upinlbs.2010.5653681.

W. F. Storms. Magnetic field aided indoor navigation. Technical report, Air Force Inst. of Tech. Wright-Patterson AFB OH Graduate School of Engineering and Management, 2009.

U. Theodor, U. Shaked, and C. E. de Souza. A game theory approach to robust discrete-time h infin;-estimation. *IEEE Transactions on Signal Processing*, 42(6): 1486–1495, Jun 1994. ISSN 1053-587X. doi: 10.1109/78.286964.

L. C. Thornton and G. J. Bierman. $UDU^\top$ Covariance Factorization for Kalman Filtering. In C.T. LEONDES, editor, *Advances in Theory and Application*, volume 16 of *Control and Dynamic Systems*, pages 177 – 248. Academic Press, 1980. doi: https://doi.org/10.1016/B978-0-12-012716-0.50011-X.

M. Toda and R. Patel. Bounds on estimation errors of discrete-time filters under modeling uncertainty. *IEEE Transactions on Automatic Control*, 25(6):1115–1121, Dec 1980. ISSN 0018-9286. doi: 10.1109/TAC.1980.1102502.

S. Turner, M. J. Hall, S.A. Harmon, and N. Hillier. Calibration of a novel three-axis fluxgate gradiometer for space applications. *IEEE Transactions on Magnetics*, 51 (1):1–4, Jan 2015. doi: 10.1109/tmag.2014.2360614.

J. F. Vasconcelos, G. Elkaim, C. Silvestre, P. Oliveira, and B. Cardeira. Geometric approach to strapdown magnetometer calibration in sensor frame. *IEEE Transactions on Aerospace and Electronic Systems*, 47(2):1293–1306, April 2011. ISSN 0018-9251. doi: 10.1109/TAES.2011.5751259.

J.F. Vasconcelos, G. Elkaim, C. Silvestre, P. Oliveira, and B. Cardeira. A geometric approach to strapdown magnetometer calibration in sensor frame. *IFAC Proceedings Volumes*, 41(1):172 – 177, 2008. ISSN 1474-6670. doi: https://doi.org/10.3182/20080408-3-IE-4914.00031. 2nd IFAC Workshop on Navigation, Guidance and Control of Underwater Vehicles.

M. Verhaegen and P. Van Dooren. Numerical aspects of different kalman filter implementations. *IEEE Transactions on Automatic Control*, 31(10):907–917, Oct 1986. ISSN 0018-9286. doi: 10.1109/TAC.1986.1104128.

D. Vissière, A. Martin, and N. Petit. Using distributed magnetometers to increase imu-based velocity estimation into perturbed area. In *Conference on Decision and Control (CDC)*, pages 4924–4931, New Orleans, LA, 2007a. doi: 10.1109/CDC.2007.4434809.

D. Vissière, A. Martin, and N. Petit. Using magnetic disturbances to improve imu-based position estimation. In *European Control Conference (ECC)*, pages 2853–2858, Kos, 2007b.

D. Vissière, A. Martin, and N. Petit. Système fournissant la vitesse et la position d'un corps en utilisant les variations du champ magnétique évaluées grâce aux mesures de un ou des magnétomètres et de une ou des centrales inertielles. *Patent FR2914739 (A1)*, 2008.

N. Wahlström, M. Kok, T. B. Schön, and F. Gustafsson. Modeling magnetic fields using gaussian processes. In *2013 IEEE International Conference on Acoustics, Speech and Signal Processing*, pages 3522–3526, May 2013. doi: 10.1109/ICASSP.2013.6638313.

Hong Wan. Magnetic field sensing device having integral coils for producing magnetic fields, September 14 1999. US Patent 5,952,825.

S. Willard. *General Topology.* Dover Publications, Inc., 2004. ISBN 0486434796.

O. J. Woodman. An introduction to inertial navigation. Technical report, University of Cambridge, Computer Laboratory, 2007.

Deng Yang, Zheng You, Bin Li, Wenrui Duan, and Binwen Yuan. Complete tri-axis magnetometer calibration with a gyro auxiliary. *Sensors*, 17(6):1223, 2017.

T. Yoshida, M. Higuchi, T. Komuro, and H. Kado. Calibration system for a multichannel squid magnetometer. In *Proceedings of 16th Annual International Conference of the IEEE Engineering in Medicine and Biology Society*, Baltimore, MD, USA, Nov 1994. doi: 10.1109/iembs.1994.411802.

A. Zikmund, P. Ripka, R. Ketzler, H. Harcken, and M. Albrecht. Precise scalar calibration of a tri-axial Braunbek coil system. *IEEE Transactions on Magnetics*, 51 (1):1–4, Jan 2015. ISSN 0018-9464. doi: 10.1109/TMAG.2014.2357783.

Abbreviations

ADC Analog Digital Converter. 34, 36

AHRS Attitude and Heading Reference System. 106

AMR Anisotropic Magneto-Resistance. 36, 38, 42, 46, 69, 129, 160

EKF Extended Kalman Filter. xiv, 3–5, 72, 74, 75, 80, 81, 83, 86, 89, 91–94, 98, 99, 102, 111, 113–116, 119, 124, 161

FPU Floating-Point Unit. 34, 73, 75, 99, 101, 102

IMU Inertial Measurement Unit. 2, 12, 120

MEKF Multiplicative EKF. 74, 76, 83, 111

MEMS Microelectromechanical Systems. 1, 2, 4, 12, 14, 21, 28, 31, 34, 37, 59, 72, 89, 99

MIDR Magneto-Inertial Dead-Reckoning. xi, xvii, 2–5, 10, 12, 17–19, 21, 23, 31, 34, 36, 37, 57, 72, 75, 89, 98, 99, 101, 102, 123, 124, 128, 129, 146, 159–163

MIMU Magneto-Inertial Measurement Unit. 34–36, 128

MINAV Magneto-Inertial NAVigation. xiii, 3, 22

PDR Pedestrian Dead Reckoning. 2, 3, 31, 119, 120, 161

SLAM Simultaneous Localization and Mapping. 2, 102

SQUID Superconducting QUantum Interference Device. 129

VIN Visual Inertial Navigation. 2, 3, 161

WGM World Gravity Model. 15

WMM World Magnetic Model. 112